Trace element signatures in rutile: characterization of standards and applications to accessory mineral behavior in metamorphic rocks

George Luiz Luvizotto

Trace element signatures in rutile: characterization of standards and applications to accessory mineral behavior in metamorphic rocks

INAUGURAL-DISSERTATION

zur Erlangung der Doktorwürde der

Mathematisch-Naturwissenschaftlichen Gesamtfakultät

der Ruprecht-Karls-Universität

Heidelberg vorgelegt von

Master of Science in Geology

George Luiz Luvizotto

aus Cerquilho – SP, Brasilien

Heidelberg, im Oktober 2008

Gutachter:
PD Dr. Thomas Zack
Prof. Dr. Gerhard Brey

Tag der mündlichen Prüfung: 12.12.2008

There are places I remember
All my life, though some have changed
Some forever not for better
Some have gone and some remain
All these places had their moments
With lovers and friends
I still can recall
Some are dead and some are living
In my life I've loved them all

Lennon and McCartney

All beings so far have created something beyond themselves; and do you want to be the ebb of this great flood and even go back to the beasts rather than overcome man? What is the ape to man? A laughingstock or a painful embarrassment. And man shall be just that for the overman: a laughingstock or a painful embarrassment. . .

Friedrich Wilhelm Nietzsche
(Also Sprach Zarathustra, 1883)

To my lovely wife, Paulinha

Contents

Contents

List of Figures

List of Tables

Summary

This study focuses on the trace element composition of rutile, a frequent accessory mineral in various rock types (mafic, pelitic and felsic protoliths; common at blueschist-, eclogite- and granulite-facies conditions) and one of the most stable minerals in sedimentary environments. Rutile is an important carrier of highly charged elements, such as Ti, V, Cr, Zr, Nb, Sn, Sb, Hf, Ta and W. Due to these characteristics rutile has attracted significant interest in various fields of geology, *e.g.*, as a likely controller of Nb and Ta budgets in subduction zones. Furthermore, it is useful as a geothermometer (Zr incorporation is strongly temperature dependent in quartz- and zircon-bearing systems), and as a geochronological tool (U-Pb and (U-Th)/He dating), and to assess the nature of an initial source rock in sediment provenance studies (Nb and Cr contents can de used to distinguish between mafic and felsic sources).

An increasing number of today's geochemical studies, which include the investigations presented here, are based on microanalysis of trace elements, several of which are carried out *in-situ*. All of these techniques depend on calibration using a homogeneous material with well documented chemical concentration. In this sense, having a **rutile standard** is a key issue. A set of rutile crystals were investigated in order to find rutiles suitable for use as mineral standards. Trace element concentrations of 15 elements (V, Cr, Fe, Zr, Nb, Mo, Sn, Sb, Hf, Ta, W, Lu, Pb, Th and U) as well as Pb and Hf isotope data are presented for four large (centimeter size) and relatively homogeneous rutile grains. Analytical techniques used are SIMS, EMP, LA–ICP–MS, ID–MC–ICP–MS and TIMS. For most elements, homogeneity is usually within $\pm 10\%$ and variations are occasionally less than ($\pm 5\%$), particularly in the core of two of the studied grains. The trace element concentrations of the grains span a broad compositional range (*e.g.*, Zr concentrations are ca. 4, 100, 300 and 800 ppm). Provisional concentration values, calculated based on the homogeneity of the element and agreement between techniques, are presented for Zr, Nb, Sn, Sb, Hf, Ta, W and U. One of the studied grains has a relatively high U concentration (ca. 30 ppm) and rather constant U–Pb ages (1085.1 to 1096.2 Ma, $^{207}Pb/^{235}U$ ages and 1086.3 to 1096.6 Ma, $^{206}Pb/^{238}U$ ages), favoring its application as an age standard for U-Pb rutile dating. The studied rutiles are useful as mineral standards in for *in-situ* rutile measurements, particularly for Zr–in–rutile thermometry, quantitative provenance studies (Nb and Cr concentrations as an index of source

rock type) and U–Pb dating. The efforts in characterizing a set of rutile standards are not only relevant for the scientific community. It also provides the analytical background for the results presented here.

Following the characterization of standards, textural observations and *in-situ* analyses were used to investigate trace element behavior during prograde and retrograde metamorphic reactions involving rutiles. The investigated samples derive from two well studied localities: the Ivrea-Verbano Zone (Italy) and the Erzgebirge (Germany).

The **Ivrea-Verbano Zone** is a classic granulite area and rocks from the Strona and d'Ossola Valleys are an example of the amphibolite to granulite facies transition, where rutile growth is associated with the breakdown of high-Ti biotite. Rutile bearing rocks show a rich inventory of textures that allow for the investigation of trace element behavior in response to prograde rutile growth, and the effect of post-peak processes on rutile chemistry. Nb concentrations in rutile from lower grade samples show a larger spread (from 500 to 5000 ppm within one sample) when compared to those from higher grades. This pattern can be modeled using prograde rutile growth formed from biotite breakdown. Zr concentrations in rutile are characterized by an anomalously large spread and a bimodal distribution. Maximum Zr concentrations increase according to the general metamorphic gradient known for this area. Temperatures (from Zr-in-rutile thermometry), although feasible, are considerably higher than previous calculations (increasing from ca. 850 to 930°C). A second cluster of Zr concentrations in rutile occurs at rather constant concentrations (ca. 1000 ppm) for all localities and is interpreted to be related to intense fluid influx at high temperature and/or to post-peak diffusional resetting favored by slow cooling rates. Alteration textures, characterized by a complex network of micro-veins, are evidence for the late fluid influx. The fluid strongly affected the rutiles, which is evidenced by corrosion of older rutile grains and the formation of rutile veinlets.

In the **Ezgebirge**, metamorphic texture support prograde rutile growth from ilmenite in low- to medium-grade ($\sim$430-630°C) metasedimentary rocks. Newly crystallized rutiles occur as polycrystalline aggregates that mimic the shape of the ilmenites. *In-situ* trace element data show that rutiles from the lowest grade samples ($\sim$480°C) mirror the Nb/Ti ratio of ilmenite. Under these conditions, rutile did not equilibrate its chemistry with the remaining ilmenites. In higher grade samples, rutiles show a larger scatter in Nb and have Nb/Ti ratios higher than relict ilmenite. In these rocks, the Nb pattern can be modeled using prograde rutile growth from ilmenite, in a model similar to the one applied to granulites from the the Ivrea-Verbano Zone. Results indicate that rutiles from these rocks were able to reequilibrate its chemistry with the remaining ilmenites. Newly formed rutiles yield tem-

peratures (from $\sim$500 to 630°C) that are in agreement with the metamorphic conditions published for the studied rocks. Detrital rutile grains, identified by their distinct chemical composition (high Zr and Nb contents) and textures (single grains surrounded by fine grained ilmenites), occur in quartzites from the medium-grade rocks ($\sim$530°C). This confirms models in which detrital rutiles survive in quartzites to higher metamorphic grade compared to rutiles in metapelites. Preliminary calculations based on the grain size distribution of rutiles in the studied rocks show that quartzites are probably the main source of rutiles in sediments derived from low-grade metamorphic sequences, even if the occurrence of quartzite is minor.

Part of the data obtained during the development of this thesis contributed to **other publications** related, directly or indirectly, to its topic. For example, to evaluate how well the Zr-in-rutile thermometer can be applied to eclogites; to evaluate the applicability of rutile trace element geochemistry to provenance studies; and to characterize the occurrence and stability of coesite-bearing tourmaline in ultra-high pressure metamorphic rocks.

Kurzfassung

Diese Studie befast sich mit dem Einbau von Spurenelementen in Rutil, ein akzessorischer Bestandteil vieler Gesteinstypen (in metabasischen, metapelitischen und felsischen Lithologien; allgemein unter Blauschiefer-, Eklogit- und Granulit-fazies Bedingungen) und eines der widerstandsfähigsten Minerale in sedimentären Systemen. Rutil ist ein wichtiger Träger von HFS Elementen, (Ti, V, Cr, Zr, Nb, Sn, Sb, Hf, Ta und W). Wegen dieser Merkmale hat Rutil das Interesse geweckt auf verschiedenen Gebieten von Geologie, z.B. spielt Rutil eine große Rolle bei Modellen von Subduktionszonen, in denen es die Gehalte von Nb und Ta kontrolliert. Außerdem ist es als Geothermometer nützlich (markante Temperaturabhängigkeit des Zr-Gehaltes im Rutil bei Koexistenz von Quarz und Zirkon); als geeigneter Kandidat für die Rekonstruktion der Liefergebietslithologie (Abgrenzung aus metabasischen und metapelitischen Lithologien ist möglich mittels Nb-Cr Verhältnisse); und in der Geochronologie (U-Pb sowie (U-Th)/He Datierung).

Eine steigende Zahl geochemischer Studien basieren auf der Mikroanalyse von Spurelementen, die meisten hiervon werden *in-situ* durchgeführt. Alle diese Techniken hängen von der Kalibrierung unter Verwendung eines homogenen Standards mit gut dokumentierten chemischen Konzentrationen ab. Deshalb war es eine wichtige Aufgabe, einen Rutilstandard zu etablieren.

Ein Vielzahl von Rutilkristallen wurden charakterisiert, um geeignete Rutile zu finden, die als **Mineralstandards** verwendet werden können. Spurenelementkonzentrationen von 15 Elementen (V, Cr, Fe, Zr, Nb, Mo, Sn, Sb, Hf, Ta, W, Lu, Pb, Th und U) sowie Pb- und Hf-Isotopdaten wurden für vier verhältnismäßig homogene und große (Zentimetergröße) Rutilkörner gemessen. Die verwendeten analytischen Techniken sind SIMS, EMP, LA–ICP–MS, ID–MC–ICP–MS and TIMS. Für die meisten Elemente ist die Homogenität innerhalb von $\pm10\%$, mit zum Teil erheblich geringeren Variationen ($\pm5\%$), besonders im Kern von zwei Rutilen. Die Spurenelementkonzentrationen der Kristalle decken ein großes Konzentrationsintervall ab (z.B., liegen die Zr-Konzentrationen bei ca. 4, 100, 300 und 800 ppm). Vorläufige Konzentrationswerte, berechnet anhand der Homogenität der Elemente und dem Vergleich zwischen den Techniken, werden für Zr, Nb, Sn, Sb, Hf, Ta, W und U angegeben. Einer der studierten Kristalle hat eine hohe U-Konzentration (ca. 30 ppm) und konstante U-Pb Alter (1085.1 zu 1096.2 Ma für ^{207}Pb/^{235}U Alter und 1086.3 zu 1096.6 Ma für ^{206}Pb/^{238}U Alter). Dies macht seine Anwendung als

Altersstandard für die U-Pb Rutildatierung möglich. Die studierten Rutile sind als Mineralstandard für *in-situ* Spurenelementmessungen an Rutil geeignet, besonders für die Zr-in-Rutil Thermometrie, für die quantitative Liefergebietsanalyse (metabasische und metapelitische Lithologien können differenziert werden aufgrund ihrer Nb und Cr Konzentrationen) und für die U-Pb Datierung. Die Bemühungen, Rutilstandards bereitzustellen, sind nicht nur für die wissenschaftliche Gemeinschaft relevant. Es bildet auch den analytischen Hintergrund für die Resultate, die hier dargestellt werden.

Nach der Charakterisierung von Standards wurden texturelle Beobachtungen und *in-situ* Analysen verwendet, um das Verhalten von Spurenelementen in den metamorphen Reaktionen, die Rutile mit einbeziehen, zu studieren. Die untersuchten Proben stammen aus zwei gut studierten Regionen: Der Ivrea–Verbano Zone (Italien) und das Erzgebirge (Deutschland).

Die **Ivrea-Verbano Zone** ist eine klassische Granulitlokalität, und Gesteinen von Val Strona und Val d' Ossolazeigen den Übergang an von der Amphibolit- zur Granulit-Fazies. In diesen Gesteinen kristallisiert Rutil in Verbindung mit dem Zusammenbruch von Ti-reichem Biotit. Rutil-führende Gesteine erschließen ein reichhaltiges Inventar von Strukturen. Sie erlauben die Untersuchung des Spurenelementverhaltens in Bezug auf prograde Rutilkristallisation und den Effekt retrograder Prozesse auf die Rutilchemie. Nb-Konzentrationen im Rutil von den niedriggradiger Proben zeigen eine größere Variation (von 500 bis 5000 ppm innerhalb einer Probe) wenn sie mit Rutilen der höhergradigen Proben verglichen werden. Dieses Verhalten kann modelliert werden durch prograde Rutilkristallisation, verbunden mit dem Zusammenbruch von Biotit. Zr–Konzentrationen im Rutil werden durch eine große Variation und einer bimodale Verteilung charakterisiert. Maximale Zr-Konzentrationen erhöhen sich entsprechend des metamorphen Gradienten, der für dieses Gebiet bekannt ist. Die berechneten Temperaturen (vom Zr-in-Rutil Thermometrer) sind beträchtlich höher als vorhergehende Berechnungen (zunehmend von ca. 850 bis 930°C), jedoch konsistent mit den petrologischen Beobachtungen. Eine zweite Gruppe von Zr-Konzentrationen im Rutil tritt bei konstanter Konzentration in allen Proben auf und wird dahingehend gedeutet, mit intensivem Fluidflüssen unter Hochtemperaturbedingungen und/oder mit Reäquilibrierung durch Diffusion unter niedrigen Abkühlraten in Zusammenhang gebracht zu werden. Alterationsetxturen, charakterisiert durch ein kompliziertes Netzwerk der Mikroadern, sind Beweis für den späten Einfluss von Fluiden. Die Fluide beeinflußten stark die Rutile, wie mit der Korrosion der älteren Rutilkörner und der Bildung von Rutil-Äderchen bewiesen wird.

Im **Ezgebirge** liefern metamorphe Texturen Beweise für prograde Rutil-Bildung aus Ilmenit in niedrig- bis mittelgradigen Metasedimenten (ca 480-630°C). Neu-

kristallisierte Rutile kommen als polykristalline Aggregate vor, die die Formvon Ilmenit nachbilden. *In-situ* Spurenelementdaten zeigen, dass Rutile von den niedriggradigsten Proben (ca 480°C) das Nb/Ti Verhältnis des Ilmenits widerspiegeln. Unter diesen Bedingungen sind die Rutile nicht chemisch äquilibriert mit den verbliebenen Ilmeniten. In höhergradigen Proben zeigen Rutile eine größere Variation der Nb-Konzentrationen und haben höhere Nb/Ti Verhältnisse als reliktische Ilmenite. In diesen Gesteinen kann das Nb Verhalten durch prograde Rutil-Bildung vom Ilmenit modelliert werden mit dem gleichen Modell, das an den Granuliten von der Ivrea-Verbano Zone angewendet wurde.Die Resultate zeigen an, dass Rutile von diesen Gesteinen mit den restlichen Ilmeniten äquilibriert sind. Neu gebildete Rutile zeigen Temperaturen von 500 bis 630°C an, die in Übereinstimmung mit den publizierten metamorphen Bedingungen der studierten Gesteinen sind. Detritische Rutile treten in Quarziten von mittelgradigen Gesteinen auf ($\sim$530°C), und sind charakterisert durch ihren eindeutigen Chemismus (hoher Zr- und Nb-Gehalt) und Strukturen (einzelne Kristalle umgeben von feinkörnigem Ilmenits). Dies bestätigt Modellen, nach denen detritische Rutile in Quarziten noch in höheren metamorphen Graden auftreten können verglichen mit Rutilen in Metapeliten.Vorläufige Berechnungen, basierend auf der Korngrößenverteilung der Rutile in den studierten Gesteinen, zeigen, dass Quarzite vermutlich die Hauptquelle der Rutile in den Sedimenten sind, die von niedriggradiger Metasedimenten stammen, auch wenn Quarzite nur in geringen Mengen auftreten.

Ein Teil der Daten, die während der Entwicklung dieser Abhandlung gesammelt wurden, haben zu **weiteren Publikationen** geführt, die sich direkt oder indirekt auf das Dissertationsthema beziehen. Zum Beispiel wurde ausgewertet, wie gut das Zr-in-Rutil Thermometer an Eklogiten angewendet werden kann; wie Spurenelemente in Rutil bei Liefergebietsanalysen Anwendung finden können; und es wurde das Vorkommen und die Stabilität von Coesit-haltigen Tourmalinen in Ultrahochdruckmetamorphen Gesteinen charakterisiert.

1 Introduction

1.1 Structure of this dissertation

This doctoral work consists of five chapters. It begins with a short introduction that summarizes its main objectives, analytical methods, essential results and related conclusions. The next three chapters represent scientific articles that were written by the author. During the development of this thesis, the author contributed to three other scientific articles. A summary of these publications are presented in the last chapter (full copies are presented in Appendix C).

1.2 Importance of rutile

Rutile (TiO_2) is one of the major Ti-phases and frequently occurs as an accessory mineral in diverse metamorphic and igneous rocks, siliciclastic sediments, placer deposits and hydrothermal ore deposits. It is the most common natural form of TiO_2, with two rarer polymorphs anatase; and brookite. It crystallizes in a tetragonal structure, with each Ti^{4+} ion surrounded by six oxygens at the corners of a slightly distorted regular octahedron. Each oxygen is surrounded by three Ti^{4+} ions and lie in a plane at the corners of an approximately equilateral triangle (Deer *et al.*, 1992). This arrangement results in a primitive tetragonal unit cell (Fig. 1.1). The local arrangement of the anions and cations leads to the (6,3)-coordination in this structure

Rutile is an important carrier for several highly charged trace elements (Graham & Morris, 1973; Haggerty, 1991; Deer *et al.*, 1992; Smith & Persil, 1997; Rice *et al.*, 1998). In eclogites, 1 modal% of rutile can carry more than 90% of the whole rock content for Ti, Nb, Ta, Sb and W and considerable amounts (5-50% of the whole rock content) of V, Cr, Mo and Sn (Zack *et al.*, 2002). Rutile has attracted significant
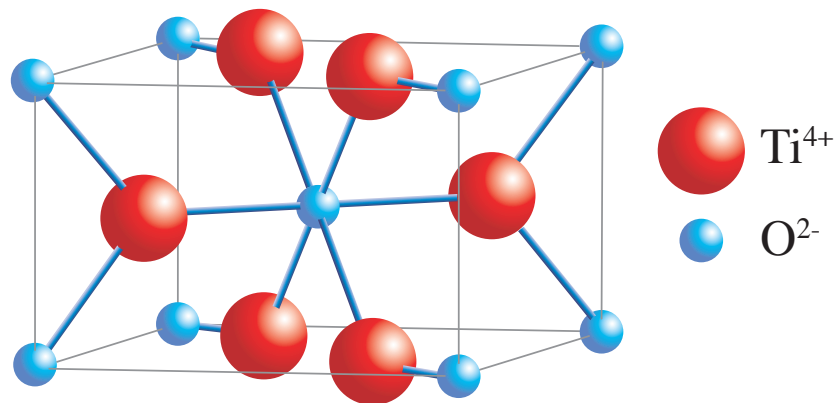
Figure 1.1 The rutile, TiO$_2$, structure. Unit cell parameters: a=4.584, and c=2.953

interest as a likely controller of Nb and Ta budgets in subduction zone processes (Saunders *et al.*, 1980; McDonough, 1991; Brenan *et al.*, 1994; Stalder *et al.*, 1998; Münker, 1998; Foley *et al.*, 2000; Klemme *et al.*, 2005, among others). It has also been shown that the Zr incorporation in rutile is strongly temperature dependent (Zack *et al.*, 2004b; Watson *et al.*, 2006; Tomkins *et al.*, 2007) in quartz- and zircon-bearing systems. Rutile is also used in U-Pb (*e.g.*, Mezger *et al.*, 1989; Davis, 1997; Mezger *et al.*, 1993; Li *et al.*, 2003; Vry & Baker, 2006) and (U-Th)/He dating (Crowhurst *et al.*, 2002; Stockli *et al.*, 2007). Its trace element geochemistry is also suitable for sediment provenance studies where, *e.g.*, Nb and Cr contents can be used to distinguish between metamafic and metapelitic rocks, and Zr content indicates metamorphic peak temperatures of the source rocks (Zack *et al.*, 2002, 2004a; Stendal *et al.*, 2006; Triebold *et al.*, 2007; Meinhold *et al.*, 2008).

The facts presented above motivated the development of a project to thoroughly investigate the rutile geochemistry.

1.3 The rutile project

This thesis is part of the project "Trace elements in rutile: Petrogenetic factors and their application to provenance studies". The project was financially supported by

the *Deutsche Forschungsgemeinschaft* – DFG (projects ZA 285/2 and EY 23/3). Its main aim is to investigate the trace element composition of rutiles from rocks and modern sands from the same drainage area. The results are used not only to assess previously established applications of rutile (*e.g.*, *single-grain* thermometer, proxy for source rock lithology) but also to extend its applications to other research fields (*e.g.*, trace element distribution and accessory mineral behavior during prograde and retrograde metamorphic reactions). Another important goal of the project is to promote the synergy between important fields of geology such as, geochemistry, metamorphic petrology, sedimentology and stratigraphy.

The project is composed of two groups. The metamorphic petrology group (PD Dr. T. Zack, MSc. G.L. Luvizotto), based in Heidelberg (Mineralogisches Institut, Universität Heidelberg), is responsible for the characterization of the trace element signatures in rutiles from metamorphic rocks. In Göttingen (Geowissenschaftliches Zentrum, Universität Göttingen), the sedimentology group (Prof. Dr. H. von Eynatten, Dipl.-Geow. S. Triebold) investigates geochemistry of detrital rutiles.

1.4 Scope of the study

The current work has two main objectives. It starts with the characterization of rutile crystals as potential standards for microanalysis (Chapter 2). The efforts in characterizing a set of rutile standards are not only relevant for the scientific community (splits of the crystals are distributed upon request). It also gives a strong analytical background for the results presented here. Furthermore, it is the backbone of the main project, in which the comparison of data obtained in different laboratories and by different techniques is a key issue (see, *e.g.*, Section 5.2).

The second major aim is to investigate trace element systematics in metamorphic rutiles. These results are used to assess trace element partitioning and accessory mineral behavior in metamorphic rocks. For example, petrographic textures are linked with trace element concentration in accessory phases involved in both prograde and retrograde metamorphic reactions (see Chapters 3 and 4). The data is also used to evaluate how well the Zr-in-rutile thermometer can be applied to

different rock types (see chapters 3 and 4 and Section 5.1) and detrital sediments (Section 5.2).

Moreover, based on the results obtained for metamorphic rutiles (textural relationships, grain-size, trace element composition, among others), the discussions are extended to other fields of interest. For example, we discuss how fluid can mobilize elements that are frequently interpreted to be immobile (such as Nb, Ti and Zr) and how to assess high temperature records in granulites (Chapter 3). We also approach aspects that are relevant in sediment provenance studies, taking into considerations the data obtained for rutiles from low-grade rocks (chapters 4).

1.5 Studied areas

The studied rutiles were collected from two different localities, the Ivrea-Verbano Zone (Northern Italy) and the Erzgebirge (Germany). These are well studied areas and are characterized by the occurrence of several rocks types that span a broad range of pressures (P) and temperatures (T).

1.5.1 Ivrea-Verbano Zone

The Ivrea-Verbano Zone (Fig. 1.2) in the Southern Alps is one of the best preserved sections through lower continental crust. It is delimited to the northwest by the Insubric Line, a major Neogene shear zone that juxtaposes pre-Alpine and Alpine structures and rocks (Schmid et al., 1987). To the southeast, the boundary of the Ivrea-Verbano Zone is tectonically delimited by the Cossato-Mergozzo-Brissago tectonic discontinuity (Boriani et al., 1990). The metamorphic foliation and primary banding are mostly steeply dipping and show a NE-SW trend, broadly parallel to the Insubric Line. The area is traditionally divided into two main units: a large basic intrusive complex of Permian age (the Mafic Formation of Zingg, 1980; Rivalenti et al., 1981, among others) and a sequence of metasedimentary rocks interlayered with bands of mafic rocks. However, this division disregards distinct lithological units occurring in the area. A more detailed division of the central part of the Ivrea-Verbano Zone is presented in Fig. 1.2.
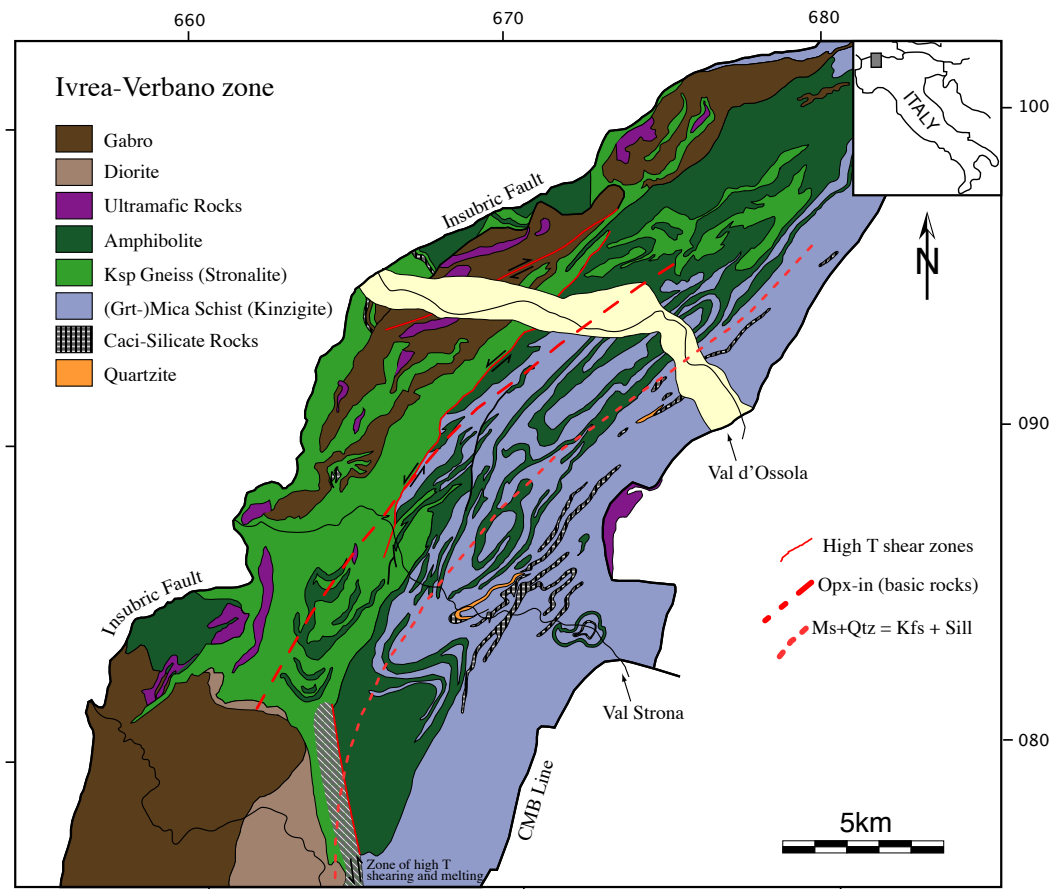
Figure 1.2 Geological map of the central part of the Ivrea-Verbano Zone. Redrawn and simplified from Rutter *et al.* (2007). Main metamorphic isograds are those presented by Zingg (1980). CMB Line = Cossato-Mergozzo-Brissago Shear Zone

Rocks, occurring in the area comprised by the Strona and d'Ossola valleys, show a metamorphic gradient with metamorphic conditions increasing from amphibolite facies in the southeast, to granulite facies in the northwest. Zingg (1980) mapped two important mineral isograds (see locations in Fig. 1.2): the muscovite-out/K-feldspar-in in metapelitic rocks and the orthopyroxene-in in mafic and intermediate rocks. In most models, the increase of metamorphic grade from southeast to northwest together with the steep foliation and primary banding has been interpreted to

be the result of an Alpine-age tilting of the Ivrea-Verbano Zone, and hence exposing a cross-section through the lower continental crust (*e.g.*, Handy *et al.*, 1999; Rutter *et al.*, 2007). Although the metamorphic grade increases more or less continuously, it has to be stressed that significant post-peak metamorphic shearing and folding is observed (Rutter *et al.*, 2007).

PT estimates of the IVZ have been presented by various authors (Zingg, 1980; Sills & Tarney, 1984; Henk *et al.*, 1997; Demarchi *et al.*, 1998; Barboza & Bergantz, 2000, among others). Maximum *PT* conditions calculated by Henk *et al.* (1997) are 810°C and 0.83 GPa and decrease to 710°C and 0.67 GPa towards the granulite to amphibolite facies boundary.

1.5.2 Ezgebirge

The Ezgebirge is situated at the northwestern border of the Bohemian Massif and is part of the metamorphic basement of the Mid-European Variscides exposed in Saxony and the northern Czech Republic (Fig. 1.3). It is characterized by a large-scale antiformal structure consisting of several tectonometamorphic units. The Erzgebirge represents a stack of five tectonometamorphic units with contrasting *P-T* histories (Willner *et al.*, 1997; Rötzler *et al.*, 1998). From the base to the top these units are: Red and Grey Gneisses Unit (RGG); Gneiss/Eclogite Unit (GEU); Micaschist/Eclogite Unit (MEU); Garnet-Phyllite Unit (GPU); and Phyllite Unit (PU). The tectonometamorphic stacking is interpreted as a result of continent-continent collision processes (deformation, metamorphism and exhumation) during the Variscan Orogeny (*e.g.*, Willner *et al.*, 1997; Rötzler *et al.*, 1998; Mingram, 1998). According to Mingram (1998), geochemical descrimination suggests that the protoliths of all metamorphic units are similar, leading to the conclusion that they represent a repetition of metasedimentary sequences. A summary of published *PT* conditions for the western part of the Ezgebirge is presented in Fig. 1.3.

The occurrence of coesite (Massonne, 2001) and micro-diamonds (Massonne, 1999) in quartz-feldspathic rocks from the GEU makes the EGB one of the few ultra-high pressure localities in the world. The occurrence of diamonds suggests that crustal rocks from Ezgebirge were subducted to depths of 100 km or more.
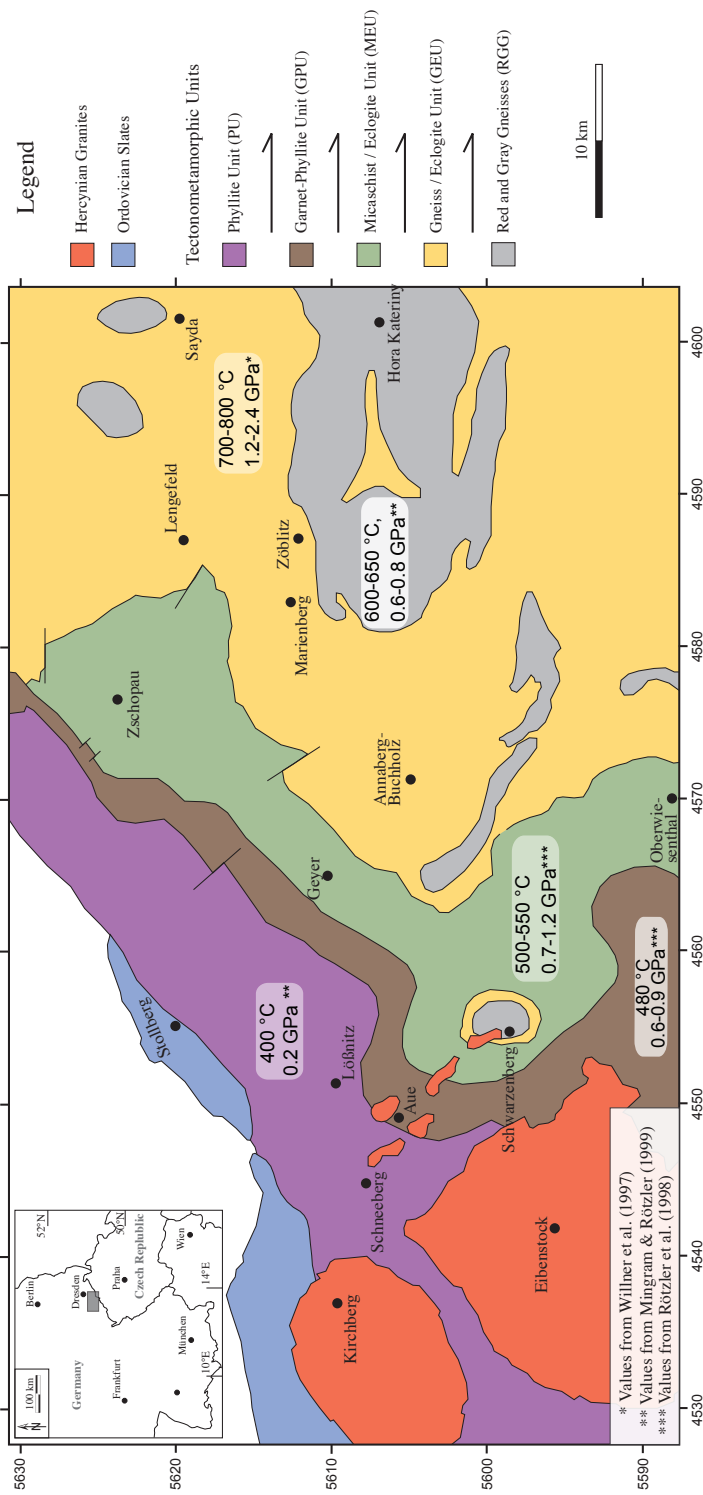
Figure 1.3 Simplified geological map of the western part of the Erzgebirge. Coordinates are provided in German coordinate system (Gauss-Krüger).

7

1.6 Main results and related conclusions

1.6.1 Characterization of rutile crystals as potential trace element and isotope mineral standards

Several large crystals (centimeter size) were analyzed in order to find rutiles suitable to be used as mineral standards. Grains were characterized with respect to their homogeneity as well as for trace element and isotope compositions. Only four out of 41 grains were designated as suitable for use as secondary mineral standards. For these grains (Sy, Diss, R19 and R10), trace element concentrations of 15 elements (V, Cr, Fe, Zr, Nb, Mo, Sn, Sb, Hf, Ta, W, Lu, Pb, Th and U) as well as Pb and Hf isotope data were obtained. Methods employed are SIMS, EMP, LA–ICP–MS, ID–MC–ICP–MS and TIMS. For most elements homogeneity is usually within ±10% and occasionally variations are even narrower (±5%), particularly in the core of two of the studied grains (R19 and R10). The trace element concentrations of the grains span a broad compositional range (*e.g.*, Zr concentrations are ca. 4, 100, 300 and 800 ppm). Provisional concentration values, calculated based on the homogeneity of the element and agreement between techniques, are presented for Zr, Nb, Sn, Sb, Hf, Ta, W and U.

Results show that trace element concentrations obtained by the techniques applied in the present work (SIMS, EMP, LA–ICP–MS, ID–MC–ICP–MS) are in good agreement. This is particularly true for Zr. For this element, concentrations obtained using for independent techniques show an outstanding agreement (Fig. 1.4). Hence, Zr-in-rutile temperature calculated based on data obtained by these techniques can be quantitatively compared.

R10 has a relatively high U concentration (ca. 30 ppm) and rather constant U–Pb ages (1085 to 1096 Ma, ^{207}Pb/^{235}U ages and 1086 to 1096 Ma, ^{206}Pb/^{238}U ages, Fig. 1.5). Moreover, LA–ICP–MS data show that the non–radiogenic Pb concentrations (measured as ^{208}Pb) are very low (average of 0.08 ppm), meaning that common Pb can be neglected for this grain. All these factors strongly favor the use of R10 as an age standard for U–Pb rutile dating.

High precision ^{176}Hf/^{177}Hf isotopic ratios and Lu concentration data, obtained
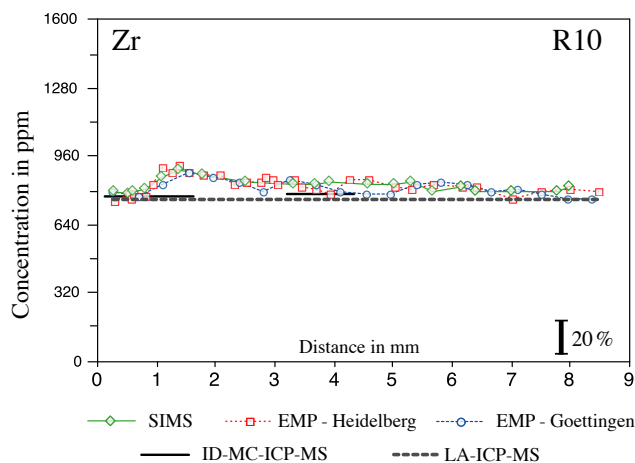
Figure 1.4 Rim-to-rim chemical profile of Zr in R10.

by ID–MC–ICP–MS, are given for R10, R19 and Diss. Since Lu concentrations in rutile are very low (no evidence of radiogenic ingrowth) and Hf concentrations can be relatively high (tens of ppm), detrital rutiles may be suitable for obtaining initial Hf isotope composition of source rocks, therefore the rutiles presented here can be used as calibration material for *in-situ* rutile Hf isotope studies.

Our efforts represent a significant step forward in finding a suitable mineral standard for rutile microanalysis and encourages not only a further search for mineral standards but also new applications of rutile in the field of geochemistry and geochronology. In this sense, the rutiles presented here are useful as mineral standards in general *in-situ* rutile measurements, particularly for Zr–in–rutile thermometry, quantitative provenance studies (Nb and Cr concentrations as an index of source rock type) and U–Pb dating.

1.6.2 Nb and Zr behavior in rutile during high-grade metamorphism and retrogression: An example from the Ivrea–Verbano Zone

Detailed textural observations and *in-situ* analyses (EMP, SIMS and LA-ICP-MS) are used to characterize trace element behavior during prograde and retrograde metamorphic reactions involving rutile.
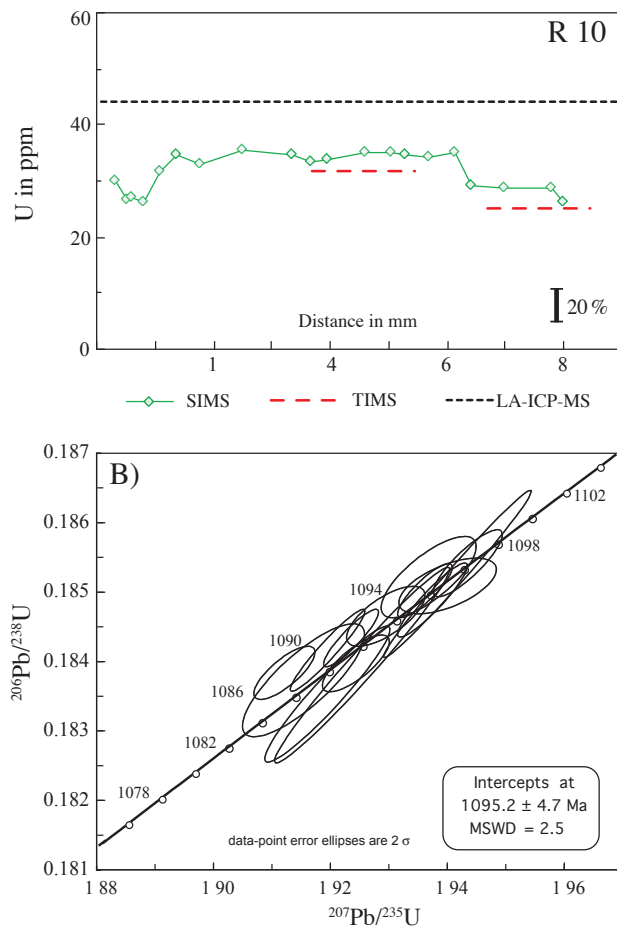
Figure 1.5 A) Rim-to-rim chemical profile of U in R10. B) U-Pb concordia plot for all analyses (TIMS) of R10.

The IVZ is a classic granulite area and rocks from the Strona and d'Ossola valleys are an example of the amphibolite to granulite facies transition. Although different rock types occur in the area, detailed sampling and petrographic work show that rutile only occurs in granulite facies paragneisses. Rutile formation is associated with a sequence of dehydration reactions, first involving muscovite (to form sillimanite and potassic feldspar) and then biotite (to form garnet and potassic feldspar) in the amphibolite to granulite facies transition. The Ti released by the breakdown of biotite leads to rutile formation, which can be described by the reac-

tion: (high-Ti) Bt + Sil + Qtz = Grt + Kfs +Rt + Melt (see also Zingg, 1980). Rutile formation from biotite is also supported by petrographic textures observed within the rocks.

Nb concentrations in rutile from lower grade samples show a larger spread (from 500 to 5000 ppm within one sample) when compared to those from higher grades. Fig. 1.6 summarizes the results obtained for the Strona Valey. This pattern can be modeled by prograde rutile growth formed from biotite breakdown (taking into consideration a $K_{DNb/Ti}^{Rt/Bt}$ of 48.7 - using partition coefficient data from LaTourrette *et al.*, 1995; Klemme *et al.*, 2005).
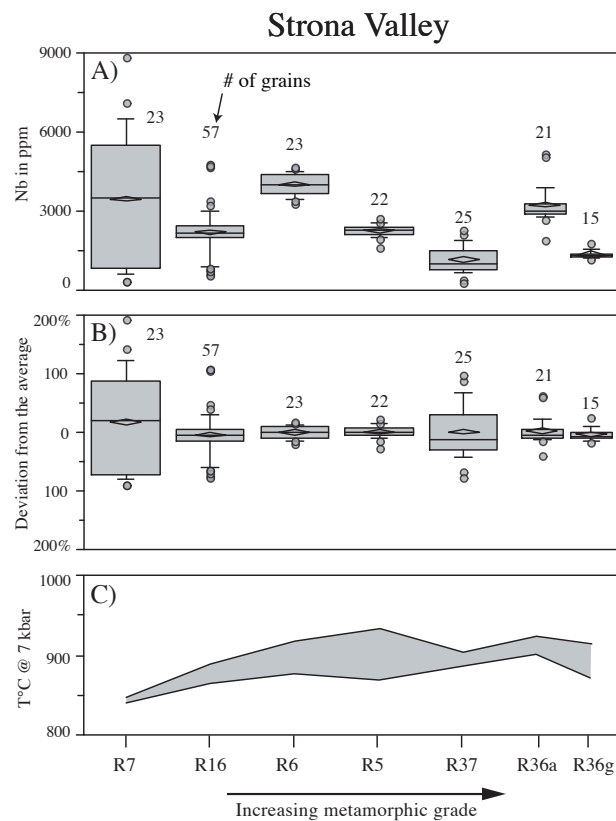
Figure 1.6 A and B - Summary of Nb concentrations (EMP, SIMS and LA-ICP-MS) obtained for the studied rutile from the Strona Valley. C - Temperatures obtained for samples from the Strona valley. Shaded area represents the interval delimited by values above the ninetieth percentile. Calculations were based on the Zr content in rutile for a pressure of 0.7 GPa (calibration of Tomkins *et al.*, 2007)

Zr concentrations in rutile are characterized by an anomalously large spread and a bimodal distribution. Maximum Zr concentrations increase according to the general metamorphic gradient known for this area. Calculated temperatures (from Zr-in-rutile thermometry), although feasible, are considerably higher than those from previous publications (increasing from ca. 850 to 930°C). Fig. 1.6c summarizes the results obtained for the Strona valey. Considering that previous calculations were mostly based on Fe-Mg exchange geothermometers and the fact that the late processes that affected the rutiles may also have changed the chemical composition of other primary phases, the high temperatures obtained are not unrealistic. As typical textural controls on the Zr concentration in rutile (*e.g.*, inclusion vs. matrix) described in the literature are not observed in our rocks, a new approach was applied for the calculation of peak temperatures where the highest concentration values were statistically selected. For granulites, this should be the preferred method instead of, *e.g.*, calculating temperature from mean Zr concentrations.

For all localities, a second cluster of Zr concentrations in rutile occurs at rather constant concentrations (ca. 1000 ppm) and is interpreted to be related to intense fluid influx at high temperature and/or to post-peak diffusional resetting favored by slow cooling rates. Alteration textures, characterized by a complex network of micro-veins, are evidence for a late influx of a K-rich fluid. The fluid strongly affected the rutiles, which is evidenced by corrosion of older rutile grains and formation of rutile veinlets (Fig. 1.7). These textures are evidence that fluids can, depending on their compositions, mobilize elements frequently interpreted to be immobile, such as Ti and Zr.

1.6.3 Rutile occurrence and trace element behavior in low- to medium-grade metasedimentary rocks

In the German Erzgebirge, low- to medium-grade rocks from the GPU and MEU show textures that support rutile crystallization from ilmenite in low-grade metamorphic conditions. As the content of Ti is higher in rutile than in ilmenite, the volume once filled up by ilmenite is not completely occupied by rutile. Moreover, as rutile cannot incorporate all the Fe present in ilmenite this element is used, to-
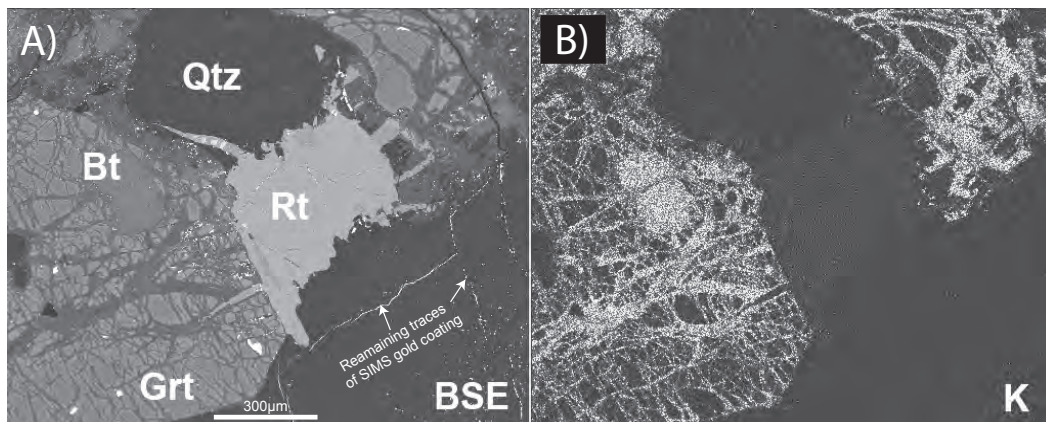
Figure 1.7 A) BSE image example of the post-peak veins present in the granulite facies rutile bearing rocks. B) Chemical composition map (EDS) for K. Higher concentrations are represented by brighter colors.

gether with the elements available in the matrix minerals (silicates), to grow chlorite (Figs. 1.8a–c). The simplified reaction can be written as (mineral abreviations after Kretz, 1983): Ilm + Silicate + H_2O → Rt + Chl. Rutile rich aggregates are characterized by a fine grained intergrowth of rutile and chlorite that mimic the shape of ilmenite. The same type of textures, although in a more developed stage, can still be found in some metasedimentary rocks from the MEU (Fig. 1.8c). Metapelitic rocks from the GEU are ilmenite free demonstrating that the rutile forming reaction is complet (Fig. 1.8d).

Trace element data (Fig. 1.9) shows that that rutiles from the GPU mirror Nb/Ti ratios of ilmenite. Rutiles from the MEU display a larger scatter in Nb concentrations and have Nb/Ti ratios higher than ilmenite. This behavior indicates that Nb concentrations in rutile are evolving towards equilibrium (according to a $K_{DNb/Ti}^{Rt/Ilm}$ value of 49), according to a model similar to the one presented by Luvizotto & Zack (2008)(see also Chapter 3). Rutiles from the GEU rocks are single crystals with a rounded shape and show narrow scatter in Nb contents. In these rocks, the homogenization of Nb contents in rutile was facilitated by higher temperature and is probably related with mechanisms like dynamic recrystalization and/or intergrain diffusion.

13
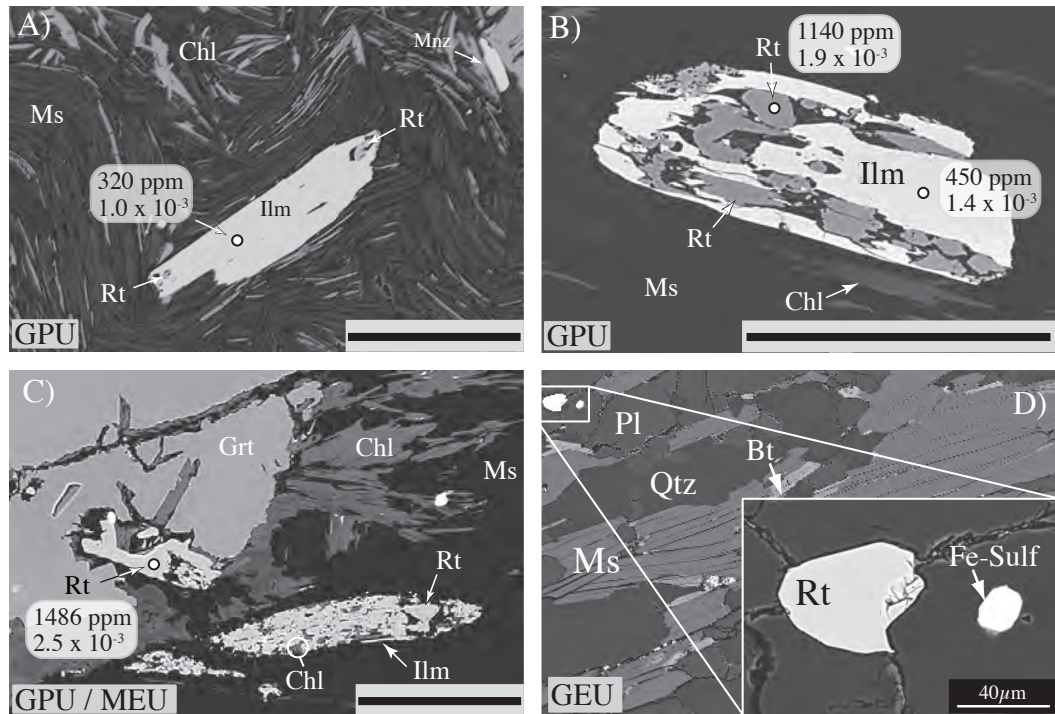
Figure 1.8 BSE images exemplifying the textures observed in metasedimentary rocks from the GPU, MEU and GEU. The images are arranged in such a way that they represent the evolution of the texture though the rocks and units. Scale bars, when not indicate, represent 100μm.
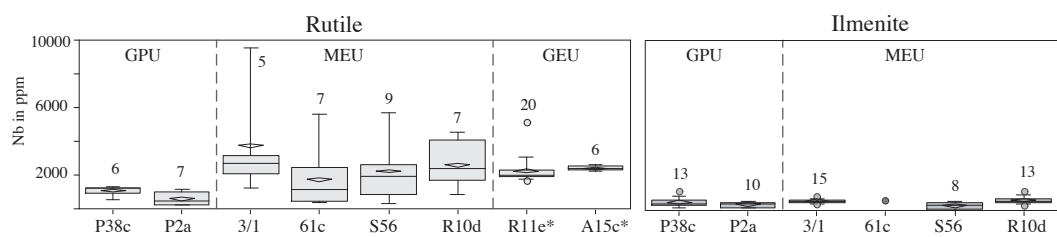
Figure 1.9 Summary of Nb concentrations obtained for the rutiles and ilmenites. Samples are sorted according to increasing metamorphic grade.

Temperature records on all but one rutile grain are in accordance with metamorphic conditions reported for the studied rocks. Rutiles from the GPU give temperature results <510°C. Temperatures within 500-560°C and 520-630°C were obtained for rutiles from MEU and GEU rocks, respectively.

The only rutile with an exceptionally high Zr content (390 ppm, T=680°C) is from a quartzite (MEU). This grain is interpreted to be a detrital relict (Fig. 1.10). Due to the lack of Fe- Ca-bearing phases, quartzites are less reactive than other rocks types (*e.g.*, phyllites and schists). This strongly decreases the ability to form ilmenite and/or titanite under metamorphic conditions where rutile is unstable. Phyllites and schists are low- to medium-grade metamorphic products of pelitic sediments (fine grained clastic sediments of less than 1/16mm). On the other hand, quartzites are often the metamorphic product of coarser grained sediments, *e.g.*, sandstones. In the investigated phyllites and schists, metamorphically grown rutiles are fine grained (smaller axis <50 μm) and occur as aggregates (easily disintegrated during weathering and mechanical transport in sediments). However, large detrital rutile grains may still be preserved in the quartzites. Preliminary calculations, taking into account grain size distributions of rutile and WR TiO_2 content, show that quartzites are the main source for rutiles in sediments derived from low-grade metamorphic rocks.

Detrital rutiles from recent sediments from this area have recently been studied (Triebold *et al.*, 2007, see also Chapter 5, Section 5.2). One interesting result that we obtained is that several detrital rutiles derived from the low-grade units still record relict temperatures (apparently above 950 °C) from a former metamorphic cycle. Therefore according to our results, these rutiles are probably derived from quartzites.

1.7 Analytical methods

For this thesis, analytical methods play an essential role. Therefore, this section presents an overview about the analytical techniques applied in this work. More detailed descriptions are presented in the following chapters.
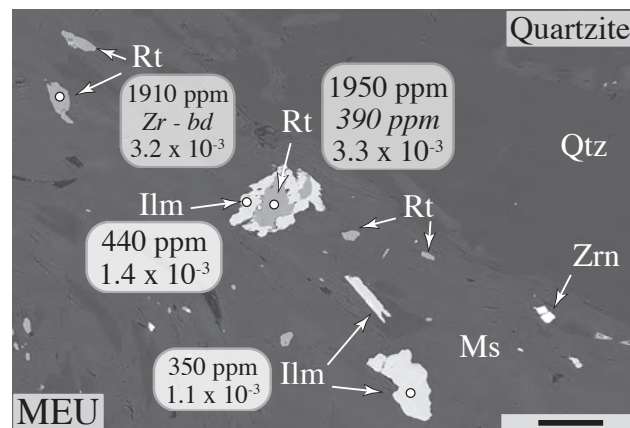
Figure 1.10 BSE image of a rutile interpreted as a detrital relict in the quartzite. Concentrations (in ppm) stand for Nb and Zr (in *italic*). Pure numbers represent Nb/Ti ratios. The scale bar represents 100μm.

1.7.1 Electron Microprobe (EMP)

Electron microprobe studies were carried out at the Mineralogisches Institut, Universität Heidelberg and at the Geowissenschaftliches Zentrum, Universität Göttingen. Analyses of rutiles followed the method outlined by Zack *et al.* (2002, 2004b). In Heidelberg, EMP analyses were carried out with a CAMECA SX51 and in Göttingen with a JEOL JXA 8900, both instruments equipped with 5 WDS detectors. The matrix correction methods were phi–rho–z: (Heinrich & Newbury, 1991) in Göttingen and PAP (Pouchou & Pichoir, 1984) in Heidelberg. The following elements were analyzed in Heidelberg: Si, V, Cr, Fe, Zr, Nb and W. In Göttingen, the following elements were analyzed: Si, V, Cr, Fe, Zr, Nb, Sn, Sb, Hf, Ta and W. In order to get "true" zero-concentration peak intensities and to exclude any machine drift, every ten analyses were bracketed by two analyses of synthetic rutile (nominally zero-concentration trace elements).

1.7.2 Secondary Ion Mass Spectrometry (SIMS)

SIMS analyses were carried out at the Mineralogisches Institut, Universität Heidelberg using a CAMECA ims 3f. Analyses were performed using a 14.5 keV/10–20

nA $^{16}O^-$ primary ion beam. Positive secondary ions were nominally accelerated to 4.5 keV (energy window set to ±20 eV) and the energy filtering technique was used with an offset of 90 eV at mass resolution m/Δm (10%) of 370. Count rates were normalized to ^{47}Ti. TiO_2 in rutile was assumed to be 100 wt%, unless other elements exceeded 1 wt% (specifically for the detrital rutile grains – see Section 2.4.1). In such cases TiO_2 concentrations obtained by EMP were used instead. The following isotopes were analyzed: ^{47}Ti, ^{90}Zr, ^{93}Nb, ^{118}Sn, ^{120}Sn, ^{121}Sb, ^{123}Sb, ^{178}Hf, ^{181}Ta, ^{184}W, ^{186}W, ^{232}Th, ^{238}U.

1.7.3 Isotopic Dilution Multi–Collector Inductively Coupled Plasma Mass Spectrometry (ID–MC–ICP–MS)

After rutile dissolution in a Hf-HNO$_3$ mixture and element separation by ion exchange chromatography, contents of some HFSE (Zr, Hf, Nb, Ta, W) and Lu together with ^{176}Hf/^{177}Hf isotope compositions were measured using the Isoprobe MC–ICP–MS at ZLG Münster. Operating conditions and analytical techniques are summarised in Münker *et al.* (2001), Weyer *et al.* (2002), and Kleine *et al.* (2004). Hf isotope results are given relative to a value of 0.282160 for JMC 475, the typical external reproducibility is ±0.5 ε–units (2σ). Concentrations of the HFSE (exept for Nb) were measured by isotope dilution using a mixed ^{94}Zr–^{180}Hf–^{180}Ta–^{183}W–^{176}Lu isotope tracer, which was calibrated against >99.9% pure AMES metals. Niobium concentrations were measured as Zr/Nb against a Zr–Nb standard prepared by AMES metals and using the Zr concentrations determined from the isotope dilution measurements. Two measurements were carried out in order to test the reproducibility of the technique and homogeneity of the grain.

1.7.4 Thermal Ionization Mass Spectrometry (TIMS)

TIMS U-Pb analyses were carried out at the University of Kansas (Department of Geology). Rutile samples were carefully hand–selected and dissolved employing the pressure–vessel HF-HNO$_3$ dissolution methods of Krogh (1973) and Parrish (1987). Elemental separation was performed with a HCl anion column chemistry

to eliminate Ti and separate both Pb and U. Isotopic analyses were determined on a VG Sector multi-collector thermal ionization mass spectrometer on separate Pb and U fractions. A mass fractionation correction of 0.16% ±0.05%/amu, as determined by standard runs on NBS 981 (common Pb) and NBS 982 (equal atom Pb), was applied to the Pb data. A mass fractionation of 0.10% ±0.05%/amu, as determined by standard runs on U500, was applied to all U data. Samples were spiked with a mixed ^{205}Pb/^{235}U spike. Errors on ^{206}Pb/^{204}Pb were minimized by the use of a Daly multiplier and are typically on the order of 1% or less. Common lead corrections were made using values determined from Stacey & Kramers (1975) for the interpreted crystallization age. Decay constants used were ^{238}U=0.155125×10^{-9} y^{-1} and ^{235}U=0.98485×10^{-9} yr^{-1} (Steiger & Jager, 1977).

1.7.5 Laser Ablation Inductively Coupled Plasma Mass Spectrometry (LA–ICP–MS)

At the Institut für Geowissenschaft, Johannes Gutenberg-Universität Mainz, trace element analyses were carried out with a New Wave Research UP-213 (wavelength 213 nm) laser system combined with an Agilent 7500ce ICP quadrupole mass spectrometer. Using a spot size of 70 μm, the samples were ablated with a laser energy of 3.55 Jcm^{-2} and a repetition rate of 10 Hz. Signals were recorded for 60 s per spot after measuring a gas blank of 60 s for background subtraction before each spot. A He–Ar mixture was used as carrier gas, which has the effect of lowering the detection limits by a factor of two to three (Jacob, 2006). Plasma torch conditions were optimized so that ThO/Th ratios were <0.5% and no further corrections for oxide production were applied. Titanium, measured as ^{49}Ti, was the internal standard element for each analysis. TiO$_2$ was assumed to be 100 wt%. Analyses were calibrated against the NIST SRM 610 glass (GeoReM preferred values: http://georem.mpch-mainz.gwdg.de/). The following isotopes were measured: ^{51}V, ^{90}Zr, ^{93}Nb, ^{95}Mo, ^{98}Mo, ^{121}Sb, ^{177}Hf, ^{178}Hf, ^{181}Ta, ^{184}W, ^{208}Pb, ^{232}Th, ^{238}U.

1.7.6 Micro-Raman Spetroscopy

Laser micro-Raman spectroscopy was applied to selected grains in order to identify the TiO_2 structure type. Raman spectra were obtained using a Horiba Jobin Yvon Labram HR-UV 800 (equipped with a Peltier-cooled CCD detector) at the Geowissenschaftliches Zentrum, Universität Göttingen. Analyzes were carried out using 633 nm laser excitation, 17 mW laser power and 1200 l/mm grating.

Bibliography

Barboza SA, Bergantz GW (2000) Metamorphism and anatexis in the mafic complex contact aureole, Ivrea zone, northern Italy. *Journal of Geology* 41: 1307–1327

Boriani A, Origoni EG, Borghi A, Caironi V (1990) The evolution of the Serie-Dei-Laghi (Strona-Ceneri and Scisti-Deilaghi) - the upper component of the Ivrea-Verbano crustal section - Southern Alps, North Italy and Ticino, Switzerland. *Tectonophysics* 182: 103–118

Brenan JM, Shaw HF, Phinney DL, Ryerson FJ (1994) Rutile-aqueous fluid partitioning of Nb, Ta, Hf, Zr, U and Th: implications for high field strength element depletions in island-arc basalts. *Earth and Planetary Science Letters* 128: 327–339

Crowhurst P, Farley K, Ryan C, Duddy I, Blacklock K (2002) Potential of rutile as a U–Th–He thermochronometer. In: *Eleventh Annual Goldschmidt Conference, LPI Contribution (CD-Rom)*, vol. 1088

Davis WJ (1997) U-Pb zircon and rutile ages from granulite xenoliths in the Slave Province; evidence for mafic magmatism in the lower crust coincident with Proterozoic dike swarms. *Geology* 25: 343–346

Deer WA, Howie R, Zussman J (1992) *An introduction to the rock-forming minerals*. Harlow, Essex, England, 696p

Demarchi G, Quick JE, Sinigoi S, Mayer A (1998) Pressure gradient and original orientation of a lower-crustal intrusion in the Ivrea-Verbano Zone, northern Italy. *Journal of Geology* 106: 609–621

Foley SF, Barth MG, Jenner GA (2000) Rutile/melt partition coefficients for trace elements and an assessment of the influence of rutile on the trace element characteristics of subduction zone magmas. *Geochimica et Cosmochimica Acta* 64: 933–938

Graham J, Morris R (1973) Tungsten- and antimony-substituted rutile. *Mineralogical Magazine* 39: 470–473

Haggerty SE (1991) *Oxide mineralogy of the upper mantle. In: Lindsley, D. H. (Ed.), Oxide mineralogy minerals: Petrological and magnetic significance*, vol. 25. Reviews in mineralogy

Handy MR, Franz L, Heller F, Janott B, Zurbriggen R (1999) Multistage accretion and exhumation of the continental crust (Ivrea crustal section, Italy and Switzerland). *Tectonics* 18: 1154–1177

Heinrich KFJ, Newbury DE (1991) *Electron probe quantitation*. New York: Plenum Press

Henk A, Franz L, Teufel S, Oncken O (1997) Magmatic underplating, extension, and crustal reequilibration: Insights from a cross-section through the Ivrea Zone and Strona-Ceneri Zone, northern Italy. *Journal of Geology* 105: 367–377

Jacob DE (2006) High sensitivity analysis of trace element poor geological reference glasses by laser-ablation inductively coupled plasma mass spectrometry (LA-ICP-MS). *Geostandards and*

Geoanalytical Research 30: 221–235

Kleine T, Mezger K, Münker C, Palme H, Bischoff A (2004) ^{182}Hf-^{182}W isotope systematics of chondrites, eucrites, and martian meteorites: chronology of core formation and early mantle differentiation in Vesta and Mars. *Geochimica et Cosmochimica Acta* 68: 2935–2946

Klemme S, Prowatke S, Hametner K, Gunther D (2005) Partitioning of trace elements between rutile and silicate melts: Implications for subduction zones. *Geochimica et Cosmochimica Acta* 69: 2361–2371

Kretz R (1983) Symbols for rock forming minerals. *American Mineralogist* 68: 277–279

Krogh TE (1973) A low contamination method for hydrothermal decomposition of zircon and extraction of U and Pb for isotopic age determinations. *Geochimica et Cosmochimica Acta* 37: 485–494

LaTourrette T, Hervig RL, Holloway JR (1995) Trace-element partitioning between amphibole, phlogopite, and basanite melt. *Earth and Planetary Science Letters* 135: 13–30

Li Q, Li S, Zheng YF, Li H, Massonne HJ, Wang Q (2003) A high precision U-Pb age of metamorphic rutile in coesite-bearing eclogite from the Dabie Mountains in central China: a new constraint on the cooling history. *Chemical Geology* 200: 255–265

Luvizotto GL, Zack T (2008) Nb and Zr behavior in rutile during high–grade metamorphism and retrogression: An example from the Ivrea–Verbano Zone. *Chemical Geology* in press

Massonne H (1999) A new occurrence of microdiamonds in quartzofeldspathic rocks of the Saxonian Erzgebirge, Germany, and their metamorphic evolution. In: *Proceedings of the 7th International Kimberlite Conference*, vol. 5, 33–539

Massonne HJ (2001) First find of coesite in the ultrahigh-pressure metamorphic area of the central Erzgebirge, Germany. *European Journal of Mineralogy* 13: 565–570

McDonough WF (1991) Partial melting of subducted oceanic crust and isolation of its residual eclogitic lithology. *Philosophical Transactions of the Royal Society of London Series A* 335: 407–418

Meinhold G, Anders B, Kostopoulos D, Reischmann T (2008) Rutile chemistry and thermometry as provenance indicator: An example from Chios Island, Greece. *Sedimentary Geology* 203: 98–111

Mezger K, Hanson GN, Bohlen SR (1989) High-precision U-Pb ages of metamorphic rutile: application to the cooling history of high-grade terranes. *Earth and Planetary Science Letters* 96: 106–118

Mezger K, Essene EJ, Vanderpluijm BA, Halliday AN (1993) U-Pb Geochronology of the Grenville Orogen of Ontario and New York: Constraints on Ancient Crustal Tectonics. *Contributions to Mineralogy and Petrology* 114: 13–26

Mingram B (1998) The Erzgebirge, Germany, a subducted part of northern Gondwana: geochemical evidence for repetition of early Palaeozoic metasedimentary sequences in metamorphic thrust units. *Geological Magazine* 135: 785–801

Münker C (1998) Nb/Ta fractionation in a Cambrian arc/back-arc system, New Zealand: source constraints and application of refined ICPMS techniques. *Chemical Geology* 144: 23–45

Münker C, Weyer S, Scherer E, Mezger K (2001) Separation of high field strength elements (Nb, Ta, Zr, Hf) and Lu from rock samples for MC-ICPMS measurements. *Geochemistry, Geophysics, Geosystems (G3)* 2: paper number 10.10292001GC000183

Parrish RR (1987) An improved micro-capsule for zircon dissolution in U-Pb geochronology. *Isotope Geoscience* 66: 99–102

Pouchou JL, Pichoir F (1984) A new model for quantitative X-ray-microanalysis. Part I: applications to the analysis of homogeneous samples. *Recherche Aerospatiale* 3: 13–38

Rice C, Darke K, Still J (1998) Tungsten-bearing rutile from the Kori Kollo gold mine Bolívia. *Mineralogical Magazine* 62: 421–429

Rivalenti G, Garuti G, Rossi A, Siena F, Sinigoi S (1981) Existence of different peridotite types and of a layered igneous complex in the Ivrea Zone of the Western Alps. *Journal of Petrology* 22: 127–153

Rötzler K, Schumacher R, Maresch WV, Willner AP (1998) Characterization and geodynamic implications of contrasting metamorphic evolution in juxtaposed high-pressure units of the western Erzgebirge (Saxony, Germany). *European Journal of Mineralogy* 10: 261–280

Rutter E, Brodie K, James T, Burlini L (2007) Large-scale folding in the upper part of the Ivrea-Verbano zone, NW Italy. *Journal of Structural Geology* 29: 1–17

Saunders A, Tarney J, Weaver S (1980) Traverse geochemical variations across the Antarctic Peninsula: implications for the genesis of calc-alkaline magmas. *Earth and Planetary Science Letters* 46: 344–360

Schmid SM, Zingg A, Handy M (1987) The kinematics of movements along the Insubric Line and the emplacement of the Ivrea Zone. *Tectonophysics* 135: 47–66

Sills JD, Tarney J (1984) Petrogenesis and tectonic significance of amphibolites interlayered with meta-sedimentary gneisses in the Ivrea Zone, Southern Alps, Northwest Italy. *Tectonophysics* 107: 187–206

Smith D, Persil EA (1997) Sb-rich rutile in the manganese concentrations at St. Marcel-Praborna, Aosta Valley, Italy; petrology and crystal-chemistry. *Mineralogical Magazine* 61: 655–669

Stacey J, Kramers J (1975) Approximation of terrestrial lead isotope evolution by a two-stage model. *Earth and Planetary Science Letters* 26: 207–221

Stalder R, Foley SF, Brey GP, Horn I (1998) Mineral-aqueous fluid partitioning of trace elements at 900-1200 °C and 3.0-5.7 GPa: new experimental data for garnet, clinopyroxene, and rutile, and implications for mantle metasomatism. *Geochimica et Cosmochimica Acta* 62: 1781–1801

Steiger RH, Jager E (1977) Subcommission on geochronology: Convention on the use of decay constants in geo- and cosmochronology. *Earth and Planetary Science Letters* 36: 359–362

Stendal H, Toteu SF, Frei R, Penaye J, Njel UO, Bassahak J, Nni J, Kankeu B, Ngako V, Hell JV (2006) Derivation of detrital rutile in the Yaounde region from the Neoproterozoic Pan-African belt in southern Cameroon (Central Africa). *Journal of African Earth Sciences* 44: 443–458

Stockli D, Wolfe M, Blackburn T, Blackburn T, Zack T, Walker J, Luvizotto G (2007) He diffusion and (U-Th)/He thermochronometry of rutile. In: *American Geophysical Union, Fall Meeting*

2007, abstract# V23C-1548

Tomkins HS, Powell R, Ellis DJ (2007) The pressure dependence of the zirconium-in-rutile thermometer. *Journal of Metamorphic Geology* 25: 703–713

Triebold S, von Eynatten H, Luvizotto GL, Zack T (2007) Deducing source rock lithology from detrital rutile geochemistry: An example from the Erzgebirge, Germany. *Chemical Geology* 244: 421–436

Vry JK, Baker JA (2006) LA-MC-ICPMS Pb-Pb dating of rutile from slowly cooled granulites: Confirmation of the high closure temperature for Pb diffusion in rutile. *Geochimica et Cosmochimica Acta* 70: 1807–1820

Watson EB, Wark DA, Thomas JB (2006) Crystallization thermometers for zircon and rutile. *Contributions to Mineralogy and Petrology* 151: 413–433

Weyer S, Münker C, Rehkämper M, Mezger K (2002) Determination of ultra-low Nb, Ta, Zr and Hf concentrations and the chondritic Zr/Hf and Nb/Ta ratios by isotope dilution analyses with multiple collector ICP-MS. *Chemical Geology* 187: 295–313

Willner AP, Rötzler K, Maresch WV (1997) Pressure-temperature and fluid evolution of quartzo-feldspathic metamorphic rocks with a relic high-pressure, granulite-facies history from the Central Erzgebirge (Saxony, Germany). *Journal of Petrology* 38: 307–336

Zack T, Kronz A, Foley SF, Rivers T (2002) Trace element abundances in rutiles from eclogites and associated garnet mica schists. *Chemical Geology* 184: 97–122

Zack T, von Eynatten H, Kronz A (2004a) Rutile geochemistry and its potential use in quantitative provenance studies. *Sedimentary Geology* 171: 37–58

Zack T, Moraes R, Kronz A (2004b) Temperature dependence of Zr in rutile: empirical calibration of a rutile thermometer. *Contributions to Mineralogy and Petrology* 148: 471–488

Zingg A (1980) Regional metamorphism in the Ivrea Zone (Southern Alps, N-Italy): Field and microscopic investiggations. *Schweizerische Mineralogische und Petrographische Mitteilungen* 60: 153–179

2 Rutile crystals as potential trace element and isotope mineral standards for microanalysis

G. L. Luvizotto, T. Zack, H.P. Meyer, T. Ludwig, S. Triebold, A. Kronz, C. Münker, D. Stockli, S. Prowatke, S. Klemme, D. E. Jacob, H. von Eynatten.

Abstract

The present paper reports trace element concentrations of 15 elements (V, Cr, Fe, Zr, Nb, Mo, Sn, Sb, Hf, Ta, W, Lu, Pb, Th and U) as well as Pb and Hf isotope data for four relatively homogeneous and large (centimeter size) rutile grains. Methods employed are SIMS, EMP, LA–ICP–MS, ID–MC–ICP–MS and TIMS. For most elements homogeneity is usually within $\pm 10\%$ and occasionally variations are even narrower ($\pm 5\%$), particularly in the core of two of the studied grains. The trace element concentrations of the grains span a broad compositional range (*e.g.*, Zr concentrations are ca. 4, 100, 300 and 800 ppm). Provisional concentration values, calculated based on the homogeneity of the element and agreement between techniques, are presented for Zr, Nb, Sn, Sb, Hf, Ta, W and U. The present work represents a significant step forward in finding a suitable mineral standard for rutile microanalysis and encourages not only further search for mineral standards but also applications of rutile in the field of geochemistry and geochronology. In this sense, the rutiles presented here are useful as mineral standard in general *in-situ* rutile measurements, particularly for Zr–in–rutile thermometry, quantitative provenance studies (Nb and Cr concentrations as index of source rock type) and U–Pb dating. One of the studied grains has a relatively high U concentration (ca. 30 ppm) and rather constant U–Pb ages (1085.1 to 1096.2 Ma, ^{207}Pb/^{235}U ages and 1086.3 to 1096.6 Ma, ^{206}Pb/^{238}U ages), favoring its application as an age standard for U-Pb rutile dating. Since Lu concentrations in rutile are very low and Hf concentrations can be relatively high (tens of ppm), detrital rutiles may be suitable for obtaining initial Hf isotope composition of source rocks, therefore the rutiles presented here can be used as calibration material for *in-situ* rutile Hf isotope studies.

Keywords: *Homogeneity test, SIMS Calibration, Rutile age standard, U–Pb geochronology, Hf isotopes, Isotopic Dilution.*

2.1 Introduction

Microanalysis of trace elements is becoming the backbone of numerous geochemical studies due to good accessibility of several analytical techniques, *e.g.*, laser ablation inductively coupled plasma mass spectrometry (LA–ICP–MS), secondary ion mass spectrometry (SIMS) and electron microprobe (EMP). All of these methods rely on calibration using homogeneous materials with known trace element concentrations. While calibration for EMP trace element analysis is usually performed by the use of pure metals and/or oxides in conjunction with rigorous matrix corrections (*e.g.*, phi–rho–*z* and PAP, Heinrich & Newbury, 1991; Pouchou & Pichoir, 1984), both LA-ICP-MS and SIMS calibration heavily rely on a series of glass standards, particularly the NIST SRM 610 and 612 glasses (see, *e.g.* Pearce *et al.*, 1997; Rocholl *et al.*, 2000; Jochum & Willbold, 2006). Homogeneity tests and accurate trace element measurements have been performed on glass standards (NIST SRM 610-617: Hinton (1999); Eggins & Shelley (2002); SRM 614-617: Horn *et al.* (1997); MPI-DING: Jochum *et al.* (2000); Jochum *et al.* (2006)). In summary, only the NIST standard reference materials (SRM) can be regarded as certified for a few elements (Rb, Sr, Th, U, etc.; see discussion in Kane, 1998). For the remaining important non-certified trace elements, the NIST SRM 610 is still the reference material of choice in terms of quality of data compilation (for a comprehensive discussion see Jochum & Willbold, 2006). Homogeneity is sufficient (variation <5%) for most elements in NIST SRM 610 and several MPI–DING glasses (but see Eggins & Shelley, 2002), as accuracy for SIMS and LA–ICP–MS is often given as 15–20%. A problem regarding the NIST SRM glasses is that the major element composition is very different from that of any geological material (Jochum *et al.*, 2000).

An ideal reference material for microanalysis requires, besides well documented major and trace element composition, a matrix that matches the sample to be analyzed (chemical and physical properties). Satisfying these requirements is not an easy task, especially when dealing with natural samples. In this sense, the lack of suitable calibration standards is a ubiquitous problem.

Remarkably, none of the widely distributed analytical standards for trace element analysis are minerals. However, they would be extremely valuable to assess problems that arise during measurements, *e.g.*, to check results obtained by a given technique; to crosscheck results obtained by different laboratories and techniques, to monitor machine drift during a measurement session by periodically checking (especially in the case of EMP, as trace element content on standard glasses are usually below detection limit); and, in the case of LA-ICP-MS and SIMS, to check interferences and matrix effects (glass vs. crystal structure). It is true that most of the tasks described above can be performed with standard glasses. However, it is undoubtedly relevant to have a standard with chemical and physical properties identical to the material that is going to be analyzed.

Rutile is a common accessory mineral in a wide range of lithologies, *e.g.*, high-grade metamorphic rocks, igneous rocks (*e.g.*, kimberlites and lamproites), silici-clastic sediments, placer deposits and hydrothermal ore deposits. It crystallizes in a tetragonal structure, with each Ti^{4+} ion surrounded by six oxygens at the corners of a slightly distorted regular octahedron and each oxygen, surrounded by three Ti^{4+} ions, lies in a plane at the corners of an approximately equilateral triangle (Deer *et al.*, 1992). It is well known that rutile is an important carrier for several highly-charged trace elements (Graham & Morris, 1973; Haggerty, 1991; Deer *et al.*, 1992; Smith & Persil, 1997; Rice *et al.*, 1998). Zack *et al.* (2002) has shown for eclogites that 1 modal-% of rutile can accommodate more than 90% of the whole rock content for Ti, Nb, Ta, Sb and W. Furthermore, it is an important carrier for V, Cr, Mo and Sn (5-50% of the whole rock content). Rutile has attracted significant interest as a likely controller of Nb and Ta budgets in subduction zone processes (Saunders *et al.*, 1980; McDonough, 1991; Brenan *et al.*, 1994; Stalder *et al.*, 1998; Münker, 1998; Foley *et al.*, 2000; Klemme *et al.*, 2005, among others). It has recently been shown that the Zr incorporation in rutile is strongly temperature dependent (Zack *et al.*, 2004b; Watson *et al.*, 2006; Tomkins *et al.*, 2007) in quartz- and zircon-bearing systems. Rutile has also been shown to yield precise U-Pb ages (*e.g.*, Mezger *et al.*, 1989; Davis, 1997; Mezger *et al.*, 1993; Li *et al.*, 2003; Vry & Baker, 2006). Its trace element geochemistry is also suitable for sediment provenance studies where,

e.g., Nb and Cr contents can be used for distinguishing between metamafic and metapelitic rocks, and Zr content indicate metamorphic peak temperatures of the source rocks (Zack *et al.*, 2002, 2004a; Triebold *et al.*, 2007).

In most of the examples given above metamorphic textures are extremely important features since rutiles occurring in different textural domains may display systematically different chemical compositions. Therefore, in many circumstances, the application of *in-situ* techniques is an essential requirement (see, *e.g.*, Zack *et al.*, 2004b; Luvizotto & Zack, 2006, in press). In several cases *in-situ* studies can be performed by EMP, but the application of this technique is limited by its relatively high detection limit. Therefore, for high precision analyses of trace elements and isotopes more sensitive techniques, such as SIMS and LA-ICP-MS, are required. Hence, having a rutile standard is a key issue.

The aim of this paper is to present homogeneity tests conducted by EMP and SIMS as well as precise and accurate trace element (ID–MC–ICP–MS and LA–ICP–MS) and isotopic (ID–MC–ICP–MS and TIMS) chemical data for four large and relatively homogeneous rutile grains. As the present work involved High Field Strength Elements (HFSE) analyses by SIMS, specific attention is given to its calibration procedure.

Ødegård *et al.* (2001) prepared calibration materials (glasses of rutile composition) for microanalysis of Ti minerals by direct fusion of natural and synthetic materials. Although it is a commendable step forward in establishing trace element mineral standards, the disadvantage of this approach is that only a small amount of material can be produced and problems related to formation of poly-crystalline aggregates must be taken into account. In contrast, in the present work large and relatively homogenous rutile crystals are proposed as mineral standards.

Terminology

The International Organization for Standardization (ISO) defines a reference material as a material or substance where one or more of its property values are sufficiently homogeneous and well established to be used for the calibration of an apparatus, the assessment of a measurement method, or for assigning values to material

(ISO, 1993).

In this sense, the rutile grains presented in this paper can be treated as reference material as they can be used to assess a measurement method. However, they are not suitable for primary calibration, due to heterogeneity of some elements and restricted amount of material.

Although not defined in the ISO guide the term *standard* is broadly used in the literature to refer to different materials used as reference for chemical analyses (*e.g.*, Baker *et al.*, 2004; Black *et al.*, 2004; Amelin & Back, 2006).

As reference material is not the appropriate term to refer to the rutiles presented here, we propose the use of the term *secondary standards* to designate well–characterized materials useful to asses measurement methods and demonstrate the quality of acquired chemical data.

2.2 Sample selection

In order to find rutiles suitable to be used as mineral standards a large number of grains were investigated. In total one synthetic and 40 natural rutile grains were analyzed. Natural grains were obtained from 15 different localities, namely: Minas Gerais (Brazil), Dobrá Voda (Czech Republic), Arendal and Gjerstad (Norway), Gediz (Turkey), Freiberg and Halbrück (Germany), Limoges (France), North Carolina (USA), Giftkuppe (Namibia), Valais, St. Gotthardt and Dissentis (Switzerland), Adelaide (Australia) and Madagascar. All grains were examined under reflected light microscopy in order to identify possible microscopic mineral inclusions and mineral exsolutions (*e.g.*, ilmenite needles). Those grains that did not show mineral inclusions and exsolution textures under reflected light microscopy were then analyzed using the scanning electron microscope (SEM), where possible submicroscopic mineral inclusions and exsolutions could be detected. With this technique strong chemical zoning can also be identified. Examples of heterogeneities found in some of the analyzed rutiles are presented in Fig. 2.1. Rutiles, which appeared to be homogenous and free of inclusions based on optical inspection and SEM analysis, were then tested for element homogeneity by EMP by conducting

rim–to–rim profiles through the grains.
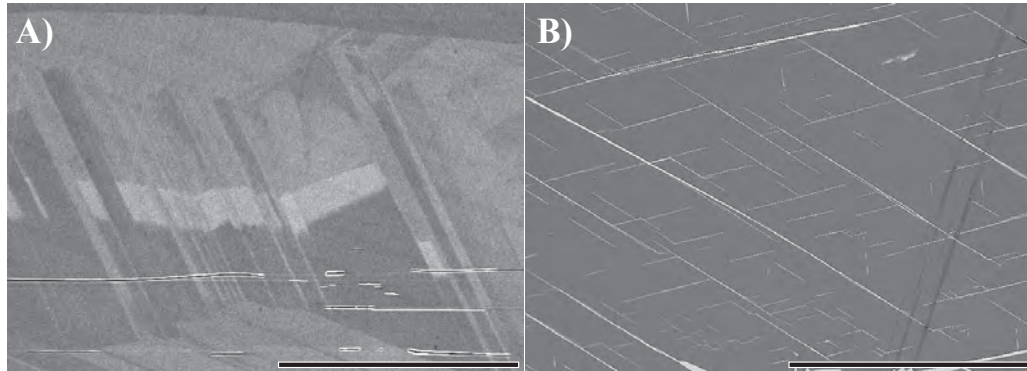
Figure 2.1 Back scattered electron images showing examples of rutiles with: A) Chemical zoning B) Ilmenite needles. Scale bars at the bottom of both images represent 200 μm.

During the selection process, 18 out of 41 rutiles were excluded because of mineral exsolution detectable using reflected light microscope. Fifteen out of the 23 remaining samples were excluded because of exsolution and/or chemical zoning visible in back-scattered electron (BSE) images. Only eight rutiles qualified for EMP studies, however, four of the grains had heterogeneities and/or low concentrations of important trace elements. After following the steps described above, four rutile grains were designed as suitable for being used as secondary mineral standards.

2.2.1 The Sy, Diss, R19 and R10 rutile grains

The rutile grains selected as potential mineral standards are labeled **Sy**, a synthetic rutile grain, **Diss**, from Dissentis – Switzerland, **R19** from Blumberg (Adelaide) – Australia, and **R10** from Gjerstad – South Norway. All of them are large (of centimeter–scale) single crystals. Sketches of the polished thick sections used for *in-situ* analyses are presented in Fig. 2.2, showing the shape and size of the grains along with the locations of analyzed spots. As the Diss grain has some minor ilmenite inclusions, a BSE image showing this feature is displayed in Fig. 2.2.
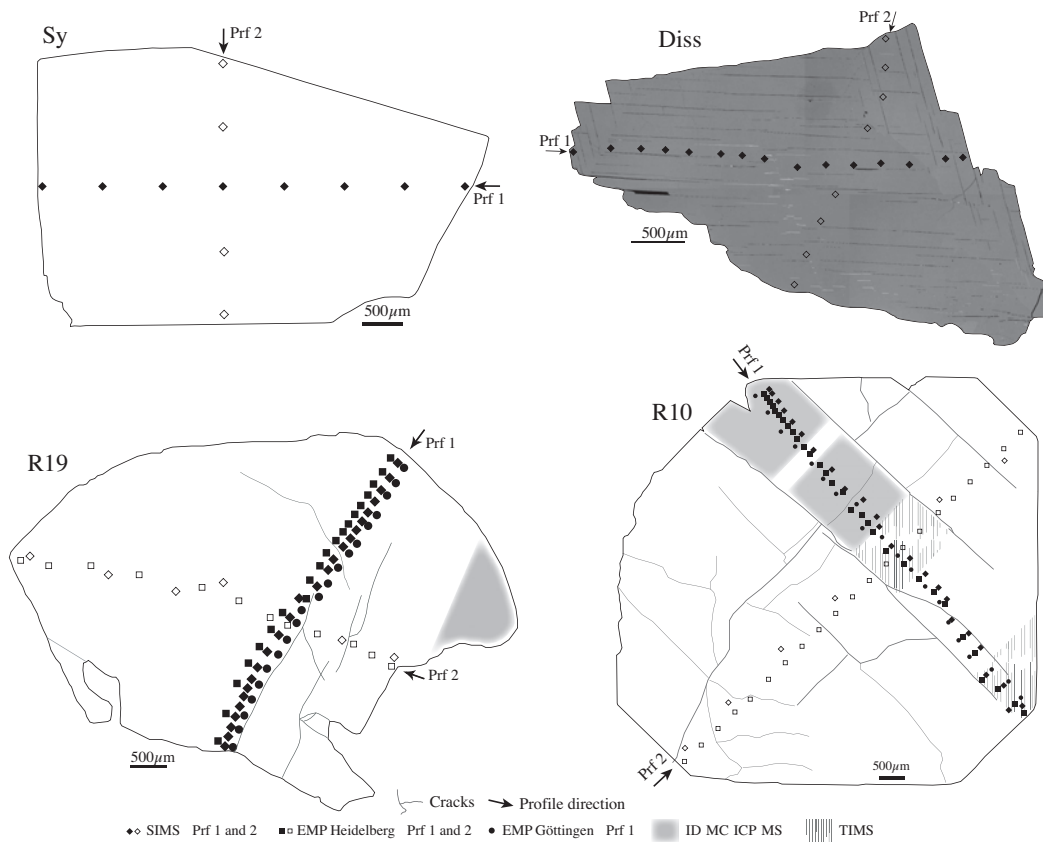
Figure 2.2 Sketch of **Sy, Diss, R19** and **R10** polished thick sections showing shape of the grains and location of analyzed spots. Symbols are not to scale. As Diss shows minor ilmenite inclusions (bright horizontal needles), a BSE images composite is presented for this grain. For the Sy and Diss grains, splits analyzed by ID–MC–ICP–MS and all LA–ICP–MS splits are from the same grain as the polished sections.

2.3 Analytical techniques

2.3.1 Secondary Ion Mass Spectrometry (SIMS)

SIMS analyses were carried out at the Mineralogisches Institut, Universität Heidelberg using a CAMECA ims 3f. Analyses were performed using a 14.5 keV/10–20 nA $^{16}O^-$ primary ion beam. Positive secondary ions were nominally accelerated to 4.5 keV (energy window set to ± 20 eV) and the energy filtering technique was used with an offset of 90 eV at mass resolution m/Δm (10%) of 370. Count rates were

normalized to ^{47}Ti. TiO$_2$ in rutile was assumed to be 100 wt%, unless other elements exceeded 1 wt% (specifically for the detrital rutile grains – see Section 2.4.1). In such cases TiO$_2$ concentrations obtained by EMP were used instead. The following isotopes were analyzed: ^{47}Ti, ^{90}Zr, ^{93}Nb, ^{118}Sn, ^{120}Sn, ^{121}Sb, ^{123}Sb, ^{178}Hf, ^{181}Ta, ^{184}W, ^{186}W, ^{232}Th, ^{238}U.

Concentrations were calculated based on relative sensitivity factors (RSF) determined following the methods described in Section 2.4.1. RSF were calculated according to:

$$RSF = \frac{I_A}{I_R} \times \frac{i_R}{i_A} \times \frac{c_R}{c_A} \times \frac{a_A}{a_R}$$

where I = secondary ions intensity; i = isotopic abundance; c = concentration of the element; a = atomic weight of the element. Indexes A and R stand for analyzed and reference elements.

2.3.2 Electron Microprobe (EMP)

Electron microprobe studies were carried out at the Mineralogisches Institut, Universität Heidelberg and at the Geowissenschaftliches Zentrum, Universität Göttingen. Analyses of rutiles followed the method outlined by Zack *et al.* (2002, 2004b). A summary of the EMP conditions is presented in Table 2.1. In Heidelberg, EMP analyses were carried out with a CAMECA SX51 and in Göttingen with a JEOL JXA 8900, both instruments equipped with 5 WDS detectors. The matrix correction methods were phi–rho–z: (Heinrich & Newbury, 1991) in Göttingen and PAP (Pouchou & Pichoir, 1984) in Heidelberg. In order to get "true" zero-concentration peak intensities and to exclude any machine drift, every ten analyses were bracketed by two analyses of synthetic rutile (nominally zero-concentration trace elements). In Göttingen, the overlap of V Kα by Ti Kβ was corrected online after the method of Fialin *et al.* (1997). This method was selected as it corrects raw intensities before matrix correction.

Table 2.1 EMP conditions applied for the rutile trace element analysis.

		Ti	V	Cr	Fe	Zr	Nb	Sn	Sb	Hf	Ta	W
	Crystal	LIF	LIF	LIF	LIF	PETH	PET	PET	PET	PETH	LIFH	LIFH
Gö	Line	Kβ	Kα	Kα	Kα	Lα	Lα	Lα	Lα	Lα	Lα	Lα
25kV	Count time[a]	30	200	200	150	300	300	200	300	300	300	200
80nA	Bckg time[b]	15	100	100	50	150	150	100	150	150	150	100
	DL[c]	922	40	30	40	40	70	60	40	50	50	80
	2σ error[d]	4050	160	30	60	30	100	40	100	50	100	140
	Crystal	PET		LIF	LIF	TAP	PET					LIF
HD	Line	Kβ		Kα	Kα	Lα	Lα					Lα
20kV	Count time[a]	100		200	100	200	300					100
100nA	Bckg time[b]	50		100	50	100	150					50
	DL[c]	130		50	40	40	60					350
	2σ error[d]	990		20	20	40	60					90

Gö - Göttingen, HD - Heidelberg.
[a] counting time on the peak position (s)
[b] counting time on the background position (s)
[c] 2σ detection limit, based on repeated measurement of variation on background, values in ppm
[d] 2σ relative standard error based on counting statistics, values in ppm

2.3.3 Isotopic Dilution Multi–Collector Inductively Coupled Plasma Mass Spectrometry (ID–MC–ICP–MS)

During the course of the ID–MC–ICP–MS measurements, two fragments of R10 (0.34 and 7.3 mg), R19 (1.7 and 2.5 mg), and Diss (3.7 and 2.4 mg) were analyzed together with one fragment of Sy (17 mg). The approximate location of these splits on the analyzed thick sections of the grains R10 and R19 is shown in Fig. 2.2. For Diss and Sy, a split from the rim of the grain was used. For all grains, except the Sy rutile, two measurements were carried out in order to test the reproducibility of the technique and homogeneity of the grain. For R10 two splits, one from the rim and another from the core were analyzed. Samples were digested in Hf-HNO$_3$ mixtures. After element separation by ion exchange chromatography, contents of some HFSE (Zr, Hf, Nb, Ta, W) and Lu together with ^{176}Hf/^{177}Hf isotope compositions were measured using the Isoprobe MC–ICP–MS at ZLG Münster. Operating conditions and analytical techniques are summarised in Münker *et al.* (2001), Weyer *et al.* (2002), and Kleine *et al.* (2004). Hf isotope results are given relative to a value of 0.282160 for JMC 475, the typical external reproducibility is ±0.5 ε–units (2σ). Concentrations of the HFSE (exept for Nb) were measured by isotope dilution using a mixed ^{94}Zr–^{180}Hf–^{180}Ta–^{183}W–^{176}Lu isotope tracer, which was calibrated against >99.9% pure AMES metals. Niobium concentrations were measured as

Zr/Nb against a Zr–Nb standard prepared by AMES metals and using the Zr concentrations determined from the isotope dilution measurements. Typical accuracies and 2σ external reproducibilities were $\pm 1\%$ for Zr, Hf, Ta, and W contents and $\pm 4\%$ for Nb contents. Typical external reproducibilities for Nb/Ta, Zr/Hf and Lu/Hf are $\pm 4\%$, $\pm 0.6\%$, and $\pm 1\%$, respectively. Errors include propagated errors originating from blank measurements, assuming a $\pm 50\%$ blank uncertainty. Measured blanks were 550 ng for Zr, 39 pg for Hf, 9 pg for Nb, 17 pg for Ta, and 140 pg for W.

2.3.4 Thermal Ionization Mass Spectrometry (TIMS)

TIMS U-Pb analyses were carried out at the University of Kansas (Department of Geology). As SIMS results showed that the rutile R10 had the highest U concentrations and was the most homogeneous among the studied grains (see below), this sample was chosen for TIMS analyses. Single fragment rutile samples were carefully hand–selected from both the core and rim of the R10 crystal and dissolved employing the pressure–vessel HF-HNO$_3$ dissolution methods of Krogh (1973) and Parrish (1987). Elemental separation was performed with a HCl anion column chemistry to eliminate Ti and separate both Pb and U. Isotopic analyses were determined on a VG Sector multi-collector thermal ionization mass spectrometer on separate Pb and U fractions. A mass fractionation correction of 0.16% $\pm 0.05\%$/amu, as determined by standard runs on NBS 981 (common Pb) and NBS 982 (equal atom Pb), was applied to the Pb data. A mass fractionation of 0.10% $\pm 0.05\%$/amu, as determined by standard runs on U500, was applied to all U data. Samples were spiked with a mixed ^{205}Pb/^{235}U spike. Errors on ^{206}Pb/^{204}Pb were minimized by the use of a Daly multiplier and are typically on the order of 1% or less. Common lead corrections were made using values determined from Stacey & Kramers (1975) for the interpreted crystallization age. Decay constants used were ^{238}U=0.155125$\times 10^{-9}$ y^{-1} and ^{235}U=0.98485$\times 10^{-9}$ yr^{-1} (Steiger & Jager, 1977).

2.3.5 Laser Ablation Inductively Coupled Plasma Mass Spectrometry (LA-ICP-MS)

At the Institut für Geowissenschaft Department of Geosciences, Johannes Gutenberg-Universität Mainz, trace element analyses were carried out with a New Wave Research UP-213 (wavelength 213 nm) laser system combined with an Agilent 7500ce ICP quadrupole mass spectrometer. The samples were ablated in spots of 70 μm at a laser energy of 3.55 Jcm^{-2} and a repetition rate of 10 Hz. Signals were recorded for 60 s per spot after measuring a gas blank of 60 s for background subtraction before each spot. A He–Ar mixture was used as carrier gas, which has the effect of lowering the detection limits by a factor of two to three (Jacob, 2006). Plasma torch conditions were optimized so that ThO/Th ratios were <0.5% and no further corrections for oxide production were applied. Titanium, measured as ^{49}Ti, was the internal standard element for each analysis. TiO$_2$ was assumed to be 100 wt%. Analyses were calibrated against the NIST SRM 610 glass (GeoReM preferred values: http://georem.mpch-mainz.gwdg.de/). Accuracy of the results was confirmed by analyses of the well-known USGS reference glass BCR-2G (Jochum *et al.*, 2005) using newly compiled values (GeoReM preferred values: http://georem.mpch-mainz.gwdg.de/). Element concentrations were calculated with the software "GLITTER" using measurements of the following isotopes: ^{51}V, ^{90}Zr, ^{93}Nb, ^{95}Mo, ^{98}Mo, ^{121}Sb, ^{177}Hf, ^{178}Hf, ^{181}Ta, ^{184}W, ^{208}Pb, ^{232}Th, ^{238}U. Typical detection limits (99% confidence) for 70 μm spots were 0.01 ppm for V, Zr, Hf, W, Th and U, 0.015 ppm for Mo and Sb, 0.005 ppm for Nb and 0.0035 ppm for Ta and U.

2.4 Results

2.4.1 SIMS HFSE calibration

The calibration of SIMS for HFS elements in rutile was twofold. First of all, as RSF are needed for converting the intensity (in counts per second) of a given isotope into element concentration, determining consistent and reliable RSF is crucial issue.

Secondly, it is necessary to test possible matrix effects that might arise from using reference materials with different structure and chemical compositions.

It is noteworthy that repeated analyses on the NIST SRM 610 show constant element ratios over a period of eleven months (Fig. 2.3). Therefore significant machine drifts can be ruled out. Consequently, the data collected in this period can be treated as one consistent data set and the RSF calculated from this data set can be used to obtain element concentrations for the rutiles analyzed in the same time interval.
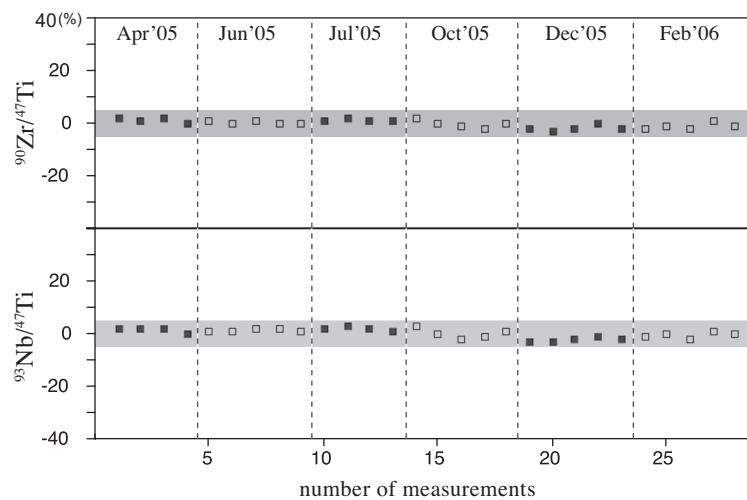
Figure 2.3 Variation with time of Zr and Nb intensity ratios (element/^{47}Ti) measured on NIST SRM 610 by SIMS. Total of 28 measurements, from April 2005 to February 2006. Each point on the plot represent one analysis. Variations are expressed in percentage and represent deviation from the average. Shaded areas represent variation of $\pm5\%$. In order to favor the comparison with obtained concentration data, variations are presented in the same scale used in Figs. 2.6 – 2.9 and in Figs. 2.10 – 2.12.

In order to calibrate SIMS for HFSE analysis in rutile, a set of detrital rutile grains from sediment samples from Erzgebirge (Germany) was used. The concentrations of Zr, Nb, Sn, Sb, Hf, Ta and W were independently determined by EMP in Göttingen, according to the operational conditions described in Section 2.3.2. Details of sampling procedures and mineral separation methods are presented in Triebold *et al.* (2007) and the complete data set will be presented elsewhere. Con-

centrations obtained by EMP were assumed as reference concentrations for the detrital rutile grains. Although the errors involved in RSF calculation using EMP data as a reference are larger than those obtained when more refined techniques (*e.g.*, ID–MC–ICP–MS) are used, the procedure adopted here involved analyses of a large number of grains and a strict, statistically robust, selection process:

1. selection of a large set of high trace element concentration rutiles. The total number of valid analyses varied from element to element as they were limited by the concentration of the target element in the grain. The number of sedimentary rutiles analyzed by EMP is presented in Table 2.2;

2. high trace element concentration grains were tested for homogeneity by conducting further EMP analyses on these grains;

3. SIMS analyses were conducted on homogeneous grains, trying to reproduce the location of EMP analyses;

4. collected data passed through two filtering processes. First, trace element concentrations above EMP detection limit (4σ minimum detection limit) were selected and RSF were calculated for these data. Gaussian error propagation was also calculated. Obtained RSF were then plotted against the EMP concentration, as shown in Fig. 2.4. Then as a second filtering process, all elements with a large data set were evaluated and only those with the highest concentration were selected. A minimum of 4 analyses were used. For elements with a restricted amount of data (Hf and Sb) all data selected according to the first filtering process were considered. The selected analyses are represented by shaded areas on Fig. 2.4. RSF corresponds to the arithmetic mean of the selected analyses.

In order to identify possible matrix effects and interferences for trace elements of interest, further analyses were carried out on a set of glass standards, namely, the NIST SRM 610 glass; three MPI–DING Glasses (Kl2 , StHs6/80 and ATHO, Jochum *et al.*, 2000); four USGS standards (BCR2G, BHVO, TB and GSD); and

two titanite glasses (TNT 150 and TNT 1500), doped with different trace element amounts (Klemme *et al.*, 2008). The overall conclusion is that for most elements (Zr, Sn, Sb and W) RSF obtained for the glass standards are consistent, within the error, with the RSF calculated using the detrital rutile grains. However, for some elements (Nb, Hf and Ta) systematic differences are observed. Hafnium and Ta RSF calculated using data obtained for silicate glasses are systematically higher than those obtained for the titanite glasses and the detrital rutile data set (respectively 0.70 and 0.40 for glasses and 0.41 and 0.32 for rutiles). This is most likely caused by interferences from REE (*e.g.*, $^{147}SmO_2$ and ^{163}DyO on ^{178}Hf and $^{149}SmO_2$ and ^{165}HoO on ^{181}Ta) present in the silicate glasses but absent in rutile. Furthermore for both elements (Hf and Ta), a positive correlation between the calculated RSF and the REE/Ti ratio is observed. RSF calculated for Nb form two distinct groups, one composed by the rutile grains and characterized by higher RSF (0.84), and another composed by all other analyzed materials (including the titanite glasses) showing distinct lower RSF (0.55). One explanation would be a mass interference of Ti isotopes ($^{46}Ti^{47}Ti$) on ^{93}Nb. However, investigations carried out on the Sy rutile grains which contain a very low concentration of Nb (0.942 ppm, see Table 2.3) yielded very few counts for Nb (which give an apparent concentration of ~4 ppm), indicating that interferences associated with the Ti isotopes are negligible in the concentration range of most naturally occurring rutiles (tens to thousands of ppm). Therefore as significant interferences can be ruled out, we tentatively attribute the observed difference in RSF to matrix effects related to structural and chemical composition differences between analyzed materials.

Another possibility for explaining the systematic differences in RSF of Nb, Hf

Figure 2.4 *(following page)* SIMS Relative Sensitivity Factor (RSF) calculated for Zr, Nb, Sn, Sb, Hf, Ta, W and U plotted against concentration in ppm. Points represent EMP analyses performed on the detrital rutile grains. Each point represents one analysis. For U, a set of standard glasses was used and each point represents the average of three measurements. In this case reference concentrations were used. Dashed lines represent EMP detection limits (according to Table 2.1). Shaded areas represent analyses used for calculating the preferred RSF shown on the plots. MPI–DING: glasses Kl2, StHs6/80 and ATHO; USGS: glasses BCR2G, BHVO, TB and GSD; Tnt: titanite glasses TNT 150 and TNT 1500 (for bibliographic references see text.)
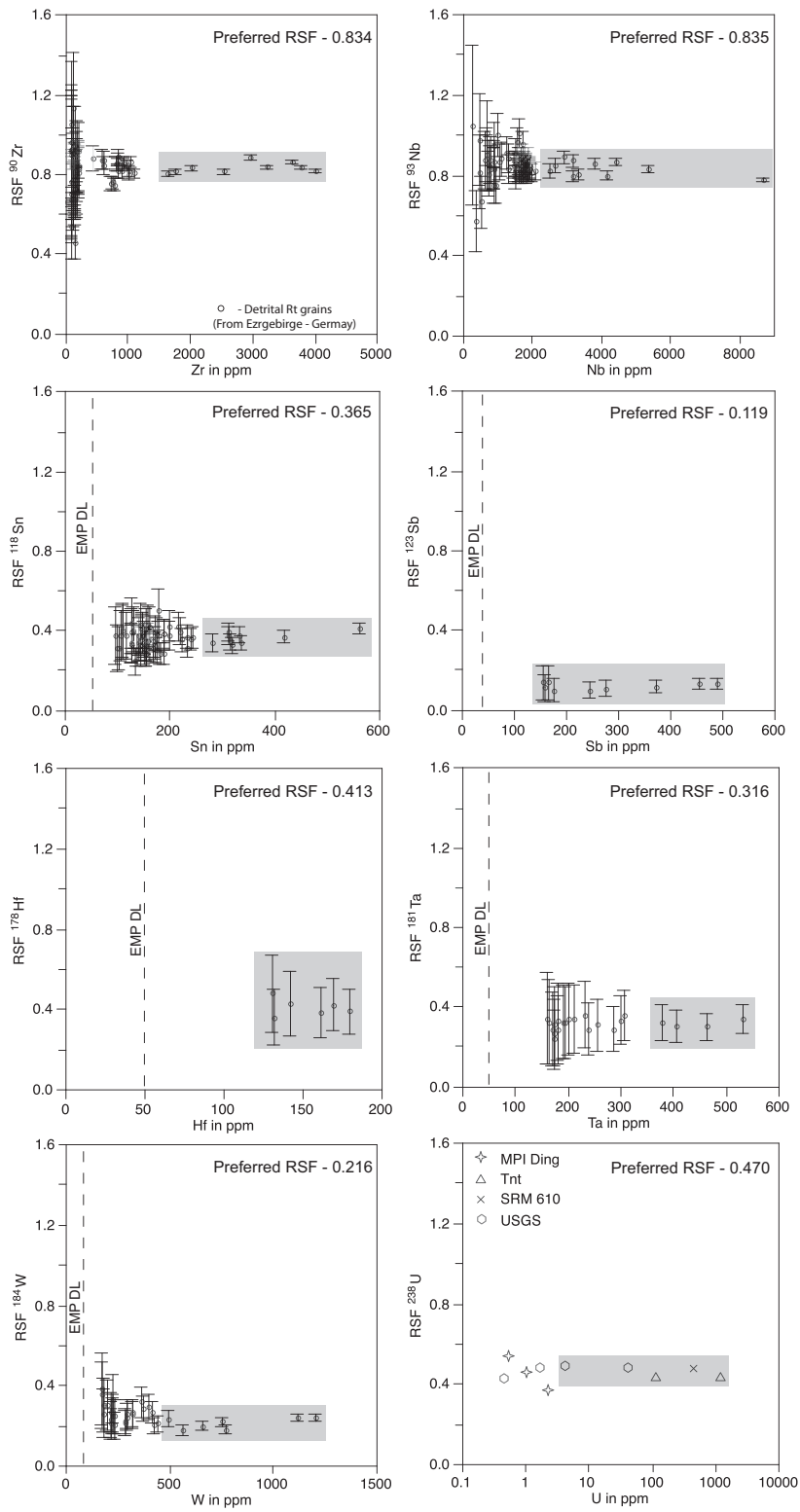
Table 2.2 Number of analyzed grains and summary of RSF calculated using the detrital rutile grains.

	Zr	Nb	Sn	Sb	Hf	Ta	W
Total analyzed grains (EMP)	188	189	181	92	89	92	166
Grains homog. (and above 2σ EMP DL + 2σ mean error)	70	81	68	9	6	22	38
Mean RSF	0.810	0.860	0.359	0.119	0.413	0.314	0.256
Standard deviation	0.139	0.120	0.045	0.016	0.041	0.029	0.049
# Selected analyses[a]	9	11	9	9	6	4	7
Mean RSF	**0.834**	**0.835**	**0.365**	**0.126**	**0.413**	**0.316**	**0.216**
Standard deviation	0.025	0.035	0.028	0.009	0.041	0.010	0.028

Values in bold are those used for calculating concentrations in ppm. For details about the selection process see discussion in the text. [a] according to the two filtering processes described in the text.

and Ta described above would be a systematic offset of EMP concentration data. However, this hypothesis can be excluded because SIMS concentrations calculated for the Diss, R19 and R10 rutile grains based on RSF obtained using the detrital rutiles match the ID–MC–ICP–MS data presented in Section 2.4.2.

The results obtained of U (Fig. 2.4) show a very low deviation indicating that matrix effects and/or interferences are negligible for this element. Therefore, the average RSF calculated for the standard glasses is assumed to be representative, given the fact that U concentration for the detrital rutile grains could not be obtained by EMP.

2.4.2 High precision HFSE concentration data

ID–MC–ICP–MS concentrations of six important trace elements in rutile (Zr, Nb, Hf, Ta, W and Lu) and $^{176}Hf/^{177}Hf$ isotopic ratios were obtained for the Sy, Diss, R19 and R10 rutile grains (Table 2.3). Zirconium and Hf results between the two replicates of each R10, R19, and Diss agree within the external reproducibilities quoted above (Table 2.3), demonstrating homogeneity for these elements. Results for Nb, Ta, W, and Lu between the replicates are outside analytical uncertainty, indicating some heterogeneity at the percent scale.

We would like to note that Nb/Ta and Zr/Hf ratios obtained by ID–MC–ICP–MS for the natural rutile grains show a large range (from 5.4 to 19.2 and from 19.2 to

30.7, respectively). The continental crust (from where the studied rutiles originate) is regarded as relatively homogeneous on a large scale with respect to its Nb/Ta and Zr/Hf ratios (see, *e.g.*, Barth *et al.*, 2000). However, several processes can change these values, at least on a local scale (*e.g.*, visible in the formation of tantalite and columbite ore deposits in pegmatites). Moreover, previous studies have shown that the Nb/Ta and Zr/Hf ratios in rutiles from the continental crust vary strongly (at least from 8 to 123 and 10 to 36, respectively; see analyses of crustal rutiles in Supplemental Table 1 of Rudnick *et al.*, 2000). These values are in contrast to rather constant ratios obtained for several other earth reservoirs like MORB and OIB (from 11 to 17 and 27 to 43, respectively, with both ratios showing a clear positive correlation; Münker *et al.*, 2003).

Table 2.3 ID–MC–ICP–MS results obtained for the rutile grains

	Zr	Nb	Hf	Ta	W	Lu	Nb/Ta	Zr/Hf	^{176}Hf/^{177}Hf
R10 Rim	768.9	2592	37.4	456	-	0.0513	5.7	20.53	0.282178
±	*7.7*	*103.7*	*0.4*	*5*	*-*	*0.0005*	*0.2*	*0.12*	*0.000009*
R10 Core	787.9	2725	38.9	504	108	0.0300	5.4	20.26	0.282178
±	*7.9*	*109*	*0.4*	*5*	*1*	*0.0100*	*0.2*	*0.12*	*0.000012*
R19	264.4	873	8.62	87.9	60.5	0.0724	9.9	30.69	0.282164
±	*2.6*	*35*	*0.09*	*0.9*	*0.6*	*0.0014*	*0.4*	*0.18*	*0.000017*
R19	262.0	945	8.67	112.6	58.1	0.1820	8.4	30.21	0.282162
±	*2.6*	*38*	*0.09*	*1.1*	*0.6*	*0.0020*	*0.3*	*0.18*	*0.000014*
Diss	97.8	145	5.09	7.56	19.7	0.0225	19.2	19.19	0.283239
±	*1.0*	*6*	*0.05*	*0.08*	*0.2*	*0.0010*	*0.8*	*0.12*	*0.000017*
Diss	98.0	147	5.07	7.75	16.2	0.0848	19.0	19.34	0.283277
±	*1.0*	*6*	*0.05*	*0.08*	*0.2*	*0.0014*	*0.8*	*0.12*	*0.000016*
Sy	4.45	0.942	0.0954	0.0037	0.338	0.0012	253	46.69	-
±	*0.04*	*0.038*	*0.002*	*0.0004*	*0.004*	*0.0002*	*10*	*0.28*	*-*
Chondritic Values[a]							19.9	34.3	
							±0.6	±0.3	

Concentrations are given in ppm. Errors refer to the 2σ external reproductibility: $\pm1\%$, except for Nb: $\pm4\%$ and both include the propagated uncertainty from blank variations. An uncertainty of $\pm50\%$ for the blank is assumed, resulting in higher errors in the case of low concentrations (*e.g.*, Ta, Lu and W in Sy). The external reproductibility of the Zr/Hf and Nb/Ta ratios are $\pm0.6\%$ and $\pm4\%$ (2σ) except if the blank uncertainty is larger.
[a] Münker *et al.* (2003).

2.4.3 U-Pb isotope data for R10

U–Pb isotope data for R10 were obtained by TIMS from fourteen fragments (nine from the rim and five from the core). Each analysis was carried out on a single fragment and represents the information of a restricted area, thus compared to *in-situ* techniques. The approximate location of the analyzed areas are presented in Fig. 2.2. The obtained data are presented in Table 2.4 and Fig. 2.5. Measured U concentrations are relatively high, in the 30 ppm range for most of the analyses (averages for rim and core are 28.15 and 31.98 ppm, respectively). Although the U concentration varies, the ages obtained are rather constant, ranging from 1085.1 to 1096.2 Ma (^{207}Pb/^{235}U ages) and from to 1086.3 to 1096.6 Ma (^{206}Pb/^{238}U ages).
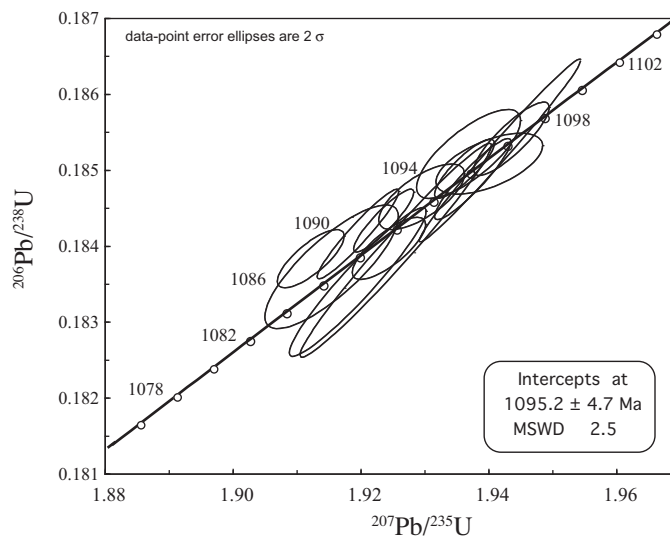
Figure 2.5 U-Pb concordia plot for all analyses of R10

R10 is from Gjerstd, South Norway and belongs to the Bamble sector of the Southwest Scandinavian Domain (SSD). This area is characterized by the occurrence of important Fe–Ti deposits (Korneliussen *et al.*, 2000), associated with magmatism early in the Sveconorwegian orogeny (Starmer, 1991; Kullerud & Dahlgren, 1993). The present structural and metamorphic configuration of the SSD formed during the Sveconorwegian (Grenvillian) Orogeny between 1.25 and 0.9 Ga. In the

Table 2.4 TIMS U-Pb isotopic data for the rutile R10

Fraction	weight	Concentrations (ppm)			$\frac{206Pb}{204Pb}$	$\frac{208Pb}{206Pb}$	Radiogenic ratios							Disc.,	Ages (Ma)		
	(mg)	U	Pb_{rad}	Pb_{com}	(meas.)		$\frac{207Pb}{235U}$	err., %	$\frac{206Pb}{238U}$	err., %	r	$\frac{207Pb}{206Pb}$	err., %	%	$\frac{207Pb}{235U}$	$\frac{206Pb}{238U}$	$\frac{207Pb}{206Pb}$
R10 c#05	261.00	38.7	6.6	32.8	3443.0	0.001	1.9366	0.35	0.18523	0.26	0.75	0.075826	0.228	-0.50	1093.8	1095.5	1090.5
R10 c#07	106.00	32.5	5.5	10.2	3708.0	0.000	1.9191	0.28	0.18418	0.26	0.95	0.075570	0.084	-0.61	1087.7	1089.8	1083.7
R10 c#83	32.00	24.1	4.2	9.7	898.6	0.006	1.9359	0.20	0.18504	0.17	0.86	0.075880	0.101	-0.25	1093.6	1094.4	1091.9
R10 c#87	31.00	31.9	5.4	13.0	851.7	0.004	1.9149	0.45	0.18374	0.36	0.81	0.075584	0.264	-0.33	1086.3	1087.4	1084.1
R10 c#90	87.00	32.7	5.6	6.4	4947.0	0.000	1.9434	0.25	0.18543	0.21	0.85	0.076009	0.131	-0.13	1096.2	1096.6	1095.3
R10 r#03	206.00	27.5	4.7	15.6	4006.5	0.002	1.9231	0.20	0.18435	0.18	0.90	0.075657	0.087	-0.47	1089.1	1090.7	1086.0
R10 r#10	8.00	49.7	8.5	5.1	875.0	0.003	1.9250	0.64	0.18396	0.63	0.98	0.075894	0.131	0.37	1089.8	1088.6	1092.3
R10 r#23	23.00	17.7	3.0	8.6	536.0	0.008	1.9240	0.25	0.18399	0.18	0.77	0.075841	0.156	0.21	1089.4	1088.7	1090.9
R10 r#24	172.00	33.6	5.8	22.1	2930.0	0.001	1.9415	0.54	0.18528	0.53	0.99	0.076000	0.082	-0.07	1095.5	1095.8	1095.1
R10 r#73	19.00	23.3	4.0	6.2	798.1	0.004	1.9190	0.46	0.18355	0.44	0.95	0.075830	0.145	0.43	1087.7	1086.3	1090.6
R10 r#74	50.00	22.5	3.9	10.1	1252.3	0.002	1.9372	0.26	0.18491	0.24	0.92	0.075986	0.098	0.10	1094.0	1093.7	1094.7
R10 r#84	32.00	27.2	4.7	18.9	528.1	0.003	1.9399	0.36	0.18511	0.18	0.59	0.076005	0.288	0.04	1095.0	1094.8	1095.2
R10 r#92	53.00	24.9	4.3	47.4	327.1	0.008	1.9292	0.29	0.18467	0.19	0.70	0.075765	0.206	-0.36	1091.2	1092.4	1088.9
R10 r#94	46.00	27.0	4.6	41.5	348.5	0.010	1.9116	0.23	0.18385	0.17	0.78	0.075409	0.142	-0.86	1085.1	1088.0	1079.4
						Avg	1.9286		0.18452			0.075804			1091.0	1091.6	1089.9
						2σ Std	0.0105		0.00065			0.000187			3.6	3.5	4.9

In the fraction labels, r and c stand for rim and core, respectively Avg - average (arithmetic mean) Std - Standard Deviation

Bamble sector, the magmatic-metamorphic event began with the intrusion of gabbroic magmas at 1.2 Ga (de Haas *et al.*, 2002a), reaching peak metamorphism at ca. 1.1 Ga (Kullerud & Dahlgren, 1993). Titanite U-Pb ages of 1091±2 Ma were obtained by de Haas *et al.* (2002b) and are interpreted as the age of peak metamorphism. According to the authors, the result is in agreement with the previously obtained Sm–Nd mineral isochron, U–Pb zircon and Pb–Pb titanite ages for peak Sveconorwegian metamorphism in the Bamble sector (Kullerud & Machado, 1991; Kullerud & Dahlgren, 1993; Cosca *et al.*, 1998). Therefore U-Pb TIMS ages obtained for R10 (1095 Ma) are in excellent agreement with the regional geological context. Recently, Bingen *et al.* (2008) carried out a comprehensive study about the geochronology of the Sveconorwegian orogeny in SW Scandinavia and according to their results the ages obtained for R10 match the age of the amphibolite–facies metamorphism that affected the Bamble sector.

2.4.4 LA–ICP–MS concentration data

Analyses of eleven trace elements were determined in splits (of millimeter size) from the Sy, Diss, R19 and R10 rutile grains. Results are presented in Table 2.5. In order to test reproducibility of the technique, three measurements were carried out on each split. It is noteworthy that concentrations of Mo, Pb and Th were obtained only using this technique. Concentrations of Pb and Th are very low for all rutiles (< 0.1 ppm). For all grains, at least one Pb concentration is anomalously (orders of magnitude) high. As it is a common feature for all grains, it is probably due to sample contamination (*e.g.*, the excess Pb may be located in micro–cracks that were accidently hit by the spot) and not element heterogeneity. Molybdenum concentrations are relatively high in R10 (average of 11.2 ppm) displaying a distinctly small standard deviation.

Table 2.5 LA-ICP-MS concentrations obtained for the rutile grains. Values within parentheses represent anomalous high concentrations that are probably due to surface contamination.

	V	Zr	Nb	Mo	Sb	Hf	Ta	W	Pb	Th	U
R10	1249	764	2824	11.2	2.08	37.3	394	61.7	(0.588)	<0.0037	44.6
	1296	756	2862	11.2	2.03	37.1	383	59.0	0.089	<0.0036	44.3
	1294	757	2849	11.3	2.13	37.1	375	62.4	0.073	<0.0035	43.4
Avg	**1279**	**759**	**2845**	**11.2**	**2.08**	**37.2**	**384**	**61.0**	**0.081**	**<0.0035**	**44.1**
2σ Std	*53*	*8*	*38*	*0.09*	*0.10*	*0.2*	*19*	*3.6*	*0.022*	*-*	*1.2*
R19	1569	246	618	1.51	1.34	8.08	21.4	72.6	(1.069)	<0.0033	14.7
	1600	252	648	1.56	1.25	8.18	22.3	67.7	0.250	0.0080	14.5
	1683	249	652	1.50	1.26	8.05	22.6	65.2	0.230	0.01	13.9
Avg	**1617**	**249**	**639**	**1.52**	**1.28**	**8.10**	**22.1**	**68.5**	**0.238**	**0.0115**	**14.4**
2σ Std	*117*	*6*	*37*	*0.07*	*0.10*	*0.14*	*1.2*	*7.6*	*0.028*	*0.0098*	*0.8*
Diss	753	129	180	0.919	0.45	6.56	11.0	83.3	0.0718	<0.0031	0.0070
	784	131	178	0.809	0.37	6.58	11.2	81.0	(0.1640)	<0.0030	0.0189
	773	126	180	0.880	0.41	6.49	11.7	83.0	0.0791	<0.0031	0.0099
Avg	**770**	**128**	**179**	**0.869**	**0.410**	**6.54**	**11.3**	**82.4**	**0.0755**	**<0.0030**	**0.0119**
2σ Std	*30*	*4.9*	*1.96*	*0.11*	*0.079*	*0.09*	*0.7*	*2.5*	*0.0103*	*-*	*0.0124*
Sy	<0.032	2.79	0.69	<0.070	<0.0380	0.060	<0.0050	0.065	(0.4550)	<0.0092	<0.0086
	0.043	2.74	0.66	<0.029	<0.0159	0.067	<0.0025	0.079	0.0780	<0.0033	<0.0035
	0.026	2.77	0.66	<0.024	<0.0131	0.059	<0.0022	0.012	0.0500	<0.0033	<0.0032
Avg	**0.035**	**2.77**	**0.667**	**<0.024**	**<0.0131**	**0.062**	**<0.0022**	**0.052**	**0.0640**	**<0.0033**	**<0.0032**
2σ Std	*0.025*	*0.057*	*0.033*	*-*	*-*	*0.009*	*-*	*0.071*	*0.0198*	*-*	*-*
SRM610	442	440	419	410	369	432	452	445	426	457.2	461.5
Unc.	43	8	58	29	28	15	39	25	1	1.2	1.1

Avg - average of measurements (arithmetic mean). 2σ Std - 2σ standard deviation of the 3 analyses.
SRM610 - preferred values used for calibration (from: http://georem.mpch-mainz.gwdg.de/ – accessed in December, 2006).
Unc - uncertainty according to GeoReM.

2.5 Discussion

2.5.1 Homogeneity test

In order to test homogeneity of the grains, two rim–to–rim profiles (perpendicularly oriented) were carried out by EMP and SIMS (location shown in Fig. 2.2). Figs. 2.6, 2.7, 2.8 and 2.9 show SIMS concentration data of the two profiles measured for the studied grains. Diagrams were normalized in such a way that the *y* axis spans a range from -40% to 40% of the concentration average (except for elements showing variations above this range). Concentrations in ppm were calculated using RSF presented in Section 2.4.1. SIMS is the method of choice for homogeneity tests as this is the most precise *in-situ* technique. Concentration data for V, Cr and Fe were not measured by SIMS. Hence, EMP are shown instead (Figs. 2.10, 2.11 and 2.12).

R10 is the most homogeneous rutile among the studied grains. It also has the highest trace element concentrations. Therefore this sample has the highest poten-
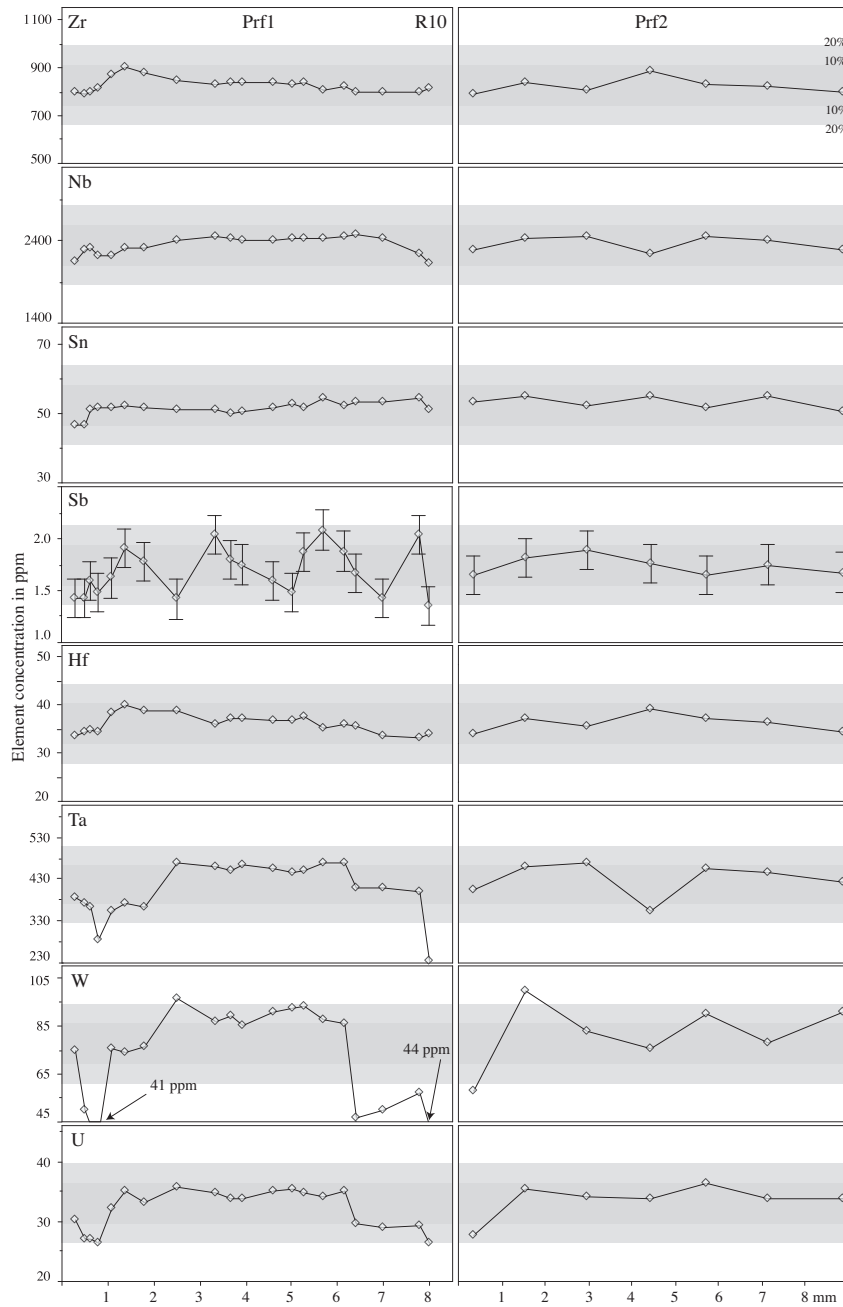
Figure 2.6 Rim-to-rim chemical profiles (SIMS) of Zr, Nb, Sn, Sb, Hf, Ta, W and U for the R10 grain. Please notice that all diagrams are normalized in a way that the *y* axis spans a range from -40% to 40% of the average for each element. Light and dark shaded areas represent 10% and 20% of variation from the average, respectively. Error bars are only shown when analytical errors (SIMS, 1 relative standard error based on counting statistics) are larger than the symbols. Prf1 - profile 1, Prf2 - profile 2.
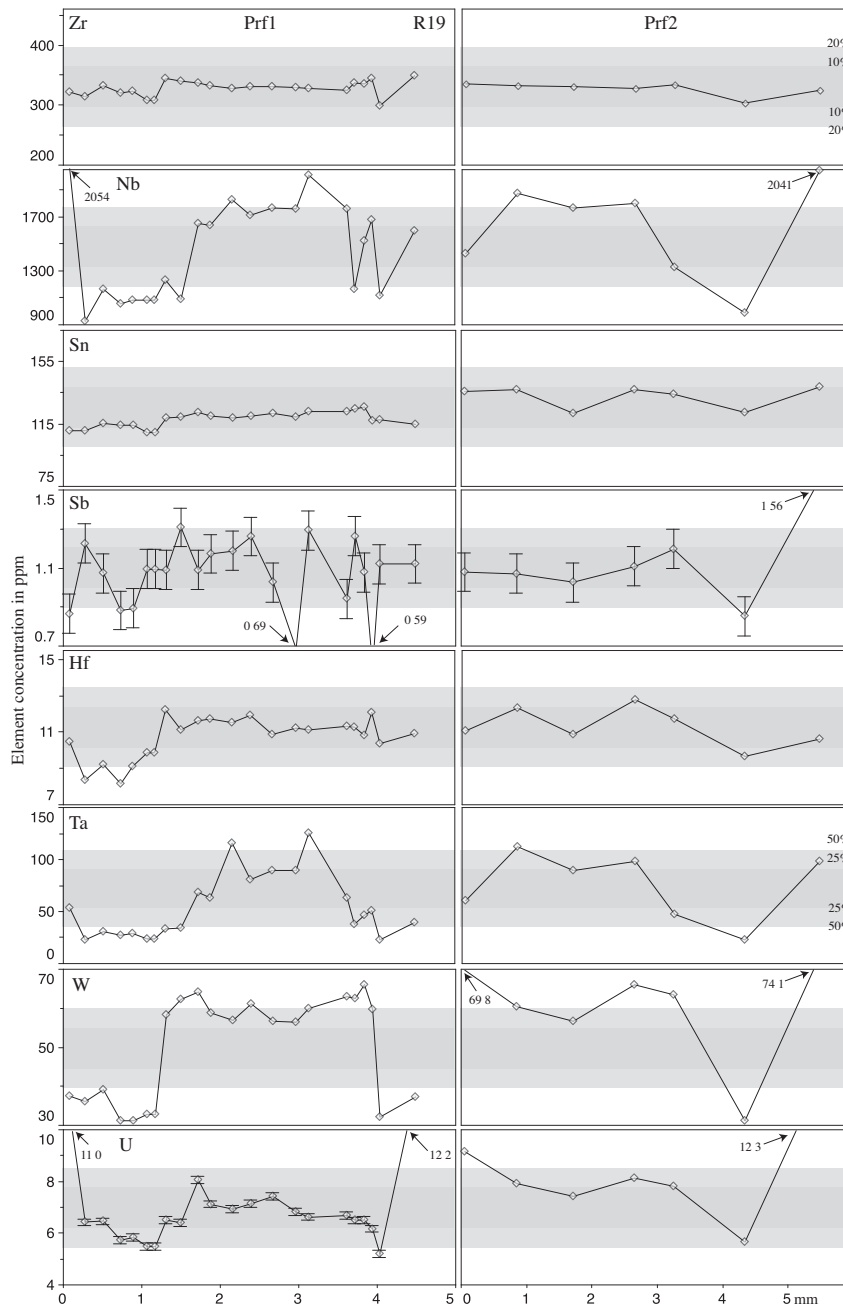
Figure 2.7 Rim-to-rim chemical profiles (SIMS) of Zr, Nb, Sn, Sb, Hf, Ta, W and U for the R19 grain. Please notice that diagrams are normalized in a way that the *y* axis spans a range from -40% to 40% of the average for each element. The only exception is the Ta diagram, where the *y* axis spans a range from -100% to 100%. Light and dark shaded areas represent 10% and 20% of variation from the average, respectively (except for Ta - see diagram). Error bars are only shown when analytical errors (SIMS, 1 relative standard error based on counting statistics) are larger than the symbols. Prf1 - profile 1, Prf2 - profile 2.
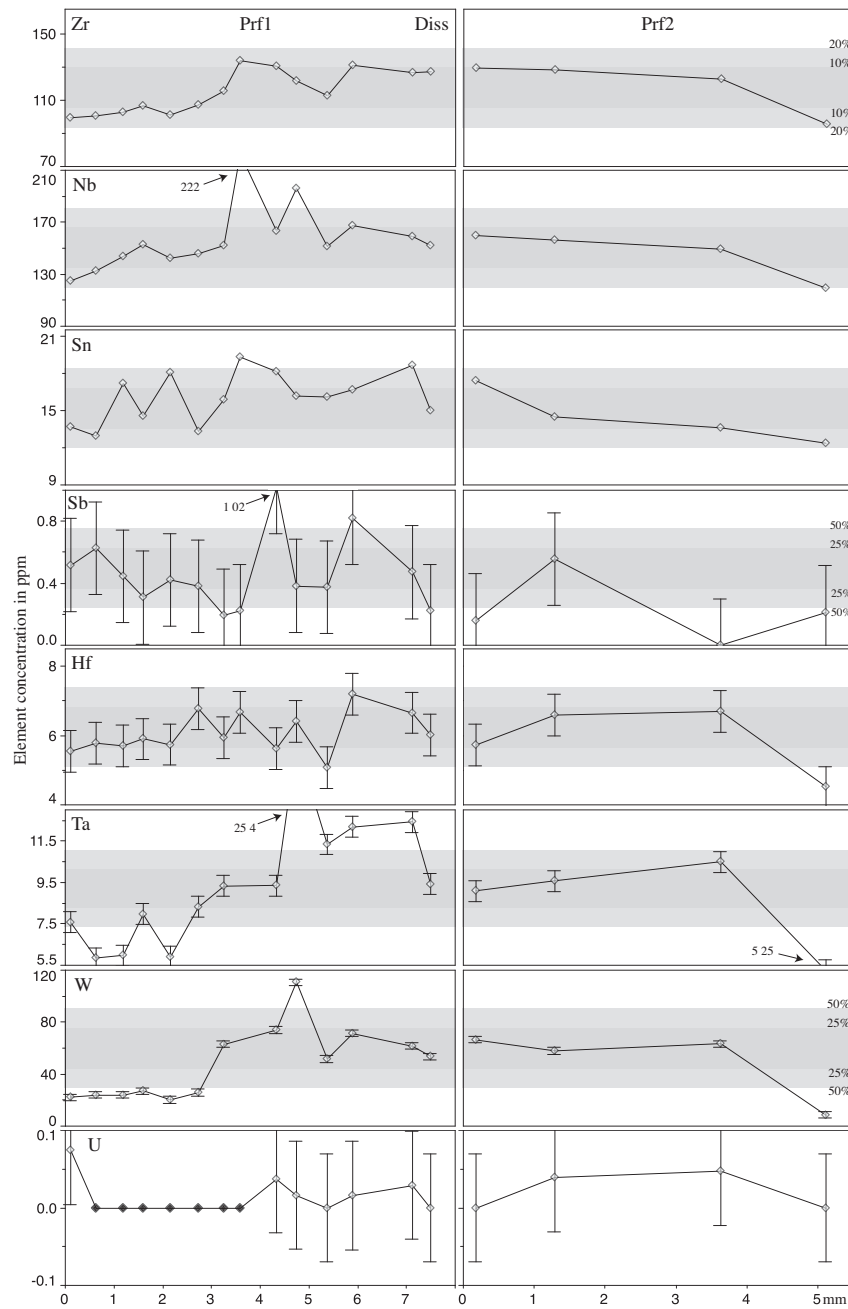
Figure 2.8 Rim-to-rim chemical profiles (SIMS) of Zr, Nb, Sn, Sb, Hf, Ta, W and U for the Diss grain. Please notice that diagrams are normalized in a way that the *y* axis spans a range from -40% to 40% of the average for each element. Exceptions are Sb and W diagrams, where the *y* axis span a range from -100% to 100%. Light and dark shaded areas represent 10% and 20% of variation from the average, respectively (except for Sb and W). Error bars are only shown when analytical errors (SIMS, 1 relative standard error based on counting statistics) are larger than the symbols. Filled symbols represent analyses where no counts where obtained for the measured time. Prf1 - profile 1, Prf2 - profile 2.

Figure 2.9 Rim-to-rim chemical profiles (SIMS) of Zr, Nb, Hf, Ta and U for the Sy grain. Intervals represented by the light and dark shaded areas are shown in the diagrams. Error bars are only shown when analytical errors (SIMS, 1 relative standard error based on counting statistics) are larger than the symbols. Filled symbols represent analyses where no counts were obtained for the measured time. Prf1 - profile 1, Prf2 - profile 2.
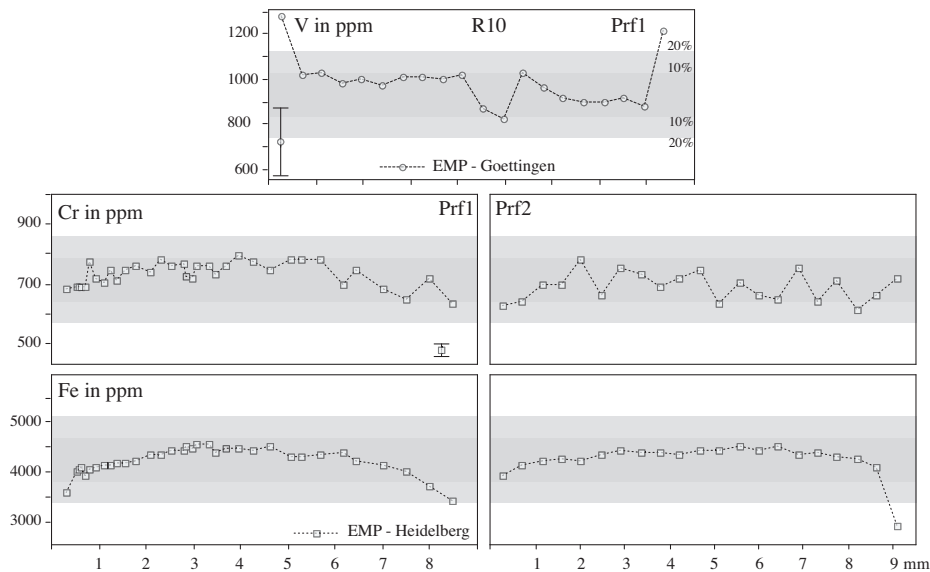
Figure 2.10 Rim-to-rim chemical profiles (EMP) of V, Cr and Fe for the R10 grain. Concentration data for V was only obtained for profile 1 in Göttingen. For Cr and Fe a greater amount of data was acquired in Heidelberg. Hence, these data are presented instead. Light and dark shaded areas represent 10% and 20% of variation from the average, respectively. Symmetric bars in the diagrams represent 2σ errors (only shown when analytical errors are larger than the symbols). Prf1 - profile 1, Prf2 - profile 2.

tial to be used as a secondary standard. For R10, Zr, Nb, and Hf are homogeneous within $\pm10\%$. Tin variations are within $\pm5\%$. However, it shows a decrease of approximately 10% close to the rim. Antimony concentrations are consistent within $\pm20\%$ but the variation can not be attributed to zoning because of high analytical errors as the concentrations are below 2 ppm. Tantalum and W show the highest variation in R10 (overall variation higher than $\pm20\%$). However, in detail, these elements show a distinct core plateau, where variations are within $\pm5\%$. Uranium behaves similarly to Ta and W. However the overall variation is smaller (within $\pm20\%$) and the plateau is wider (also showing variations within $\pm5\%$). Vanadium, Cr and Fe are present in relatively high concentrations in R10. For V, only the two rim analyses are outside the $\pm40\%$ interval. However errors are large for this element. Iron shows a clear trend, with concentrations decreasing towards the rim. This is mirrored by Cr, although the scattering is greater. However zoning is con-
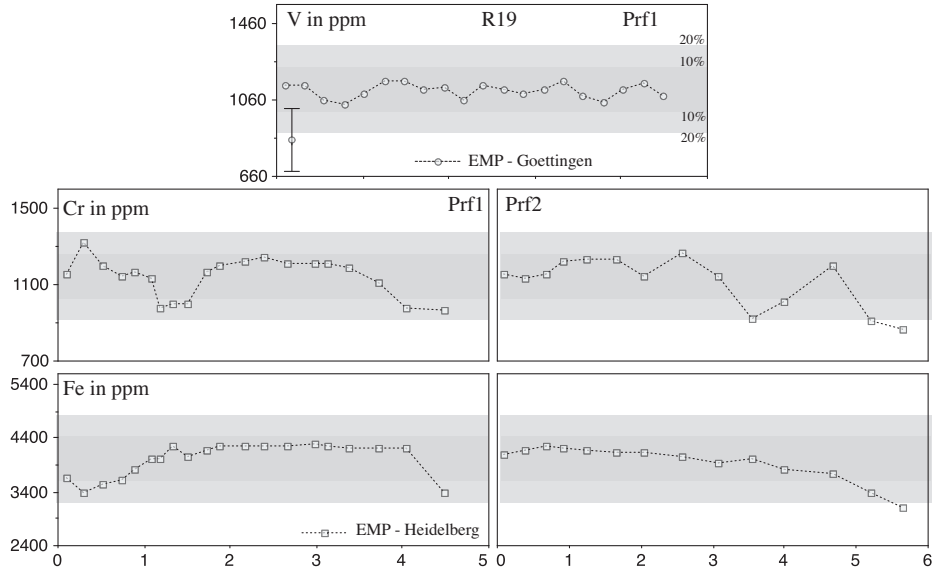
Figure 2.11 Rim-to-rim chemical profiles (EMP) of V, Cr and Fe for the R19 grain. For details see caption of Fig. 2.10.
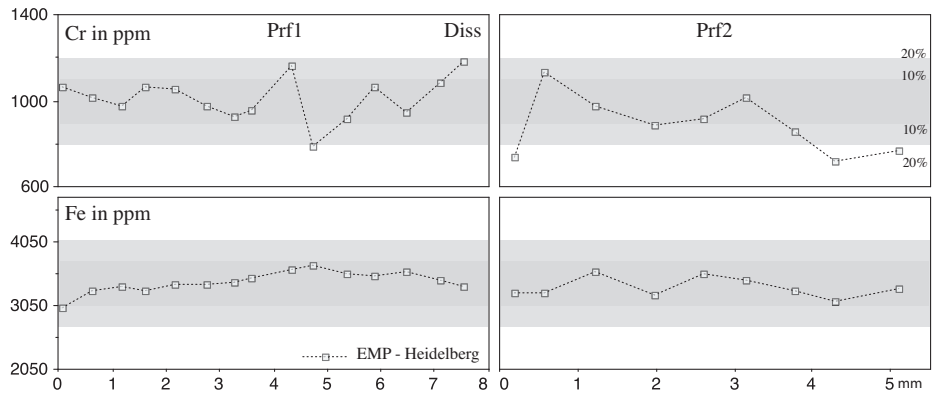
Figure 2.12 Rim-to-rim chemical profiles (EMP) of Cr and Fe for the Diss grain. For details see caption of Fig. 2.10.

strained within ±10%.

The most homogeneous trace elements in R19 are Zr and Sn which show variations within ±10%. Remarkably, Sn concentrations in R19 are relatively high (SIMS average of 125 ppm). Hafnium shows an overall variation of approximately ±20% but, in detail, shows a plateau with variation less than ±5%. Tungsten shows an overall variation higher than ±20% but displays a plateau where variations are much smaller (within ±10%). Antimony concentrations are low (approximate 1 ppm), and due to high analytical errors the scatter observed on the plot cannot be attributed to zoning. Uranium variations for most of the R19 grain is within ±20%, however an abrupt increase of approximate 40% is observed very close to the rim. As for R10, concentrations of V, Cr and Fe are relatively high in R19 (Cr is even higher, with an average of 1000 ppm). Variations are within ±10%, ±20% and ±15%, respectively.

The Diss grain has trace element concentrations considerably lower than those of the R19 and R10 grains. This implies that for some elements (Zr, Nb, V and Fe for EMP and Hf, Sb and U for SIMS) analytical errors are significantly higher. Zirconium and Sn display variations within ±20%. Niobium variations are mainly within ±20%, however a high concentration peak was recorded in the core of the grain for profile 1 (Fig. 2.8). Zirconium and Nb show an asymmetric zoning with concentrations progressively increasing (approximate 40%) from one rim to another in both profiles. A less pronounced increase is also displayed by Sn but part of the scatter is due to slightly higher analytical errors. The asymmetric zoning suggests that the grain is probably a split from a larger crystal. Antimony and U concentrations are very low (below 1 and 0.1 ppm, respectively) therefore errors are too high to draw conclusions about homogeneity. Hafnium yields concentrations consistent within ±20% (but errors are also high). Chromium and Fe show variations of ±20% and ±10%, respectively.

Sy is homogeneous within ±5% for Zr and Nb. Concentrations of Hf, Ta and U are too low to draw any conclusions about homogeneity.

2.5.2 Comparison of techniques

The comparison of all concentration data, obtained by the different applied techniques, is graphically displayed on the chemical profiles (grouped by element) presented in Figs. 2.13–2.23. Only data for the profile with the most data is displayed (profile 1 in previous figs.). The location of the splits analyzed by ID–MC–ICP–MS (except for the R10 grain) and LA–ICP–MS do not match the orientation of the profiles. Data obtained by these techniques are presented as horizontal lines through the chemical profiles presented in this section.

Zirconium

Five different concentration measurements were obtained for Zr, using four independent techniques. The results show an outstanding agreement, particularly for the R10 grain (highest concentration). The only exception is the Sy grain, where higher ID–MC–ICP–MS concentrations (approximately 2 ppm higher than SIMS and LA–ICP–MS) were recorded. The discrepancy is not yet understood but is probably related to complications due to the low concentration range. The good agreement between the Zr data is relevant, as the Zr incorporation in rutile is temperature dependent (Zack *et al.*, 2004b; Watson *et al.*, 2006; Tomkins *et al.*, 2007). Therefore, according to our data, temperatures calculated with the different techniques assessed in the present work can be directly compared.

Niobium

Concentration data obtained for Nb show an excellent agreement. However, EMP concentrations obtained in Heidelberg are higher than those obtained in Göttingen, showing a systematic linear offset (average ratios of 1.18 and 1.25 for the R10 and R19 grains). The observed discrepancy is probably due to different matrix correction methods applied by the laboratories (PAP in Heidelberg (the only method allowed by the CAMECA software) and phi-rho-z in Göttingen). In order to evaluate the influence of different matrix correction methods on the results, analyses performed in in Göttingen where recalculated using phi-rho-z and ZAF. Results show

that concentrations calculated using the phi-rho-z method are systematic lower than those calculated by the ZAF method, giving a systematic linear offset of approximate 10%. For the Sy grain, concentrations obtained by ID–MC–ICP–MS and LA–ICP–MS agree within $\pm 5\%$ (even within the 1 ppm range). On the other hand, SIMS concentrations are significantly higher ($\sim 60\%$) and probably reflect mass interference of Ti isotopes (^{46}Ti^{47}Ti) on ^{93}Nb measurements (see discussion in Section 2.4.1).

Tin

The only grain where Sn concentrations are above EMP detection limit (referring to the Göttingen laboratory) is R19. Therefore, this is the only grain that allows comparison between this technique and SIMS. Although EMP errors are relatively high, concentrations obtained with this technique fit, within the error, with results obtained by SIMS.

Antimony

Both SIMS and LA–ICP–MS data were obtained for R10, R19 and Diss. For all grains, results agree within the error. However, when concentrations are so low (*i.e.*i.e., <3ppm) inevitably the SIMS errors are relatively large.

Hafnium

For R10, Hf concentrations obtained by three independent techniques show an outstanding agreement. If LA–ICP–MS results are compared to concentrations obtained by SIMS and ID–MC–ICP–MS for the core region of the grain, the agreement is within 5% or less. For the other grains the agreement is also remarkable, however results have to be interpreted with caution due to lower concentration ranges (higher errors) and heterogeneities (zoned profiles, *e.g.*, R19).
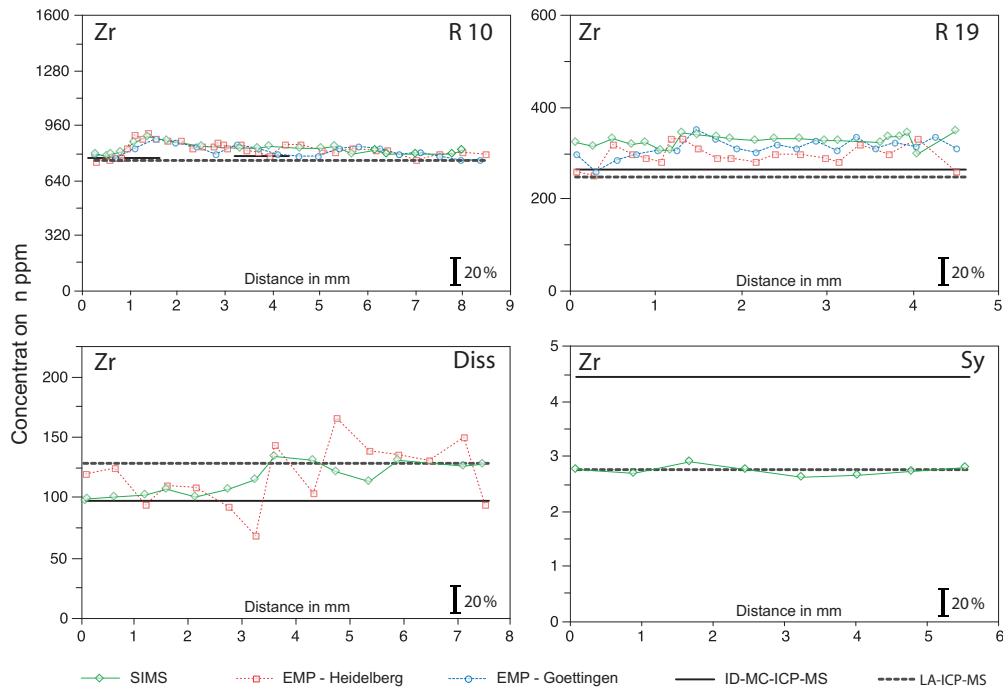
Figure 2.13 Rim-to-rim chemical profiles of Zr. Errors (1 relative standard error) are smaller then the symbols.

Figure 2.14 Rim-to-rim chemical profiles of Nb. Errors (1 relative standard error) are smaller then the symbols.

Figure 2.15 Rim-to-rim chemical profiles of Sn. Error bars (EMP) represent 2σ. For SIMS, errors are smaller than the symbols

Tantalum

For Ta, the comparison of techniques must be done cautiously as this element shows heterogeneous profiles for the R10, R19 and Diss grains. Furthermore, Ta concentration in Sy is very low (below 0.02 ppm). As it has been said before, R10 is the only grain where ID–MC–ICP–MS matches the SIMS profile. For this grain, SIMS and ID–MC–ICP–MS obtained for rim and core agree within $\pm10\%$. Moreover, for all grains, if ID–MC–ICP–MS and LA–ICP–MS concentrations are extrapolated through the profiles, results of at least two techniques match the profile in specific parts. For example, for the rim of the R10 and Diss grains (Fig. 2.18), concentrations obtained by SIMS, ID–MC–ICP–MS and LA–ICP–MS agree within ±10 and $\pm15\%$ respectively.

Tungsten

As with Ta, W shows heterogeneous profiles for the R10, R19 and Diss grains and therefore the observations made for that element are also valid. However, for W, the R19 grain display a wide and relatively homogeneous core plateau, where SIMS, ID–MC–ICP–MS and LA–ICP–MS concentration agree within $\pm10\%$.
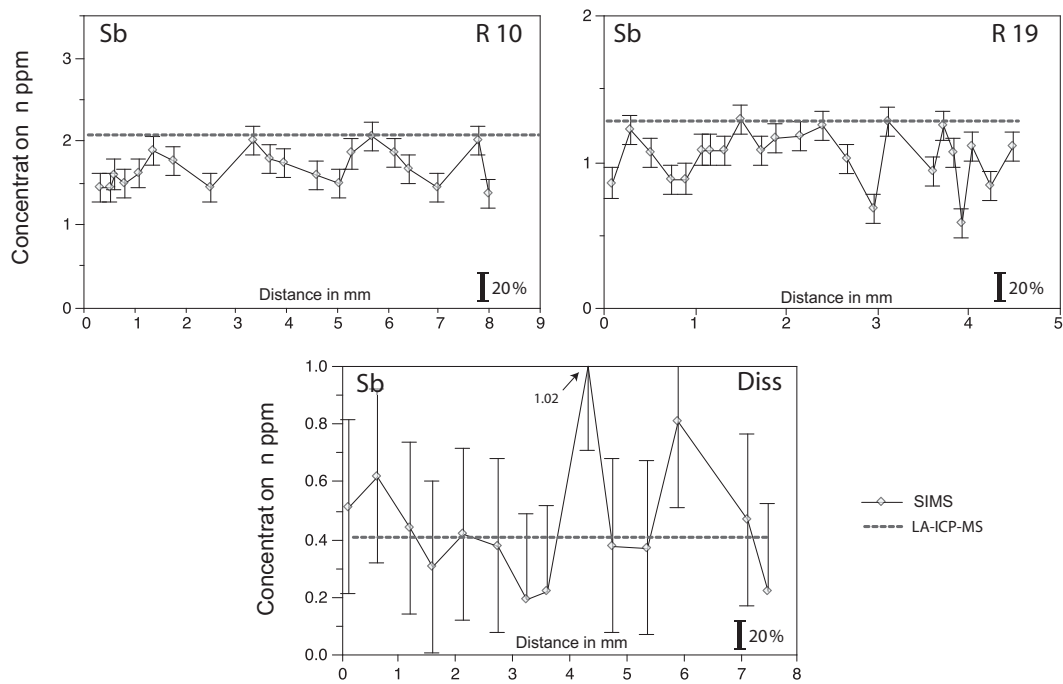
Figure 2.16 Rim-to-rim chemical profiles of Sb. Error bars represent 1 relative standard error.
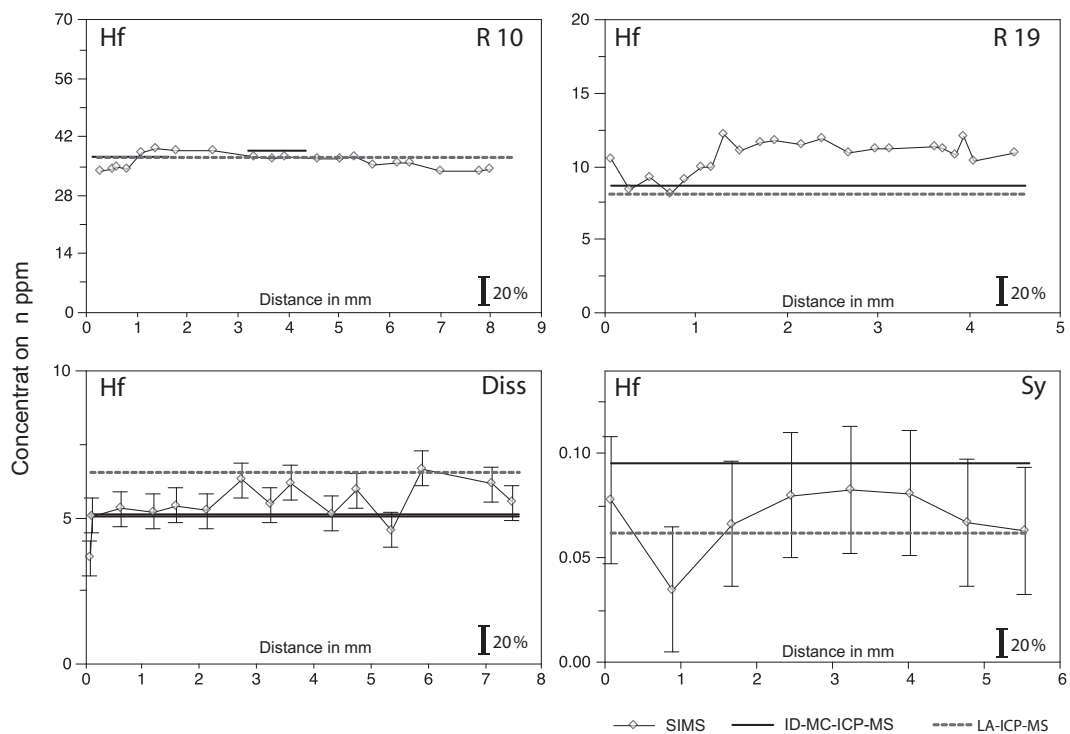
Figure 2.17 Rim-to-rim chemical profiles of Hf. Error bars are only shown when errors (1 relative standard error) are larger than the symbols.
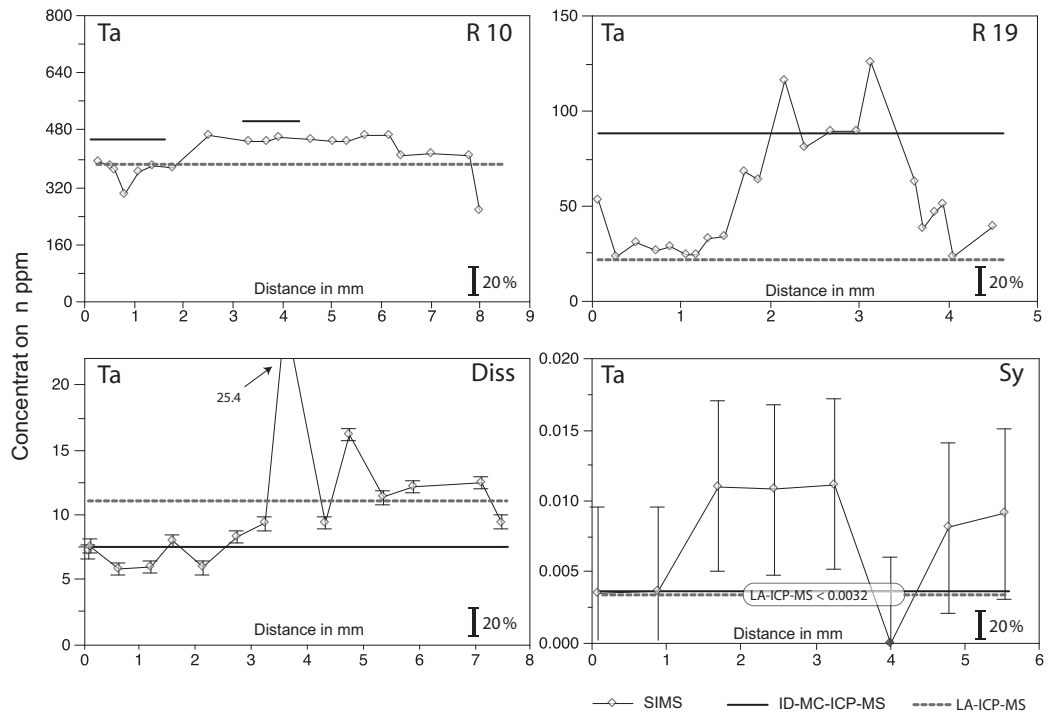
Figure 2.18 Rim-to-rim chemical profiles of Ta. Error bars are only shown when errors (1 relative standard error) are larger than the symbols.
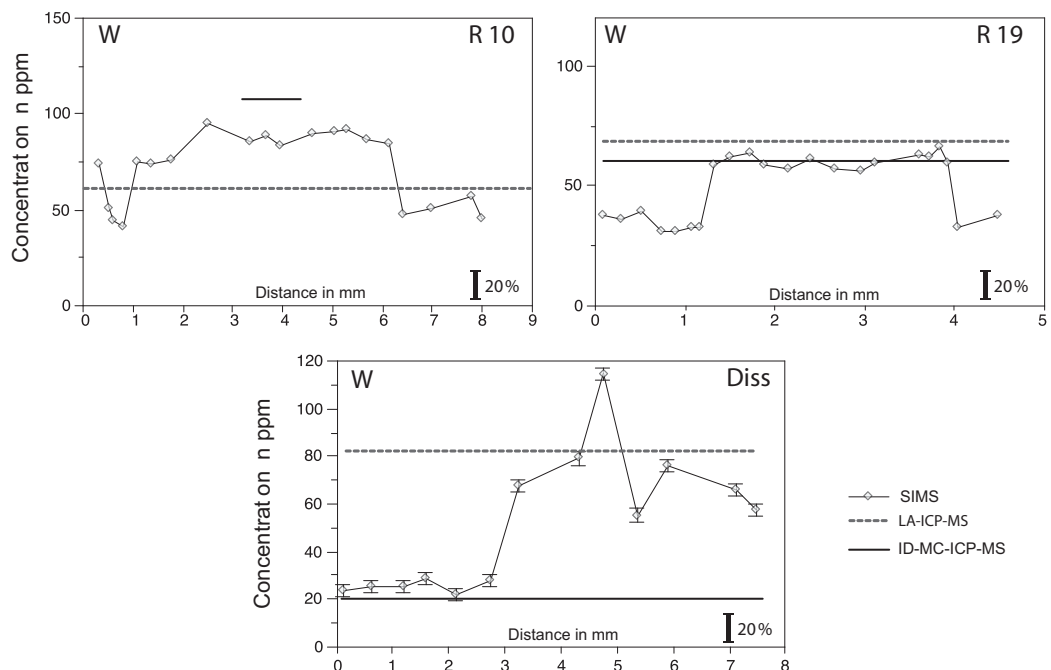
Figure 2.19 Rim-to-rim chemical profiles of W. Error bars are only shown when errors (1 relative standard error) are larger than the symbols.

Uranium

The only grain where U concentrations were obtained by three different techniques is the R10. For this grain, SIMS and TIMS (average) concentrations agree (for both core and rim) within ±10%. For the core region concentrations obtained by LA–ICP–MS, SIMS and TIMS agree within ±20%. LA–ICP–MS concentrations obtained for the R19 grain are too high (average of 14.4 ppm) when compared to SIMS (average of 7.40 ppm). However it is difficult to evaluate whether this is due to analytical error limitations or to heterogeneity as U shows a zoned profile with concentrations significantly increasing towards the rim. Low concentrations of U for the Diss and Sy grains are confirmed by both SIMS and LA–ICP–MS.
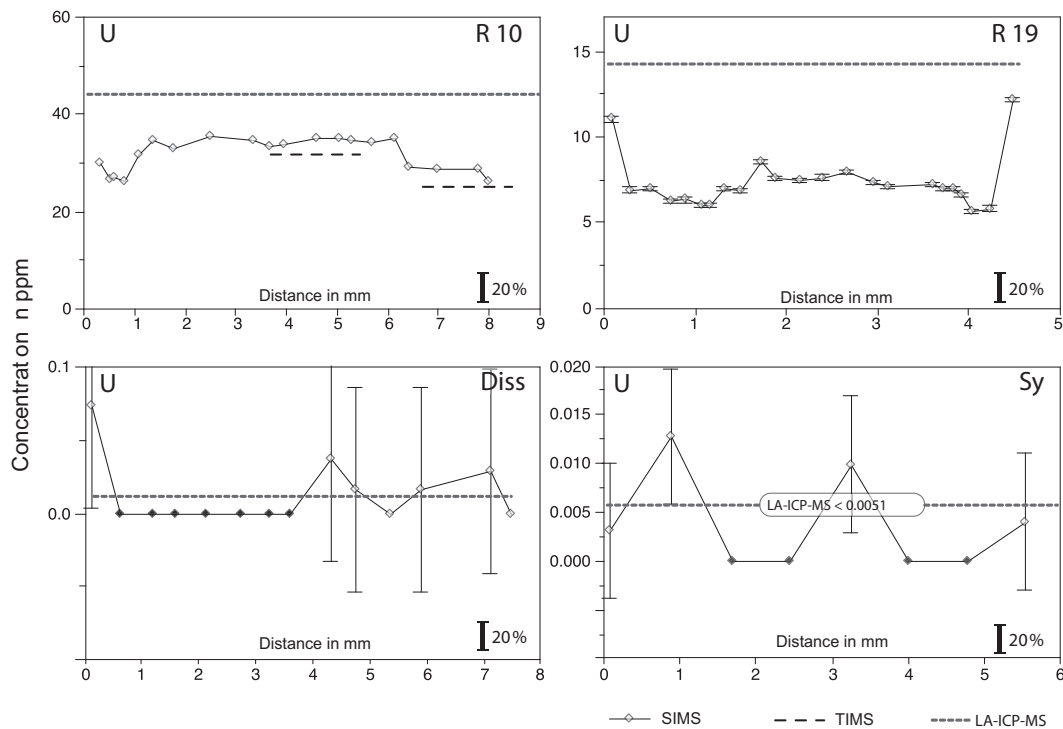
Figure 2.20 Rim-to-rim chemical profiles of U. Error bars are only shown when errors (1 relative standard error) are larger than the symbols. Filled symbols represent analyses where no counts where obtained during the measurement time.

Vanadium

For both R10 and R19, LA–ICP–MS concentrations are higher then those obtained by EMP (up to 40%). However, more data is necessary to judge if this is due to analytical error limitations or to heterogeneity of the grains (*e.g.*, LA–ICP–MS match EMP concentrations for R10 rim).

Chromium and Iron

Concentrations of Cr and Fe were obtained by EMP in Heidelberg and Göttingen for the R10 and R19 grains. Results obtained by both laboratories are almost identical (discrepancies smaller than the heterogeneities of the grains) showing an outstanding agreement. Cr is particularly important in rutile as it can be used, together with Nb, in quantitative provenance studies (see, *e.g.*, Zack *et al.*, 2004a; Triebold *et al.*, 2007).

2.5.3 Rutile mineral standards

A summary of all concentration data obtained for the studied rutile grains is presented in Table 2.6. Analyzed rutiles fall in four distinct compositional ranges, namely the difference in concentration between the grains that vary by orders of magnitude. The large difference in concentration for a given element observed from one grain to another enables not only the evaluation of detection limits of a given analytical technique but also the cross calibration of methods having different sensitivity ranges. In addition, the Sy rutile can be used in EMP studies for determining "true" zero-concentrations for a matched matrix. It can also be used to check interferences, for instance, from the Ti isotopes, by monitoring pure counts of a given element. In the present work, this was particularly useful to investigate interferences on Nb during SIMS measurements as described in Section 2.4.1.

Tables 2.7, 2.8, 2.9 and 2.10 show average concentrations of selected elements. Weighted averages were calculated at 95% confidence level using "IsoplotEx Version 2.49" (Ludwig, 2001). Only homogeneous elements (according to Section 2.5.1), for which concentrations obtained by at least three techniques agreed within
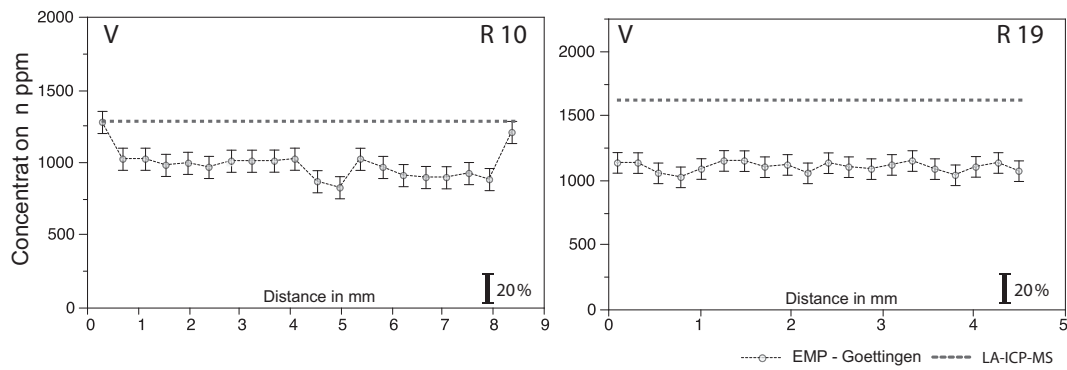
Figure 2.21 Rim-to-rim chemical profiles of V. Error bars represent 2σ.
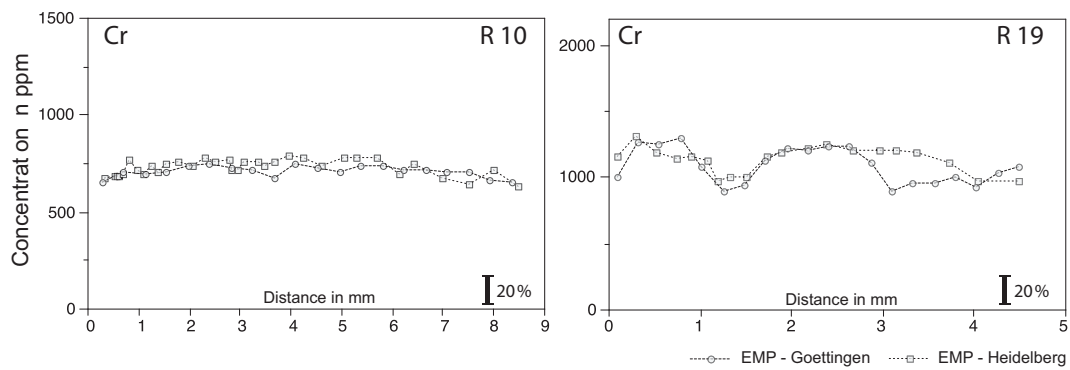
Figure 2.22 Rim-to-rim chemical profiles of Cr. Errors (1 relative standard error) are smaller then the symbols.
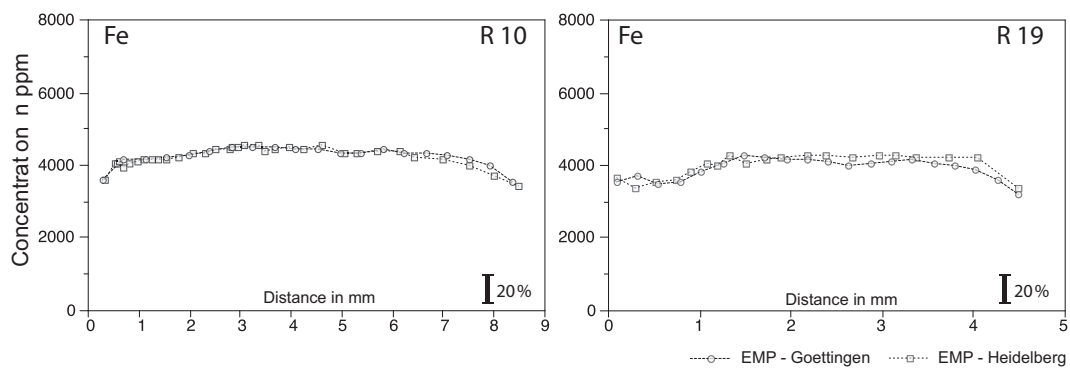
Figure 2.23 Rim-to-rim chemical profiles of Fe. Errors (1 relative standard error) are smaller then the symbols.

Table 2.6 Summary of all rutile analyses.

			V	Cr	Fe	Zr	Nb	Mo	Sn	Sb	Hf	Ta	W	Lu	Pb	Th	U
R10	EMP	Min		611	2926	731	2490						bdl				
	Heidelberg	Max		797	4570	914	3073						bdl				
	55 analyses	**Avg**		**716**	**4240**	**811**	**2864**										
		Std		48	296	43	134										
	EMP	Min	833	651	3553	760	2071		bdl				bdl				
	Göttingen	Max	1283	755	4513	888	2578		bdl				bdl				
	20 analyses	**Avg**	**991**	**710**	**4255**	**811**	**2423**										
		Std	107	29	271	34	120										
	SIMS	Min				782	2411		53.3	1.56	36.3	304	50.4				29.6
	32 analyses	Max				898	2841		66.4	2.84	42.5	557	123.1				45.9
		Avg				**823**	**2695**		**59.6**	**1.98**	**39.1**	**501**	**93.6**				**37.3**
		Std				29	118		2.7	0.29	1.7	62	21.4				4.0
	ID-MC-ICP-MS	Rim				768.9	2592				37.4	456			0.0513		28.2[a]
		Core				787.9	2725				38.9	504	108		0.0300		32.0[a]
	LA-ICP-MS	**Avg**	**1279**			**759**	**2845**	**11.2**		**2.08**	**37.2**	**384**	**61.0**		**0.0810**	**<0.0035**	**44.1**
		Std	27			4	19	0.1		0.05	0.1	9	1.8		0.0110	-	0.6
R19	EMP	Min		868	3088	250	1169						bdl				
	Heidelberg	Max		1320	4290	340	2680						bdl				
	34 analyses	**Avg**		**1130**	**3984**	**302**	**1954**										
		Std		114	323	23	414										
	EMP	Min	1036	896	3227	260	849		114				bdl				
	Göttingen	Max	1164	1307	4264	355	2453		165				bdl				
	20 analyses	**Avg**	**1110**	**1090**	**3909**	**312**	**1556**										
		Std	39	137	292	20	392		15								
	SIMS	Min				299	1064		126.3	0.67	8.8	25.2	34.3				6.3
	35 analyses	Max				349	2367		159.8	1.76	13.8	149.9	90.2				14.3
		Avg				**326**	**1698**		**140.0**	**1.20**	**11.5**	**66.7**	**62.0**				**8.8**
		Std				12	413		9.8	0.22	1.3	36.9	18.0				2.1
	ID-MC-ICP-MS	**Avg**				263	909				8.6	100.3	59.3	0.1272			
		Std				2	51				0.04	17.5	1.7	0.0775			
	LA-ICP-MS	**Avg**	**1617**			**249**	**639**	**1.52**		**1.28**	**8.10**	**22.1**	**68.5**		**0.2380**	**0.0115**	**14.4**
		Std	59			3	19	0.03		0.05	0.07	0.6	3.8		0.014	0.0049	0.4
Diss	EMP	Min		715	3009	60	112						bdl				
	Heidelberg	Max		1185	3689	166	210						bdl				
	24 analyses	**Avg**		**966**	**3392**	**116**	**172**										
		Std		129	169	26	27										
	SIMS	Min				95	137		14.2	0.14	3.9	6.25	10.3				bdl
	22 analyses	Max				137	276		91.2	5.60	7.3	30.20	134.8				0.084
		Avg				**118**	**186**		**24.4**	**0.94**	**5.8**	**12.10**	**62.0**				**0.042**
		Std				14	38		20.2	1.40	0.9	5.16	32.7				0.020
	ID-MC-ICP-MS	**Avg**				98	146				5.1	7.7	18.0	0.0537			
		Std				0.14	1.4				0.0	0.1	2.5	0.0441			
	LA-ICP-MS	**Avg**	**770**			**128**	**179**	**0.869**		**0.410**	**6.54**	**11.3**	**82.4**		**0.0755**	**<0.0030**	**0.0119**
		Std	15			2.5	0.98	0.06		0.04	0.05	0.4	1.2		0.0052	-	0.0062
Sy	SIMS	Min				2.61	4.26				0.038	bdl					bdl
	13 analyses	Max				2.93	4.66				0.094	0.018					0.015
		Avg				**2.75**	**4.43**				**0.075**	**0.011**					**0.008**
		Std				0.10	0.12				0.018	0.004					0.005
	ID-MC-ICP-MS					4.45	0.94				0.095	0.0037	0.338	0.0012			
	LA-ICP-MS	**Avg**	**0.04**			**2.77**	**0.667**	**<0.041**			**0.062**	**<0.0022**	**0.052**		**0.0640**	**<0.0087**	**<0.0051**
		Std	0.01			0.03	0.016	-			0.004	-	0.035		0.0198	-	-

[a] TIMS - University of Kansas (average of rim and core values presented in Table 2.4)
Avg - average (arithmetic mean). Std - Standard deviation (1σ)
bdl - Below detection limit

errors (including the standard deviation of the data and the analytical error of the technique), are presented. The values presented here can be classified as *provisional values* according to the classification scheme proposed by Potts & Kane (1992). However for most elements, confidence limits are within those proposed by the authors for the *recommended values* (category where confidence limits are lower). Therefore, the classification as *provisional value* is mostly due to the analytical criteria and not the confidence limits (the recommended value category requires data obtained by at least six laboratories and two techniques). For all grains, data of profiles 1 and 2 (according to Figs. 2.6, 2.7, 2.8 and 2.9) were included in the calculations. For R10, as various elements show chemical profiles with a core plateau, only data from this area of the grain were included (area represented by the W core plateau in Fig. 2.6). For R19, Diss and Sy, concentration data for the whole profile (grain) were included in the calculations. Except for W in R19, where only data from the core plateau were taken into account. For Sb in R10, Sn and Sb in R19 and Sb in Diss, concentration data were obtained by only two techniques. These elements show homogeneous profiles and the data obtained by the two techniques show a good agreement. Taking into account that these are important trace elements that can be incorporated in rutile, these elements were included in Tables 2.7, 2.8 and 2.9. Fig. 2.24 summarizes the Zr data obtained for R10 (core) and exemplifies how the provisional values were calculated. Each point on the diagram corresponds to the average of concentration data obtained by the technique and the provisional value corresponds to the average of these values. This figure is also an estimate of the accuracy of the presented value, as results from four independent techniques (including two different EMP laboratories) give an overall variation (including errors) less than $\pm\,5\%$.

Though some elements were analyzed only by one technique (*e.g.*, Cr and Fe by EMP; Mo, Pb and Th by LA–ICP–MS and Lu by ID–MC–ICP–MS) the obtained data is still important. For example, very low concentrations obtained for Th by LA–ICP–MS (analyzed as ^{232}Th) for all grains are favourable in U/Pb rutile dating as ^{208}Pb can be assumed to be from common Pb (Zack *et al.*, 2007).

Although some elements show heterogeneous distribution (*e.g.*, Ta and W in

Table 2.7 Provisional values (in ppm) for the **R10** grain.

R10	Technique	#	avg ppm	2σ error
Zr	SIMS	13	828	44
	EMP-HD	25	820	67
	EMP-Gö	9	817	60
	ID–MC–ICP–MS	1	788	8
	LA–ICP–MS	3	759	49
	Wtd Avg		**789 ±13**	
	MSWD		**1.6**	
Nb	SIMS	13	2395	112
	EMP-HD	25	2932	150
	EMP-Gö	9	2474	141
	ID–MC–ICP–MS	1	2725	109
	LA–ICP–MS	3	2845	188
	Wtd Avg		**2633 ±280**	
	MSWD		**11.7**	
Sb	SIMS	13	1.78	0.37
	LA–ICP–MS	3	2.08	0.19
	Wtd Avg		**2.02 ±0.17**	
	MSWD		**2.1**	
Hf	SIMS	13	36.8	2.0
	ID–MC–ICP–MS	1	38.9	0.4
	LA–ICP–MS	3	37.2	2.3
	Wtd Avg		**38.8 ±1.5**	
	MSWD		**3.1**	
Ta	SIMS	13	449	55
	ID–MC–ICP–MS	1	504	5
	LA–ICP–MS	3	384	30
	Wtd Avg		**504 ±63**[*]	
	MSWD		**4.0**[*]	
U	SIMS	13	34.5	1.7
	TIMS	5	32	10.4
	LA–ICP–MS	3	44.1	3.0
	Wtd Avg		**34.4 ±1.7**[*]	
	MSWD		**0.22**[*]	

As profiles for Hf, Ta and U show a core plateau, only analyses referent to this area were taken into account.
[*] calculations excluded LA–ICP–MS data. Calculations including this technique yielded similar Wtd Avgs but extremely high MSWD.
Data for both profiles 1 and 2 (for detail see diagrams in Section 2.5.1) were included in the calculations. Only homogeneous elements, for which concentrations obtained by at least three different techniques agreed within the error, are presented here. The only exception is Sb, where concentrations were obtained by two techniques (also valid for R19 (Table 2.8) and Diss (Table 2.9). Errors, expressed in 2σ, were calculated based on gaussian error propagation and include the analytical error of the given technique and the 2σ standard deviation of the analyses. # – number of analyses. Wtd Avg – weighted average. MSWD – mean square of weighted deviates.

Table 2.8 Provisional values (in ppm) for the **R19** grain.

R19	Technique	#	avg ppm	2σ error
Zr	SIMS	29	328	24
	EMP-HD	34	302	61
	EMP-Gö	20	312	50
	ID–MC–ICP–MS	2	263	3
	LA–ICP–MS	3	249	17
	Wtd Avg		**264 ±12**	
	MSWD		**93**	
Sn	SIMS	29	121	16
	EMP-Gö	20	143	57
	Wtd Avg		**123 ±15**	
	MSWD		**0.55**	
Sb	SIMS	29	1.08	0.43
	LA–ICP–MS	3	1.28	0.15
	Wtd Avg		**1.26 ±0.14**	
	MSWD		**0.77**	
W - Core	SIMS	17	60.7	6.4
	ID–MC–ICP–MS	2	59.0	0.6
	LA–ICP–MS	3	68.5	8.8
	Wtd Avg		**59 ±2**	
	MSWD		**2.5**	

For W only core analyses were included in the calculations, as this element shows a core plateau. Further explanations see Table 2.7. Note that Sn concentrations were obtained by only two techniques (SIMS and EMP).
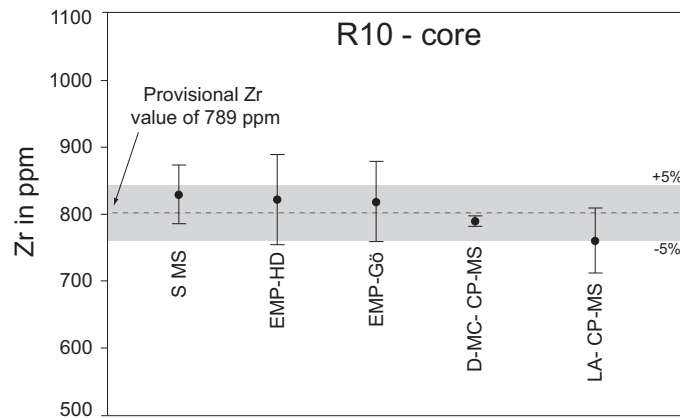
Figure 2.24 Average of Zr concentrations obtained by all techniques for the R10 grain (core). Each point on the plot represents the average (arithmetic mean) of the selected analyses performed by the technique (according to data presented in Table 2.7). Error bars are 2σ.

Table 2.9 Provisional values (in ppm) for the **Diss** grain.

Diss	Technique	#	avg ppm	2σ error
Zr	SIMS	18	116	26
	EMP-HD	24	116	66
	ID–MC–ICP–MS	2	98	1
	LA–ICP–MS	3	128	9
	Wtd Avg		**98.03 ±0.98**[*]	
	MSWD		**1.11**[*]	
Nb	SIMS	18	155	48
	EMP-HD	24	173	81
	ID–MC–ICP–MS	2	146	6
	LA–ICP–MS	3	179	12
	Wtd Avg		**146.3 ±5.8**[*]	
	MSWD		**0.29**[*]	
Sb	SIMS	18	0.407	0.775
	LA–ICP–MS	3	0.410	0.092
	Wtd Avg		**0.410 ±0.089**	
	MSWD		**0.000**	
Hf	SIMS	18	5.53	1.34
	ID–MC–ICP–MS	2	5.08	0.05
	LA–ICP–MS	3	6.54	0.44
	Wtd Avg		**5.081 ±0.049**[*]	
	MSWD		**0.45**[*]	
Ta	SIMS	17	9.2	2.82
	ID–MC–ICP–MS	2	7.66	0.08
	LA–ICP–MS	3	11.3	1.06
	Wtd Avg		**7.66 ±0.55**[*]	
	MSWD		**1.19**[*]	

[*] calculations excluded LA–ICP–MS data. Calculations including this technique yielded similar Wtd Avgs but extremely high MSWD.
Further explanations see Table 2.7.

R10 and Diss and Nb, Ta and W in R19), sometimes a good correlation between two elements is observed (correlation coefficients larger than 0.75). This is observed for Hf vs. Zr, Nb vs. Ta and W vs. U in R10, Nb vs. Ta, Sn vs. W and Hf vs. W a in R19 and Zr vs. W, Ta vs. W and Ta vs. Zr in Diss. Binary diagrams showing the correlation between these elements are presented in Figs. 2.25 and 2.26. The strong correlations of the different element pairs probably reflects similar mechanism of substitution in the rutile lattice particularly because these are all highly charged elements (in rutile, Ti, Zr, Hf, Sn, U are 4+; Nb, Ta are 5+, W is 6+; see, *e.g.*,

Table 2.10 Provisional values (in ppm) for the **Sy** grain.

Sy	Technique	#	avg ppm	2σ error
Hf	SIMS	13	0.078	0.068
	ID–MC–ICP–MS	1	0.095	0.002
	LA–ICP–MS	3	0.062	0.018
	Wtd Avg		**0.0954 ±0.0020**[*]	
	MSWD		**0.27**[*]	
Ta	SIMS	13	0.0109	0.0140
	ID–MC–ICP–MS	1	0.0037	0.0004
	LA–ICP–MS	3	<0.0022	-
	Wtd Avg		**0.00371 ±0.00039**	
	MSWD		**1.06**	

[*] calculations excluded LA–ICP–MS data. Calculations including this technique yielded similar Wtd Avgs but extremely high MSWD.
Further explanations see Table 2.7.

discussion in Zack *et al.*, 2002) with similar ionic radii (0.60 to 0.72 – except for U 0.89). The trends observed are helpful in two different aspects. They can be used to roughly estimate concentrations of certain elements that were not measured. For instance, if EMP is obtained for an element, the concentration of a second element, not analyzed by this technique, can be estimated (*e.g.*, by analysing Zr in R10, an estimate of the Hf in R10 can be made). The observed trends can also be used to estimate the approximate location of the analyzed split in the crystal (*e.g.*, rim or core), also helping to assess concentration ranges and chemical variations of other elements (many elements show profiles with distinct plateaus, where variations are much more restricted).

2.6 Outlook

Since our sample set may be valuable for geochemical and geochronological microanalytical work, we are willing to distribute fragments of all studied rutiles to the scientific community upon request (e-mail addresses: gluvizot@min.uni-heidelberg.de or tzack@min.uni-heidelberg.de). All analyzed crystals were carefully sawn in sub-millimeter slices, parallel to the sections used for *in-situ* analyses. This way, *e.g.*, more than 200 fragments (of millimeter size) from R10 core can be
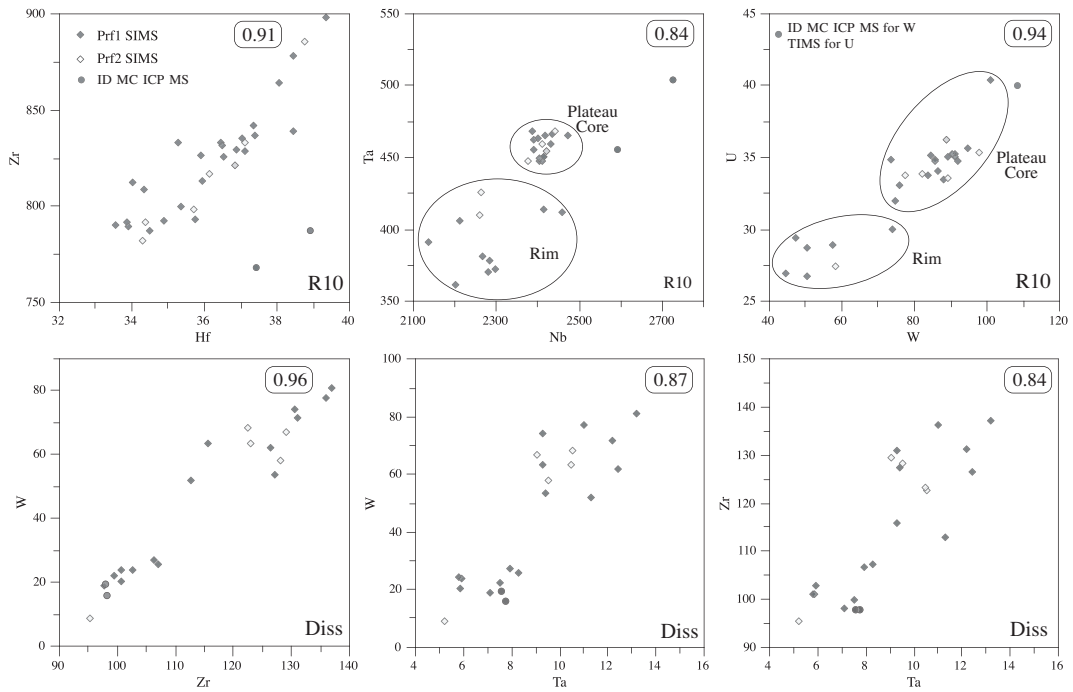
Figure 2.25 Element–element correlation for R10 and Diss. Only element pairs with correlation coefficients higher than 0.75 are shown. Concentrations are in ppm.
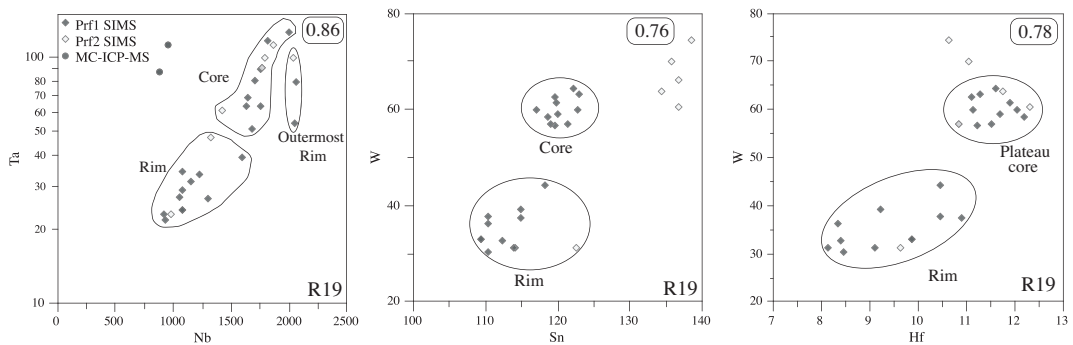
Figure 2.26 Element–element correlation for R19. Only element pairs with correlation coefficients higher than 0.75 are shown. Concentrations are in ppm.

distributed.

Among the many applications of the rutile mineral standards presented here, it is worthwhile to highlight the following:

1. Nowadays, one of the most important applications of rutile in petrological studies is as a geothermometer, as Zr is temperature dependent in this mineral (Zack *et al.*, 2004b; Watson *et al.*, 2006; Tomkins *et al.*, 2007). In this sense, the rutile grains presented here are useful to check results obtained by a given technique and to compare results obtained by different laboratories.

2. Rutile is also useful in quantitative provenance studies, as the Nb and Cr concentrations can be used to distinguish between mafic and pelitic sources of sediment (Zack *et al.*, 2004a; Triebold *et al.*, 2007). As for Zr, the rutiles presented here are useful to control data obtained by a given technique or laboratory and to compare data obtained by different laboratories.

3. Rutile has drawn particular attention in geochronology as it can incorporate high U concentrations and has been shown to yield precise U-Pb ages (*e.g.*, Mezger *et al.*, 1989; Corfu & Muir, 1989; Davis, 1997; Li *et al.*, 2003; Vry & Baker, 2006; Zack *et al.*, 2007). The R10 grain has a relatively high U concentration (average of 36.9 ppm in Table 2.7). TIMS results show that, besides minor heterogeneities in U concentrations, ages are rather constant for this grain, ranging from 1085.1 to 1096.2 Ma (^{207}Pb/^{235}U ages) and from to 1086.3 to 1096.6 Ma (^{206}Pb/^{238}U ages). Furthermore, LA–ICP–MS data show that the non–radiogenic Pb concentrations (measured as ^{208}Pb) are very low (average of 0.08 ppm), meaning that common Pb can be neglected for this grain. All these facts strongly favor the use of R10 as an age standard for U–Pb rutile dating.

4. High precision ^{176}Hf/^{177}Hf isotopic ratios and Lu concentration data, obtained by ID–MC–ICP–MS, are presented for the R10, R19 and Diss. Therefore these grains may also be useful in Hf isotope studies. Very low Lu concentrations (see Table 2.3) obtained for all grains are evidence for no radiogenic ingrowth, making rutile particularly useful for calculating Hf isotope

composition of source rocks (*e.g.*, Griffin *et al.*, 2004; Choukroun *et al.*, 2005; Hawkesworth & Kemp, 2006; Kemp *et al.*, 2006).

5. The results presented here may also encourage a search for other applications, as interpretation hinges critically on analytical certainty. The Sy can be used to check for interferences, as it has very low abundances of trace elements.

Acknowledgments

Bibliography

Amelin Y, Back M (2006) Opal as a U-Pb geochronometer: Search for a standard. *Chemical Geology* 232: 67–86

Baker J, Peate D, Waight T, Meyzen C (2004) Pb isotopic analysis of standards and samples using a Pb-207-Pb-204 double spike and thallium to correct for mass bias with a double-focusing MC-ICP-MS. *Chemical Geology* 211: 275–303

Barth M, McDonough W, Rudnick R (2000) Tracking the budget of Nb and Ta in the continental crust. *Chemical Geology* 165: 197–213

Bingen B, Davis WJ, Hamilton MA, Engvik A, Stein HJ, Skår Ø, Nordgulen Ø (2008) Geochronology of high-grade metamorphism in the Sveconorwegian belt, S. Norway: U-Pb, Th-Pb and Re-Os data. *Norwegian Journal of Geology* 88: 13–42

Black LP, Kamo SL, Allen CM, Davis DW, Aleinikoff JN, Valley JW, Mundil R, Campbell IH, Korsch RJ, Williams IS, Foudoulis C (2004) Improved Pb-206/U-218 microprobe geochronology by the monitoring of a trace-element-related matrix effect; SHRIMP, ID-TIMS, ELA-ICP-MS and oxygen isotope documentation for a series of zircon standards. *Chemical Geology* 205: 115–140

Brenan JM, Shaw HF, Phinney DL, Ryerson FJ (1994) Rutile-aqueous fluid partitioning of Nb, Ta, Hf, Zr, U and Th: implications for high field strength element depletions in island-arc basalts. *Earth and Planetary Science Letters* 128: 327–339

Choukroun M, O'Reilly SY, Griffin WL, Pearson NJ, Dawson JB (2005) Hf isotopes of MARID, (mica-amphibole-rutile-ilmenite-diopside) rutile trace metasomatic processes in the lithospheric mantle. *Geology* 33: 45–48

Corfu F, Muir TL (1989) The Hemlo-Heron Bay greenstone belt and Hemlo Au—Mo deposit, Superior Province, Ontario, Canada 2. Timing of metamorphism, alteration and Au mineralization from titanite, rutile, and monazite U—Pb geochronology. *Chemical Geology: Isotope Geoscience section* 79: 201–223

Cosca M, Mezger K, Essene E (1998) The Baltica–Laurentia connection: Sveconorwegian (Grenvillian) metamorphism, cooling, and unroofing in the Bamble sector, Norway. *Journal of Geology* 106: 539–552

Davis WJ (1997) U-Pb zircon and rutile ages from granulite xenoliths in the Slave Province; evidence for mafic magmatism in the lower crust coincident with Proterozoic dike swarms. *Geology* 25: 343–346

de Haas GJ, Nijland T, Valbracht P, Maijer C, Verschure R, Andersen T (2002a) Magmatic versus metamorphic origin of olivine-plagioclase coronas. *Contributions to Mineralogy and Petrology* 143: 537–550

de Haas GJ, TG N, Andersen F T Corfu (2002b) New constraints on the timing of deposition and metamorphism in the Bamble sector, south Norway: Zircon and titanite U-Pb data from the Nelaug area. *GFF* 124: 73–78

Deer WA, Howie R, Zussman J (1992) *An introduction to the rock-forming minerals*. Harlow, Essex, England, 696p

Eggins SM, Shelley JMG (2002) Compositional heterogeneity in NIST SRM 610-617 glasses. *Geostandards Newsletter* 26: 269–286

Fialin M, Outrequin M, Staub PF (1997) A new tool to treat overlaps in electron-probe microanalysis of rare-earth element L-series X-rays. *European Journal of Mineralogy* 9: 965–968

Foley SF, Barth MG, Jenner GA (2000) Rutile/melt partition coefficients for trace elements and an assessment of the influence of rutile on the trace element characteristics of subduction zone magmas. *Geochimica et Cosmochimica Acta* 64: 933–938

Graham J, Morris R (1973) Tungsten- and antimony-substituted rutile. *Mineralogical Magazine* 39: 470–473

Griffin WL, Belousova EA, Shee SR, Pearson NJ, O'Reilly SY (2004) Archean crustal evolution in the northern Yilgam Craton: U-Pb and Hf-isotope evidence from detrital zircons. *Precambrian Research* 131: 231–282

Haggerty SE (1991) *Oxide mineralogy of the upper mantle. In: Lindsley, D. H. (Ed.), Oxide mineralogy minerals: Petrological and magnetic significance*, vol. 25. Reviews in mineralogy

Hawkesworth CJ, Kemp AIS (2006) Using hafnium and oxygen isotopes in zircons to unravel the record of crustal evolution. *Chemical Geology* 226: 144–162

Heinrich KFJ, Newbury DE (1991) *Electron probe quantitation*. New York: Plenum Press

Hinton R (1999) NIST SRM 610, 611 and SRM 612, 613 multi-element glasses: Constraints from element abundance ratios measured by microprobe techniques. *Geostandards Newsletter* 12: 197–207

Horn I, Hinton R, Jackson SE (1997) Ultra-trace element analysis of NIST SRM 616 and 614 using laser ablation microprobe inductively coupled plasma mass spectrometry (LAM-ICP-MS): a comparison with secondary ion mass spectrometry (SIMS). *Geostandards Newsletter* 21: 191–203

ISO (1993) *International vocabulary of basic and general terms in metrology (VIM)*. BIPM/IEC/IFCC/ISO/IUPAC/IUPAP/OIML, International Organization for Standardization (ISO), Geneva, second edn.

Jacob DE (2006) High sensitivity analysis of trace element poor geological reference glasses by laser-ablation inductively coupled plasma mass spectrometry (LA-ICP-MS). *Geostandards and Geoanalytical Research* 30: 221–235

Jochum K, Dingwell D, Rocholl A, Stoll B, Hofmann A, Becker S, Besmehn A, Besesette D, Dietze HJ, Dulski P, Erzinger J, Hellebrand E, Hoppe P, Horn I, Janssens K, Jenner G, Klein M, McDonough W, Mätz M, Mezger K, Münker C, Nikogosian I, Pickhart C, Raczek I, Rhede D, Seufert H, Simakin S, Sobolev A, Spettel B, Straub S, Vincze L, Wallianos A, Weckwerth G,

Weyer S, Wolf D, M Z (2000) The Preparation and Preliminary Characterisation of Eight Geological MPI-DING Reference Glasses for In-Situ Microanalysis. *Geostandards Newsletter* 24: 87–133

Jochum K, Willbold M, Raczek I, Stoll B, Herwig K (2005) Chemical characterization of the USGS reference glasses GSA-1G, GSC-1G, GSD-1G, GSE-1G, BCR-2G, BHVO-2G and BIR-1G using EPMA, ID-TIMS, ID-ICPMS and LA-ICPMS. *Geostandards and Geoanalytical Research* 29: 285–302

Jochum KP, Willbold M (2006) Reference materials in geoanalytical research - Review for 2004 and 2005. *Geostandards and Geoanalytical Research* 30: 143–156

Jochum KP, Stoll B, Herwig K, Willbold M, Hofmann AW, Amini M, Aarburg S, Abouchami W, Hellebrand E, Mocek B, Raczek I, Stracke A, Alard O, Bouman C, Becker S, Dücking M, Brätz H, Klemd R, de Bruin D, Canil D, Cornell D, de Hoog CJ, Dalpé C, Danyushevsky L, Eisenhauer A, Gao Y, Snow JE, Groschopf N, Günther D, Latkoczy C, Guillong M, Hauri EH, Höfer HE, Lahaye Y, Horz K, Jacob DE, Kasemann SA, Kent AJR, Ludwig T, Zack T, Mason PRD, Meixner A, Rosner M, Misawa K, Nash BP, Pfänder J, Premo WR, Sun WD, Tiepolo M, Vannucci R, Vennemann T, Wayne D, Woodhead JD (2006) MPI-DING reference glasses for in situ microanalysis: New reference values for element concentrations and isotope ratios. *Geochemistry Geophysics Geosystems* 7: Art No. Q02 008

Kane JS (1998) A history of the development and certification of NIST glass SRM 610. *Geostandards Newsletter* 22: 7–13

Kemp AIS, Hawkesworth CJ, Paterson BA, Kinny PD (2006) Episodic growth of the Gondwana supercontinent from hafnium and oxygen isotopes in zircon. *Nature* 439: 580–583

Kleine T, Mezger K, Münker C, Palme H, Bischoff A (2004) ^{182}Hf-^{182}W isotope systematics of chondrites, eucrites, and martian meteorites: chronology of core formation and early mantle differentiation in Vesta and Mars. *Geochimica et Cosmochimica Acta* 68: 2935–2946

Klemme S, Prowatke S, Hametner K, Gunther D (2005) Partitioning of trace elements between rutile and silicate melts: Implications for subduction zones. *Geochimica et Cosmochimica Acta* 69: 2361–2371

Klemme S, Prowatke S, Münker C, Magee CW, Lahaye Y, Zack T, Kasemann SA, Cabato EJA, Kaeser B (2008) Synthesis and preliminary characterisation of new silicate, phosphate and titanite reference glasses. *Geostandards and Geoanalytical Research* 32: 39–4

Korneliussen A, Mcenroe SA, Milsson lP, Schiellerup H, Gautneb H, Meyer GB, Storseth lR (2000) An overview of titanium deposits in Norway. *NGU-BULL* 436: 27–38

Krogh TE (1973) A low contamination method for hydrothermal decomposition of zircon and extraction of U and Pb for isotopic age determinations. *Geochimica et Cosmochimica Acta* 37: 485–494

Kullerud L, Dahlgren S (1993) Sm-Nd geochronology of Sveconorwegian granulite facies mineral assemblages in the Bamble shear belt, South Norway. *Precambrian Research* 64: 389–402

Kullerud L, Machado N (1991) End of a controversy: U–Pb geochronological evidence for significant Grenvillian activity in the Bamble area, Norway. *Terra Abstracts, supplement to Terra Nova*

3: 504

Li Q, Li S, Zheng YF, Li H, Massonne HJ, Wang Q (2003) A high precision U-Pb age of metamorphic rutile in coesite-bearing eclogite from the Dabie Mountains in central China: a new constraint on the cooling history. *Chemical Geology* 200: 255–265

Ludwig K (2001) Isoplot/Ex version 2.49; a geochronological toolkit for Mocrosoft Excel. Berkeley Geochronology Center Special Publication, 1A.

Luvizotto GL, Zack T (2006) Tracing Dehydration Melting and Late Fluid Influx of Metapelitic Rocks Using the Texture and Geochemistry of Rutile. In: *Granulites and Granulites 2006 (available on: http://www.geol.umd.edu/pages/meetings/Gran&GranTables.htm)*, 45

Luvizotto GL, Zack T (in press) Nb and Zr behavior in rutile during high–grade metamorphism and retrogression: An example from the Ivrea–Verbano Zone. *Chemical Geology*

McDonough WF (1991) Partial melting of subducted oceanic crust and isolation of its residual eclogitic lithology. *Philosophical Transactions of the Royal Society of London Series A* 335: 407–418

Mezger K, Hanson GN, Bohlen SR (1989) High-precision U-Pb ages of metamorphic rutile: application to the cooling history of high-grade terranes. *Earth and Planetary Science Letters* 96: 106–118

Mezger K, Essene EJ, Vanderpluijm BA, Halliday AN (1993) U-Pb Geochronology of the Grenville Orogen of Ontario and New York: Constraints on Ancient Crustal Tectonics. *Contributions to Mineralogy and Petrology* 114: 13–26

Münker C (1998) Nb/Ta fractionation in a Cambrian arc/back-arc system, New Zealand: source constraints and application of refined ICPMS techniques. *Chemical Geology* 144: 23–45

Münker C, Weyer S, Scherer E, Mezger K (2001) Separation of high field strength elements (Nb, Ta, Zr, Hf) and Lu from rock samples for MC-ICPMS measurements. *Geochemistry, Geophysics, Geosystems (G3)* 2: paper number 10.10292001GC000183

Münker C, Pfänder J, Weyer S, Buchl A, Kleine K T amd Mezger (2003) Evolution of planetary cores and the earth-moon system from Nb/Ta systematics. *Science* 301: 84–87

Ødegård M, Mansfeld J, Dundas S (2001) Preparation of calibration materials for microanalysis of Ti minerals by direct fusion of synthetic and natural materials: experience with LA-ICP-MS analysis of some important minor and trace elements in ilmenite and rutile. *Fresenius Journal of Analytical Chemistry* 370: 819–827

Parrish RR (1987) An improved micro-capsule for zircon dissolution in U-Pb geochronology. *Isotope Geoscience* 66: 99–102

Pearce J, Perkins WT, Wetgate JA, Gorton MP, Jackson SE, Neal CR, Cheney SP (1997) A compilation of new and published major and trace element data for NIST SRM 610 and NIST SRM 612 glass reference materials. *Geostandards Newsletter* 06: 115–144

Potts PJ, Kane JS (1992) Terminology for geological reference material values: A proposal to the International Organisation for Standardisation (ISO), producers and users. *Geostandards Newsletter* 16: 300–341

Pouchou JL, Pichoir F (1984) A new model for quantitative X-ray-microanalysis. Part I: applications to the analysis of homogeneous samples. *Recherche Aerospatiale* 3: 13–38

Rice C, Darke K, Still J (1998) Tungsten-bearing rutile from the Kori Kollo gold mine Bolívia. *Mineralogical Magazine* 62: 421–429

Rocholl A, Dulski P, Raczek I (2000) New ID-TIMS, ICP-MS and SIMS data on the trace element composition and homogeneity of NIST certified reference material SRM 610-611. *Geostandards newsletter-the journal of geostandards and geoanalysis* 24: 261–274

Rudnick RL, Barth M, Horn I, McDonough WF (2000) Rutile-bearing refractory eclogites: Missing link between continents and depleted mantle. *Science* 287: 278–281

Saunders A, Tarney J, Weaver S (1980) Traverse geochemical variations across the Antarctic Peninsula: implications for the genesis of calc-alkaline magmas. *Earth and Planetary Science Letters* 46: 344–360

Smith D, Persil EA (1997) Sb-rich rutile in the manganese concentrations at St. Marcel-Praborna, Aosta Valley, Italy; petrology and crystal-chemistry. *Mineralogical Magazine* 61: 655–669

Stacey J, Kramers J (1975) Approximation of terrestrial lead isotope evolution by a two-stage model. *Earth and Planetary Science Letters* 26: 207–221

Stalder R, Foley SF, Brey GP, Horn I (1998) Mineral-aqueous fluid partitioning of trace elements at 900-1200 °C and 3.0-5.7 GPa: new experimental data for garnet, clinopyroxene, and rutile, and implications for mantle metasomatism. *Geochimica et Cosmochimica Acta* 62: 1781–1801

Starmer I (1991) The Proterozoic evolution of the Bamble Sector shear belt, southern Norway; correlations across southern Scandinavia and the Grenvillian controversy. *Precambrian Research* 49: 107–139

Steiger RH, Jager E (1977) Subcommission on geochronology: Convention on the use of decay constants in geo- and cosmochronology. *Earth and Planetary Science Letters* 36: 359–362

Tomkins HS, Powell R, Ellis DJ (2007) The pressure dependence of the zirconium-in-rutile thermometer. *Journal of Metamorphic Geology* 25: 703–713

Triebold S, von Eynatten H, Luvizotto GL, Zack T (2007) Deducing source rock lithology from detrital rutile geochemistry: An example from the Erzgebirge, Germany. *Chemical Geology* 244: 421–436

Vry JK, Baker JA (2006) LA-MC-ICPMS Pb-Pb dating of rutile from slowly cooled granulites: Confirmation of the high closure temperature for Pb diffusion in rutile. *Geochimica et Cosmochimica Acta* 70: 1807–1820

Watson EB, Wark DA, Thomas JB (2006) Crystallization thermometers for zircon and rutile. *Contributions to Mineralogy and Petrology* 151: 413–433

Weyer S, Münker C, Rehkämper M, Mezger K (2002) Determination of ultra-low Nb, Ta, Zr and Hf concentrations and the chondritic Zr/Hf and Nb/Ta ratios by isotope dilution analyses with multiple collector ICP-MS. *Chemical Geology* 187: 295–313

Zack T, Kronz A, Foley SF, Rivers T (2002) Trace element abundances in rutiles from eclogites and associated garnet mica schists. *Chemical Geology* 184: 97–122

Bibliography

Zack T, von Eynatten H, Kronz A (2004a) Rutile geochemistry and its potential use in quantitative provenance studies. *Sedimentary Geology* 171: 37–58

Zack T, Moraes R, Kronz A (2004b) Temperature dependence of Zr in rutile: empirical calibration of a rutile thermometer. *Contributions to Mineralogy and Petrology* 148: 471–488

Zack T, Luvizotto GL, Barth M, Stockli DF (2007) U/Pb Rutile Dating in Granulite-Facies Rocks by LA-ICP-MS. In: *Eos Trans. AGU*, vol. 88(52), Fall Meet. Suppl., Abstrac V34C-05

3 Nb and Zr behavior in rutile during high-grade metamorphism and retrogression: An example from the Ivrea–Verbano Zone

G. L. Luvizotto and T. Zack.

Abstract

Detailed textural observations and *in-situ* analyses (EMP, SIMS and LA-ICP-MS) are used to characterize trace element behavior during prograde and retrograde metamorphic reactions involving rutile. The Ivrea-Verbano Zone is a classic granulite area and rocks from the Strona and d'Ossola valleys are an example of the amphibolite to granulite facies transition. Although different rock types occur in the area, detailed sampling and petrographic work show that rutile only occurs in granulite facies paragneisses. These rocks show a rich inventory of textures that allow not only for the investigation of trace element behavior in response to prograde rutile growth, but also for the effect of post-peak processes on rutile chemistry. Nb concentrations in rutile from lower grade samples show a larger spread (from 500 to 5000 ppm within one sample) when compared to those from higher grades. This pattern can be modeled using prograde rutile growth formed from biotite breakdown. Zr concentrations in rutile are characterized by an anomalously large spread and a bimodal distribution. Maximum Zr concentrations increase according to the general metamorphic gradient known for this area. Temperatures (from Zr-in-rutile thermometry), although feasible, are considerably higher than previous calculations (increasing from ca. 850 to 930°C). A second cluster of Zr concentrations in rutile occurs at rather constant concentrations (ca. 1000 ppm) for all localities and is interpreted to be related to intense fluid influx at high temperature and/or to post-peak diffusional resetting favored by slow cooling rates. Alteration textures, characterized by a complex network of micro-veins, are evidence for the late fluid influx. The fluid strongly affected the rutiles, which is evidenced by corrosion of older rutile grains and formation of rutile veinlets.

Keywords: *accessory phases, trace element, partitioning, slow cooling, diffusion, fluids.*

3.1 Introduction

Despite the relative fluid immobility of high field strength elements (HFSE; *e.g.*, Zr, Nb, Sn, Sb, Hf, Ta, W) under subsolidus conditions (*e.g.*, Pearce & Cann, 1973), unequivocal evidence for their mobility on a thin section scale (*e.g.*, Zack *et al.*, 2004b; Rasmussen, 2005; Gao *et al.*, 2007) has sparked intense research on the behavior of HFSE distribution in metamorphic environments. Most of these efforts involve the calibration and evaluation of HFSE thermometers in the system Ti-Zr-Si-O (Zr-in-rutile or rutile thermometry, Ti-in-zircon, Ti-in-quartz, Zr-in-titanite; Zack *et al.*, 2004b; Zack & Luvizotto, 2006; Watson *et al.*, 2006; Tomkins *et al.*, 2007; Wark & Watson, 2006; Hayden *et al.*, 2007; Miller *et al.*, 2007). Furthermore, applications to provenance studies have been realized by coupling the rutile thermometer with Nb-Cr source characteristics (Zack *et al.*, 2002, 2004a; Stendal *et al.*, 2006; Triebold *et al.*, 2007; Meinhold *et al.*, 2008). With several areas of HFSE behavior in metamorphic environments virtually unexplored, we have focused this study on the response of HFSE in rutile forming reactions in granulite facies rocks using samples from the Ivrea-Verbano Zone (IVZ) as a test case.

Rutile is a frequent HFSE phase, occurring as an accessory mineral in a wide range of rocks, *i.e.*, high-grade metamorphic rocks, igneous rocks, siliciclastic sediments, placer deposits and hydrothermal ore deposits. It is widely known that rutile is an important carrier for several highly charged trace elements (Graham & Morris, 1973; Haggerty, 1991; Deer *et al.*, 1992; Smith & Persil, 1997; Rice *et al.*, 1998). For example, Zack *et al.* (2002) has shown for eclogites that 1 modal% of rutile can carry more than 90% of the whole rock content for Ti, Nb, Ta, Sb and W and considerable amounts (5-50% of the whole rock content) of V, Cr, Mo and Sn. It has recently been shown that the Zr incorporation in rutile in quartz- and zircon-bearing systems is strongly temperature dependent (Zack *et al.*, 2004b; Watson *et al.*, 2006; Tomkins *et al.*, 2007). Rutile has also been shown to yield precise U-Pb ages (*e.g.*, Mezger *et al.*, 1989; Davis, 1997; Mezger *et al.*, 1993; Li *et al.*, 2003; Vry & Baker, 2006).

The Ivrea-Verbano Zone is one of the world's classic granulite facies areas and

has been the subject of study for several decades (*e.g.*, Berckhemer, 1969; Schmid & Wood, 1976; Zingg, 1980, 1983; Zingg *et al.*, 1990; Sills & Tarney, 1984; Schmid *et al.*, 1987; Boriani *et al.*, 1990; Rivalenti *et al.*, 1997; Barboza *et al.*, 1999; Barboza & Bergantz, 2000; Vavra *et al.*, 1996; Vavra & Schaltegger, 1999; Peressini *et al.*, 2002, 2007; Rutter *et al.*, 2007). The area is also a textbook example of the amphibolite granulite facies transition and its associated processes (*e.g.*, dehydration melting and melt loss). The IVZ is, therefore, an excellent site to investigate the interplay between metamorphism, cooling, diffusion and trace element distributions during metamorphic reactions.

The aim of the present study is to characterize, through detailed textural observations and *in-situ* analyses, the behavior of HFSE elements during prograde and retrograde reactions involving rutile.

3.2 The Ivrea-Verbano Zone

3.2.1 Geological setting

The Ivrea-Verbano Zone (Fig. 3.1) in the Southern Alps is one of the best preserved sections through lower continental crust. It is delimited to the northwest by the Insubric Line, a major Neogene shear zone that juxtaposes pre-Alpine and Alpine structures and rocks (Schmid *et al.*, 1987). To the southeast, the boundary of the IVZ is tectonically delimited by the Cossato-Mergozzo-Brissago tectonic discontinuity (Boriani *et al.*, 1990). The metamorphic foliation and primary banding are mostly steeply dipping and show a NE-SW trend, parallel to the Insubric Line. The area is traditionally divided into two main units: a large basic intrusive complex of Permian age (the Mafic Formation of Zingg, 1980; Rivalenti *et al.*, 1981, among others) and a sequence of metasedimentary rocks interlayered with bands of mafic rocks (see Fig. 3.1).

Rocks, occurring in the area comprised by the Strona and d'Ossola valleys, show a metamorphic gradient with metamorphic conditions increasing from amphibolite facies in the southeast, to granulite facies in the northwest. Zingg (1980) mapped two important mineral isograds (see location in Fig. 3.1): the muscovite-out/K-

feldspar-in in metapelitic rocks and the orthopyroxene-in in mafic and intermediate rocks. In most models, the increase of metamorphic grade from southeast to north-west together with the steep foliation and primary banding has been interpreted to be the result of an Alpine-age tilting of the IVZ, and hence exposing a cross-section through the lower continental crust (*e.g.*, Handy *et al.*, 1999; Rutter *et al.*, 2007). Although the metamorphic grade increases more or less continuously, it has to be stressed that significant post-peak metamorphic shearing and folding is observed (Rutter *et al.*, 2007).
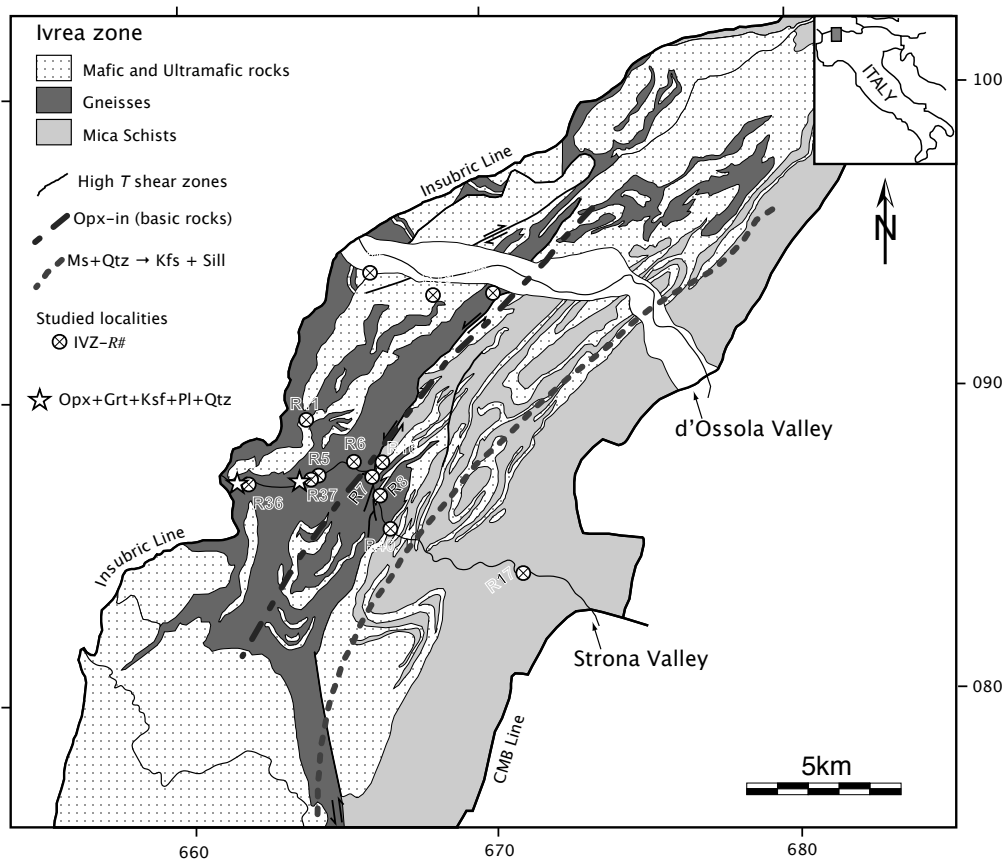
Figure 3.1 Geological map of the central part of the IVZ. Redrawn and simplified from Rutter *et al.* (2007). Main metamorphic isograds are those presented by Zingg (1980). CMB Line = Cossato-Mergozzo-Brissago Shear Zone

Pressure (*P*) and temperature (*T*) estimates of the IVZ have been presented by

various authors (Zingg, 1980; Sills & Tarney, 1984; Henk *et al.*, 1997; Demarchi *et al.*, 1998; Barboza & Bergantz, 2000, among others). Maximum *PT* conditions calculated by Henk *et al.* (1997) are 810°C and 0.83 GPa and decrease to 710°C and 0.67 GPa towards the granulite to amphibolite facies boundary.

The heat source for the regional granulite facies metamorphism has long been a subject of debate in the literature. It has traditionally been attributed to the intrusion of the mafic rocks of the Mafic Formation (Zingg, 1980; Zingg *et al.*, 1990). Recently, Peressini *et al.* (2007) presented geochronological data on the duration of the mafic intrusion. The authors allocated an age of $\sim$310 Ma (^{206}Pb/^{238}U zircon ages) to a Carboniferous orogenic event that affected the metasedimentary rocks (see also Köppel, 1974; Vavra *et al.*, 1996; Henk *et al.*, 1997). One of the main conclusions of Peressini *et al.* (2007) is that the granulite grade metamorphism affected the metasedimentary rocks about 20 Ma before the crystallization of the Mafic Complex. Their observations are in agreement with the previous findings of Barboza *et al.* (1999) and Barboza & Bergantz (2000), who inferred that the granulite facies metamorphism preceded the emplacement of the Mafic Complex. Peressini *et al.* (2007) presented a detailed investigation on the heat transfer caused by the intrusion of the Mafic Complex. They concluded that the thermal anomaly caused by the intrusion lasted several million years. This leads to the conclusion that the post-intrusion tectonic evolution of the IVZ rocks is characterized by distinctly slow cooling rates.

As rutile is the main focus of our research, we carried out detailed sampling and petrographic work in order to evaluate its occurrence in the IVZ rocks. Investigation of more than 60 thin sections derived from 38 localities within the area of the Strona and d'Ossola valleys by petrographic microscope, BSE imaging and EDS analyses led to the identification of six main rock types: K-feldspar and sillimanite bearing gneisses (Grt + Sil + Kfs + Qtz + Rt $\pm$ Pl $\pm$ Bt; mineral abbreviations after Kretz, 1983), strongly restitic sillimanite bearing and garnet-rich (up to 70%) gneisses (Grt + Sil + Qtz + Pl + Rt $\pm$ Kfs $\pm$ Bt), mafic rocks (Amph + Pl + Ilm $\pm$ Qtz $\pm$ Cpx $\pm$ Grt; Grt + Opx + Pl + Ilm $\pm$ Amph $\pm$ Qtz $\pm$ Cpx), plagioclase-rich and sillimanite-free gneisses (Grt + Pl + Kfs + Qtz + Ilm $\pm$ Opx $\pm$ Bt), garnet-

sillimanite micaschists (Grt + Bt + Sil + Qtz $\pm$ Ms $\pm$ Pl) and calcsilicate rocks (Cal + Cpx + Scp + Ttn $\pm$ Qtz $\pm$ Pl). Our findings are in agreement with results reported by Zingg (1980) and show that rutile is only present in the granulite facies paragneisses also know in the literature as *"stronalite"*.

3.2.2 Critical evaluation of PT conditions from former studies

As previously stated, several *PT* estimates are available in the literature for the IVZ rocks. However, they are all based on Fe-Mg exchange thermometers (garnet-biotite, garnet-orthopyroxene). Various studies have shown that temperatures calculated using these thermometers may be underestimated due to Fe-Mg exchange from cooling after peak metamorphic conditions and, therefore, the results must be corrected for this late exchange (Harley, 1989; Fitzsimons & Harley, 1994; Pattison & Begin, 1994; Pattison *et al.*, 2003). For example, Pattison *et al.* (2003) have shown that the amphibolite to granulite facies transition (defined by mineral associations in metapelitic rocks developed at *PT* conditions analog to the appearance of orthopyroxene in mafic and intermediate compositions) occurs at temperatures of about 850°C and are therefore significantly higher than those determined for the IVZ.

Despite calculating absolute temperatures with Fe-Mg exchange thermometry, which is is prone to diffusional resetting; imprecise, but robust *PT* estimates can be made with the typical granulite facies mineral assemblage in the IVZ: Grt + Kfs + Sil + Rt $\pm$ Pl $\pm$ (+ liq). In the simplified system NaKFMASH presented in Fig. 3.2, the shaded area represents the stability field for the mineral assemblage which is bounded by the reactions Bt + Sil = Grt + Crd + liq on the low pressure side, Sil = Ky on the high pressure side and for high-Mg bulk compositions Bt + Grt = Opx + Sil + liq on the high temperature side. Minimum temperatures are given by the reaction Bt + Sil = Grt + Kfs + liq. With Fe/(Fe+Mg) ratios of 0.6-0.8 in garnets from such samples (Schmid & Wood, 1976; Henk *et al.*, 1997), a minimum temperature of ca. 780°C can be designated. The incorporation of Ti shifts the stability of biotite to higher *T* conditions (Dooley & Patiño-Douce, 1996; Patiño-Douce, 1993; Patiño-Douce & Beard, 1995; Henry & Guidott, 2002; Henry *et al.*,

2005) for the reaction Bt + Grt = Opx + Sil + liq by ca. 40°C (White *et al.*, 2007).
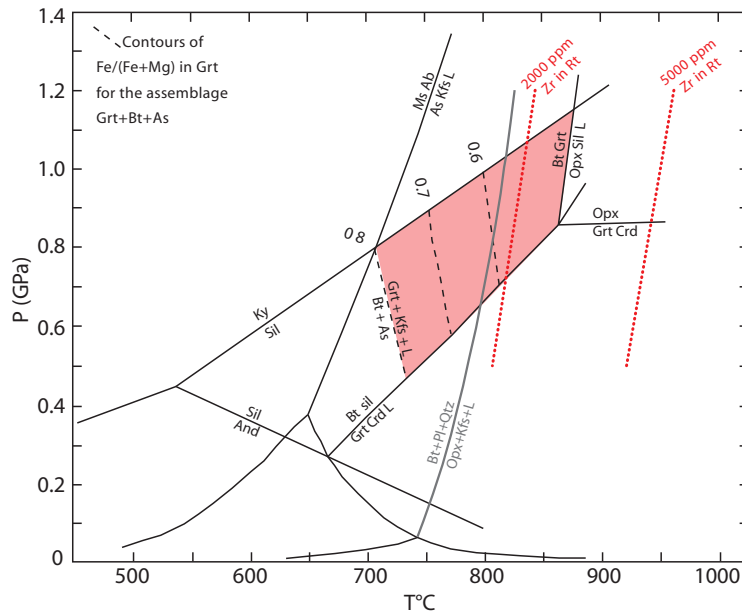
Figure 3.2 Minimum *PT* estimates for the granulite facies rocks from the IVZ. Solid lines represent main reactions for the NaKFMASH system Spear *et al.* (1999). The position of the Bt + Pl + Qtz = Opx + Kfs + liq reaction (stippled lines) is from Spear (1995). Shaded area represents the stability field for the paragenesis present in the granulite facies metapelitc rocks from the IVZ. Dotted lines represent temperatures calculated using the Zr-in-Rt thermometer (calibration of Tomkins *et al.*, 2007) for the maximum concentrations recorded in IVZ samples.

The mineral assemblage Opx + Grt + Kfs + Pl + Qtz in metagraywackes has been recorded in a few localities near Forno (Sills, 1984, see also Fig. 3.1 for location and Fig. 3.3 for BSE image). This mineral assemblage is bounded at lower temperature (ca. 800°C at 0.7 GPa) by the reaction Bt + Pl + Qtz = Opx + Ksp + liq (see Fig. 3.2).

In summary, temperature conditions for the rutile-bearing samples in the IVZ can be estimated from phase mineral assemblages to be between ca 770°C to 940°C at 0.6 to 1.0 GPa, probably with a general increase in metamorphic grade from the southeast to the northwest.
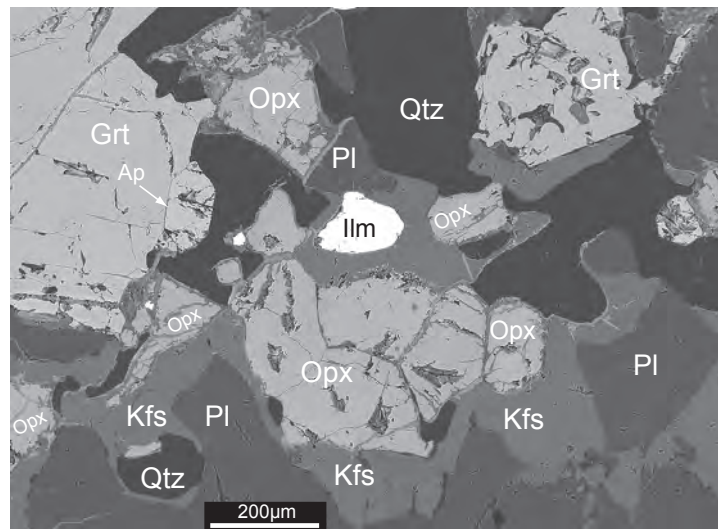
Figure 3.3 BSE image example of the mineral assemblage Opx + Grt + Kfs + Pl + Qtz in a plagioclase-rich sillimanite-free gneiss from the Strona Valley. Note that this rock is rutile free.

3.3 Analytical techniques

3.3.1 Electron Microprobe (EMP)

Electron microprobe studies were carried out at the Mineralogisches Institut, Universität Heidelberg using a CAMECA SX51 equipped with 5 WDS detectors. Analyses of rutiles were carried out with 20 kV and 100 nA and followed the method outlined by Luvizotto *et al.* (in press). The following elements were analyzed: Si, V, Cr, Fe, Zr, Nb and W. With the chosen setup, the detection limits (2σ) are 50 ppm for Cr, 40 ppm for Fe and Zr, 60 ppm for Nb and 350 ppm for W and the 2σ relative standard errors are 20 ppm for Cr and Fe, 40 ppm for Zr, 60 ppm Nb and 90 ppm W. In order to get "true" zero-concentration peak intensities and to exclude any machine drift, every ten analyses of unknowns were bracketed by two analyses of synthetic rutile (nominally zero-concentration trace elements). Si concentrations were used as a quality control to detect and avoid contamination associated with submicroscopic zircon inclusions (according to the method outlined by Zack *et al.*, 2004b). Rutile measurements with Si concentrations higher than 300 ppm

that showed abnormally high Zr contents were excluded from the data set. Measurements with Si content slightly above 300 ppm and Zr concentrations similar to rutiles with low Si contents were included for small (20-30μm) rutile grains (high Si values were interpreted to be related to the surrounding silicates). The same quality controls are applied to SIMS and LA-ICP-MS analyses. In total, less than 2% of the measurements had to be discarded due to contamination. Although the EMP beam's diameter was set to 5μm, the minimum grain size for obtaining reliable analyses was 20μm.

3.3.2 Secondary Ion Mass Spectrometry (SIMS)

SIMS analyses were carried out at the Mineralogisches Institut, Universität Heidelberg using a CAMECA ims 3f. Analyses were performed using a 14.5 keV/ 10-20 nA $^{16}O^-$ primary ion beam, which resulted in spot sizes of 20-30μm. However, by using a field aperture the effective spot size could be reduced to 12μm, leading to the smallest analyzable grain sizes of 20-30μm. Positive secondary ions were nominally accelerated to 4.5 keV (energy window set to $\pm$20 eV) and the energy filtering technique was used with an offset of 90 eV at mass resolution m/δm (10%) of 370. Count rates were normalized to ^{47}Ti. TiO_2 in rutile is assumed to be 100 wt%. The following isotopes were analyzed: ^{27}Al, ^{30}Si, ^{47}Ti, ^{90}Zr, ^{93}Nb, ^{118}Sn, ^{120}Sn, ^{121}Sb, ^{123}Sb, ^{178}Hf, ^{181}Ta, ^{184}W, ^{186}W, ^{232}Th, ^{238}U. Results obtained for the two isotopes analyzed for Sn, Sb and W do not display any systematic differences, showing that no mass interference affected these isotopes in rutile analyses by SIMS (for further discussion see Luvizotto *et al.*, in press). Therefore, concentrations presented in Appendix A represent the average of the values obtained for the two measured isotopes. Concentrations were calculated based on relative sensitivity factors (RSF) obtained from the rutile R10 (Luvizotto *et al.*, in press). Although no reliable RSF can be calculated for Th, the intensity ratios obtained for the studied rutiles suggest that Th concentrations are extremely low (below the 0.1 ppm level when using RSF from U). SIMS analyses carried out on some biotite grains followed the procedure described above.

3.3.3 Laser Ablation Inductively Coupled Plasma Mass Spectrometry (LA-ICP-MS)

Trace element analyses were carried out at the Institut für Geowissenschafent, Johannes Gutenberg-Universität Mainz, using a New Wave Research UP-213 (wavelength 213 nm) laser system combined with an Agilent 7500ce ICP quadrupole mass spectrometer. Analyses followed the procedures presented by Luvizotto *et al.* (in press). Element concentrations were calculated with the software "GLITTER" using the measurements of the following isotopes: ^{90}Zr, ^{93}Nb, ^{177}Hf, ^{178}Hf, ^{181}Ta, ^{238}U. Typical detection limits (99% confidence) for 70 μm spots are 0.01 ppm for Zr and Hf, 0.005 ppm for Nb and 0.004 ppm for Ta and U.

LA-ICP-MS analyses were carried out on rutiles and biotites from sample IVZ-R19 in order to investigate how Nb and Ti partition between these minerals and to confirm results obtained by SIMS.

3.3.4 X-Ray Fluorescence (XRF)

Bulk-rock chemical concentrations were obtained by XRF analyses at Universität Heidelberg using a SRS 300 wavelength-dispersive spectrometer (Bruker AXS). Major and trace elements were determined using pressed powder tablets. International reference materials were used for the calibration.

3.4 Results

In the this section, we present the trace element composition of the studied rutiles, focusing on Zr and Nb. The samples derive from 10 different localities within the area of the Strona and d'Ossola valleys (Fig. 3.1). Key information of the studied rocks is presented in Table 3.1. A table including concentration data for all analyzed elements is presented in Appendix A.

Table 3.1 Summarized description of the rutile bearing granulite facies gneisses. Modal proportions are based on visual inspection with a petrographic microscope and BSE images.

Locality	Thin Sec.	Valley	Coordinates E	N	Late alter.	Qtz	Grt	Sil	Bt	Kfs	Pl	Rt	Zrn	Ilm
IVZ-R7	a	Strona	444899	5086949	H	xx	x	xx	2-3%	xx	–	<1%	<1%	
IVZ-R16[a]	a	Strona	445276	5087496	M-L	xx	xx	I	3%	xx	–	2%	<1%	
	f				M	x	xx	xx	7%	xx	–	<1%	<1%	
	g				M	xx	x	–	5%	I	xx	<1%	<1%	
IVZ-R6	b	Strona	444327	5087510	M	I	xx	x	<1%	–	x	2-3%	<1%	
IVZ-R5	b	Strona	443321	5087041	H	xx	x	x	5%	x	–	<1%	<1%	
IVZ-R37	b	Strona	443504	5086997	M	x	xx	–	<1%	I	X	2%	<1%	<2%[b]
IVZ-R36	a	Strona	440850	5086389	M-L	xx	x	x	<1%	I	x	2%	<1%	
	g[c]				M-L	xx	x	x	<1%	I	x	2%	<1%	
IVZ-R11		Between	442376	5088973	H	xx	xx	–	3%	x	x	1%	<1%	
IVZ-R20	a	d'Ossola	449102	5092801	M-H	x	x	xx	<1%	xx	–	3%	<1%	
	j				M-L	xx	xx	I	2%	x	x	1%	<1%	
IVZ-R19	e	d'Ossola	447111	5092780	L	x	xx	xx	3%	x	x	1%	<1%	
IVZ-R25	b	d'Ossola	445116	5096942	M	x	xx	xx	<1%	I	xx	2%	<1%	

Modal proportion: I - 1 to 10%, x - 10 to 20%, xx >20%. Intensity of the late alteration (Late Alt.): high (H), medium (M) and low (L). Coordinates are presented in UTM (WGS84).
[a] - banded gneiss with portions rich in Kfs+Sil (R16a), portions slightly richer in Bt (R16f) and portions rich in Pl (R16g).
[b] - included in Grt core and alteration product of Rt
[c] - collected ∼40 m north (higher metamorphic grade) of IVZ-R36a.

3.4.1 Microtextural observations of rutile and other Ti-bearing phases

In the studied area, the appearance of rutile is associated with the amphibolite to granulite facies transition. Amphibolite facies micaschists are rutile-free and biotite is the main Ti carrier (up to 7.00 wt% TiO_2). Fig. 3.4 shows a BSE image of this rock. The transition is associated to a sequence of dehydration reactions first involving muscovite (to form sillimanite and potassic feldspar) and then biotite (to form garnet and potassic feldspar). The Ti released by the breakdown of biotite leads to rutile formation, which can be described by the reaction: (high-Ti) Bt + Sil + Qtz = Grt + Kfs +Rt + Melt (see also Zingg, 1980).

The metamorphic textures support the theory of rutile formation associated with the biotite breakdown. For example, in some samples from the upper amphibolite facies (garnet-biotite-sillimanite schist), small ($\sim 20\mu$m) rutile and ilmenite grains
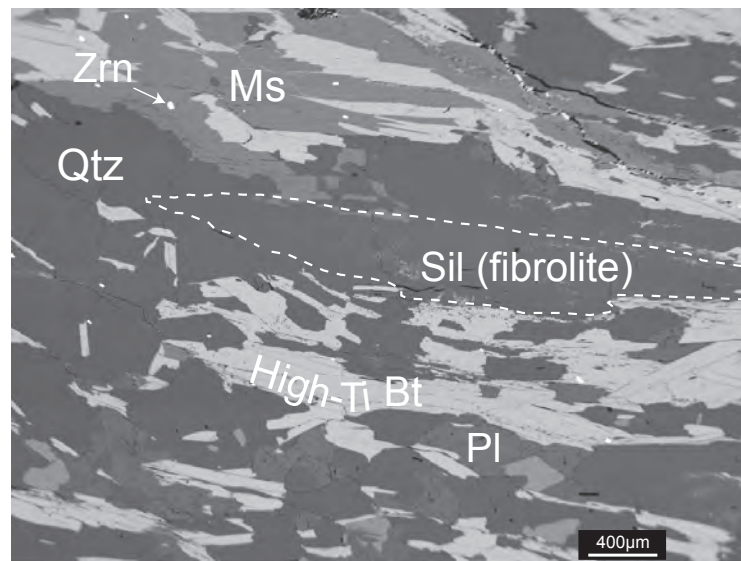
Figure 3.4 BSE image example of the amphibolite facies micaschist (IVZ-R17b). Although not shown in this figure, garnet may also be present. In these rocks, the main Ti carrier is the High-Ti Bt (up to 7.00 wt% TiO_2).

are present. The grains occur preferentially along biotite rims and within cleavage planes (Fig. 3.5). In the granulite facies rocks, rutile occurs as large grains (often larger than 100 μm) in the matrix and included in garnet (preferentially at the rim) indicating synmetamorphic crystallization of rutile and garnet (Fig. 3.6). In addition, only a few relict biotite grains occur in these rocks and are mostly present as rounded inclusion in garnets.

Although some ilmenite grains occur together with rutile in some upper amphibolite facies rocks (Fig. 3.5), the paragenesis (metamorphic equilibrium) rutile + ilmenite is not observed in granulite facies rocks.

The studied rocks are clearly affected by a post-peak alteration that is evidenced by a complex network of micro-veinlets that affect virtually all mineral phases, including rutile. Although frequent, the intensity of the alteration varies from sample to sample (a classification is given in Table 3.1). Fig. 3.7 shows BSE images exemplifying how these infiltrating fluids chemically altered the minerals. The veins are composed of very fine crystallized phases (too small for the *in-situ* analyses
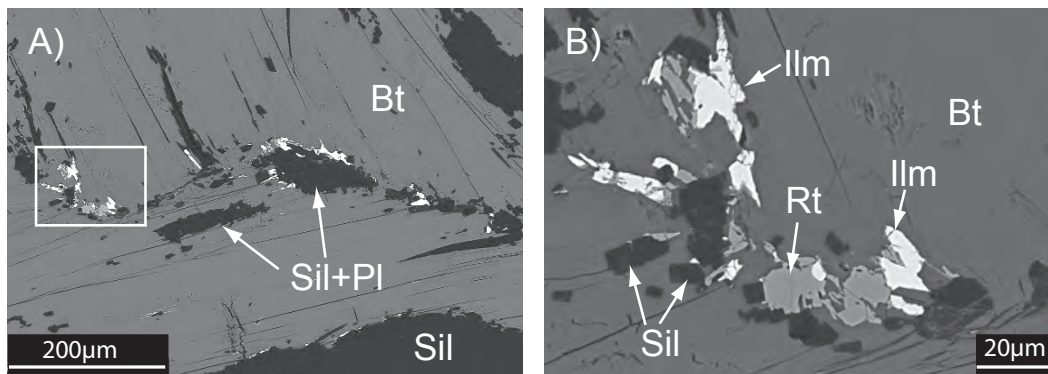
Figure 3.5 BSE images showing examples of small rutile and ilmenite grains found in high amphibolite facies Grt-Sil-Bt schists from the IVZ (sample IVZ-R40c). The white rectangle delimits the close-up in Fig. 3.5 B.
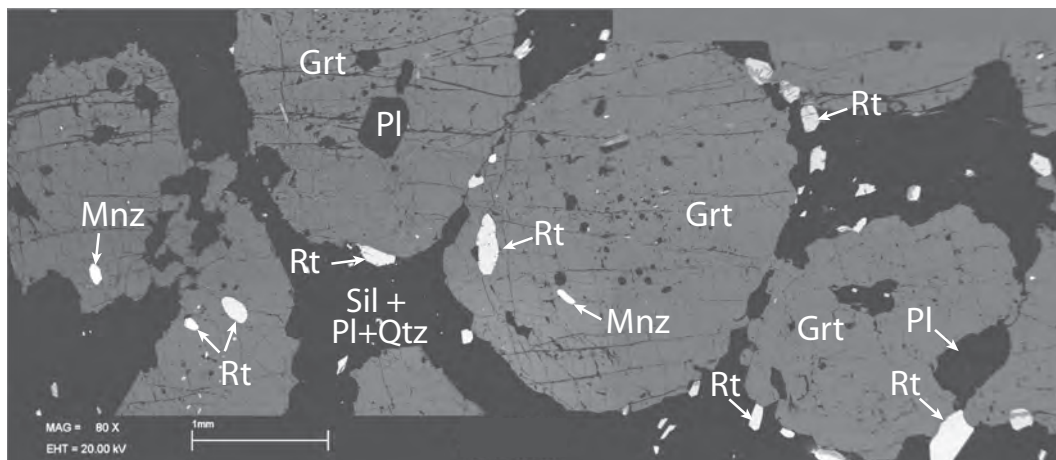
Figure 3.6 BSE image showing a texture observed in granulite facies restitic rocks from the IVZ (sample IVZ-R6b). Note that large rutile grains are only present in the matrix and in the garnet rims.

used in this study) with a platy habit. As shown in the chemical maps presented in Figs. 3.7d and f, they are characterized by a high K content. In Fig. 3.7b veins cut through garnet crystals indicating that the fluids were able to chemically alter the garnet composition (brighter colors closer to the rims of the cracks). Even rutiles included in garnets (see detail in Fig. 3.7a) are affected by fluids inferred to have accessed the rock via the vein system now observed within it. The late alteration affected the rutiles in two ways. Large, granulite facies rutile grains often show corroded rims and internal alterations that follows the orientation of the veins. In rutiles, the alteration product is characterized by a patchy distribution of very fine grained material composed of rutile, ilmenite, titanite and a fine-grained platy material, probably chlorite. A second, and notable texture, shows that the alteration was coupled with crystallization of anhedral rutile veinlets along the veins (Figs. 3.7e and g). Rutile was identified by Raman bands at 245, 446 and 610 cm^{-1} (Fig. 3.7h, for a compilation of Raman bands for Ti polymorphs see Meinhold *et al.*, 2008). To our knowledge such rutile veinlets have not been described in the literature. This texture implies substantial local remobilization of Ti.

3.4.2 Zirconium concentrations in rutile

Zirconium concentrations in rutiles from the IVZ rocks are characterized by an anomalously large spread, varying from less than 700 to more than 5000 ppm (Fig. 3.8, for a complete data set refer to Appendix A). As the Zr incorporation in rutile is temperature dependent (Zack *et al.*, 2004b; Watson *et al.*, 2006; Tomkins *et al.*, 2007) and granulite facies rocks are usually well equilibrated due to the high temperatures, these results are rather unexpected. Furthermore, such a large spread

Figure 3.7 *(following page)* BSE image examples of the post-peak veins present in the granulite facies rutile bearing rocks. Note how the veins affect not only the rock-forming minerals but also the rutiles, even those included in garnet (detail in Fig. 3.7a). Chemical maps presented in Figs. 3.7d and f correspond to the same areas shown in Figs. 3.7c and e and were obtained by EDS. Higher concentrations are represented by brighter colors. Zircons in contact with rutile, such as the example given in Fig. 3.7b, are frequently observed. Fig. 3.7g shows an enlargement of the rutile *veinlet* observed in Fig. 3.7e showing location of the Laser Raman spot (the spectrum is displayed in Fig. 3.7h). Samples: B - IVZ-R16a, C - IVZ-R20a, E - IVZ-R11.
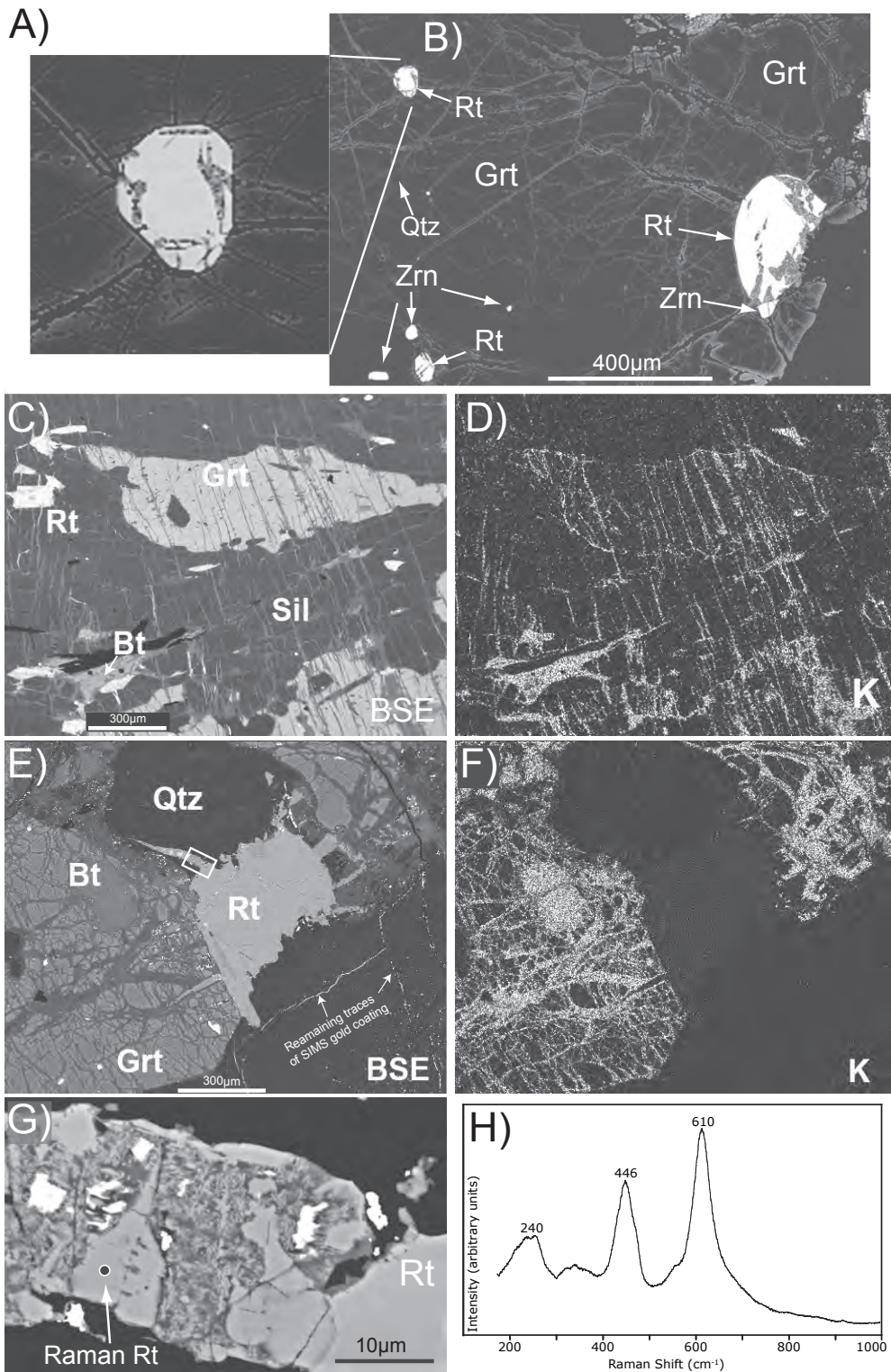
in concentration has so far not been reported in other metamorphic rocks (Zack *et al.*, 2004b; Zack & Luvizotto, 2006; Triebold *et al.*, 2007; Spear *et al.*, 2006). The only exception is greenschist facies quartzites, where the large spread of Zr concentration in rutile is probably from premetamorphic detrital relicts (Triebold *et al.*, 2007).

In order to evaluate if the large variations observed were associated to internal zoning, rim and core analyses were carried out in some rutile grains. The results show that although some intra-grain variations occur, the inter-grain variations are much more expressive (Fig. 3.9). Furthermore, no relation between grain size and Zr concentration is observed. Additionally, no systematic internal variations are observed (*e.g.*, lower concentrations at the rim of the grains). As intra-grain variations are not significant, the average concentrations obtained for the rim and the core of the grains are presented in Fig. 3.8.

The Zr data is often characterized by a bimodal distribution with a first cluster occurring in a rather restricted concentration range (about 1000 ppm Zr) for all samples. Interestingly, the second cluster is not always as pronounced. Still, if the localities are arranged by increasing metamorphic grade (according to what is postulated in the literature), maximum Zr concentrations increase with increasing metamorphism. This behavior is observed best in the Strona Valley (higher sampling density) where an increase of about 3000 ppm in Zr is registered from the localities IVZ-R7 to R5 (Fig. 3.8). Curiously, locations expected to record the highest temperatures do not have the highest Zr concentration.

Previous work (*e.g.*, Zack *et al.*, 2004b; Triebold *et al.*, 2007; Spear *et al.*, 2006) has reported systematic differences in the Zr composition for those rutiles occurring in the matrix and those included in other phases (*e.g.*, garnet or pyroxene). However, in our samples high Zr concentrations are not controlled by such textural relationships (matrix vs. inclusion). Examples presented in Figs. 3.10a-d show that rutiles with high Zr concentrations occur in contact with garnet (Fig. 3.10a), in the matrix (Fig. 3.10b) or are included in garnet (sometimes associated with cracks, Figs. 3.10c and d, respectively). Rather, low Zr values are preferentially obtained for rutiles that are occurring close to or in contact with zircons. Figs. 3.10e-h present BSE images
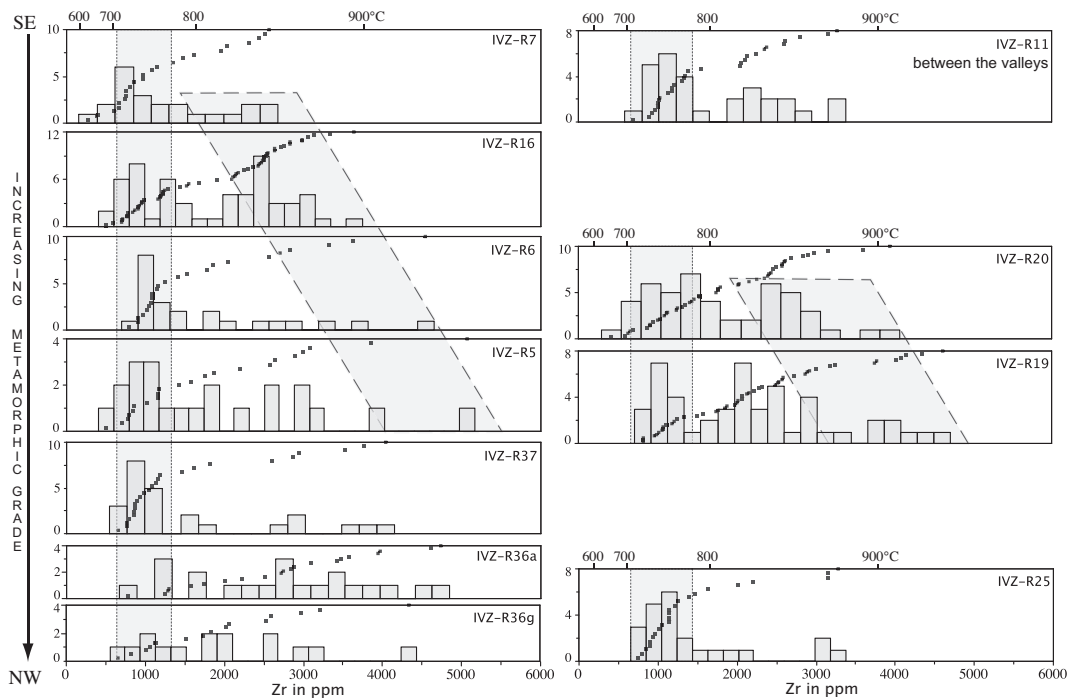
Figure 3.8 Histograms showing frequencies of Zr content in rutile (in ppm) for all studied samples (grouped by locality). Dots in the diagrams represent cumulative data points (each point represents one grain). For grains with more then one analysis the average values is presented (see discussion in the text). Notably, concentration data are characterized by a large spread and often by a bimodal distribution. Localities are arranged in such a way that the distance from Insubric Line increases upwards (Fig. 3.1). Location IVZ-R11 is between the river sections. Sample IVZ-R36g was collected ∼40m NW of sample IVZ-R36a and therefore is presented in a separate diagram. For grains with both EMP and SIMS analyses (total of 19 grains) only SIMS data is plotted (concentrations obtained by both techniques were always within the intra-grain variation - for a complete data set refer to Appendix A).

of such textural relationships. It is noteworthy that similar observations have been presented by Harley (2008) for rutiles from the Napier Complex. Although some of the low Zr rutiles presented here show effects of the late alteration (corroded grains presented in Figs. 3.10e and h) the low Zr contents are not restricted to these grains (compare with Fig. 3.10c).

93
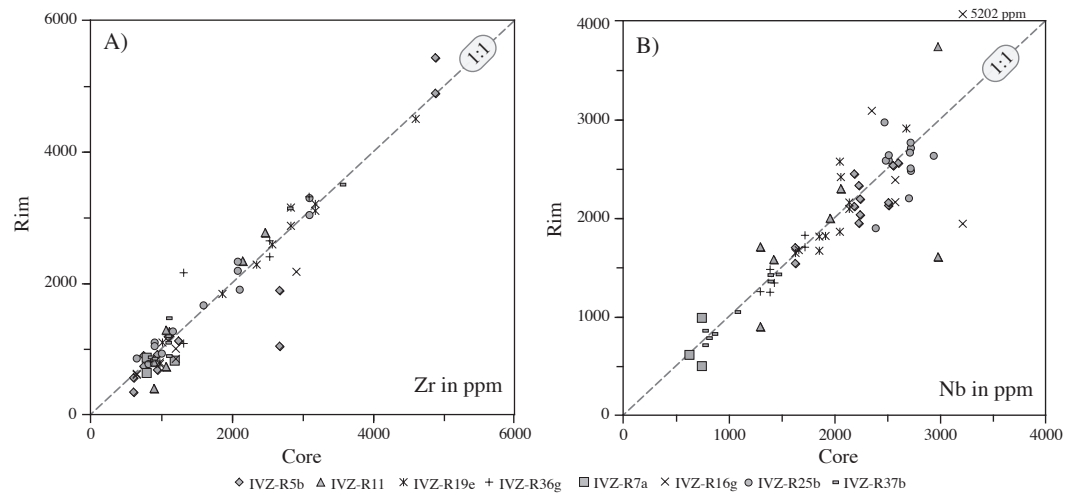
Figure 3.9 Comparison of Zr and Nb concentrations obtained for the rim ($\sim$20-30 μm from the edge of the grains to avoid contamination from surrounding silicates) and the core of some rutile grains. For both Zr and Nb the inter-grain variation is much more expressive than the intra-grain

3.4.3 Niobium concentrations in rutile

A summary of all Nb concentrations obtained for the studied localities is presented in Fig. 3.11 (for a complete data set refer to Appendix A). The results show that not only does the absolute concentration range considerably (maximum variation ranging from 300 to 8800 ppm in sample IVZ-R7), but also that the spread of the values vary from locality to locality. If the data is normalized by the average and arranged according to increasing metamorphic grade, it becomes clear that the spread of the values decreases with increasing metamorphism. This trend can be observed both in the Strona and d'Ossola valley sections. As for Zr, analyses obtained at the rim and at the core of some rutile grains show that the inter-grain variations of Nb are much more pronounced than the intra-grain (Fig. 3.9). Systematic internal variations are also not observed for Nb.

In order to evaluate the *in-situ* concentrations data, the results obtained for rutiles from five samples (three from the Strona and two from the d'Ossola valley) were compared to the WR data. As rutile is the main Nb and Ti carrier, its Nb/Ti ratio should match the ratio of the WR. The comparison is presented in Fig. 3.12 (WR analyses are presented in Table 3.2). It shows that, although variation is high
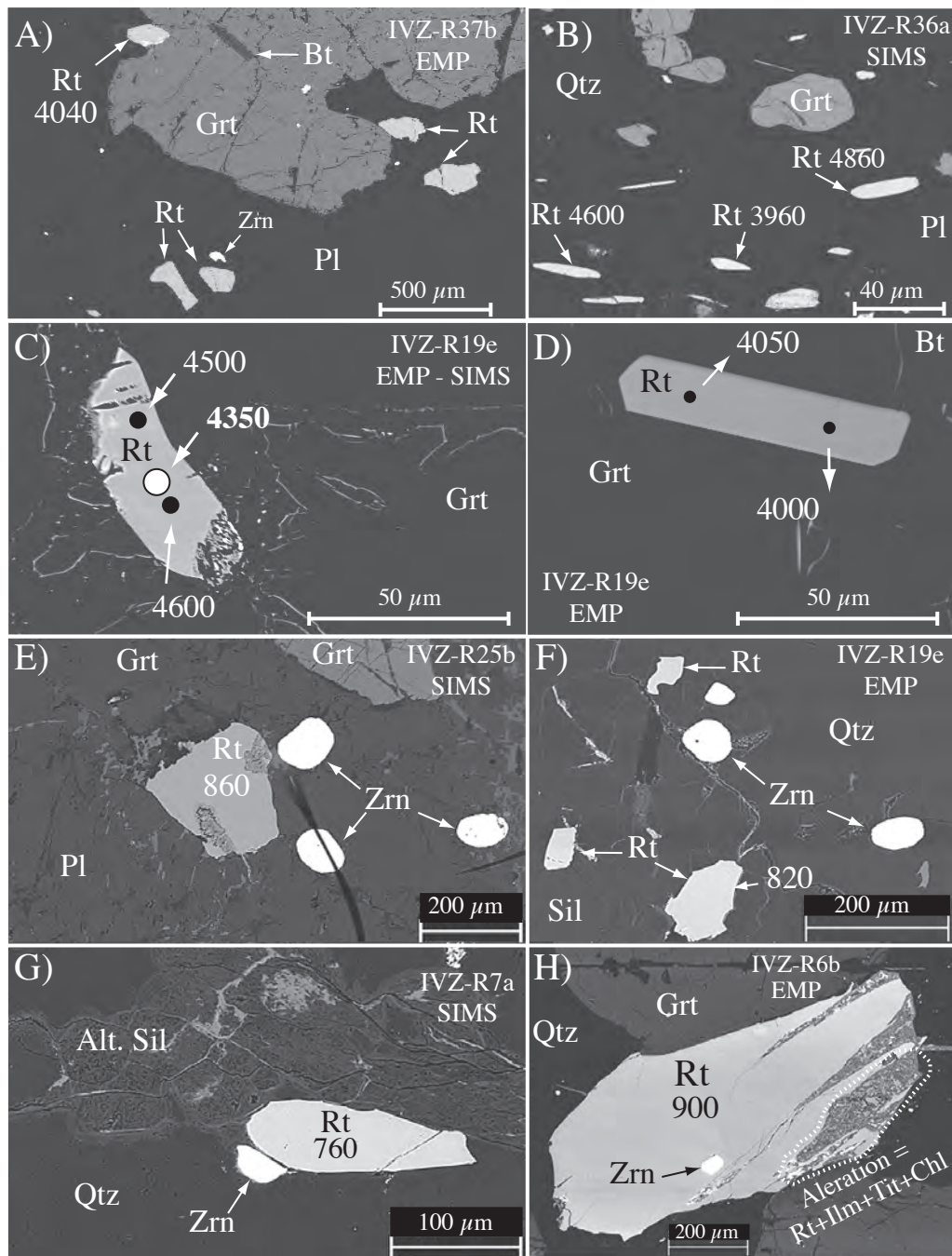
Figure 3.10 BSE images showing examples of rutiles with: high Zr concentrations - Figs. 3.10a-d; and low Zr concentrations - Figs. 3.10e-h. Notice that high Zr concentrations are not controlled by textural relationships. On the other hand, low Zr contents are preferentially obtained for those rutiles that are occurring near to or in contact with zircons. Numbers correspond to Zr concentrations (in ppm) The white circle in Fig. 3.10d represents the position of the SIMS spot (notice the agreement between EMP and SIMS results).
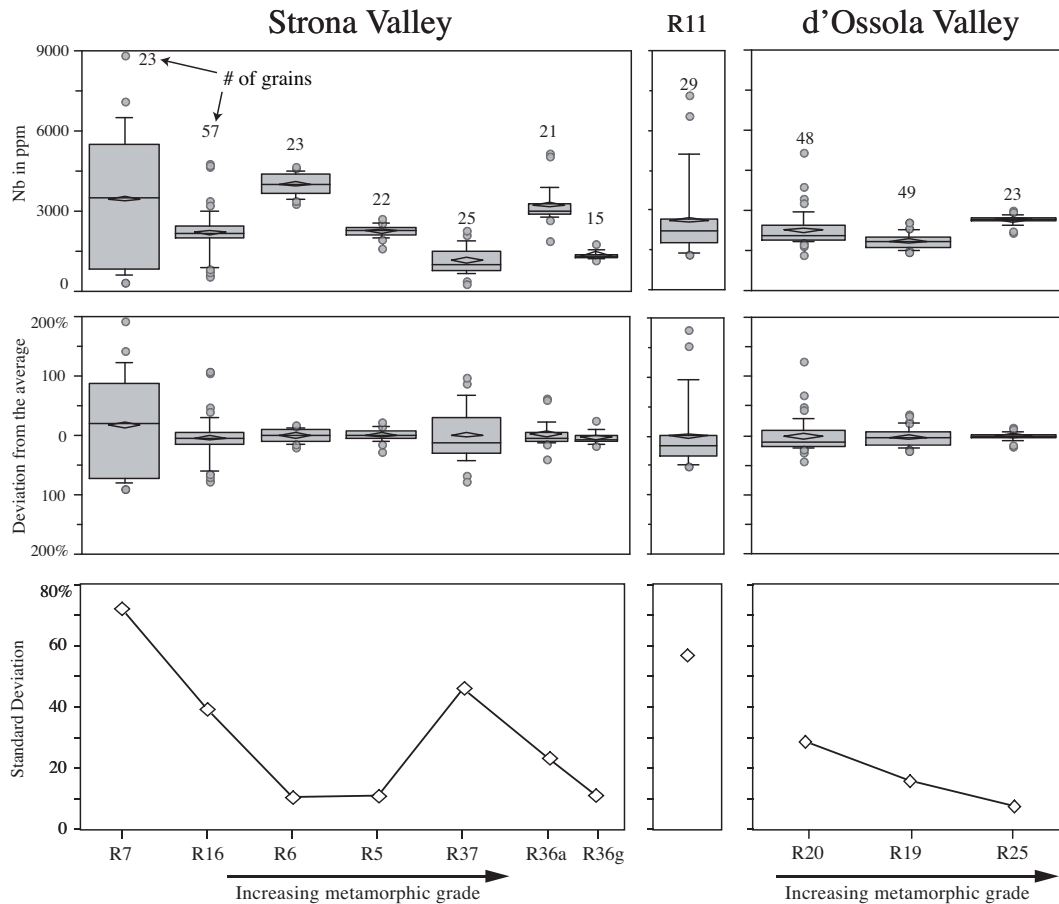
Figure 3.11 Summary of Nb concentrations (EMP, SIMS and LA-ICP-MS) obtained for the studied rutiles. Samples are sorted according to increasing metamorphic grade. The boxes represent, from bottom to top, the second and third quartile (25 and 75% of the population). The bar inside the box represents the median, while the lozenge represents the average. Whiskers represent the 10th and the 90th percentile. Outliers, when they occur, are represented by small circles. The number on top of the whiskers represents the number of analyzed grains (the same for all diagrams presented in this figure). As intra-grain variations are not significant for grains with more than one analysis, average values are presented. For grains with both EMP and SIMS analyses (total of 19 grains) only SIMS data is plotted (concentrations were always within the intra-grain variation).

for some samples, the *in-situ* results match the WR data.

Table 3.2 Whole rock chemical data (XRF) obtained for selected IVZ samples.

Sample	IVZ-R17B[a]	IVZ-R7A	IVZ-R16G	IVZ-R6B	IVZ-R20A	IVZ-19E
Valley	Strona	Strona	Strona	Strona	d'Ossola	d'Ossola
Peak Paragenesis	Grt+Bt+ Sill	Grt+Sill+ Kfs+Rt	Grt+Kfs+Rt	Grt+Sill+Rt	Grt+Sill+ Kfs+Rt	Grt+Sill+ Kfs+Rt
SiO_2	60.9	79.2	66.7	39.9	57.3	58.1
TiO_2	1.05	0.60	0.59	2.31	1.39	1.42
Al_2O_3	20.9	9.4	15.3	27.5	22.7	21.1
$Fe_2O_3^{tot}$	9.07	5.3	6.1	18.8	11.0	11.3
MnO	0.07	0.05	0.10	0.23	0.15	0.11
MgO	2.53	1.12	2.46	5.22	2.94	2.86
CaO	0.23	0.21	3.65	4.03	0.68	0.45
Na_2O	0.62	0.29	2.75	1.00	0.68	0.39
K_2O	3.75	1.17	0.66	0.27	1.74	3.30
P_2O_5	0.09	0.03	0.13	0.05	0.06	0.06
LOI	0.58	1.54	0.71	0.14	1.33	0.25
Total	99.81	98.91	99.15	99.45	99.95	99.45
Cr	123	66	103	265	156	158
Mn	467	420	737	1518	989	728
Ni	55	25	15	61	76	18
Cu	24	11	12	21	30	36
Zn	142	66	74	146	118	125
Ga	33	14	23	37	36	36
Rb	174	40	22	6	48	111
Sr	97	29	82	360	143	130
Y	30	25	37	90	53	45
Zr	156	242	78	583	279	265
Nb	19	10	9	85	29	24
Ba	618	373	150	113	1172	887
Pb	25	4	5	4	13	18
Th	13.5	12.1	0.4	7.4	20.9	19.2
Co	26	14	13	45	32	22
V	169	78	109	353	220	211

[a] - WR data used for the calculations presented in Section 3.5.2 and Figure 3.16

It has been speculated by Zack *et al.* (2004a) that rutile with high Nb (>3000 ppm) may originate in biotite-bearing mineral assemblages, where biotite prefers Ti over Nb in comparison to rutile. However, this was only based on experimental phlogopite/melt partitioning data (LaTourrette *et al.*, 1995). We therefore analyzed several biotites by LAM-ICP-MS and SIMS for HFSE (see Appendix A) in one sample (IVZ-R19e) that shows little Nb variation between different rutile grains. In

this sample, relict biotite inclusions in garnet were compared with coexisting rutile (Fig. 3.13). Nb concentrations in biotite range between 0.34 and 4.90 ppm (average 1.9 ppm) with no observable difference between SIMS and LAM-ICP-MS analysis. With 7 wt% TiO_2 in biotite, 100 wt% TiO_2 and ca. 2000 ppm Nb in rutile, this confirms the prediction of a strong fractionation of the Nb/Ti ratio between rutile and biotite (ca. 50, according to the data presented by LaTourrette *et al.*, 1995).

3.5 Discussion

3.5.1 Rutile thermometry and thermal constraints of the granulite facies metamorphism

Interpretation of the complex Zr data, with the aim of extracting temperature information for the IVZ, presents a challenge in comparison to relatively straightforward results in previous studies on natural rocks (Zack *et al.*, 2004b; Zack & Luvizotto, 2006; Spear *et al.*, 2006). With the absence of perfectly shielded rutile inclusions in garnet (see Fig. 3.7a), we are left with an open system scenario, in which rutiles have been variously affected by late resetting of their Zr content. This resetting seems to have produced a marked cluster of rutiles with Zr concentrations of about 1000 ppm (Fig. 3.8). This observation will be further explored in Section 3.5.3. Here we concentrate on the rutiles that are the least affected by this resetting, which we interpret to be represented by those towards higher Zr on the distribution diagrams presented in Fig. 3.8.

The calculations of apparent temperatures from Zr concentrations in rutile have been conducted using the calibration of Tomkins *et al.* (2007), which includes a pressure effect on the geothermometer. With the strong resetting of the Zr content, we attempt to constrain the granulite facies metamorphism by selecting the values between the 90th percentile and the maximum (values that are usually overlooked by standard statistical methods). Results are graphically presented in Fig. 3.14.

Temperatures calculated using the rutile thermometer are significantly higher than those previously presented in the literature, spanning from ca. 850 to 930°C (about 100°C higher than those obtained by Henk *et al.*, 1997). Our data, however,
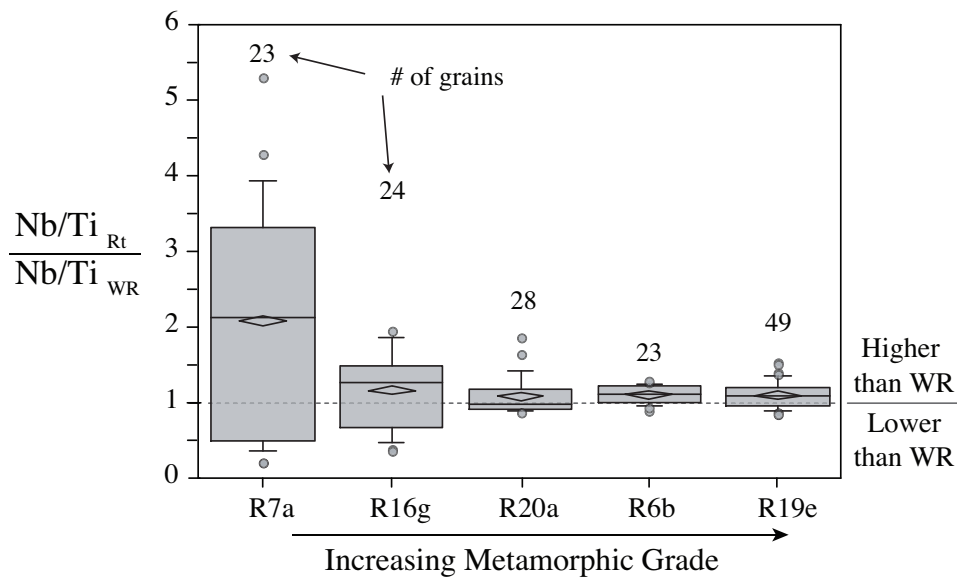
Figure 3.12 Whisker and box plots (for explanation please refer to Fig. 3.11) summarizing Nb concentrations (EMP and SIMS) in rutiles from samples selected for WR analyses. Samples are displayed according to increasing metamorphic grade. To keep the data consistent, only rutile data from the same rock fragments analyzed for WR are presented here (therefore the number of grains differs slightly from those presented in Fig. 3.11).
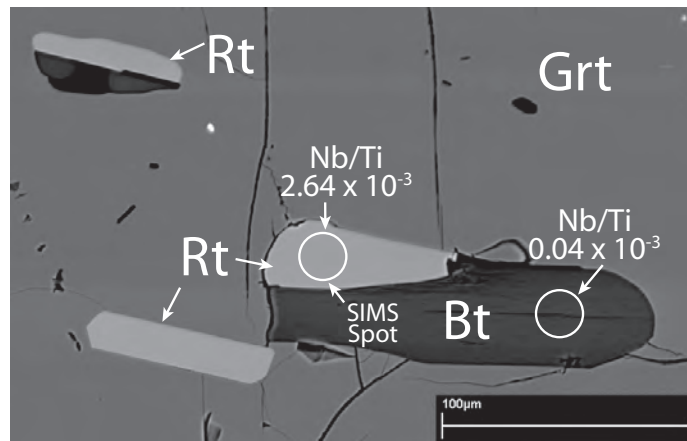
Figure 3.13 Nb/Ti ratios (SIMS analyses) of coexisting rutile and biotite occurring in granulite facies metapelitic rocks from the IVZ.

99
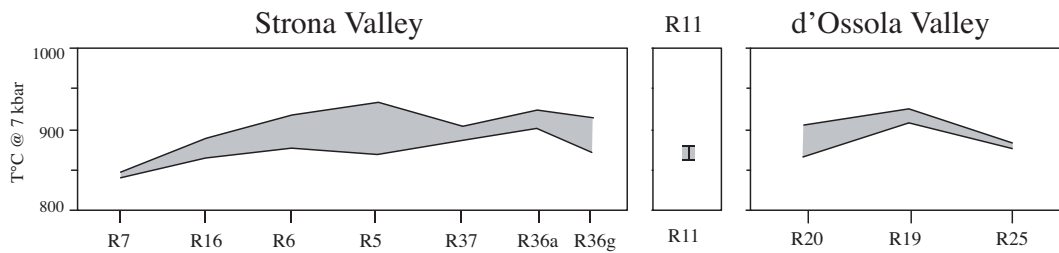
Figure 3.14 Temperatures obtained for the studied localities. Shaded area represents the interval delimited by values above the ninetieth percentile. Calculations were based on the Zr content in rutile for a pressure of 0.7 GPa (calibration of Tomkins *et al.*, 2007)

point to a temperature gradient of about 80°C within the granulite facies metapelitic rocks, which is in agreement with Henk *et al.* (1997). The higher temperatures obtained by the rutile thermometer are not completely unexpected, as the previously determined data were based on Fe-Mg exchange geothermometers. However, the differences are significant and the results have to be treated with caution. Preliminary results obtained by SIMS in Heidelberg show that some zircon grains from the studied samples seem also to record high temperatures, with some values above 900°C (temperatures calculated using the Ti-in-Zrn thermometer, calibration of Watson *et al.*, 2006). Although preliminary, these results suggest that zircon was able to form and recrystallize even at high temperatures (see also Baldwin *et al.*, 2007; Kelsey *et al.*, 2008).

We would like to note that overestimation of temperatures with the rutile thermometer is only possible where mineral assemblages in equilibrium with rutile are quartz-free, while underestimation can happen in zircon-absent and/or in partially reset mineral assemblages (Zack *et al.*, 2004b; Harley, 2008). Since quartz is always present in the investigated rutile-bearing mineral assemblages, but resetting is significant, temperatures have to be treated as minimum values. Sixteen rutile grains with Zr >3800 ppm (apparently representing >900°C) have been found in 6 different localities (IVZ-R5, R6, R19, R20, R36 and R37). All analyses give low Si signals, excluding contamination from minute zircon inclusions.

While temperature estimates from the IVZ granulite facies rocks based on Fe-Mg exchange are ca. 100°C lower than results based on rutile thermometry, mineral

phase assemblage considerations are broadly consistent with our results. As summarized above, minimum temperatures can be given as 800°C based on the coexistence of Opx + Kfs as well as the absence of biotite in Grt + Kfs + Sil mineral assemblages with Fe/(Fe+Mg) ratios of 0.6 (see Fig. 3.2). An independent maximum temperature estimate is difficult to make due to the absence of Mg-Al-rich rocks in the IVZ, where the presence or absence of coexisting Sil + Opx points to temperatures above or below 900°C, respectively. However, as a final note, we would like to point out that several Kfs-Sil-bearing gneisses are very restitic (sillimanite and garnet-rich), indicating significant melt loss. Schnetger (1994) modeled melt extraction rates of up to 40% based on trace element abundances. Such high melt losses are only achieved in typical metapelites at temperatures above 870°C at 1.0 GPa (see Fig. 6 in Spear *et al.*, 1999).

3.5.2 Rutile formation from biotite and expected Nb behavior

As previously presented, textures observed in the studied rocks are evidence for prograde rutile growth associated with the breakdown of high-Ti biotite. With the marked contrast in Nb partitioning between biotite and rutile, we explore in this section how the observed Nb systematics in rutile can be linked to biotite breakdown. The simplified conceptual model (Fig. 3.15) basically includes four main steps: (1) An initial step where only biotite is present and all Ti and Nb in the system (whole rock) is incorporated in this mineral. (2) An early stage where a few rutile grains exist. Biotite is still the main Ti-carrier (high Bt/Rt ratio). Nb is distributed between both phases. (3) As the reaction continues, the Bt/Rt ratio decreases and rutile becomes the main Ti- and Nb-carrier. (4) The final stage is reached when all biotite is consumed and only rutile is present, incorporating all Ti and Nb of the whole rock.

Combining the crystallization model presented above with exchange coefficients, it is possible to quantitatively model the behavior of Nb through these stages. Klemme *et al.* (2005) presented experimentally derived rutile/melt partition coefficients for a range of trace elements, including Nb. Combined with Ti partitioning between rutile and melt, an exchange coefficient of the Nb/Ti ratio between rutile

Stages

Initial: *Rt-free*   Early   Intermediate   Final: *only Rt*

Rt

Bt

200µm

host WR
Ti & Nb

Chemical diffusion of Ti & Nb

host WR
Ti & Nb

Increasing metamorphism

Continuous reaction
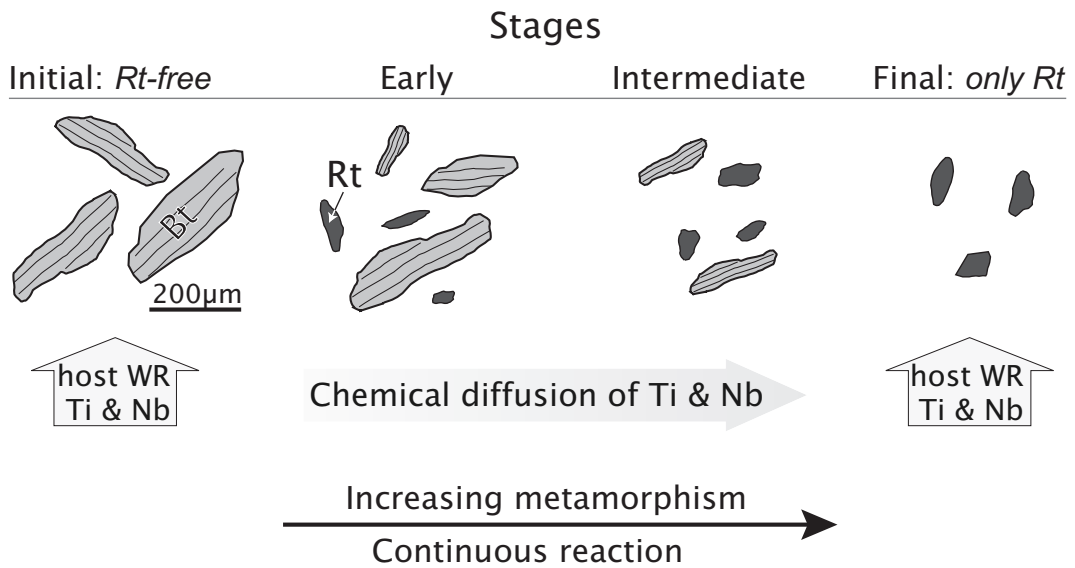
Figure 3.15 Illustration showing the four main stages during prograde rutile crystallization from biotite. WR = whole rock chemistry.

and melt can be calculated as 2.47 ($K_{DNb/Ti}^{Rt/melt}$; following the terminology of Beattie *et al.*, 1993). The compatible behavior of Nb in rutile compared to melt contrasts strongly with the partitioning behavior of biotite. LaTourrette *et al.* (1995) found Nb to be incompatible in phlogopite compared to melt, with a $K_{DNb/Ti}^{Bt/melt}$ of 0.050. Neglecting minor differences of melt composition in both studies, we can calculate an exchange coefficient for Nb/Ti between rutile and biotite $K_{DNb/Ti}^{Rt/Bt}$ of 48.7. This compares well with results from sample IVZ-R19e, where a $K_{DNb/Ti}^{Rt/Bt}$ of ca. 60 has been measured (see Fig. 3.13).

As an example, calculations were carried out for an amphibolite facies garnet-sillimanite-biotite schist from Val Strona (sample IVZ-R17b). Ti concentrations in biotite do not show any systematic variation throughout the upper-amphibolite to granulite facies transition (unpublished EDS and WDS analyses). Therefore, the Ti concentration of biotite was kept constant throughout the calculation steps. Results are graphically depicted in Fig. 3.16.

As Nb is more compatible in rutile than in biotite, the first rutiles to form have
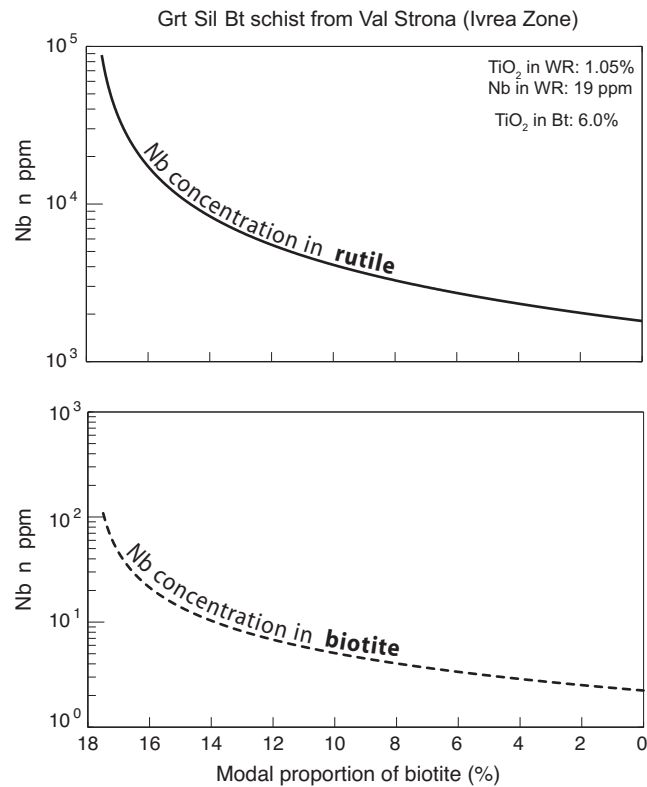
Figure 3.16 Quantitative simulation of Nb concentration in rutile and biotite with decreasing modal proportion of biotite. The model reproduces rutile growth in equilibrium with biotite. The calculations were run for an amphibolite facies garnet-sillimanite-biotite schist from Val Strona, (sample IVZ-R17b). The parameters used for the calculations are presented in the diagrams (a complete WR data set is presented in Table 3.2). Note that Nb concentration is expressed in log scale.

high Nb concentrations. As the reaction continues, and the rutile crystallizes, the remaining biotite has lower Nb contents. It can be seen that during the initial stages of the reaction the decrease of only 3% in the modal proportion of biotite leads to a reduction of one order of magnitude in the Nb concentration of both rutile and biotite. Rutiles formed during later stages of this reaction have low Nb contents and eventually the Nb/Ti ratios in rutile is lower than in the whole rock sample.

These simple calculations imply that rutile grains formed by biotite breakdown are expected to record large variations in Nb concentrations (both inter- and intra-grain). Indeed, the Nb concentration data obtained for the studied rutiles (Fig. 3.11)

show that a large spread in Nb concentrations is displayed by rutiles from the lower grade localities. The Nb behavior in these samples is in agreement with the crystallization model proposed and supports the theory that during continuous formation of rutile from biotite, a high spread in Nb concentration is created. Here, we interpret rutiles with the highest Nb concentrations (up to a factor of 5.5 higher than WR Nb/Ti ratios; see Fig. 3.12) to be formed first from a biotite-rich mineral assemblage and rutiles with lower Nb concentrations lower than WR Nb/Ti ratios forming last. However, we notice that no pronounced intra-grain variability has been observed in any sample, an observation we cannot satisfactorily explain (see Fig. 3.9).

In contrast, samples further away from the lowest-grade samples show decreasing variability of Nb in rutile. It can be seen that variability steadily decreases and the average values (diamonds in Fig. 3.12) approach the WR ratios in the highest grade samples. This observation can be best explained by a homogenization of formerly heterogeneous rutiles during increasing temperature, facilitating dynamic recrystallization, intergrain diffusion and/or communication between rutile grains by a melt phase.

3.5.3 Post-peak metamorphic processes and their effects on trace element concentrations in rutile

Textures showing rutiles strongly altered by post-peak processes are frequently observed and are characterized not only by corrosion of the rutile grains but also by crystallization of rutile veinlets along K-rich veins (Figs. 3.7 and 3.10). In addition, Zr concentrations in rutiles are distinguished by an anomalously large spread and bimodal distribution (Fig. 3.8).

A dominance of rutiles with Zr concentrations of ca. 1000 ppm is observed for all localities. These rutiles preferentially occur close to or in contact with zircons (Fig. 3.10). We interpret this as evidence for diffusional resetting related to the slow cooling postulated for the IVZ (see above). We noticed that an apparent temperature of 700°C (for Zr concentrations of 1000 ppm in rutile) is in surprising agreement to a closure temperature of Zr in rutile determined by diffusion experiments (Cherniak *et al.*, 2007). The reequilibration of the Zr content in rutile is favored since

zircons are abundant in the rocks, which facilitates ion exchange. We would like to add that with respect to Zr, the small variations in zoning and large intergrain variation (Fig. 3.9a) are in good agreement with the fluid diffusion controlled regime of Dohmen & Chakraborty (2003, their Fig. 3B). In this regime, transport of an element (in this case Zr) in a fluid is much less efficient than transport within a given mineral (in this case rutile). In contrast, Nb in rutile will not be reset, because no other significant Nb carrier is available for ion exchange in the investigated samples. This process is also favored by Harley (2008) for ultra-high-temperperature rocks from the Napier Complex. The author shows that rutiles occurring adjacent to zircons are zoned with Zr concentrations decreasing from 1100 ppm in the core to 500 ppm in the rim close to adjacent zircon. In addition, Ti concentrations in recrystallized zircon rims are also lower than expected (19-33 ppm Ti). For these data, temperatures obtained by the Zr-in-rutile and the Ti-in-zircon thermometers (Watson *et al.*, 2006) are about 200°C lower than the peak temperature, overlapping at 775-800°C. Preliminary results obtained by SIMS in Heidelberg show that, although several zircon grains from our samples seem to record high temperatures (*i.e.*, >900°C), some grains have rather low Ti concentrations giving apparent temperatures as low as 700°C (calibration of Watson *et al.*, 2006).

The complex network of veins that cut through the granulite facies mineral assemblage is evidence for post-peak fluid influx. The presence of a fluid phase would only enhance the ion exchange between rutile and zircon. Franz & Harlov (1998) described the presence of extensive networks of K-feldspar micro-veins in the IVZ rocks and suggested a model with intrusion and partial crystallization of the Mafic Complex, with a high-temperature, probably alkali-rich fluid (most likely a concentrated brine) accumulating at the top of the Mafic Complex, and percolating through the overlaying rocks at late stages of emplacement. Although the nature and the exact composition of the fluid is not completely understood, textures and chemical data show that Ti and Zr were mobilized, at least on the thin section scale. This leads to the conclusion that fluids, depending on their composition, can indeed mobilize elements, which are usually assumed to be immobile (*e.g.*, HFSE).

Considering the evidence for both slow cooling and strong fluid ingress, we are

left to conclude that both processes could be responsible for the significant resetting of Zr concentrations in the investigated rutiles from the IVZ. Since this is the first study of rutile behavior in slowly cooled granulite facies rocks, it will be insightful to investigate whether or not rutiles in other slowly cooled granulite facies rocks that lack evidence for strong fluid ingress show the same resetting in Zr concentration.

3.5.4 Behavior of other trace elements

In principle, the same crystallization model proposed for Nb and Ti can also be extended to other trace elements. However, it is important to keep in mind that the modeling will only be valid for elements that are only incorporated in phases involved in the reaction. The same effect observed for Nb is expected to occur for elements with partition coefficients ($D_{Elem.}^{Ti-phase/melt}$) significantly different (higher or lower) from those obtained for rutile ($D_{Elem.}^{Rt/melt}$). Furthermore, the modeling will not be suitable for any trace element that is temperature or pressure dependent (*e.g.*, Zr).

According to our data, no systematic variation is observed for the elements V, Cr, Fe, Sn, Sb and W. However, the same behavior described for Zr and Nb is observed for Hf and Ta, respectively. Hf data show a relatively large spread and a bimodal distribution. Furthermore, a strong correlation between Zr and Hf is observed (Fig. 3.17), implying that the Hf incorporation in rutiles, at least in our samples, is temperature dependent. This observation may help to target high-Hf rutiles for Hf isotope studies. As for Nb, the spread in Ta concentration is higher in samples from the lower metamorphic grade, and decreases with increasing metamorphism (Fig. 3.18). This observation is corroborated by the strong correlation between Nb and Ta concentrations in rutile (Fig. 3.17) and suggests that the crystallization model proposed for Nb can be extended to Ta. Another important conclusion is that the processes that affected the rutiles in the Ivrea Zone rocks were not able to fractionate Zr from Hf and Nb from Ta, at least with respect to rutile. The average Nb/Ta ratio obtained for the studied rutiles (23.8) is slightly higher than the chondritic value (19.9; Münker *et al.*, 2003) but still completely within the scatter of a highly heterogeneous continental crust (at least from 8 to 123; see analyses of

crustal rutiles in Supplemental Table of Rudnick *et al.*, 2000).
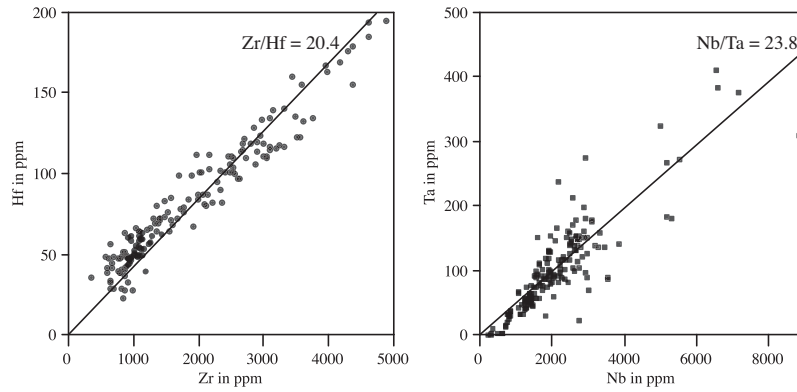
Figure 3.17 Diagram showing a strong correlation between Zr and Hf and Nb and Ta in rutiles from IVZ. All data obtained is presented here.
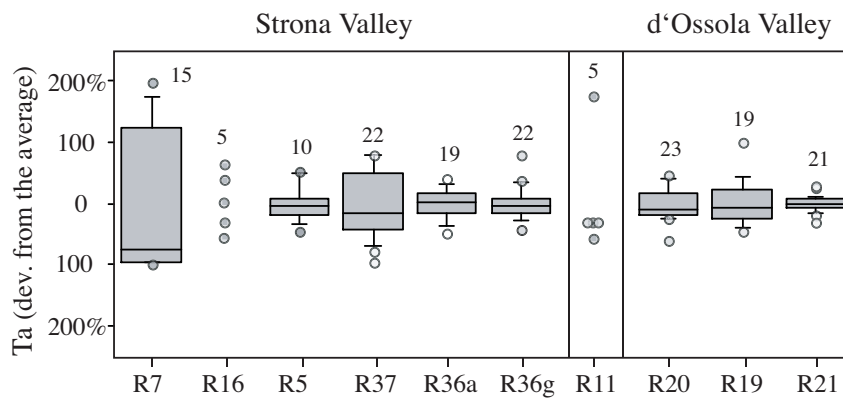
Figure 3.18 Variations of Ta content in rutile (SIMS and LA-ICP-MS) from the studied localities. Samples are only plotted for localities with more than 5 analyses.

3.6 Conclusions

One of the major findings of the present work is that it is possible to couple textures with trace element concentration in accessory phases involved in both prograde and retrograde metamorphic reactions.

The granulite facies metapelitic rocks from the IVZ show a rich inventory of textures and trace element distribution in rutile, making it possible to investigate comprehensively the behavior of important elements (*i.e.*, Ti, Nb, Zr) during metamorphic processes.

Our results show that prograde rutile growth associated with biotite breakdown generates a large spread in Nb concentrations in rutile. After the final stages of the reaction, rutile is the main Ti and Nb carrier, and through continuous dynamic recrystallization the Nb concentrations in rutile evolve towards equilibrium reducing the spread in Nb.

Typical textural controls on the Zr concentration in rutile (*e.g.*, inclusion vs. matrix) described in the literature are not observed in our rocks. Additionally, the Zr concentrations are often characterized by a bimodal distribution. Therefore, a new approach where the highest concentration values were statistically selected was applied for the calculation of peak temperatures. For granulites, this method should be preferred against, *e.g.*, calculating temperature from mean Zr concentrations.

Temperatures obtained by the Zr-in-rutile thermometer for the granulite facies rocks are in the range of 850 to 930°C and are significantly higher than those previously reported in the literature. However, considering that previous calculations were mostly based on Fe-Mg exchange geothermometers and the fact that the late processes that affected the rutiles may also have changed the chemical composition of other primary phases, the high temperatures obtained are not unrealistic. The anomalously large spread in Zr concentrations obtained for the rutiles is interpreted to be related to post-peak diffusional resetting associated with slow cooling rates and/or the presence of fluid.

Another finding of the present work is that fluids can, depending on their compositions, mobilize elements frequently interpreted to be immobile, such as Ti and

Zr. This is evidenced by the corrosion of the granulite facies rutile and the crystallization of rutile veinlets associated with textures that suggest late influx of a K-rich fluid. Here we would like to note that HFSE mobility in fluids may be significantly enhanced by the addition of complexing chemical compounds (*e.g.*, Rapp *et al.*, 2008).

Our results encourage further studies in the field of trace element partitioning associated with metamorphic reactions using accessory phases as tools. It also demonstrates the importance of detailed petrographic and textural investigations. Furthermore, our findings spur on the search for other terrains characterized by slow cooling rates in order to evaluate whether the textures and chemical characteristics observed in the IVZ rocks are also present in other localities. This can lead to, *e.g.*, reinterpretations about peak granulite facies temperatures, and element mobility during geological processes.

Acknowledgments

Bibliography

Baldwin J, Brown M, Schmitz M (2007) First application of titanium-in-zircon thermometry to ultrahigh-temperature metamorphism. *Geology* 35: 295–298

Barboza SA, Bergantz GW (2000) Metamorphism and anatexis in the mafic complex contact aureole, Ivrea zone, northern Italy. *Journal of Geology* 41: 1307–1327

Barboza SA, Bergantz GW, Brown M (1999) Regional granulite facies metamorphism in the Ivrea zone: Is the Mafic Complex the smoking gun or a red herring? *Geology* 27: 447–450

Beattie P, Drake M, Jones J, Leeman W, Longhi J, McKay G, Nielsen R, Palme H, Shaw D, Takahashi E, Watson B (1993) Terminology for trace-element partitioning. *Geochimica et Cosmochimica Acta* 57: 1605–1606

Berckhemer H (1969) Direct evidence for the composition of the lower crust and Moho. *Tectonophysics* 8: 97–105

Boriani A, Origoni EG, Borghi A, Caironi V (1990) The evolution of the Serie-Dei-Laghi (Strona-Ceneri and Scisti-Deilaghi) - the upper component of the Ivrea-Verbano crustal section - Southern Alps, North Italy and Ticino, Switzerland. *Tectonophysics* 182: 103–118

Cherniak DJ, Manchester J, Watson EB (2007) Zr and Hf diffusion in rutile. *Earth and Planetary Science Letters* 261: 267–279

Davis WJ (1997) U-Pb zircon and rutile ages from granulite xenoliths in the Slave Province; evidence for mafic magmatism in the lower crust coincident with Proterozoic dike swarms. *Geology* 25: 343–346

Deer WA, Howie R, Zussman J (1992) *An introduction to the rock-forming minerals*. Harlow, Essex, England, 696p

Demarchi G, Quick JE, Sinigoi S, Mayer A (1998) Pressure gradient and original orientation of a lower-crustal intrusion in the Ivrea-Verbano Zone, northern Italy. *Journal of Geology* 106: 609–621

Dohmen R, Chakraborty S (2003) Mechanism and kinetics of element and isotopic exchange mediated by a fluid phase. *American Mineralogist* 88: 1251–1270

Dooley DF, Patiño-Douce AE (1996) Fluid-absent melting of F-rich phlogopite plus rutile plus quartz. *American Mineralogist* 81: 202–212

Fitzsimons I, Harley S (1994) The Influence of Retrograde Cation Exchange on Granulite P-T Estimates and a Convergence Technique for the Recovery of Peak Metamorphic Conditions. *Journal of Petrology* 35: 543–576

Franz L, Harlov DE (1998) High-grade K-feldspar veining in granulites from the Ivrea-Verbano Zone, northern Italy: Fluid flow in the lower crust and implications for granulite facies genesis. *Journal of Geology* 106: 455–472

Gao J, John T, Klemd R, Xiong X (2007) Mobilization of Ti–Nb–Ta during subduction: Evidence from rutile-bearing dehydration segregations and veins hosted in eclogite, Tianshan, NW China. *Geochimica et Cosmochimica Acta* 71: 4974–4996

Graham J, Morris R (1973) Tungsten- and antimony-substituted rutile. *Mineralogical Magazine* 39: 470–473

Haggerty SE (1991) *Oxide mineralogy of the upper mantle. In: Lindsley, D. H. (Ed.), Oxide mineralogy minerals: Petrological and magnetic significance*, vol. 25. Reviews in mineralogy

Handy MR, Franz L, Heller F, Janott B, Zurbriggen R (1999) Multistage accretion and exhumation of the continental crust (Ivrea crustal section, Italy and Switzerland). *Tectonics* 18: 1154–1177

Harley S (1989) The origins of granulites; a metamorphic perspective. *Geological Magazine* 126: 215–247

Harley SL (2008) Refining the P–T records of UHT crustal metamorphism. *Journal of Metamorphic Geology* 26: 125–154

Hayden LA, Watson EB, Wark DA (2007) A thermobarometer for sphene (titanite). *Contributions to Mineralogy and Petrology* 155: 529–540

Henk A, Franz L, Teufel S, Oncken O (1997) Magmatic underplating, extension, and crustal reequilibration: Insights from a cross-section through the Ivrea Zone and Strona-Ceneri Zone, northern Italy. *Journal of Geology* 105: 367–377

Henry DJ, Guidott CV (2002) Titanium in biotite from metapelitic rocks: Temperature effects, crystal-chemical controls, and petrologic applications. *American Mineralogist* 87: 375–382

Henry DJ, Guidotti CV, Thomson JA (2005) The Ti-saturation surface for low-to-medium pressure metapelitic biotites: Implications for geothermometry and Ti-substitution mechanisms. *American Mineralogist* 90: 316–328

Kelsey D, Clark C, Hand M (2008) Thermobarometric modelling of zircon and monazite growth in melt-bearing systems: examples using model metapelitic and metapsammitic granulites. *Journal of Metamorphic Geology* 26: 199–212

Klemme S, Prowatke S, Hametner K, Gunther D (2005) Partitioning of trace elements between rutile and silicate melts: Implications for subduction zones. *Geochimica et Cosmochimica Acta* 69: 2361–2371

Köppel V (1974) Isotopic U-Pb ages of monazites and zircons from crust-mantle transition and adjacent units of Ivrea and Ceneri Zones (Southern-Alps, Italy). *Contributions to Mineralogy and Petrology* 43: 55–70

Kretz R (1983) Symbols for rock forming minerals. *American Mineralogist* 68: 277–279

LaTourrette T, Hervig RL, Holloway JR (1995) Trace-element partitioning between amphibole, phlogopite, and basanite melt. *Earth and Planetary Science Letters* 135: 13–30

Li Q, Li S, Zheng YF, Li H, Massonne HJ, Wang Q (2003) A high precision U-Pb age of metamorphic rutile in coesite-bearing eclogite from the Dabie Mountains in central China: a new constraint on the cooling history. *Chemical Geology* 200: 255–265

Luvizotto G, Zack T, Meyer H, Ludwig T, Triebold S, Kronz A, Münker C, Stockli D, Prowatke S,

Klemme S, Jacob DE, von Eynatten H (in press) Rutile crystals as potential secondary standards for microanalysis. *Chemical Geology*

Meinhold G, Anders B, Kostopoulos D, Reischmann T (2008) Rutile chemistry and thermometry as provenance indicator: An example from Chios Island, Greece. *Sedimentary Geology* 203: 98–111

Mezger K, Hanson GN, Bohlen SR (1989) High-precision U-Pb ages of metamorphic rutile: application to the cooling history of high-grade terranes. *Earth and Planetary Science Letters* 96: 106–118

Mezger K, Essene EJ, Vanderpluijm BA, Halliday AN (1993) U-Pb Geochronology of the Grenville Orogen of Ontario and New York: Constraints on Ancient Crustal Tectonics. *Contributions to Mineralogy and Petrology* 114: 13–26

Miller C, Zanetti A, Thoni M, Konzett J (2007) Eclogitisation of gabbroic rocks: Redistribution of trace elements and Zr in rutile thermometry in an Eo-Alpine subduction zone (Eastern Alps). *Chemical Geology* 239: 96–123

Münker C, Pfänder J, Weyer S, Buchl A, Kleine K T amd Mezger (2003) Evolution of planetary cores and the earth-moon system from Nb/Ta systematics. *Science* 301: 84–87

Patiño-Douce AE (1993) Titanium substitution in biotite - an empirical-model with applications to thermometry, O_2 and H_2O barometries, and consequences for biotite stability. *Chemical Geology* 108: 133–162

Patiño-Douce AE, Beard JS (1995) Dehydration-melting of biotite gneiss and quartz amphibolite from 3 to 15 kbar. *Journal of Petrology* 36: 707–738

Pattison D, Begin N (1994) Zoning patterns in orthopyroxene and garnet in granulites: implications for geothermometry. *Journal of Metamorphic Geology* 12: 387–410

Pattison DRM, Chacko T, Farquhar J, McFarlane CRM (2003) Temperatures of Granulite-facies Metamorphism: Constraints from Experimental Phase Equilibria and Thermobarometry Corrected for Retrograde Exchange. *Journal of Petrology* 44: 867–900

Pearce JA, Cann JR (1973) Tectonic setting of basic volcanic rocks determined using trace element analysis. *Earth and Planetary Science Letters* 19: 290–300

Peressini G, Poller U, Todt W, Quick JE, Sinigoi S, Sbisa A (2002) Age of magmatism in the Ivrea Zone, NW Italy: a zircon study to test the emplacement model. *Geochimica et Cosmochimica Acta* 66: A590–A590

Peressini G, Quick JE, Sinigoi S, Hofmann AW, Fanning M (2007) Duration of a large Mafic intrusion and heat transfer in the lower crust: A SHRIMP U-Pb zircon study in the Ivrea-Verbano Zone (Western Alps, Italy). *Journal of Petrology* 48: 1185–1218

Rapp J, Klemme S, Harley SL (2008) Experimental Studies on Rutile Solubility. In: *Goldschmidt 2008, Abstracts*

Rasmussen B (2005) Zircon growth in very low grade metasedimentary rocks: evidence for zirconium mobility at similar to 250 degrees C. *Contributions to Mineralogy and Petrology* 150: 146–155

Rice C, Darke K, Still J (1998) Tungsten-bearing rutile from the Kori Kollo gold mine Bolívia.

Mineralogical Magazine 62: 421–429

Rivalenti G, Garuti G, Rossi A, Siena F, Sinigoi S (1981) Existence of different peridotite types and of a layered igneous complex in the Ivrea Zone of the Western Alps. *Journal of Petrology* 22: 127–153

Rivalenti G, Mazzucchelli M, Barbieri MA, Parenti M, Schmid R, Zanetti A (1997) Garnetite-forming processes in the deep crust: The Val Fiorina case study (Ivrea-Verbano Zone, NW Alps). *European Journal of Mineralogy* 9: 1053–1071

Rudnick RL, Barth M, Horn I, McDonough WF (2000) Rutile-bearing refractory eclogites: Missing link between continents and depleted mantle. *Science* 287: 278–281

Rutter E, Brodie K, James T, Burlini L (2007) Large-scale folding in the upper part of the Ivrea-Verbano zone, NW Italy. *Journal of Structural Geology* 29: 1–17

Schmid SM, Wood BJ (1976) Phase relationships in granulitic metapelites from the Ivrea–Verbano zone (northerns Italy). *Contributions to Mineralogy and Petrology* 54: 255–279

Schmid SM, Zingg A, Handy M (1987) The kinematics of movements along the Insubric Line and the emplacement of the Ivrea Zone. *Tectonophysics* 135: 47–66

Schnetger B (1994) Partial Melting During The Evolution Of The Amphibolite-Facies To Granulite-Facies Gneisses Of The Ivrea Zone, Northern Italy. *Chemical Geology* 113: 71–101

Sills JD (1984) Granulite facies metamorphism in the Ivrea Zone, NW Italy. *Schweizerische Mineralogische und Petrographische Mitteilungen* 64: 169–191

Sills JD, Tarney J (1984) Petrogenesis and tectonic significance of amphibolites interlayered with meta-sedimentary gneisses in the Ivrea Zone, Southern Alps, Northwest Italy. *Tectonophysics* 107: 187–206

Smith D, Persil EA (1997) Sb-rich rutile in the manganese concentrations at St. Marcel-Praborna, Aosta Valley, Italy; petrology and crystal-chemistry. *Mineralogical Magazine* 61: 655–669

Spear FS (1995) *Metamorphic Phase Equilibria and Pressure-Temperature-Time Paths*. Mineralogical Society of America

Spear FS, Kohn MJ, Cheney JT (1999) P-T paths from anatectic pelites. *Contributions to Mineralogy and Petrology* 134: 17–32

Spear FS, Wark DA, Cheney JT, Schumacher JC, Watson EB (2006) Zr-in-rutile thermometry in blueschists from Sifnos, Greece. *Contributions to Mineralogy and Petrology* 152: 375–385

Stendal H, Toteu SF, Frei R, Penaye J, Njel UO, Bassahak J, Nni J, Kankeu B, Ngako V, Hell JV (2006) Derivation of detrital rutile in the Yaounde region from the Neoproterozoic Pan-African belt in southern Cameroon (Central Africa). *Journal of African Earth Sciences* 44: 443–458

Tomkins HS, Powell R, Ellis DJ (2007) The pressure dependence of the zirconium-in-rutile thermometer. *Journal of Metamorphic Geology* 25: 703–713

Triebold S, von Eynatten H, Luvizotto GL, Zack T (2007) Deducing source rock lithology from detrital rutile geochemistry: An example from the Erzgebirge, Germany. *Chemical Geology* 244: 421–436

Vavra G, Schaltegger U (1999) Post-granulite facies monazite growth and rejuvenation during Per-

mian to Lower Jurassic thermal and fluid events in the Ivrea Zone (Southern Alps). *Contributions to Mineralogy and Petrology* 134: 405–414

Vavra G, Gebauer D, Schmid R, Compston W (1996) Multiple zircon growth and recrystallization during polyphase Late Carboniferous to Triassic metamorphism in granulites of the Ivrea Zone (Southern Alps): An ion microprobe (SHRIMP) study. *Contributions to Mineralogy and Petrology* 122: 337–358

Vry JK, Baker JA (2006) LA-MC-ICPMS Pb-Pb dating of rutile from slowly cooled granulites: Confirmation of the high closure temperature for Pb diffusion in rutile. *Geochimica et Cosmochimica Acta* 70: 1807–1820

Wark DA, Watson EB (2006) TitaniQ: a titanium-in-quartz geothermometer. *Contributions to Mineralogy and Petrology* 152: 743–754

Watson EB, Wark DA, Thomas JB (2006) Crystallization thermometers for zircon and rutile. *Contributions to Mineralogy and Petrology* 151: 413–433

White RW, Powell R, Holland TJB (2007) Progress relating to calculation of partial melting equilibria for metapelites. *Journal of Metamorphic Geology* 25: 511–527

Zack T, Luvizotto GL (2006) Application of rutile thermometry to eclogites. *Mineralogy and Petrology* 88: 69–85

Zack T, Kronz A, Foley SF, Rivers T (2002) Trace element abundances in rutiles from eclogites and associated garnet mica schists. *Chemical Geology* 184: 97–122

Zack T, von Eynatten H, Kronz A (2004a) Rutile geochemistry and its potential use in quantitative provenance studies. *Sedimentary Geology* 171: 37–58

Zack T, Moraes R, Kronz A (2004b) Temperature dependence of Zr in rutile: empirical calibration of a rutile thermometer. *Contributions to Mineralogy and Petrology* 148: 471–488

Zingg A (1980) Regional metamorphism in the Ivrea Zone (Southern Alps, N-Italy): Field and microscopic investiggations. *Schweizerische Mineralogische und Petrographische Mitteilungen* 60: 153–179

Zingg A (1983) The Ivrea and Strona-Ceneri zones (Southern Alps, Ticino and N, Italy) - a review. *Schweizerische Mineralogische und Petrographische Mitteilungen* 63: 361–392

Zingg A, Handy MR, Hunziker JC, Schmid SM (1990) Tectonometamorphic history of the Ivrea Zone and its relationship to the crustal evolution of the Southern Alps. *Tectonophysics* 182: 169–192

4 Rutile occurrence and trace element behavior in low- to medium-grade metasedimentary rocks

G. L. Luvizotto, T. Zack., S. Triebold, H. von Eynatten

Manuscript submitted to Mineralogy and Petrology

Abstract

Metamorphic textures in low- to medium-grade ($\sim$500-550°C) metasedimentary rocks from the Erzgebirge give evidence for prograde rutile growth from ilmenite. Newly formed grains occur as rutile-rich polycrystalline aggregates that mimic the shape of the ilmenites. *In-situ* trace element data (EMP and SIMS) show that rutiles from the lowest grade samples ($\sim$480°C) mirror the Nb/Ti ratio of ilmenite. Under these conditions, rutile did not equilibrate chemically with the remaining ilmenites. In higher grade samples, rutiles show a larger scatter in Nb and have Nb/Ti ratios higher than ilmenite. This behavior can be modeled using prograde rutile growth from ilmenite and indicates that rutiles are reequilibrating with remaining ilmenites. Newly formed rutiles yield temperatures (from $\sim$500 to 630°C, Zr-in-rutile thermometry) that are in agreement with the metamorphic conditions published for the studied rocks. Detrital rutile grains, identified by their distinct chemical composition (high Zr and Nb contents) and textures (single grains surrounded by fine grained ilmenites), occur in quartzites from the medium-grade rocks ($\sim$530°C). Preliminary calculations based on the grain size distribution of rutiles in the studied rocks show that quartzites are probably the main source of rutiles in sediments derived from low-grade metamorphic sequences, even if the occurrence of quartzite is minor.

Keywords: *accessory phases, rutile, ilmenite, geochemistry, provenance studies*

4.1 Introduction

Rutile is one of the major Ti-phases and frequently occurs as an accessory mineral in diverse metamorphic and igneous rocks, siliciclastic sediments, placer deposits and hydrothermal ore deposits. It is an important carrier of several highly-charged trace elements (*e.g.*, Ti, Zr, Nb, Ta, Sn, Sb, W, V, Cr and Mo, Graham & Morris, 1973; Haggerty, 1991; Deer *et al.*, 1992; Smith & Persil, 1997; Rice *et al.*, 1998; Zack *et al.*, 2002) and therefore has attracted significant attention in studies focused on subduction zone processes, particularly as a likely controller of Nb and Ta budgets (Saunders *et al.*, 1980; McDonough, 1991; Brenan *et al.*, 1994; Stalder *et al.*, 1998; Münker, 1998; Foley *et al.*, 2000; Rudnick *et al.*, 2000; Klemme *et al.*, 2005, among others). Recently, the calibration of the Zr-in-rutile thermometer for quartz and zircon bearing rocks (Zack *et al.*, 2004b; Watson *et al.*, 2006; Tomkins *et al.*, 2007) has broadened the application of rutile, which is becoming an important tool for assessing metamorphic temperatures, especially in eclogite and granulite facies rocks (Zack & Luvizotto, 2006; Spear *et al.*, 2006; Harley, 2008; Luvizotto & Zack, in press). Rutile is also becoming an important tool in sediment provenance studies where its Nb and Cr composition can be used to assess the nature of the initial source rock (*i.e.*, pelitic vs mafic, Zack *et al.*, 2004a; Stendal *et al.*, 2006; Triebold *et al.*, 2007; Meinhold *et al.*, 2008). In addition, as pelitic rocks are always quartz and zircon bearing , the Zr-in-rutile thermometer can be applied to detrital rutiles derived from these rocks. It is generally accepted that rutile is not stable under low-grade metamorphic conditions (see, *e.g.*, Force, 1980; Zack *et al.*, 2004a), breaking down during greenschist facies metamorphic overprints. However, the exact boundary is not well understood (see, *e.g.*, Stendal *et al.*, 2006; Triebold *et al.*, 2007; Meinhold *et al.*, 2008). Still, this instability at greenschist-facies conditions makes rutile an important tool in sediment provenance studies as, unlike zircon, it records only the latest metamorphic cycle. In this sense, understanding rutile formation and/or breakdown in metamorphic rocks is an important issue.

In the German Erzgebirge detrital rutiles from recent sediments from this area have been studied in an accompanying paper by Triebold *et al.* (2007). One impor-

tant result is that several detrital rutiles derived from the low-grade units still record high temperatures (up to 1000 °C) from a former metamorphic cycle.

In order to shed more light on the occurrence of such rutiles in low grade metamorphic rocks, this study focuses on the transition from low- to high-grade rocks in the Erzgebirge. We present textures that indicate rutile growth from ilmenite in low- to medium-grade metapelitic rocks and discuss the trace element partitioning between these minerals. We also discuss the temperature records in rutiles from these rocks. To conclude, we briefly explore the influence of the source rock (*i.e.*, fine grained, metapelitic, vs. coarser grained, psammitic rocks) in the sedimentary record of rutile, highlighting some relevant aspects for sediment provenance studies.

4.2 Geological setting and studied samples

The Erzgebirge is located in eastern Germany, at the border to the Czech Republic. Geologically, it is situated at the northwestern border of the Bohemian Massif and is part of the metamorphic basement of the Mid-European Variscides (Fig. 4.1). It is characterized by a large-scale antiformal structure consisting of several tectonometamorphic units.

Currently it is accepted that the Erzgebirge represents a stack of five tectonometamorphic units with contrasting *P-T* histories (Willner *et al.*, 1997; Rötzler *et al.*, 1998). From the base to the top these units are: Red and Grey Gneisses (RGG); Gneiss/Eclogite Unit (GEU); Micaschist/Eclogite Unit (MEU); Garnet-Phyllite Unit (GPU); and Phyllite Unit (PU). The tectonometamorphic stacking is interpreted as a result of continent-continent collision processes during the Variscan Orogeny (*e.g.*, Willner *et al.*, 1997; Rötzler *et al.*, 1998; Mingram, 1998). A summary of published *PT* conditions for the western part of the Erzgebirge is presented in Fig. 4.1. Geochemical discriminations suggest that the protoliths of all metamorphic units are similar, leading to the conclusion that they represent a repetition of metasedimentary sequences (Mingram, 1998).

The present study focuses on the western part of the Erzgebirge, more specifically on metasedimentary rocks from the GPU and MEU. Metassediments from the

GPU are characterized by the occurrence of limestones, graphite phyllites, garnet- and albite-bearing phyllites, feldspar-free, chloritoid-bearing phyllites, quartzites and metatuffites, with garnet-free phyllites as the most common rock type. Metassediments from the MEU are characterized by the occurrence of graphite mica schists, albite-bearing mica schists, feldspar-free, chloritoid-bearing mica schists, paragneisses and marbles. Garnet- and cloritoid-bearing schists are the most common rock type. Metassediments from the GEU are distinguished by the occurrence of feldspar-bearing mica schists, feldspar-free, kyanite-bearing mica schists and migmatitic paragneisses (Willner *et al.*, 1997; Rötzler *et al.*, 1998; Mingram, 1998).
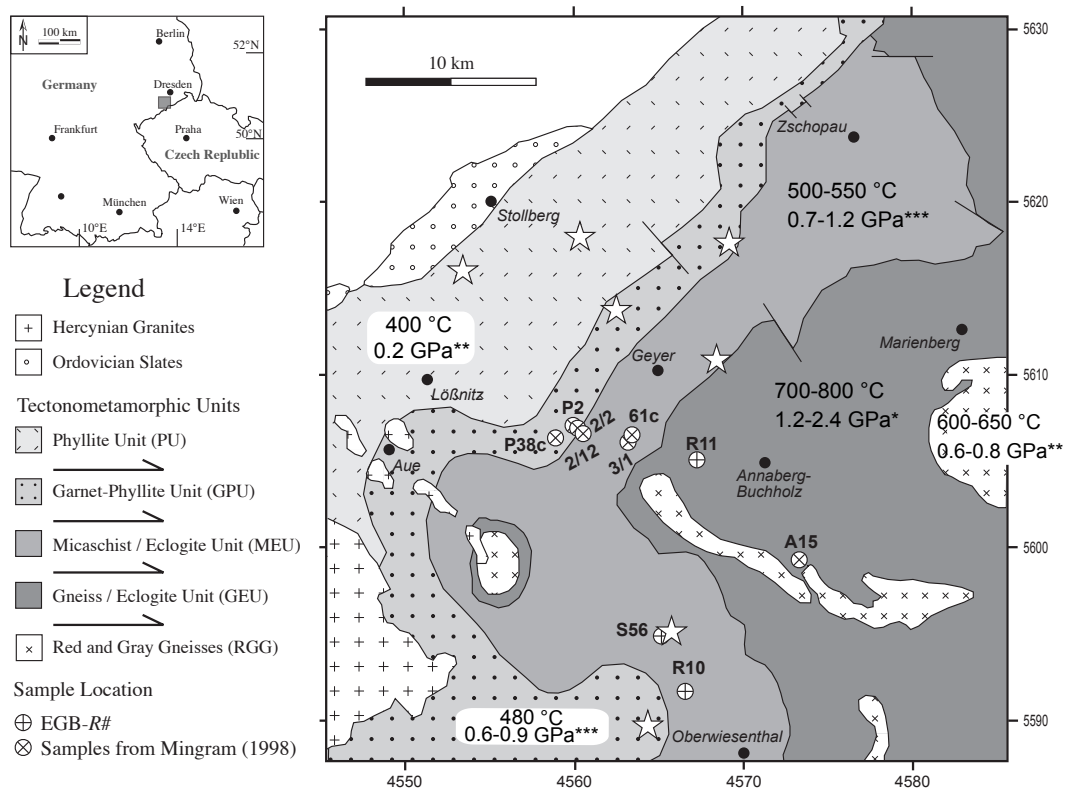
Figure 4.1 Simplified geological map of the western part of the Erzgebirge. Coordinates are provided in German coordinate system (Gauss-Krüger). *PT* conditions from: *Willner *et al.* (1997), **Mingram & Rötzler (1999) and ***Rötzler *et al.* (1998). Stars represent areas where relic rutiles (Zr-in-rutile temperatures strongly exceeding unit temperatures) were found by Triebold *et al.* (2007).

Key information about the studied samples are presented in Tab. 4.1. Seven of the studied samples have been investigated by Mingram (1996, see Tab. 4.1). Sample EGB04-S56 corresponds to the quartzite sample presented in Triebold *et al.* (2007).

Table 4.1 Summarized description of the studied samples. Modal proportions are based on visual inspection with a petrographic microscope and BSE images.

Sample	Coordinates E	N	Unit	Rock Type	Kfs	Pl	Grt	Bt	Cld	Chl	Ms	Qtz	Ilm	Other Phases (<1%)
P38c[a]	4559100	5606200	GPU	Phyllite	-	-	-	-	-	x	x	xx	1-2%	Rt, Ant, Zrn, Ap, Mnz
P2[a]	4559800	5606750	GPU	Phyllite	-	-	-	-	-	xx	xx	xx	1-2%	Rt, Ant, Zrn, Ap, Mnz
2/2[a,b]	4560902	5606520	GPU	Grt-phyllite	-	-	<1%	-	-	x	xx	xx		Rt, Ant, Ilm, Zrn, Ap, Mnz
2/12[a,b]	4560902	5606520	GPU/ MEU	Grt micaschist	-	-	I	-	I	x	xx	xx		Rt, Ant, Ilm, Zrn, Ap, Mnz
3/1[a,b]	4563150	5606432	MEU	Grt-Cld micashist	-	-	x	-	I	I	xx	xx		Rt, Ant, Ilm, Zrn, Ap, Mnz
61c[a]	4563250	5606500	MEU	Grt-Cld micashist	-	-	I	-	I	I	xx	xx		Rt, Ant, Ilm, Zrn, Ap, Mnz
EGB04-S56	4565203	5594976	MEU	Ms quartzite	-	I	-	-	-	-	x	xx		Rt, Ant, Ilm, Zrn, Ap, Mnz
EGB04-R10d	4566669	5591770	MEU	Grt-Cld micashist	-	-	x	-	I	I	xx	xx		Rt, Ant, Ilm, Zrn, Ap, Mnz
EGB04-R11e	4567403	5605187	GEU	Grt-Bt gneiss	I	xx	I	x	-		x	xx		Rt, Zrn, Ap, Mnz
A15c[a]	4573660	5599650	GEU	Grt micaschist	-	-	I	I	-	-	xx	xx		Rt, Ant, Zrn, Ap, Mnz

Modal proportion: I - 1 to 10%, x - 10 to 20%, xx >20% (mineral abreviations after Kretz, 1983). Coordinates are provided in German coordinate system (Gauss-Krüger).
[a] - samples from Mingram (1996)
[b] - coordinates correspond to the location of the borehole (depths: 2/2 - 100m, 2/12 - 338m, 3/1 - 19m)

4.3 Analytical techniques

4.3.1 Electron Microprobe (EMP)

Electron microprobe analyses of rutile and ilmenite were carried out at the Mineralogisches Institut, Universität Heidelberg with a CAMECA SX51 equipped with 5 WDS detectors. The beam was set to 20 kV and 100 nA and analyses followed the method outlined by Luvizotto *et al.* (in press). The following elements were analyzed: Si, Ti, V, Cr, Fe, Zr, Nb and W. With this setup, the detection limits are 220 ppm for V, 50 ppm for Cr, 40 ppm for Fe and Zr, 60 ppm for Nb and

350 ppm for W. To assure "true" zero-concentration peak intensities and to exclude any machine drift, every ten analyses of unknowns were bracketed by two analyses of synthetic rutile (nominally zero-concentration trace elements). Si concentrations were used as a quality control in order to detect and avoid contamination associated with submicroscopic zircon inclusions (according to the method outlined by Zack *et al.*, 2004b). Rutile measurements with apparent Si concentrations higher than 300 ppm that showed abnormally high Zr contents were excluded from the data set. Measurements with Si content above 300 ppm and Zr concentrations similar to rutiles with low Si contents were included for small (20-30μm) rutile grains (high Si values were interpreted to be related to the nearby silicates). The same quality controls are applied to SIMS analyses. Although the EMP beam diameter was set to 5μm, the minimum grain size for obtaining reliable analyses was ~ 20 μm.

4.3.2 Secondary Ion Mass Spectrometry (SIMS)

SIMS measurements of rutile and ilmenite were performed at the Mineralogisches Institut, Universität Heidelberg with a CAMECA ims 3f. Analyses were carried out using a 14.5 keV / 10-20 nA ^{16}O$^-$ primary ion beam, which resulted in spot sizes of 20-30 μm. By using a field aperture the effective spot size was reduced to 12 μm, leading to the smallest analyzable grain sizes of 20-30μm. Positive secondary ions were nominally accelerated to 4.5 keV (energy window set to ± 20 eV) and the energy filtering technique was used with an offset of 90 eV at mass resolution m/δm (10%) of 370. Count rates were normalized to ^{47}Ti. TiO$_2$ in rutile is assumed to be 100 wt%. In ilmenite, the Ti concentration was based on the values obtained by EMP. The following isotopes were analyzed: ^{27}Al, ^{30}Si, ^{47}Ti, ^{90}Zr, ^{93}Nb, ^{118}Sn, ^{120}Sn, ^{121}Sb, ^{123}Sb, ^{178}Hf, ^{181}Ta, ^{184}W, ^{186}W, ^{232}Th, ^{238}U. Concentrations were calculated based on relative sensitivity factors (RSF) as outlined in Luvizotto *et al.* (in press). Although no reliable RSF can be calculated for Th, the intensity ratios obtained for the studied rutiles suggest that Th concentrations are extremely low (below the 0.1 ppm level when using RSF from U).

4.3.3 Micro-Raman Spetroscopy

Laser micro-Raman spectroscopy was applied to selected grains in order to identify the TiO_2 structure type. Raman spectra were obtained using a Horiba Jobin Yvon Labram HR-UV 800 (equipped with a Peltier-cooled CCD detector) at the Geowissenschaftliches Zentrum, Universität Göttingen. Analyzes were carried out using 633 nm laser excitation, 17 mW laser power and 1200 l/mm grating.

4.4 Results

4.4.1 Textural evidence of rutile growth in low- to medium-grade metapelitic rocks

In the low-grade metapelitic rocks from the GPU rutile starts to grow from ilmenite. As the content of Ti is higher in rutile than in ilmenite, the volume once filled up by ilmenite is not completely occupied by rutile. Moreover, most of the Fe from ilmenite is used, together with the elements available in matrix minerals (silicates), to form chlorite. The simplified reaction can be written as (mineral abreviations after Kretz, 1983): Ilm + silicates + H_2O → Rt + Chl. Rutiles occur as polycrystalline aggregates, which are characterized by a fine grained intergrowth of rutile and chlorite that mimic the shape of ilmenite. The same type of textures, although in more developed stages, can still be found in some metasedimentary rocks from the MEU. The BSE images presented in Fig. 4.2 are examples of the textures described above. The images are arranged according to increasing rutile/ilmenite ratio, interpreted to represent the evolution of the texture. In Figs. 4.2a and 4.2b only minor amounts of rutile are present and ilmenite grains still preserve their euhedral/subhedral elongated (lath) habit. Figs. 4.2c to 4.2f show more evolved stages of the texture. Notice that two grains (the large polycrystalline rutile aggregate at the center and the ilmenite grain at the top right of the image) that represent distinct evolutional stages of the reaction occur in a micrometric scale. This gives an indication about the reaction domain. In Figs. 4.2g and 4.2h ilmenite is virtually absent. However, rutile still occur as aggregates that have the elongated shape inherited from ilmenite. Rutiles

are often present as inclusion in garnet bearing rocks from the MEU (Fig. 4.2h). The texture presented in Fig. 4.2d derives from a quartzite (EGB04-S56). Although this sample comes from the MEU it still preserves textures usually observed in rocks from the GPU. This fact supports the theory that quartzites are less reactive when compared with pelitic rocks (see also discussion in Triebold *et al.*, 2007).

Metapelitic rocks from the GEU are ilmenite free demonstrating that the rutile forming reaction was completed. In these rocks rutiles show no traces of the texture described above and have rounded shape (Fig. 4.3). Although rutile is the main Ti carrier in these rocks, part of the Ti is also accommodated in biotite and phengite, with Ti incorporation in these minerals being temperature dependent (see, *e.g.*, Douce, 1993; Henry & Guidotti, 2002; Henry *et al.*, 2005; Hermann & Spandler, 2008).

4.4.2 Identification of TiO_2 polymorphs

TiO_2 polymorphs were identified by different methods. A group of samples containing Ti-oxide crystals with distinct characteristics (such as color and shape under petrographic microscope and/or BSE images) were selected for Raman spectroscopy analyses. Rutile was identified by Raman bands at 147, 242, 449 and 614 cm^{-1} (for a compilation of Raman bands for Ti polymorphs see Meinhold *et al.*, 2008) and anatase was identified by Raman bands at 146, 199, 400, 517 and 642 cm^{-1} (Fig. 4.4). Brookite was not present in the studied samples. In the investigated rocks rutile is brownish/reddish under the optical microscope (transmitted light) while anatases is light-colored to colorless. Some Ti-oxides displayed cathodoluminescence (CL) emission during EMP measurements (a bright spot when the mineral was under the focused electron beam). All of these grains were identified as anatase by Raman spectroscopy. Therefore this characteristic was also used as an

---

Figure 4.2 *(following page)* BSE images exemplifying the textures observed in metasedimentary rocks from the GPU and MEU. The images are arranged in such a way that they represent the evolution of the texture though the rocks and units. Numbers given in the figures correspond to Nb concentrations (in ppm) and Nb/Ti ratios. All scale bars represent 100μm. See text for further information. Samples: A, B and E - P38c; C and F - P2; D - EGB04-S56; G - 2/2; H - 2/12.
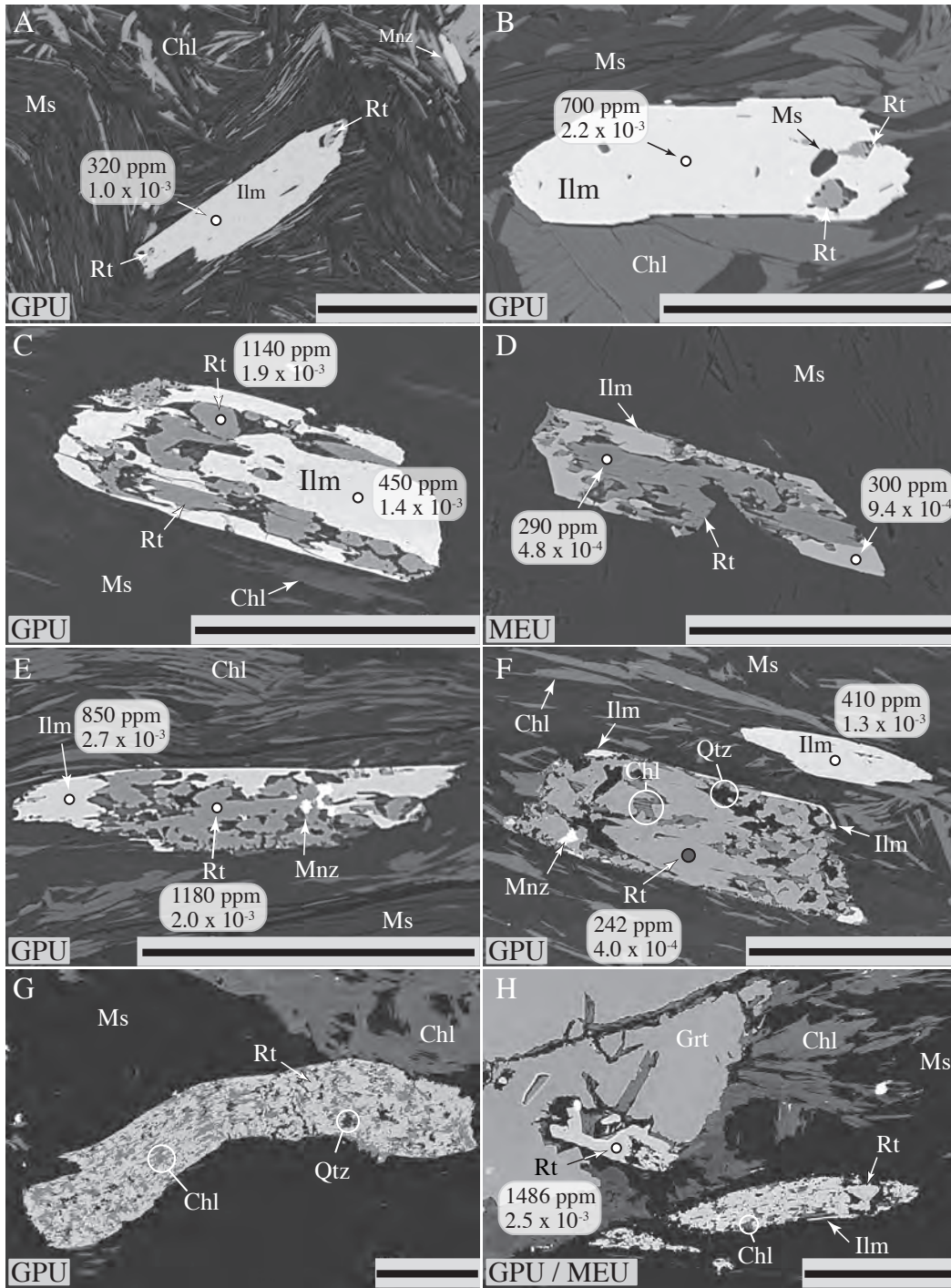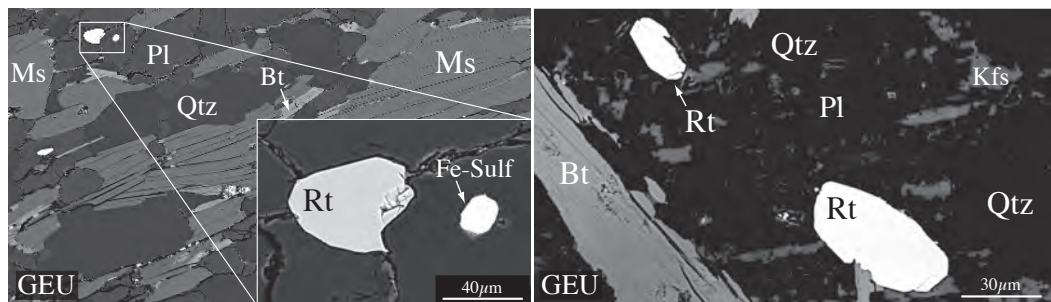
Figure 4.3 BSE images exemplifying rutiles occurring in metasedimentary rocks from the GEU. Fe-Sulf — Fe sulfide.

identification method. Detailed BSE imaging carried out in grains previously analyzed by Raman shows that rutile is brighter than anatase (Fig. 4.4). This feature was also used to differentiate between the two polymorphs.

The current work focuses only on the textural and chemical relationships between rutile and ilmenite. A more detailed work about identification and chemical composition of TiO_2 polymorphs in Erzgebirge rocks and recent sediments can be found in Triebold *et al.* (in prep.).

4.4.3 Niobium concentrations in rutile and ilmenite

Fig. 4.5 summarizes Nb concentrations obtained for rutiles and ilmenites (for a complete data set please refer to Appendix B). Nb concentrations in ilmenite are rather constant when compared to those in rutile, with average concentration of ∼500 ppm in ilmenite in almost all samples. Nb concentrations in rutile are characterized by three distinct patterns. In samples from the GPU rutiles show small spread in Nb content. Moreover, their Nb/Ti ratios are comparable with values obtained for ilmenites from the same samples. Rutiles from the MEU display a larger spread in Nb concentrations with Nb/Ti ratios spanning from values as low as the ones obtained for the ilmenites to values significantly higher. Rutiles from the GEU show a narrow spread in Nb concentration. These samples are ilmenite free and therefore no direct comparison can be made. However, when compared with results obtained for ilmenites from other units, the Nb/Ti ratios in rutiles from the GEU are slightly
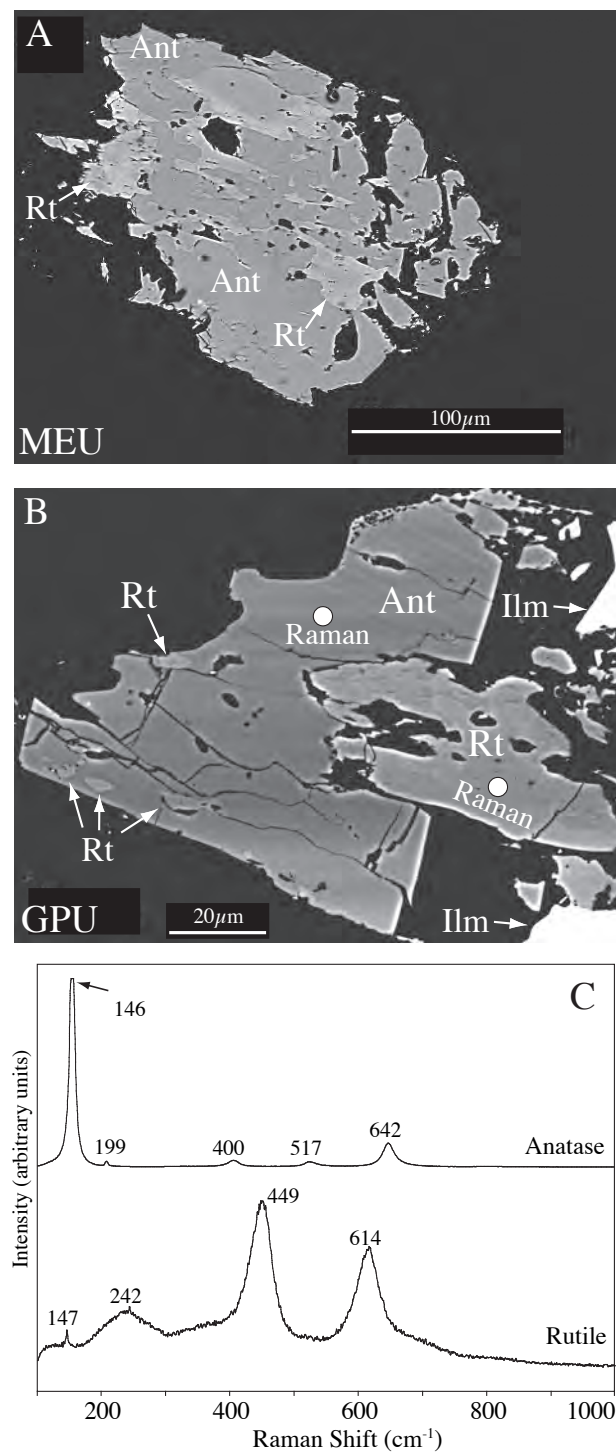
Figure 4.4 A and B: High-contrast BSE images showing rutile coexisting with anatase. Notice that rutile has brighter colors. C: Raman spectra of anatase and rutile (spot location presented in B).

higher. This is probably due to the presence of Ti-bearing micas (phengite and biotite) in these rocks. Therefore, in these samples rutile does not mirror the Nb/Ti ratio of the whole rock (WR).
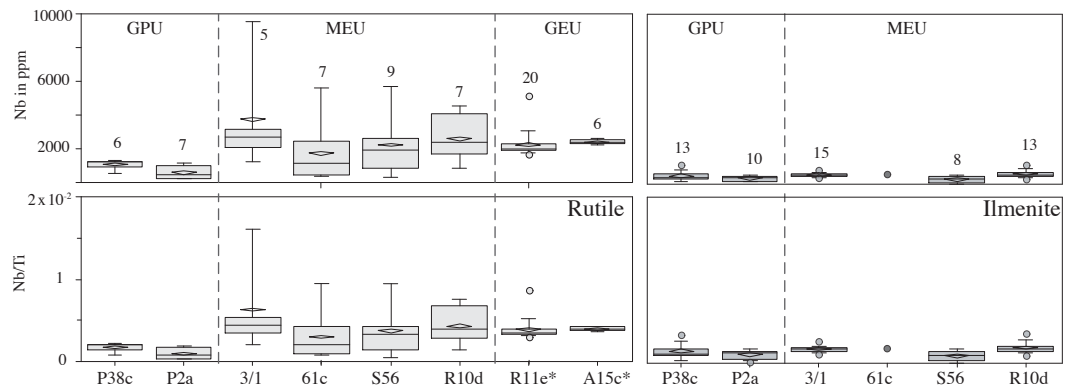
Figure 4.5 Summary of Nb concentrations (EMP and SIMS) obtained for the rutiles and ilmenites. Samples are sorted according to increasing metamorphic grade. The boxes represent, from bottom to top, the second and third quartile (25 and 75% of the population). The bar inside the box represents the median, while the lozenge represents the average. Whiskers represent the 10th and the 90th percentile. Outliers, when they occur, are represented by small circles. Numbers on top of the whiskers represent the number of analyzed grains (one spot per grain). As EMP and SIMS results are within error, for grains analyzed by both techniques only EMP data is plotted (better spacial resolution). *ilmenite-free samples.

4.4.4 Zirconium concentrations in rutile

Zr concentrations obtained for the studied rutiles are presented in Tab. 4.2. Temperatures were calculated based on the Zr-in-rutile thermometer, using the calibration of Tomkins *et al.* (2007). Calculations were based on the pressure values presented in Fig. 4.1.

Zr contents in all rutiles from the GPU are below the EMP detection limit (40 ppm, $\sim$500°C) and are in accordance with estimates based on *PT* conditions (<500°C, 0.6-0.9 GPa) reported for this unit (also valid for one SIMS analysis of 46 ppm obtained for sample P2). Several rutiles from the MEU (15 out of 28) have Zr contents below the EMP detection limit. Still, some grains have higher Zr contents

(60-80 ppm), which is confirmed by EMP as well as by SIMS. These results are in agreement with concentrations estimated from the metamorphic conditions known for this area (500-550°C, 0.7-12. GPa), especially taking pressure into consideration. The only exception is one rutile grain with Zr concentration of 390 ppm from the quartzite sample (EGB04-S56). Analyses of rutiles from the GPU and the MEU often give high Si signals. In these units rutiles occur as polycrystalline aggregates (see Fig. 4.2) and are difficult to measure by the techniques applied in this work. High Si values are interpreted to be related to the nearby silicates (measurements with high Si and high Zr contents were excluded from the data set).

Only few rutiles from the higher grade samples (EGB04-R11e, A15c) have Zr contents below the EMP detection limit. Here again, Zr contents obtained by SIMS and EMP are in agreement with mineral assemblage and metamorphic textures observed in these rocks (with Zr concentrations up to 200 ppm for sample A15, corresponding to temperatures of ca. 630°C).

It is noteworthy that highest Zr content in rutiles from garnet bearing rocks are usually obtained for rutiles included in garnet (see also Fig. 7 in Triebold *et al.*, 2007).

4.5 Discussion

4.5.1 Rutile formation from ilmenite and expected Nb behavior

Textures observed in the investigated samples support prograde rutile crystallization associated with the breakdown of ilmenite in low- to medium grade metapelitic rocks. These samples give us the opportunity to assess crystallization conditions of rutile and to investigate the partitioning of trace elements between rutile and ilmenite. With the strong difference in Nb partitioning between rutile and ilmenite, we investigate in this section how the observed Nb systematics in rutile can be correlated with ilmenite breakdown.

In the studied rocks, rutile's formation is simplified by the conceptual model presented in Fig. 4.6. Initially, only ilmenite is present and hosts the Nb and Ti contents of the WR. Under metamorphic conditions analogues to those of the

Table 4.2 Zirconium concentrations obtained for the studied rutiles.

Sample	Technique	Rock Type	Unit	Grain	Txt.	Si[a]	Zr	T°C[b]
P2	EMP	Phyllite	GPU	Rt1	M	1140	bd	<500
P2	EMP	Phyllite	GPU	Rt2	M	580	bd	<500
P2	EMP	Phyllite	GPU	Rt3	M	1310	bd	<500
P2	EMP	Phyllite	GPU	Rt4	M	4060	bd	<500
P2	EMP	Phyllite	GPU	Rt5	M	2370	bd	<500
P2	EMP	Phyllite	GPU	Rt6	M	3180	bd	<500
P2	EMP	Phyllite	GPU	Rt7	M	630	bd	<500
P2	EMP	Phyllite	GPU	Rt9	M	99	bd	<510
P2	SIMS	Phyllite	GPU	Rt8	M	7947	46	516
P38c	EMP	Phyllite	GPU	Rt1	M	190	bd	<510
P38c	EMP	Phyllite	GPU	Rt3	M	170	bd	<510
P38c	EMP	Phyllite	GPU	Rt6	M	1160	bd	<510
P38c	EMP	Phyllite	GPU	Rt7	M	51	bd	<510
P38c	EMP	Phyllite	GPU	Rt8	M	536	bd	<510
P38c	EMP	Phyllite	GPU	Rt9	M	474	46	516
2/12	EMP	Grt Schist	GPU	Rt1	I	57	bd	<510
2/12	EMP	Grt Schist	GPU	Rt2	I	306	bd	<510
3/1	EMP	Grt-Cld Schist	MEU	Rt1	I	116	42	522
3/1	EMP	Grt-Cld Schist	MEU	Rt2	I	120	bd	<520
3/1	EMP	Grt-Cld Schist	MEU	Rt3	I	87	bd	<520
3/1	EMP	Grt-Cld Schist	MEU	Rt4	I	37	bd	<520
3/1	EMP	Grt-Cld Schist	MEU	Rt5	I	97	bd	<520
3/1	EMP	Grt-Cld Schist	MEU	Rt6	I	41	bd	<520
3/1	EMP	Grt-Cld Schist	MEU	Rt8	I	80	46	528
3/1	SIMS	Grt-Cld Schist	MEU	Rt3	I	34707	28	499
3/1	SIMS	Grt-Cld Schist	MEU	Rt4	I	948	23	489
3/1	SIMS	Grt-Cld Schist	MEU	Rt9	I	3556	25	493
3/1	SIMS	Grt-Cld Schist	MEU	Rt10	I	4576	87	567
61c	EMP	Grt-Cld Schist	MEU	Rt3	I	140	bd	<520
61c	EMP	Grt-Cld Schist	MEU	Rt4	I	50	bd	<520
61c	EMP	Grt-Cld Schist	MEU	Rt6	I	50	50	533
61c	EMP	Grt-Cld Schist	MEU	Rt7	I	60	70	554
61c	EMP	Grt-Cld Schist	MEU	Rt10	I	-	62	546
61c	EMP	Grt-Cld Schist	MEU	Rt11	I	64	80	562
61c	EMP	Grt-Cld Schist	MEU	Rt12	I	16	77	559
EGB04-R10d	EMP	Grt-Cld Schist	MEU	Rt3	I	40	bd	<520
EGB04-R10d	EMP	Grt-Cld Schist	MEU	Rt4	I	90	bd	<520
EGB04-R10d	EMP	Grt-Cld Schist	MEU	Rt5	I	70	50	533
EGB04-R10d	EMP	Grt-Cld Schist	MEU	Rt6	I	150	bd	<520
EGB04-R10d	EMP	Grt-Cld Schist	MEU	Rt7	M	470	bd	<520
EGB04-R10d	SIMS	Grt-Cld Schist	MEU	Rt1	M	-	32	507
EGB04-R10d	SIMS	Grt-Cld Schist	MEU	Rt2	M	-	31	504
EGB04-S56	EMP	Quartzite	MEU	Rt1	M	240	50	533
EGB04-S56	EMP	Quartzite	MEU	Rt2	M	420	bd	<520
EGB04-S56	EMP	Quartzite	MEU	Rt3	M	60	60	544
EGB04-S56	EMP	Quartzite	MEU	Rt4	M	120	50	533
EGB04-S56	EMP	Quartzite	MEU	Rt5	M	90	**390**	**680**
EGB04-S56	EMP	Quartzite	MEU	Rt6	M	120	bd	<520
EGB04-S56	EMP	Quartzite	MEU	Rt7	M	110	bd	<520
EGB04-S56	EMP	Quartzite	MEU	Rt8	M	90	bd	<520
EGB04-S56	EMP	Quartzite	MEU	Rt9	M	100	60	544
EGB04-R11e	EMP	Grt-Bt Gneiss	GEU	Rt1	M	50	140	600
EGB04-R11e	EMP	Grt-Bt Gneiss	GEU	Rt2	M	20	50	533
EGB04-R11e	EMP	Grt-Bt Gneiss	GEU	Rt3	M	60	bd	<520
EGB04-R11e	EMP	Grt-Bt Gneiss	GEU	Rt4	M	40	70	554
EGB04-R11e	EMP	Grt-Bt Gneiss	GEU	Rt5	M	40	bd	<520
EGB04-R11e	EMP	Grt-Bt Gneiss	GEU	Rt6	M	130	80	562
EGB04-R11e	EMP	Grt-Bt Gneiss	GEU	Rt7	M	180	bd	<520
EGB04-R11e	EMP	Grt-Bt Gneiss	GEU	Rt8	M	100	70	554
EGB04-R11e	EMP	Grt-Bt Gneiss	GEU	Rt9	M	140	60	544
EGB04-R11e	EMP	Grt-Bt Gneiss	GEU	Rt10	M	280	bd	<520
EGB04-R11e	EMP	Grt-Bt Gneiss	GEU	Rt11	M	410	50	533
EGB04-R11e	EMP	Grt-Bt Gneiss	GEU	Rt12	M	510	bd	<520
EGB04-R11e	EMP	Grt-Bt Gneiss	GEU	Rt13	M	130	80	562
EGB04-R11e	EMP	Grt-Bt Gneiss	GEU	Rt14	M	180	bd	<520
EGB04-R11e	SIMS	Grt-Bt Gneiss	GEU	Rt15	M	-	88	568
EGB04-R11e	SIMS	Grt-Bt Gneiss	GEU	Rt16	M	511	53	536
EGB04-R11e	SIMS	Grt-Bt Gneiss	GEU	Rt17	M	1675	71	554
EGB04-R11e	SIMS	Grt-Bt Gneiss	GEU	Rt18	M	3	79	561
EGB04-R11e	SIMS	Grt-Bt Gneiss	GEU	Rt20	I	19	94	573
A15c	EMP	Grt Schist	GEU	Rt1	M	21	117	587
A15c	EMP	Grt Schist	GEU	Rt1	M	36	115	587
A15c	EMP	Grt Schist	GEU	Rt2	I	-	58	542
A15c	EMP	Grt Schist	GEU	Rt3	I	-	148	604
A15c	EMP	Grt Schist	GEU	Rt4	I	144	120	590
A15c	EMP	Grt Schist	GEU	Rt5	M	31	105	580
A15c	EMP	Grt Schist	GEU	Rt6	I	172	201	627
A15c	SIMS	Grt Schist	GEU	Rt1	M	-	103	579
A15c	SIMS	Grt Schist	GEU	Rt5	M	-	151	606

Text. - textural relationship: matriz (M), inlcuded in garnet (I). [a] apparent Si content used as quality control (analyses with high Si and Zr were excluded from the data set). [b] calculated after Tomkins et al. (2007) using pressure values presented in Fig. 4.1.

GPU (~480°C, 0.6-0.9 GPa) rutile starts to grow associated with the breakdown of ilmenite. With increasing metamorphic grade, the reaction evolves and the rutile/ilmenite ratio increases. In these intermediate stages rutiles occur as polycrystalline aggregates that have the shape of ilmenite. Nb is distributed between both phases. The excess Fe is used to crystallize chlorite, with other elements available in the surrounding silicates. At higher metamorphic grade rutile is the only Ti-phase. At this stage, rutile has its own shape (by dynamic recrystallization) and is the main carrier of Nb and Ti. Rutile may mirror the WR Nb/Ti ratio in rocks where Ti-rich micas (biotite and phengite) are minor to absent.

Stages

	Initial	Early	Intermediate	Final
	Only Ilm	Rt + Ilm	Rt + Ilm	Only Rt
Units $\longrightarrow$		GPU	MEU	GEU

Ilm is the main Nb and Ti carrier

Chemical diffusion of Ti and Nb
Increasing metamorphic grade

Rt is the main Nb and Ti carrier
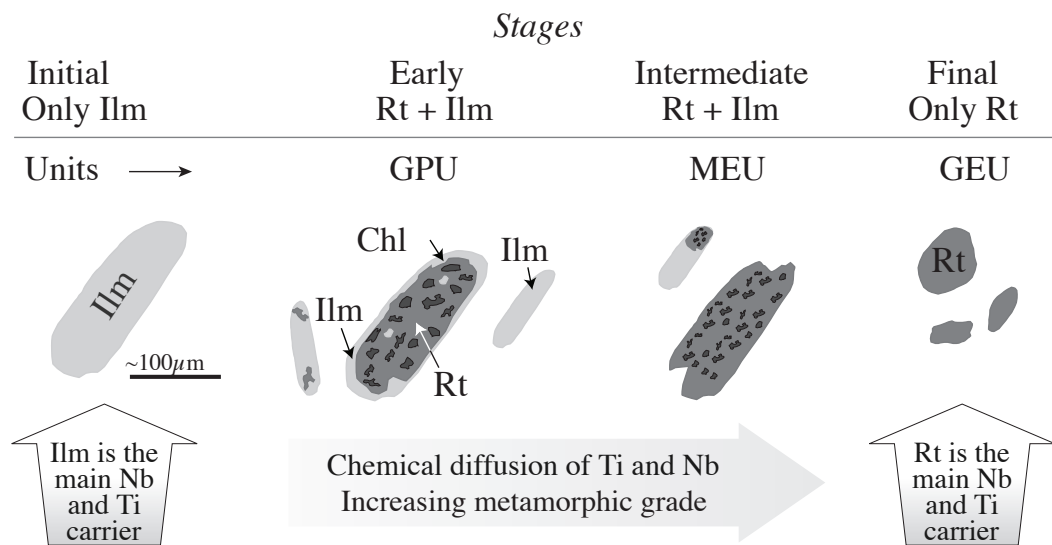
Figure 4.6 Illustration showing the main stages during prograde rutile crystallization from ilmenite.

The exchange coefficient for Nb/Ti between rutile and ilmenite ($K_{DNb/Ti}^{Rt/Ilm}$, following the terminology of Beattie *et al.*, 1993) can be used to evaluate the behavior of Nb through the steps described above. Klemme *et al.* (2005) and Klemme *et al.* (2006) have recently presented experimentally derived rutile/melt and ilmenite/melt partition coefficients for several elements, including Nb. The results confirm previously obtained data (*e.g.*, Green & Pearson, 1987; Foley *et al.*, 2000; Green,

2000; Horng & Hess, 2000; Schmidt *et al.*, 2004) and show that Nb is strongly compatible in rutile ($D_{Nb}^{Rt/melt}$ = 22 for andesitic melt composition) and moderately compatible to incompatible in ilmenite ($D_{Nb}^{Ilm/melt}$ = 0.88 − 1.9 for basaltic and D_{Nb}^{Ilm} = 0.55 for basaltic andesite melt compositions). With the data presented above a $K_{DNb/Ti}^{Rt/Ilm}$ value of 49.4 can be calculated (assuming similar partitioning behavior for the andesitic and basaltic andesite melt composition). The data show that rutile strongly favors Nb over Ti when compared with ilmenite. Hence, rutiles occurring in chemical equilibrium with ilmenite are expected to have Nb/Ti ratios significantly higher than the ones in ilmenite. Similar calculations were carried out for rutile and biotite by Luvizotto & Zack (in press). A very similar K_D value was obtained for these minerals ($K_{DNb/Ti}^{Rt/Bt}$ = 48.7) based on the data presented by Klemme *et al.* (2005) and LaTourrette *et al.* (1995). Luvizotto & Zack (in press) quantitatively modeled the Nb behavior in rutile during its continuous crystallization from biotite in granulite-facies. The results show that first rutiles to form have a high Nb content, as Nb is more compatible in rutile than in biotite. Furthermore, the continuous crystallization leads to a high inter-grain spread in Nb concentrations in rutile. Taking into account the similarity between the exchange coefficient and crystallization model presented by Luvizotto & Zack (in press) and the ones presented here, the same behavior is expected to be observed in rutiles crystallizing from ilmenite.

As shown in Fig. 4.5, rutiles from the GPU are characterized by small scatter in Nb content and by Nb/Ti ratios close to the ones obtained for ilmenites from the same unit. These results indicate that rutiles from the GPU are mirroring the Nb/Ti ratio of ilmenite rather than behaving as predicted by the exchange coefficient. However, rutiles from the MEU display higher variations in Nb content and have Nb/Ti ratios significantly higher than ilmenite (up to ∼15 times in sample 3/1). The results suggest that the reaction is evolving towards equilibrium (according to what is predicted from the K_D values). For example, with a $K_{DNb/Ti}^{Rt/Ilm}$ of 49.4, the highest Nb concentration obtained for a rutile from sample 3/1 (9526 ppm) is coherent with a rutile occurring in equilibrium with an ilmenite containing ∼100 ppm of Nb. Interestingly, our results suggest that temperature controls the Nb behavior,

as just rutiles from the MEU (T >500-550°C) tend to behave in agreement with the model successfully applied to granulites. Rutiles from the GEU show small spread in Nb concentrations. These rocks are ilmenite-free, indicating that the rutile forming reaction was completed. This observation suggests homogenization of Nb contents in rutile through mechanisms like dynamic recrystalization and/or intergrain diffusion, which are facilitated by higher temperatures.

4.5.2 Temperature records in rutile from low- to medium-grade metasedimentary rocks

The textures presented above indicate that rutile crystallization took place in metasedimentary rocks from the GPU under *PT* conditions of ∼480°C and 0.6-0.9 GPa. Zr concentrations obtained for rutiles from this unit (Tab. 4.2) confirm previous geothermometric data as all EMP measurements were below detection limit (40 ppm of Zr, ∼500°C). All but one rutile from the MEU rocks give temperatures that match the literature data (500-560°C). Temperatures in the 560-680°C range are obtained for rutiles from the two investigated samples from the GEU and are coherent with the mineral assemblages and metamorphic textures observed in these rocks. Therefore, all metamorphically grown rutiles record temperatures coherent with metamorphic condition under which they were formed.

One of the main findings of Triebold *et al.* (2007) is that no complete reequilibration of formal Zr content in detrital rutiles is reached under prograde metamorphism below 600°C in the Erzgebirge (note that absolute *T* may vary depending on the calibration used, *e.g.*, Zack *et al.*, 2004b; Watson *et al.*, 2006; Tomkins *et al.*, 2007). The existence of an *"equilibration temperature"* was also observed in rutiles from other localities (Stendal *et al.*, 2006; Meinhold *et al.*, 2008). According to Triebold *et al.* (2007), the highest frequency of rutiles with high Zr contents is recorded in detrital grains from the lowest grade units (Phyllite and Garnet-Phyllite units). Exceptions are rutile grains from a quartzite sample from the MEU (EGB04-S56, also investigated in this paper).

4.5.3 Detrital rutiles from low- to medium-grade metasedimentary rocks

An important exception are rutile grains from the only analyzed quartzite sample from the MEU (EGB04-S56). Rutiles obtained from a heavy mineral separate from a large sample have Zr concentrations up to 1000 ppm (ca. 740-770°C for *P* 0.7-1.2 GPa, Triebold *et al.*, 2007). In the present work, one rutile with a Zr content of 390 ppm (ca. 660-680°C for *P* 0.7-1.2 GPa) was found *in-situ* in this sample. A BSE image of this grain is presented in Fig. 4.7a. Interestingly, this rutile shows a texture that is distinctly different from the ones observed for grains with low Zr contents. Close inspection shows that this grain is not an aggregate but a single large crystal that is surrounded by fine-grained ilmenite. Furthermore, the lath shape, typical for newly grown rutiles, is not observed. After this finding, more grains displaying similar textures have been found in the quartzite (Fig. 4.7b). Although not all grains have high Zr contents, their Nb/Ti ratios are significantly higher than the ratios of the coexisting ilmenites (Fig. 4.7a and b). We interpret these rutiles as detrital relicts. We further interpret that ilmenite grew from this grains during prograde metamorphism under low-grade conditions (greenschist or below). This is evidenced by the textures and Nb/Ti ratios, in accordance with the exchange coefficients presented above. The fact that rutile was not completely replaced by ilmenite reinforces the theory that quartzites are less reactive when compared with other rocks (see also discussion in Triebold *et al.*, 2007). This observation is corroborated by additional textures observed in the quartzite. Although this rock is from the MEU, several newly formed rutiles display rutile/ilmenite textures (Fig. 4.2d) that occur only in GPU rocks (*e.g.*, Fig. 4.2c and e). In contrast, micaschists from the MEU show more evolved stages of the texture (Fig. 4.2h).

Preliminary calculations were carried out in order to evaluate the impact of our observations for the sedimentary record of rutile, *i.e.*, which type of lithology is most capable to deliver high amounts of rutile from low- to medium-grade metasedimentary rocks. We focus here on sand-sized sediment, because rutile in provenance studies is mostly related to heavy mineral analysis which usually concentrates on the finer grained sand fraction. Based on BSE images (see, *e.g.*, Figs 4.2 and 4.7) and petrographic observation, average rutile grain sizes (size of the smaller dimen-
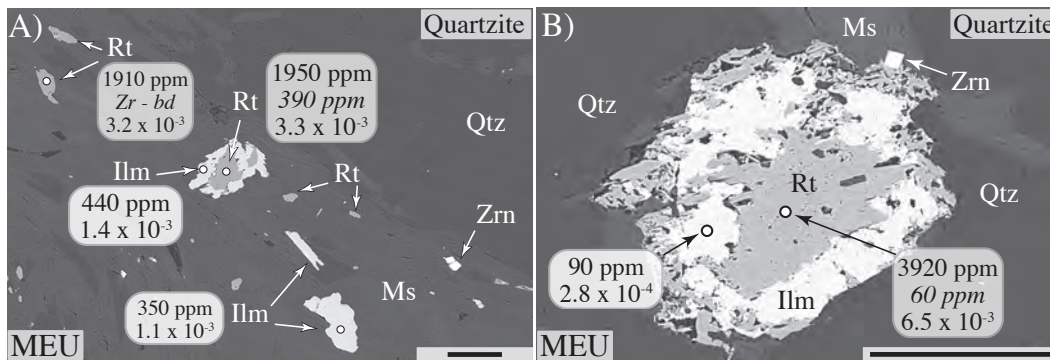
Figure 4.7 BSE images of rutiles interpreted as detrital relics in the quartzite. Concentrations (in ppm) stand for Nb and Zr (in *italic*). Pure numbers represent Nb/Ti ratios. Scale bars represent 100μm.

sion) of 50 μm and 100 μm can be estimated for the metapelites (phyllites/schists) and quartzites, respectively.

Calculations were performed assuming a gaussian grain size distribution and a standard deviation of 20% (in accordance with results obtained for garnet porphyroblasts by Hirsch, 2008). Probabilities were calculated for three grain size fractions (Tab. 4.3): 63 μm, which corresponds to the silt-sand threshold, fraction used in traditional heavy mineral analyzes (see, *e.g.*, Weltje & von Eynatten, 2004); 80 μm, grain size fraction employed our quantitative provenance studies of rutile (see von Eynatten *et al.*, 2005; Triebold *et al.*, 2007) and 100 μm, the average rutile diameter in the quartzite, which relates via hydrodynamic equivalence to a typical fine- to medium grained sand sample of average grain size ~200 μm. Results clearly show how small volumes of quartzite may dominate the detrital record of rutile in sand sized sediments derived from low-grade metasedimentary sequences. For example, in a section with a quartzite volume of 2.6%, all grains larger than 80 μm would derive from the quartzite. For the 100 μm fraction the effect is even more pronounced, as quartzites would virtually be the only source of rutiles. However, results show that pelites would still be the main contributor for the 63 μm fraction.

Textures and trace element data presented above show that quartzites may preserve detrital rutile grains up to temperatures higher than those needed to crystal-

Table 4.3 Probabilities of occurrence of rutiles in metapelites and quartzites; and percentage contribution of quartzites in the sedimentary record of rutiles from low- to medium-grade metasedimentary sequences.

Rutile	Prob.	Prob.	Prob. Ratio	Percentage contrib. in sediment		
Fraction	Pel (%)	Qzt (%)	Qzt/Pel (vol.)	1% Qzt	%5 Qzt	10% Qzt
63 μm	10	96	0.6	0.6	3	6
80 μm	0.14	84	38	38	100	100
100 μm	<0.003	50	>1000	100	100	100

Parameters: Metapelite (Pel) - average grain size = 50μm, standard deviation = 20%, TiO_2 (whole rock) 1.0%.
  Quartzite (Qzt) - average grain size = 100μm, standard deviation = 20%, TiO_2 (whole rock) 0.5%.

lize new rutiles in metapelitic rocks. This observation, combined with the results presented in Tab. 4.3, suggest that sand sized rutiles derived from low- to medium-grade metasediments that contain in addition quartzites may not provide information about the metapelites. They may, indeed, record information (*e.g.*, Nb and Cr systematics and *T*) inherited from an earlier geological cycle recorded in the quartzite.

4.6 Conclusions

Textures and trace element data indicate rutile growth from ilmenite in low- to medium-grade metasedimentary rocks from the Erzgebirge. In samples from the GPU rutiles occur as polycrystalline aggregates and mirror the shape and Nb/Ti ratios of ilmenite. In MEU rocks, rutile aggregates still have the shape inherited from ilmenite. However, rutiles from this unit display a larger scatter in Nb concentratios and have Nb/Ti ratios higher than ilmenite. This behavior indicates that Nb concentrations in rutile are evolving towards equilibration with relict ilmenites (according to a $K_{DNb/Ti}^{Rt/Ilm}$ value of 49.4). GEU rocks are ilmenite free showing that the rutile forming reaction was completed. Rutiles from these rocks show a narrow scatter in Nb contents, are single crystals and have rounded shape (typical for metamorphic rutiles). In these rocks, the homogenization of Nb contents in rutile was facilitated by higher temperature and is probably related with mechanisms like

dynamic recrystalization and/or intergrain diffusion.

Temperature records on all but one rutile grain are in accordance with metamorphic conditions previously presented for the studied rocks. Rutiles from the GPU give temperatures <510°C. Temperatures within 500-560°C and 520-630°C were obtained for rutiles from MEU and GEU rocks, respectively.

The only rutile with an exceptionally high Zr content (390 ppm, T=680°C) is from a quartzite from the MEU. This grain is interpreted to be a detrital relict. Due to the lack of Fe- Ca-bearing phases, quartzites are less reactive then other rocks types (*e.g.*, phyllites and schists). This strongly decreases the abilbity to form ilmenite and/or titanite under metamorphic conditions where rutile is unstable.

Phyllites and schists are low- to medium-grade metamorphic products of pelitic sediments (fine grained clastic sediments of less than 1/16mm; Pettijohn, 1975). On the other hand, quartzites are often the metamorphic product of coarser grained sediments, *e.g.*, sandstones. In the investigated phyllites and schists, metamorphically grown rutiles are fine grained (smaller axis <50 μm) and occur as polycrystalline aggregates (easily disintegrated during weathering and mechanical transport in sediments). However, large detrital rutile grains may still be preserved in the quartzites. Preliminary calculations, taking into account rutile frequency and grain size distributions, show that quartzites may often be the main source for rutiles in sediments derived from low-grade metamorphic rocks. This may be the case of the Erzgebirge, where high-temperature rutile relicts are frequently found in sediments derived from low- to medium-grade rocks (even though the volume of quartzite is less than 5%).

Acknowledgments

Bibliography

Beattie P, Drake M, Jones J, Leeman W, Longhi J, McKay G, Nielsen R, Palme H, Shaw D, Takahashi E, Watson B (1993) Terminology for trace-element partitioning. *Geochimica et Cosmochimica Acta* 57: 1605–1606

Brenan JM, Shaw HF, Phinney DL, Ryerson FJ (1994) Rutile-aqueous fluid partitioning of Nb, Ta, Hf, Zr, U and Th: implications for high field strength element depletions in island-arc basalts. *Earth and Planetary Science Letters* 128: 327–339

Deer WA, Howie R, Zussman J (1992) *An introduction to the rock-forming minerals*. Harlow, Essex, England, 696p

Douce AEP (1993) Titanium substitution in biotite - an empirical-model with applications to thermometry, O$_2$ and H$_2$O barometries, and consequences for biotite stability. *Chemical Geology* 108: 133–162

Foley SF, Barth MG, Jenner GA (2000) Rutile/melt partition coefficients for trace elements and an assessment of the influence of rutile on the trace element characteristics of subduction zone magmas. *Geochimica et Cosmochimica Acta* 64: 933–938

Force E (1980) The provenance of rutile. *Journal of Sedimentary Research* 50: 485–488

Graham J, Morris R (1973) Tungsten- and antimony-substituted rutile. *Mineralogical Magazine* 39: 470–473

Green TH (2000) New partition coefficient determinations pertinent to hydrous melting processes in subduction zones. In: Davidson JA J P Gamble, Price RC (eds.) *States os the Arc 2000: Processes and Timescales*, 92–95, Wellington

Green TH, Pearson NJ (1987) An experimental-study of Nb and Ta partitioning between Ti-rich minerals and silicate liquids at high-pressure and temperature. *Geochimica et Cosmochimica Acta* 51: 55–62

Haggerty SE (1991) *Oxide mineralogy of the upper mantle. In: Lindsley, D. H. (Ed.), Oxide mineralogy minerals: Petrological and magnetic significance*, vol. 25. Reviews in mineralogy

Harley SL (2008) Refining the P–T records of UHT crustal metamorphism. *Journal of Metamorphic Geology* 26: 125–154

Henry DJ, Guidotti CV (2002) Titanium in biotite from metapelitic rocks: Temperature effects, crystal-chemical controls, and petrologic applications. *American Mineralogist* 87: 375–382

Henry DJ, Guidotti CV, Thomson JA (2005) The Ti-saturation surface for low-to-medium pressure metapelitic biotites: Implications for geothermometry and Ti-substitution mechanisms. *American Mineralogist* 90: 316–328

Hermann J, Spandler CJ (2008) Sediment melts at sub-arc depths: An experimental study. *Journal of Petrology* 49: 717–740

Hirsch D (2008) Controls on porphyroblast size along a regional metamorphic field gradient. *Contributions to Mineralogy and Petrology* 155: 401–415

Horng WS, Hess PC (2000) Partition coefficients of Nb and Ta between rutile and anhydrous haplogranite melts. *Contributions to Mineralogy and Petrology* 138: 176–185

Klemme S, Prowatke S, Hametner K, Günther D (2005) Partitioning of trace elements between rutile and silicate melts: Implications for subduction zones. *Geochimica et Cosmochimica Acta* 69: 2361–2371

Klemme S, Günther D, Hametner K, Prowatke S, Zack T (2006) The partitioning of trace elements between ilmenite, ulvospinel, annalcolite and silicate melts with implications for the early differentiation of the moon. *Chemical Geology* 234: 251–263

Kretz R (1983) Symbols for rock forming minerals. *American Mineralogist* 68: 277–279

LaTourrette T, Hervig RL, Holloway JR (1995) Trace-element partitioning between amphibole, phlogopite, and basanite melt. *Earth and Planetary Science Letters* 135: 13–30

Luvizotto G, Zack T, Meyer H, Ludwig T, Triebold S, Kronz A, Münker C, Stockli D, Prowatke S, Klemme S, Jacob DE, von Eynatten H (in press) Rutile crystals as potential secondary standards for microanalysis. *Chemical Geology*

Luvizotto GL, Zack T (in press) Nb and Zr behavior in rutile during high–grade metamorphism and retrogression: An example from the Ivrea–Verbano Zone. *Chemical Geology*

McDonough WF (1991) Partial melting of subducted oceanic crust and isolation of its residual eclogitic lithology. *Philosophical Transactions of the Royal Society of London Series A* 335: 407–418

Meinhold G, Anders B, Kostopoulos D, Reischmann T (2008) Rutile chemistry and thermometry as provenance indicator: An example from Chios Island, Greece. *Sedimentary Geology* 203: 98–111

Mingram B (1996) Geochemische Signaturen der Metasedimente des erzgebirgischen Krustenstapels. *Geo Forschungs Zentrum Potsdam Scientific Technical Report STR96/04* 1–104

Mingram B (1998) The Erzgebirge, Germany, a subducted part of northern Gondwana: geochemical evidence for repetition of early Palaeozoic metasedimentary sequences in metamorphic thrust units. *Geological Magazine* 135: 785–801

Mingram B, Rötzler K (1999) Geochemische, petrologische und geochronologische Untersuchungen im Erzgebirgskristallin - Rekonstruktion eines Krustenstapels. *Schriftenreihe für Geologische Wissenschaften* 9: 80 p

Münker C (1998) Nb/Ta fractionation in a Cambrian arc/back-arc system, New Zealand: source constraints and application of refined ICPMS techniques. *Chemical Geology* 144: 23–45

Pettijohn F (1975) *Sedimentary Rocks*. Harper and Row, New York, 628 pp

Rice C, Darke K, Still J (1998) Tungsten-bearing rutile from the Kori Kollo gold mine Bolívia. *Mineralogical Magazine* 62: 421–429

Rötzler K, Schumacher R, Maresch WV, Willner AP (1998) Characterization and geodynamic implications of contrasting metamorphic evolution in juxtaposed high-pressure units of the western Erzgebirge (Saxony, Germany). *European Journal of Mineralogy* 10: 261–280

Rudnick RL, Barth M, Horn I, McDonough WF (2000) Rutile-bearing refractory eclogites: Missing link between continents and depleted mantle. *Science* 287: 278–281

Saunders A, Tarney J, Weaver S (1980) Traverse geochemical variations across the Antarctic Peninsula: implications for the genesis of calc-alkaline magmas. *Earth and Planetary Science Letters* 46: 344–360

Schmidt MW, Dardon A, Chazot G, Vannucci R (2004) The dependence of Nb and Ta rutile-melt partitioning on melt composition and Nb/Ta fractionation during subduction processes. *Earth and Planetary Science Letters* 226: 415–432

Smith D, Persil EA (1997) Sb-rich rutile in the manganese concentrations at St. Marcel-Praborna, Aosta Valley, Italy; petrology and crystal-chemistry. *Mineralogical Magazine* 61: 655–669

Spear FS, Wark DA, Cheney JT, Schumacher JC, Watson EB (2006) Zr-in-rutile thermometry in blueschists from Sifnos, Greece. *Contributions to Mineralogy and Petrology* 152: 375–385

Stalder R, Foley SF, Brey GP, Horn I (1998) Mineral-aqueous fluid partitioning of trace elements at 900-1200 °C and 3.0-5.7 GPa: new experimental data for garnet, clinopyroxene, and rutile, and implications for mantle metasomatism. *Geochimica et Cosmochimica Acta* 62: 1781–1801

Stendal H, Toteu SF, Frei R, Penaye J, Njel UO, Bassahak J, Nni J, Kankeu B, Ngako V, Hell JV (2006) Derivation of detrital rutile in the Yaounde region from the Neoproterozoic Pan-African belt in southern Cameroon (Central Africa). *Journal of African Earth Sciences* 44: 443–458

Tomkins HS, Powell R, Ellis DJ (2007) The pressure dependence of the zirconium-in-rutile thermometer. *Journal of Metamorphic Geology* 25: 703–713

Triebold S, von Eynatten H, Luvizotto GL, Zack T (2007) Deducing source rock lithology from detrital rutile geochemistry: An example from the Erzgebirge, Germany. *Chemical Geology* 244: 421–436

von Eynatten H, Tolosana-Delgado R, Triebold S, Zack T (2005) Interactions between grain size and composition of sediments: two examples. In: Mateu-Figueiras G, Barcelo-Vidal C (eds.) *Proceedings CoDaWork'05 - 2nd Compositional Data Analysis Workshop*, Universitat de Girona, Girona

Watson EB, Wark DA, Thomas JB (2006) Crystallization thermometers for zircon and rutile. *Contributions to Mineralogy and Petrology* 151: 413–433

Weltje G, von Eynatten H (2004) Quantitative provenance analysis of sediments: review and outlook. *Sedimentary Geology* 171: 1–11

Willner AP, Rötzler K, Maresch WV (1997) Pressure-temperature and fluid evolution of quartzo-feldspathic metamorphic rocks with a relic high-pressure, granulite-facies history from the Central Erzgebirge (Saxony, Germany). *Journal of Petrology* 38: 307–336

Zack T, Luvizotto GL (2006) Application of rutile thermometry to eclogites. *Mineralogy and Petrology* 88: 69–85

Zack T, Kronz A, Foley SF, Rivers T (2002) Trace element abundances in rutiles from eclogites and associated garnet mica schists. *Chemical Geology* 184: 97–122

Zack T, von Eynatten H, Kronz A (2004a) Rutile geochemistry and its potential use in quantitative

provenance studies. *Sedimentary Geology* 171: 37–58

Zack T, Moraes R, Kronz A (2004b) Temperature dependence of Zr in rutile: empirical calibration of a rutile thermometer. *Contributions to Mineralogy and Petrology* 148: 471–488

5 Co-authorship on scientific articles related to the topic of the thesis

During the development of this work, the author contributed to three scientific articles that approach topics related to this thesis. The abstracts of these articles are presented in this chapter. Full copies of the publications are included in Appendix C).

5.1 Application of Zr-in-rutile thermometry to eclogites

T. Zack. and G. L. Luvizotto

Article published in Mineralogy and Petrology[1]

5.1.1 Abstract

Metamorphic temperatures can be derived from the Zr content in rutiles coexisting with quartz and zircon. To evaluate how well this recently calibrated rutile thermometer can be applied to eclogites, we analyzed 8 samples that cover the whole temperature range of naturally-occurring eclogites (400-900 °C). Due to low concentrations expected at only 400 °C, very high precision (better than 5 percent on a 10 ppm level) secondary ion mass spectrometry (SIMS) is used in this study. In general, temperatures calculated from rutiles agree favorably with literature data as well as with our own estimates, based on several geothermobarometers and phase assemblages. However, the most important result of this study is the observation that temperatures calculated from 4–8 rutiles within a single sample always agree to within better than 25 °C, hence enforcing the claim that rutile thermometry is a powerful tool for relative temperature determinations.

---

[1]Zack T, Luvizotto GL (2006) Application of rutile thermometry to eclogites. *Mineralogy and Petrology* 88, 69–85.

5.2 Deducing source rock lithology from detrital rutile geochemistry: An example from the Erzgebirge, Germany

Triebold, S., von Eynatten, H., Luvizotto, G. L., Zack, T.

Article published in Chemical Geology[2]

5.2.1 Abstract

This study evaluates the applicability of rutile trace element geochemistry to provenance studies. The study area is the Erzgebirge in eastern Germany, where metamorphic rocks ranging from lower greenschist facies conditions up to granulite facies conditions are exposed. We collected sand and rock samples from small catchment areas for a comparative analysis of rutile geochemistry using wavelength-dispersive electron microprobe. Our results show that rutile geochemistry is a powerful tool in provenance studies, allowing for the identification of source lithologies and an evaluation of the host orogen's metamorphic history.

The log (Cr/Nb) ratio has proven to be decisive in discriminating between mafic and metapelitic lithologies. It is also useful for identifying different source rocks when plotted versus a third element or proxy. Furthermore, our results suggest that rutile thermometry can be applied to a much wider range of lithologies than previously assumed.

A quantification of temperature populations within single sand samples shows that at high-grade metamorphic conditions, such as those found in the Erzgebirge, more than 65% of rutiles do not re-equilibrate during retrograde metamorphism and thus retain their peak temperature chemistry. Such samples, which have equilibrated at recent metamorphic conditions, can be identified by their 2-σ standard deviations of less than 120 °C. Below 550–600 °C, no complete equilibration is reached. Rutiles from greenschist facies and lower metamorphic conditions in the Erzgebirge still inherit relict temperatures from a former metamorphic cycle. They partly record very high temperatures > 950 °C and supposedly derive from erosion of the west African craton in Ordovician time.

---

[2]Triebold S, von Eynatten H, Luvizotto GL, Zack T (2007) Deducing source rock lithology from detrital rutile geochemistry: An example from the Erzgebirge, Germany. *Chemical Geology* 244, 421–436.

5.3 On the occurrence and boron isotopic composition of tourmaline in (ultra)high-pressure metamorphic rocks

Marschall, H. R., Korsakov, A. V., Luvizotto, G. L., Nasdala, L., Ludwig, T.

Article submitted to Journal of the Geological Society[3]

5.3.1 Abstract

The extensive *P-T* stability and the high chemical variability of tourmaline (Tur) together with its common occurrence in meta-sediments suggests a high potential of this mineral group for petrologic and (isotope) geochemical studies on fluid-rock interaction in subduction and collision-related rocks. This paper presents a short review on the occurrence, major element chemistry and boron isotopic composition of Tur in high and ultra-high pressure (UHP) metamorphic rocks, and presents a new discovery of coesite-bearing Tur (schorl) from the Erzgebirge (Germany), as well as Tur (dravite) related to the retrograde history of coesite and diamond-bearing rocks from the Erzgebirge and the Kokchetav Massif (Kazakhstan).

The scarce data on world-wide occurrences of (U)HP Tur available to date, do not reveal any distinctiveness in its major element composition when compared to Tur from low-*P* rocks, except for the high occupation of the crystallographic X-site (dominated by Na) and the presence of excess B. Tourmaline with exceptionally high K_2O contents from Kokchetav is crowded with quartz inclusions and thus must have formed during or after decompression of the rock unit. The B isotopic composition of (U)HP Tur analysed so far ranges in $\delta^{11}B$ from -16 to +1‰ with many samples in or below the range of continental crust. In contrast, Tur formed during retrograde fluid influx in most cases shows high $\delta^{11}B$ values, bearing evidence for heavy-B fluids infiltrating the exhuming (U)HP units.

Appendices

A Trace element concentrations of rutiles and biotites

Table A.1: Rutile trace element concentrations (in ppm) obtained for the studied IVZ samples. Rutile measurements with apparent Si concentrations higher than 300 ppm that showed abnormally high Zr contents were excluded from the data set. Textural relationship (Text. Rel.): M - matrix, I - included in garnet. Spot Position (Spot Pos.): C - core, R - rim. IVZR19[a] = biotites analyzed by SIMS, IVZR19[b] = biotites analyzed by LA–ICP–MS. IVZ-R36g[c] collected aprox. 40m NW of IVZ-R36a.

Tech.	Locality	Thin Sect.	Grain	Text. Rel.	Spot Pos.	V	Cr	Fe	Zr	Nb	Sn	Sb	Hf	Ta	W	U
SIMS	IVZ-R7	a	Rt1	M	C				1352	3537	35	0.16	80	87	65	21
SIMS	IVZ-R7	a	Rt3	M	C				758	5279	44	bd	40	181	99	18
SIMS	IVZ-R7	a	Rt4	M	C				853	4989	33	bd	41	324	56	14
SIMS	IVZ-R7	a	Rt5	M	C				599	6531	46	bd	39	410	77	13
SIMS	IVZ-R7	a	Rt6	M	C				1091	1102	42	0.19	64	34	36	20
SIMS	IVZ-R7	a	Rt7	M	C				669	2721	64	bd	41	23	89	19
SIMS	IVZ-R7	a	Rt8	M	C				1480	7138	36	0.21	74	375	76	15
SIMS	IVZ-R7	a	Rt9	M	C				752	314	43	0.13	29	2.4	2.0	20
SIMS	IVZ-R7	a	Rt10	M	C				1187	623	50	0.16	40	4.7	5.1	24
SIMS	IVZ-R7	a	Rt10	M	R				828	615	49	bd	23	2.9	5.4	19
SIMS	IVZ-R7	a	Rt10	M	R				871	504	39	0.19	28	3.6	5.1	21
SIMS	IVZ-R7	a	Rt11	M	C				2441	8827	30	0.30	110	308	83	10
SIMS	IVZ-R7	a	Rt12	M	C				1950	5531	38	0.45	112	271	106	16
EMP	IVZ-R7	a	Rt13	M	C	2125	448	542	788	741					bd	
EMP	IVZ-R7	a	Rt13	M	C	2097	478	523	803	658					bd	
EMP	IVZ-R7	a	Rt13	M	R	2312	453	534	639	990					bd	
EMP	IVZ-R7	a	Rt14	I	M	3090	563	767	2560	3517					bd	
EMP	IVZ-R7	a	Rt15	M	M	2764	731	628	2307	4326					bd	
EMP	IVZ-R7	a	Rt16	M	M	3196	749	519	802	4311					bd	
EMP	IVZ-R7	a	Rt17	M	C	2204	621	793	963	2490					bd	
EMP	IVZ-R7	a	Rt18	M	C	3516	667	1423	1140	5640					bd	
EMP	IVZ-R7	a	Rt20	M	C	1403	547	1153	670	600					bd	
EMP	IVZ-R7	a	Rt25	M	C	2315	850	781	270	2970					bd	
EMP	IVZ-R7	a	Rt21	M	C	2775	767	512	2030	1480					bd	
EMP	IVZ-R7	a	Rt22	M	C	2696	502	279	390	310					bd	
EMP	IVZ-R7	a	Rt23	M	C	2331	343	753	1620	730					bd	
EMP	IVZ-R7	a	Rt24	M	C	2424	519	753	2500	5770					bd	
EMP	IVZ-R16	a	Rt1	M	C	2815	714	388	3331	2185					bd	
EMP	IVZ-R16	a	Rt2	I	C	3219	729	1372	3139	4746					bd	
EMP	IVZ-R16	a	Rt3	M	C	2997	864	506	1668	1993					bd	
EMP	IVZ-R16	a	Rt4	M	C	2525	844	441	765	2257					bd	
EMP	IVZ-R16	a	Rt5	I	C	3094	1075	1964	2486	2672					bd	
EMP	IVZ-R16	a	Rt6	M	C	3368	662	335	920	2110					bd	
EMP	IVZ-R16	a	Rt7	M	C	4058	682	279	1240	2360					bd	
EMP	IVZ-R16	a	Rt8	M	C	3975	546	474	950	2060					bd	
EMP	IVZ-R16	a	Rt9	M	C	3305	565	865	2440	2990					bd	
EMP	IVZ-R16	a	Rt10	M	C	3849	758	419	1220	2110					bd	
EMP	IVZ-R16	a	Rt11	M	C	3100	550	530	700	2420					bd	
EMP	IVZ-R16	a	Rt12	M	C	3186	488	465	2630	2190					bd	
EMP	IVZ-R16	a	Rt13	M	C	2329	650	447	2460	2160					bd	
EMP	IVZ-R16	a	Rt14	M	C	2938	525	428	2710	3210					bd	
EMP	IVZ-R16	a	Rt15	M	C	2699	938	484	2530	2340					bd	
EMP	IVZ-R16	a	Rt16	M	C	3095	758	484	3640	2240					bd	
EMP	IVZ-R16	a	Rt17	M	C	2972	583	288	1430	2010					bd	
EMP	IVZ-R16	f	Rt1	M	C	2382	891	532	2983	2198					bd	
EMP	IVZ-R16	f	Rt2	M	C	2228	693	362	3055	2173					bd	
EMP	IVZ-R16	f	Rt3	M	C	2197	751	456	835	2196					bd	
EMP	IVZ-R16	f	Rt4	I	C	2715	629	1067	861	4762					bd	
EMP	IVZ-R16	f	Rt5	M	C	2153	608	461	2293	2172					bd	
EMP	IVZ-R16	f	Rt6	M	C	3753	534	2076	2980	4680					bd	

Continued on next page

A Trace element concentrations of rutiles and biotites

Tech.	Locality	Thin Sect.	Grain	Text. Rel.	Spot Pos.	V	Cr	Fe	Zr	Nb	Sn	Sb	Hf	Ta	W	U
EMP	IVZ-R16	f	Rt7	M	C	2403	559	1553	2240	1810					bd	
EMP	IVZ-R16	f	Rt8	M	C	2122	607	744	2760	1970					bd	
EMP	IVZ-R16	f	Rt9	M	C	2198	585	549	760	2370					bd	
EMP	IVZ-R16	f	Rt10	M	C	2303	522	539	900	2450					bd	
EMP	IVZ-R16	f	Rt12	M	C	1753	726	614	2140	2320					bd	
EMP	IVZ-R16	f	Rt13	I	C	2543	665	2344	2820	2470					bd	
EMP	IVZ-R16	f	Rt14	M	C	1869	514	520	2520	2090					bd	
EMP	IVZ-R16	f	Rt15	M	C	1534	990	586	1160	2290					bd	
EMP	IVZ-R16	f	Rt16	M	C	1530	554	781	690	2290					bd	
EMP	IVZ-R16	f	Rt18	M	C	1655	312	1181	960	3360					bd	
SIMS	IVZ-R16	g	Rt1	M	C				2476	2926	53	0.02	101	275	287	12
SIMS	IVZ-R16	g	Rt2	M	C				2546	2170	50	0.19	100	237	216	16
SIMS	IVZ-R16	g	Rt3	M	C				2133	1862	59	0.44	87	76	212	19
SIMS	IVZ-R16	g	Rt4	M	C				898	2168	48	0.07	43	116	80	11
SIMS	IVZ-R16	g	Rt5	M	C				580	2577	60	bd	42	172	126	9
EMP	IVZ-R16	g	Rt1	M	C	3579	507	453	2902	3189					bd	
EMP	IVZ-R16	g	Rt2	M	C	2297	473	457	2915	2356					bd	
EMP	IVZ-R16	g	Rt2	M	R	2544	476	582	2173	3087					bd	
EMP	IVZ-R16	g	Rt3	M	C	2354	333	520	2284	1833					bd	
EMP	IVZ-R16	g	Rt4	M	R	4339	595	759	1002	2159					bd	
EMP	IVZ-R16	g	Rt4	M	C	4315	576	412	1210	2578					bd	
EMP	IVZ-R16	g	Rt4	M	R	4220	559	422	848	2384					bd	
EMP	IVZ-R16	g	Rt5	M	R	5692	588	377	603	1941					bd	
EMP	IVZ-R16	g	Rt5	M	C	6123	685	283	653	3216					bd	
EMP	IVZ-R16	g	Rt5	M	R	6818	795	657	619	5202					bd	
EMP	IVZ-R16	g	Rt6	M	C	1298	421	842	2424	1992					bd	
EMP	IVZ-R16	g	Rt7	M	C	2606	261	1213	778	2316					bd	
EMP	IVZ-R16	g	Rt8	M	C	3453	570	286	1909	778					bd	
EMP	IVZ-R16	g	Rt9	M	C	1777	338	526	1199	582					bd	
EMP	IVZ-R16	g	Rt10	M	C	1912	424	627	502	539					bd	
EMP	IVZ-R16	g	Rt11	M	C	2213	376	447	973	685					bd	
EMP	IVZ-R16	g	Rt12	M	C	3648	545	263	1287	894					bd	
EMP	IVZ-R16	g	Rt13	M	C	2443	518	820	1517	796					bd	
EMP	IVZ-R16	g	Rt14	M	C	4299	299	372	2630	2630					bd	
EMP	IVZ-R16	g	Rt15	M	C	2147	139	725	1190	2110					bd	
EMP	IVZ-R16	g	Rt16	M	C	2087	439	1042	1550	2820					bd	
EMP	IVZ-R16	g	Rt17	I	C	1250	452	614	2100	1480					bd	
EMP	IVZ-R16	g	Rt18	I	C	1713	876	977	710	1540					bd	
EMP	IVZ-R16	g	Rt19	M	C	4321	666	381	2170	1340					bd	
EMP	IVZ-R16	g	Rt20	M	C	2197	774	623	2090	1100					bd	
EMP	IVZ-R16	g	Rt21	M	C	2340	611	530	2490	1850					bd	
EMP	IVZ-R16	g	Rt22	M	C	5773	506	837	2820	1910					bd	
EMP	IVZ-R16	g	Rt23	I	C	3224	309	1822	1220	2820					bd	
EMP	IVZ-R16	g	Rt24	M	C	2260	424	341	2347	1983					bd	
SIMS	IVZ-R20	a	Rt1	M	0				1541	2421	16	0.65	64	83	37	20
SIMS	IVZ-R20	a	Rt2	M	0				657	1815	19	bd	44	86	56	11
SIMS	IVZ-R20	a	Rt3	M	0				1766	2013	19	0.30	77	89	43	16
SIMS	IVZ-R20	a	Rt4	M	0				2024	1879	18	0.42	101	128	69	24
SIMS	IVZ-R20	a	Rt5	M	0				1523	1891	10	0.27	76	97	42	19
SIMS	IVZ-R20	a	Rt5	M	0				1406	1791	9	bd	73	93	49	18
SIMS	IVZ-R20	a	Rt6	M	0				1084	1890	11	0.08	65	103	46	12
SIMS	IVZ-R20	a	Rt7	M	0				859	2945	19	bd	63	90	44	11
SIMS	IVZ-R20	a	Rt8	M	0				632	2462	20	0.08	56	159	68	16
EMP	IVZ-R20	a	Rt1	M	C	2345	591	795	2160	2288					bd	
EMP	IVZ-R20	a	Rt2	M	R	3268	704	899	398	2599					bd	
EMP	IVZ-R20	a	Rt4	M	R	2354	481	654	2105	1895					bd	
EMP	IVZ-R20	a	Rt4	M	R	2893	655	704	1276	1895					bd	
EMP	IVZ-R20	a	Rt5	M	C	2966	683	532	1653	1856					bd	
EMP	IVZ-R20	a	Rt5	M	C	2980	703	549	1519	1833					bd	
EMP	IVZ-R20	a	Rt6	M	C	3386	671	721	1073	1888					bd	
EMP	IVZ-R20	a	Rt6	M	R	3358	702	1158	1198	3165					bd	
EMP	IVZ-R20	a	Rt7	M	C	3407	631	1063	521	3424					bd	
EMP	IVZ-R20	a	Rt8	M	C	2720	600	510	861	2232					bd	
EMP	IVZ-R20	a	Rt8	M	R	2591	564	554	1070	2129					bd	
EMP	IVZ-R20	a	Rt9	M	C	2416	584	398	2405	1870					bd	
EMP	IVZ-R20	a	Rt10	M	M	2439	541	351	2409	1823					bd	
EMP	IVZ-R20	a	Rt11	M	M	2416	616	697	2617	2445					bd	
EMP	IVZ-R20	a	Rt12	M	C	2551	635	530	1800	2030					bd	
EMP	IVZ-R20	a	Rt13	M	C	2767	311	623	2360	1850					bd	

Tech.	Locality	Thin Sect.	Grain	Text. Rel.	Spot Pos.	V	Cr	Fe	Zr	Nb	Sn	Sb	Hf	Ta	W	U
EMP	IVZ-R20	a	Rt14	M	C	2707	422	577	1120	2000					bd	
EMP	IVZ-R20	a	Rt15	M	C	2627	464	558	1360	1770					bd	
EMP	IVZ-R20	a	Rt16	M	C	2547	466	734	2580	2510					bd	
EMP	IVZ-R20	a	Rt17	M	C	2669	681	1079	1770	3420					bd	
EMP	IVZ-R20	a	Rt18	M	C	2807	607	837	2580	2520					bd	
EMP	IVZ-R20	a	Rt19	M	C	2430	419	679	1530	1880					bd	
EMP	IVZ-R20	a	Rt21	M	C	2610	415	660	2920	2320					bd	
EMP	IVZ-R20	a	Rt22	M	C	2349	462	865	900	2390					bd	
EMP	IVZ-R20	a	Rt23	M	C	1958	512	465	2440	1860					bd	
EMP	IVZ-R20	a	Rt24	M	C	2351	570	907	2037	2063					bd	
EMP	IVZ-R20	a	Rt25	M	C	2015	411	688	3953	1888					bd	
EMP	IVZ-R20	a	Rt26	M	C	2957	603	634	695	1851					bd	
EMP	IVZ-R20	a	Rt27	M	C	2779	489	564	2255	2022					bd	
EMP	IVZ-R20	a	Rt28	M	R	3516	667	903	418	3866					bd	
EMP	IVZ-R20	a	Rt29	M	R	3074	650	1267	583	2931					bd	
SIMS	IVZ-R20	j	Rt1	M	C				1308	2482	13	0.38	72	142	42	18
SIMS	IVZ-R20	j	Rt2	M	C				950	5148	15	0.64	59	268	79	8.0
SIMS	IVZ-R20	j	Rt3	M	C				1131	2593	14	0.17	60	98	34	15
SIMS	IVZ-R20	j	Rt4	M	C				2167	2353	14	0.31	103	103	43	17
SIMS	IVZ-R20	j	Rt5	M	C				1244	2204	14	0.14	58	102	33	21
SIMS	IVZ-R20	j	Rt6	M	C				1259	3278	17	0.19	66	136	37	19
SIMS	IVZ-R20	j	Rt7	M	C				2690	2186	12	0.37	121	93	36	16
SIMS	IVZ-R20	j	Rt8	M	C				2469	2722	15	0.26	106	105	30	14
SIMS	IVZ-R20	j	Rt9	I	C				3612	1945	7.7	0.40	133	154	34	24
SIMS	IVZ-R20	j	Rt11	I	C				1407	1888	10	0.18	71	86	37	17
SIMS	IVZ-R20	j	Rt11	I	R				1400	1949	10	bd	73	93	38	19
SIMS	IVZ-R20	j	Rt12	M	C				1432	1993	11	0.15	62	83	32	19
SIMS	IVZ-R20	j	Rt13	M	C				904	1300	14	bd	33	43	21	14
SIMS	IVZ-R20	j	Rt15	M	C				2983	2021	13	0.55	119	93	29	19
EMP	IVZ-R20	j	Rt16	M	C	2933	505	400	1030	1630					bd	
EMP	IVZ-R20	j	Rt17	M	C	2965	574	465	2510	2230					bd	
EMP	IVZ-R20	j	Rt18	M	C	2977	563	558	1750	1730					bd	
EMP	IVZ-R20	j	Rt19	M	C	3365	563	344	3170	2170					bd	
EMP	IVZ-R20	j	Rt20	M	C	2362	451	539	1000	1930					bd	
EMP	IVZ-R20	j	Rt21	M	C	2490	716	549	2840	2060					bd	
EMP	IVZ-R20	j	Rt22	M	C	2557	764	447	2610	2180					bd	
EMP	IVZ-R6	b	Rt1	I	C	4441	1284	491	1074	4634					bd	
EMP	IVZ-R6	b	Rt2	I	C	4191	1073	825	3313	3468					bd	
EMP	IVZ-R6	b	Rt3	I	C	4391	1047	1466	3619	3643					bd	
EMP	IVZ-R6	b	Rt4	M	C	5158	1681	210	1137	4447					bd	
EMP	IVZ-R6	b	Rt5	M	C	5161	1541	404	903	4010					bd	
EMP	IVZ-R6	b	Rt6	M	C	4742	1425	131	794	3608					bd	
EMP	IVZ-R6	b	Rt7	M	C	4761	1289	220	1411	3994					bd	
EMP	IVZ-R6	b	Rt8	I	C	4625	1413	4320	4543	3250					bd	
EMP	IVZ-R6	b	Rt9	M	C	5006	1446	179	1240	4398					bd	
EMP	IVZ-R6	b	Rt10	M	C	3193	835	316	1520	3390					bd	
EMP	IVZ-R6	b	Rt11	M	C	3853	817	539	1080	4680					bd	
EMP	IVZ-R6	b	Rt12	M	C	3936	845	372	1780	3930					bd	
EMP	IVZ-R6	b	Rt13	M	C	4021	971	586	2040	3580					bd	
EMP	IVZ-R6	b	Rt14	M	C	4134	770	325	1090	3720					bd	
EMP	IVZ-R6	b	Rt15	M	C	3543	716	325	1010	4510					bd	
EMP	IVZ-R6	b	Rt16	M	C	3979	794	390	2560	4080					bd	
EMP	IVZ-R6	b	Rt17	M	C	4118	829	279	1850	3810					bd	
EMP	IVZ-R6	b	Rt18	M	C	3915	697	335	1160	4150					bd	
EMP	IVZ-R6	b	Rt19	M	C	4553	838	419	2700	4040					bd	
EMP	IVZ-R6	b	Rt20	M	C	3952	894	353	1040	3850					bd	
EMP	IVZ-R6	b	Rt21	M	C	4789	1030	1079	960	4300					bd	
EMP	IVZ-R6	b	Rt22	M	C	4439	1039	614	2830	4440					bd	
EMP	IVZ-R6	b	Rt23	M	C	4072	742	539	900	4340					bd	
SIMS	IVZ-R19	e	Rt1	I	C				3013	1928	17	0.06	110	130	31	23
SIMS	IVZ-R19	e	Rt2	I	C				4157	1581	13	0.31	169	151	151	15
SIMS	IVZ-R19	e	Rt3	I	C				4349	2565	13	0.46	155	213	253	15
SIMS	IVZ-R19	e	Rt4	M	C				2286	1568	18	0.09	95	58	25	25
SIMS	IVZ-R19	e	Rt5	M	C				1767	1498	19	0.08	79	64	31	23
SIMS	IVZ-R19	e	Rt6	M	C				1986	1412	19	bd	87	64	25	25
SIMS	IVZ-R19	e[a]	Bt						8.66	1.56			0.23	0.20		
EMP	IVZ-R19	e	Rt1	I	R	3058	522	791	3098	2093					bd	
EMP	IVZ-R19	e	Rt1	I	C	3208	518	663	3183	2142					bd	
EMP	IVZ-R19	e	Rt1	I	R	3118	520	1471	3202	2157					bd	

A Trace element concentrations of rutiles and biotites

Table A.1 – continued from previous page

Tech.	Locality	Thin Sect.	Grain	Text. Rel.	Spot Pos.	V	Cr	Fe	Zr	Nb	Sn	Sb	Hf	Ta	W	U
EMP	IVZ-R19	e	Rt3	I	C	2954	355	2766	4605	2683					bd	
EMP	IVZ-R19	e	Rt3	I	R	2863	358	3113	4499	2908					bd	
EMP	IVZ-R19	e	Rt4	M	C	2323	710	325	2354	1665					bd	
EMP	IVZ-R19	e	Rt4	M	R	2313	711	415	2282	1675					bd	
EMP	IVZ-R19	e	Rt5	M	C	2171	685	654	1866	1638					bd	
EMP	IVZ-R19	e	Rt7	I	C	3070	422	911	3196	2348					bd	
EMP	IVZ-R19	e	Rt8	M	M	3205	736	426	1019	1774					bd	
EMP	IVZ-R19	e	Rt9	I	C	2914	580	1293	1071	2052					bd	
EMP	IVZ-R19	e	Rt10	M	C	3051	512	773	827	2146					bd	
EMP	IVZ-R19	e	Rt11	M	C	2981	514	389	993	2267					bd	
EMP	IVZ-R19	e	Rt12	I	C	2956	643	543	1512	2086					bd	
EMP	IVZ-R19	e	Rt13	I	C	2945	574	526	3781	2045					bd	
EMP	IVZ-R19	e	Rt14	I	C	2899	595	476	3760	2001					bd	
EMP	IVZ-R19	e	Rt15	M	C	3084	461	749	2573	1915					bd	
EMP	IVZ-R19	e	Rt15	M	R	3103	500	1764	2588	1816					bd	
EMP	IVZ-R19	e	Rt16	M	C	2714	323	596	1021	2061					bd	
EMP	IVZ-R19	e	Rt16	M	R	2758	381	1121	1098	2413					bd	
EMP	IVZ-R19	e	Rt17	M	C	2446	697	636	2168	1603					bd	
EMP	IVZ-R19	e	Rt18	M	C	2174	675	449	1869	1634					bd	
EMP	IVZ-R19	e	Rt18	M	R	2441	677	428	1837	1646					bd	
EMP	IVZ-R19	e	Rt19	M	C	2697	720	676	2074	1649					bd	
EMP	IVZ-R19	e	Rt20	I	C	2817	310	3701	1749	1608					bd	
EMP	IVZ-R19	e	Rt21	I	C	2962	325	4114	4614	1450					bd	
EMP	IVZ-R19	e	Rt22	M	C	2417	728	521	817	1936					bd	
EMP	IVZ-R19	e	Rt23	M	R	1852	505	808	2873	1811					bd	
EMP	IVZ-R19	e	Rt23	M	M	2386	510	329	2831	1895					bd	
EMP	IVZ-R19	e	Rt23	M	C	2046	520	297	2837	1858					bd	
EMP	IVZ-R19	e	Rt23	M	M	2402	490	352	2954	1807					bd	
EMP	IVZ-R19	e	Rt23	M	R	2406	510	979	3150	1666					bd	
EMP	IVZ-R19	e	Rt24	M	R	2721	521	318	792	1858					bd	
EMP	IVZ-R19	e	Rt24	M	M	2621	524	423	906	1841					bd	
EMP	IVZ-R19	e	Rt24	M	C	2582	485	492	981	2051					bd	
EMP	IVZ-R19	e	Rt24	M	M	3661	534	1418	643	2808					bd	
EMP	IVZ-R19	e	Rt24	M	R	2741	520	2572	768	2570					bd	
EMP	IVZ-R19	e	Rt25	I	C	2129	210	4612	4052	1451					bd	
EMP	IVZ-R19	e	Rt25	I	C	1919	216	4685	4009	1478					bd	
EMP	IVZ-R19	e	Rt26	I	C	2553	257	4943	4083	1748					bd	
EMP	IVZ-R19	e	Rt39	M	C	2699	601	520	2230	1720					bd	
EMP	IVZ-R19	e	Rt40	M	C	2731	709	455	2010	1410					bd	
EMP	IVZ-R19	e	Rt41	M	C	2597	613	1069	2080	1680					bd	
EMP	IVZ-R19	e	Rt42	M	C	2971	623	772	1890	1930					bd	
EMP	IVZ-R19	e	Rt43	M	C	2582	485	335	2730	1610					bd	
EMP	IVZ-R19	e	Rt44	M	C	2927	604	363	2030	2010					bd	
EMP	IVZ-R19	e	Rt45	M	C	2720	600	586	1070	1890					bd	
EMP	IVZ-R19	e	Rt46	M	C	2824	617	353	1190	1850					bd	
EMP	IVZ-R19	e	Rt47	M	C	2756	649	512	1250	1740					bd	
EMP	IVZ-R19	e	Rt48	M	C	2805	766	437	2590	2540					bd	
EMP	IVZ-R19	e	Rt49	M	C	3009	781	586	2140	1880					bd	
LAM	IVZ-R19	e	Rt27		C				1123	1610			50	94		28
LAM	IVZ-R19	e	Rt28		C				1570	1553			71	99		30
LAM	IVZ-R19	e	Rt29		C				1216	1626			56	111		24
LAM	IVZ-R19	e	Rt30		C				2337	1553			102	89		28
LAM	IVZ-R19	e	Rt31		C				2529	1948			104	80		28
LAM	IVZ-R19	e	Rt32		C				2503	1706			111	70		24
LAM	IVZ-R19	e	Rt33		C				966	1658			49	83		22
LAM	IVZ-R19	e	Rt34		C				2901	2061			114	147		27
LAM	IVZ-R19	e	Rt35		C				1342	1687			65	93		21
LAM	IVZ-R19	e	Rt36		C				2536	1820			101	119		26
LAM	IVZ-R19	e	Rt37		C				3245	1872			118	113		26
LAM	IVZ-R19	e	Rt38		C				2872	2302			106	121		22
LAM	IVZ-R19	e[b]	Bt1						1.9	3.5			<0.18	<0.11		<0.10
LAM	IVZ-R19	e[b]	Bt2						8.9	3.8			0.19	0.06		<0.05
LAM	IVZ-R19	e[b]	Bt3						4.2	0.3			<0.07	<0.03		<0.03
LAM	IVZ-R19	e[b]	Bt4						5.0	1.5			0.15	0.07		<0.02
LAM	IVZ-R19	e[b]	Bt5						5.6	4.9			0.21	0.13		<0.02
LAM	IVZ-R19	e[b]	Bt6						5.7	3.8			0.20	0.18		<0.02
LAM	IVZ-R19	e[b]	Bt7						1.7	0.9			0.12	0.06		<0.02
LAM	IVZ-R19	e[b]	Bt8						1.4	0.5			0.08	<0.01		0.05
LAM	IVZ-R19	e[b]	Bt9						5.4	2.6			0.19	0.09		<0.02

Tech.	Locality	Thin Sect.	Grain	Text. Rel.	Spot Pos.	V	Cr	Fe	Zr	Nb	Sn	Sb	Hf	Ta	W	U
LAM	IVZ-R19	e[b]	Bt10						0.5	2.3			0.06	0.06		0.01
LAM	IVZ-R19	e[b]	Bt11						0.6	2.2			0.06	0.07		<0.02
LAM	IVZ-R19	e[b]	Bt12						4.6	0.5			0.17	0.05		<0.01
LAM	IVZ-R19	e[b]	Bt13						6.2	0.5			0.30	<0.01		<0.01
LAM	IVZ-R19	e[b]	Bt14						6.5	0.3			0.19	0.02		<0.01
LAM	IVZ-R19	e[b]	Bt15						1.7	0.7			0.05	0.05		<0.01
SIMS	IVZ-R5	b	Rt1	M	R				678	1946	6.2	0.39	49	100	6.4	10
SIMS	IVZ-R5	b	Rt1	M	C				947	2232	6.9	0.77	61	118	6.4	13
SIMS	IVZ-R5	b	Rt1	M	R				911	2328	6.8	0.21	61	116	6.3	12
SIMS	IVZ-R5	b	Rt2	M	C				2677	2243	5.8	0.21	119	89	5.8	16
SIMS	IVZ-R5	b	Rt2	M	R				1889	2032	5.7	0.40	99	95	6.3	12
SIMS	IVZ-R5	b	Rt2	M	R				1042	2193	6.2	bd	66	110	6.8	12
SIMS	IVZ-R5	b	Rt3	M	C				611	2187	5.6	bd	48	82	3.4	12
SIMS	IVZ-R5	b	Rt3	M	R				560	2446	6.8	0.15	49	161	4.8	11
SIMS	IVZ-R5	b	Rt3	M	R				340	2116	5.3	bd	36	167	6.4	10
SIMS	IVZ-R5	b	Rt4	M	C				780	2038	8.0	0.20	48	59	6.5	8.5
EMP	IVZ-R5	b	Rt5	M	R	2389	461	325	734	2126					bd	
EMP	IVZ-R5	b	Rt5	M	C	2441	529	458	750	2511					bd	
EMP	IVZ-R5	b	Rt5	M	R	2291	533	342	897	2156					bd	
EMP	IVZ-R5	b	Rt6	M	R	2184	486	450	4890	1542					bd	
EMP	IVZ-R5	b	Rt6	M	C	2289	463	235	4878	1630					bd	
EMP	IVZ-R5	b	Rt6	M	R	2155	447	387	5428	1698					bd	
EMP	IVZ-R5	b	Rt7	M	C	1736	379	603	1244	2606					bd	
EMP	IVZ-R5	b	Rt7	M	R	1822	357	789	1112	2533					bd	
EMP	IVZ-R5	b	Rt7	M	R	1787	299	981	1122	2557					bd	
EMP	IVZ-R5	b	Rt8	M	R	2348	581	432	1185	2533					bd	
EMP	IVZ-R5	b	Rt8	M	C	2387	580	437	1099	2557					bd	
EMP	IVZ-R5	b	Rt8	M	R	2432	598	561	1233	2533					bd	
EMP	IVZ-R5	b	Rt9	M	C	1901	653	777	3934	2066					bd	
EMP	IVZ-R5	b	Rt9	M	C	1943	681	725	3788	2148					bd	
EMP	IVZ-R5	b	Rt10	M	C	2301	532	400	1420	2720					bd	
EMP	IVZ-R5	b	Rt11	M	C	2359	501	344	2630	2280					bd	
EMP	IVZ-R5	b	Rt12	M	C	2531	526	586	1150	2390					bd	
EMP	IVZ-R5	b	Rt13	M	C	2674	512	419	1010	2420					bd	
EMP	IVZ-R5	b	Rt14	M	C	2745	540	623	690	2250					bd	
EMP	IVZ-R5	b	Rt15	M	C	2462	597	772	2570	2180					bd	
EMP	IVZ-R5	b	Rt16	M	C	2487	616	539	2890	2490					bd	
EMP	IVZ-R5	b	Rt17	M	C	2501	527	484	1570	2370					bd	
EMP	IVZ-R5	b	Rt18	M	C	1790	586	419	830	1910					bd	
EMP	IVZ-R5	b	Rt19	M	C	1701	251	837	1750	2400					bd	
EMP	IVZ-R5	b	Rt20	M	C	2750	411	1004	2200	2300					bd	
EMP	IVZ-R5	b	Rt21	M	C	2381	530	372	3080	2130					bd	
EMP	IVZ-R5	b	Rt22	M	C	2120	428	447	2990	2000					bd	
SIMS	IVZ-R37	b	Rt1	M	R				896	716	41	0.12	43	15	9.4	19
SIMS	IVZ-R37	b	Rt1	M	C				1083	759	44	0.33	55	20	21	22
SIMS	IVZ-R37	b	Rt1	M	R				1472	860	46	0.15	83	37	39	23
SIMS	IVZ-R37	b	Rt2	I	C				827	797	26	0.06	52	33	27	19
SIMS	IVZ-R37	b	Rt2	I	R				878	786	25	0.13	49	32	28	20
SIMS	IVZ-R37	b	Rt3	I	C				936	1625	37	0.16	48	110	15	22
SIMS	IVZ-R37	b	Rt4	I	C				860	724	36	0.22	51	13	5.5	24
SIMS	IVZ-R37	b	Rt5	I	C				762	1057	57	0.18	47	43	38	22
SIMS	IVZ-R37	b	Rt6	M	R				2669	1467	51	0.26	114	45	79	20
SIMS	IVZ-R37	b	Rt6	M	C				2796	1452	52	0.09	119	48	79	22
SIMS	IVZ-R37	b	Rt6	M	R				3144	1432	52	0.27	139	55	87	21
SIMS	IVZ-R37	b	Rt7	M	C				974	377	46	0.17	28	10	1.1	8.3
SIMS	IVZ-R37	b	Rt8	M	C				882	849	45	0.09	49	37	41	19
SIMS	IVZ-R37	b	Rt8	M	R				857	828	46	0.10	42	30	32	20
SIMS	IVZ-R37	b	Rt9	M	C				650	245	37	0.31	29	2.1	bd	7.4
SIMS	IVZ-R37	b	Rt10	M	R				1099	1359	53	bd	60	66	50	23
SIMS	IVZ-R37	b	Rt10	M	C				1073	1376	54	bd	61	62	50	23
SIMS	IVZ-R37	b	Rt10	M	R				1200	1424	53	0.29	66	78	49	21
SIMS	IVZ-R37	b	Rt11	I	C				3542	1064	50	0.82	122	65	38	25
SIMS	IVZ-R37	b	Rt11	I	R				3506	1050	53	0.56	122	67	39	22
SIMS	IVZ-R37	b	Rt12	M	C				2937	1697	51	0.16	124	78	64	17
SIMS	IVZ-R37	b	Rt13	I	C				1087	736	39	0.20	59	34	7.3	23
SIMS	IVZ-R37	b	Rt14	I	C				3752	810	67	0.33	134	25	28	24
EMP	IVZ-R37	b	Rt15	M	C	4468	374	465	1810	2130					bd	
EMP	IVZ-R37	b	Rt16	M	C	4355	386	921	1190	1330					bd	
EMP	IVZ-R37	b	Rt17	M	C	5553	661	409	1620	1490					bd	

A Trace element concentrations of rutiles and biotites

<div align="center">Table A.1 – continued from previous page</div>

Tech.	Locality	Thin Sect.	Grain	Text. Rel.	Spot Pos.	V	Cr	Fe	Zr	Nb	Sn	Sb	Hf	Ta	W	U
EMP	IVZ-R37	b	Rt18	M	C	4788	662	260	890	1000					bd	
EMP	IVZ-R37	b	Rt19	M	C	6243	493	186	790	880					bd	
EMP	IVZ-R37	b	Rt20	M	C	5798	337	967	760	1900					bd	
EMP	IVZ-R37	b	Rt21	M	C	4016	803	307	1050	660					bd	
EMP	IVZ-R37	b	Rt22	M	C	4333	993	233	4040	800					bd	
EMP	IVZ-R37	b	Rt23	M	C	2458	538	493	1460	1000					bd	
EMP	IVZ-R37	b	Rt24	I	C	3942	597	669	850	2250					bd	
EMP	IVZ-R37	b	Rt25	I	C	5190	532	1749	2610	1780					bd	
SIMS	IVZ-R25	b	Rt1	M	C				899	2719	18	bd	48	155	61	16
SIMS	IVZ-R25	b	Rt1	M	R				1103	2713	17	bd	54	150	60	15
SIMS	IVZ-R25	b	Rt1	M	R				1050	2481	16	0.22	49	138	54	15
SIMS	IVZ-R25	b	Rt2	M	C				644	2699	22	0.21	33	115	47	12
SIMS	IVZ-R25	b	Rt2	M	R				862	2205	21	bd	37	97	47	11
SIMS	IVZ-R25	b	Rt3	M	R				2196	2591	17	0.76	82	133	56	15
SIMS	IVZ-R25	b	Rt3	M	C				2075	2511	17	0.20	81	144	57	15
SIMS	IVZ-R25	b	Rt3	M	R				2337	2641	18	0.39	90	178	77	18
SIMS	IVZ-R25	b	Rt4	M	C				1593	2470	16	bd	68	117	46	15
SIMS	IVZ-R25	b	Rt4	M	R				1670	2974	17	bd	73	126	45	14
SIMS	IVZ-R25	b	Rt5	M	C				1159	2708	15	0.35	54	149	50	11
SIMS	IVZ-R25	b	Rt5	M	R				1274	2669	15	bd	61	154	59	10
SIMS	IVZ-R25	b	Rt6	M	C				2103	2387	14	0.71	80	151	50	13
SIMS	IVZ-R25	b	Rt6	M	R				1909	1903	11	0.38	68	131	52	14
SIMS	IVZ-R25	b	Rt7	M	C				1002	2934	18	0.16	51	182	63	14
SIMS	IVZ-R25	b	Rt7	M	R				936	2635	17	0.18	48	153	71	11
SIMS	IVZ-R25	b	Rt9	M	R				3046	2771	16	0.68	111	137	46	12
SIMS	IVZ-R25	b	Rt9	M	C				3092	2715	18	0.59	115	140	49	13
SIMS	IVZ-R25	b	Rt9	M	R				3302	2509	16	0.14	117	149	55	13
SIMS	IVZ-R25	b	Rt10	M	R				780	2586	19	bd	39	140	62	13
SIMS	IVZ-R25	b	Rt10	M	C				812	2481	18	0.31	41	127	56	12
EMP	IVZ-R25	b	Rt11	M	R	4126	988	260	760	2340					bd	
EMP	IVZ-R25	b	Rt11	M	C	4355	982	260	850	2250					bd	
EMP	IVZ-R25	b	Rt11	M	R	4206	986	241	1070	2000					bd	
EMP	IVZ-R25	b	Rt12	M	R	4702	913	307	770	2800					bd	
EMP	IVZ-R25	b	Rt12	M	C	4552	1026	298	900	2710					bd	
EMP	IVZ-R25	b	Rt12	M	R	4505	1018	372	990	2770					bd	
EMP	IVZ-R25	b	Rt13	M	C	4757	891	325	1140	2630					bd	
EMP	IVZ-R25	b	Rt14	M	C	5077	1181	428	1150	3000					bd	
EMP	IVZ-R25	b	Rt15	M	C	4535	1463	437	850	2640					bd	
EMP	IVZ-R25	b	Rt16	M	C	4253	995	307	940	2490					bd	
EMP	IVZ-R25	b	Rt17	M	C	4665	865	353	1250	2660					bd	
EMP	IVZ-R25	b	Rt18	M	C	3534	786	288	1400	2720					bd	
EMP	IVZ-R25	b	Rt19	M	C	4629	885	233	1460	2720					bd	
EMP	IVZ-R25	b	Rt20	M	C	4717	892	307	3280	2660					bd	
EMP	IVZ-R25	b	Rt21	M	C	4399	931	372	1050	2610					bd	
EMP	IVZ-R25	b	Rt22	M	C	4500	998	372	1140	2820					bd	
EMP	IVZ-R25	b	Rt23	M	C	4088	1277	186	1140	2600					bd	
EMP	IVZ-R25	b	Rt24	M	C	4297	1202	186	3160	2920					bd	
SIMS	IVZ-R36	a	Rt1	M	R				1013	3004	2.0	0.15	49	71	3.6	12
SIMS	IVZ-R36	a	Rt1	M	R				1684	3443	1.9	bd	99	136	11	14
SIMS	IVZ-R36	a	Rt1	M	R				1041	2552	1.6	1.21	56	104	5.8	13
SIMS	IVZ-R36	a	Rt1	M	R				1363	3513	4.4	0.46	69	90	7.7	11
SIMS	IVZ-R36	a	Rt2	I	C				3425	3187	1.4	0.17	160	140	15	18
SIMS	IVZ-R36	a	Rt3	I	C				1568	3828	3.1	0.17	85	141	15	12
SIMS	IVZ-R36	a	Rt4	M	C				3472	2963	1.4	0.26	136	153	13	17
SIMS	IVZ-R36	a	Rt5	M	C				2882	2748	1.7	0.26	120	149	13	16
SIMS	IVZ-R36	a	Rt6	M	C				2714	2826	1.8	0.28	110	122	13	15
SIMS	IVZ-R36	a	Rt7	M	C				3093	2655	1.8	1.54	116	132	15	15
SIMS	IVZ-R36	a	Rt8	M	C				2840	2875	2.0	0.83	128	152	14	11
SIMS	IVZ-R36	a	Rt9	M	C				4862	3080	1.4	bd	194	177	17	25
SIMS	IVZ-R36	a	Rt9	M	C				4613	2852	1.8	0.24	194	197	21	23
SIMS	IVZ-R36	a	Rt10	M	C				3968	2862	1.6	0.53	163	162	17	23
SIMS	IVZ-R36	a	Rt11	M	C				3935	3089	2.1	0.26	167	179	20	20
SIMS	IVZ-R36	a	Rt12	M	C				781	1907	1.3	0.18	39	119	14	16
SIMS	IVZ-R36	a	Rt14	M	C				1998	2900	1.6	1.09	84	96	5.2	16
SIMS	IVZ-R36	a	Rt15	M	C				4608	3290	1.5	bd	185	159	16	23
SIMS	IVZ-R36	a	Rt16	M	C				3584	5167	3.0	bd	155	184	14	17
EMP	IVZ-R36	a	Rt17	M	C	3935	547	642	1240	3290					bd	
EMP	IVZ-R36	a	Rt18	M	C	4564	609	1051	2220	5030					bd	
EMP	IVZ-R36	a	Rt19	M	C	3908	498	400	1290	3880					bd	

Tech.	Locality	Thin Sect.	Grain	Text. Rel.	Spot Pos.	V	Cr	Fe	Zr	Nb	Sn	Sb	Hf	Ta	W	U
EMP	IVZ-R36	a	Rt20	M	C	3365	563	558	2740	2780					bd	
EMP	IVZ-R36	a	Rt21	M	C	3741	493	549	2510	2990					bd	
EMP	IVZ-R36	a	Rt22	M	C	3727	582	2009	1740	3570					bd	
SIMS	IVZ-R36	g^c	Rt1	M	C				1054	1192	1.8	0.28	50	33	1.5	18
SIMS	IVZ-R36	g^c	Rt2	I	C				1009	1399	1.8	0.58	53	53	1.5	17
SIMS	IVZ-R36	g^c	Rt3	I	C				1729	1249	1.5	0.19	79	50	2.0	19
SIMS	IVZ-R36	g^c	Rt4	M	C				1827	1354	1.6	bd	85	52	2.2	18
SIMS	IVZ-R36	g^c	Rt5	M	C				649	1422	1.9	0.18	34	50	1.9	17
SIMS	IVZ-R36	g^c	Rt6	M	C				2070	1271	2.2	0.26	87	74	2.2	19
SIMS	IVZ-R36	g^c	Rt7	M	C				4295	1527	2.1	0.43	176	74	1.7	19
SIMS	IVZ-R36	g^c	Rt7	M	C				4372	1526	2.0	bd	179	76	1.9	17
SIMS	IVZ-R36	g^c	Rt8	M	C				1134	1296	2.0	0.25	63	52	1.3	20
SIMS	IVZ-R36	g^c	Rt9	M	C				2976	1256	1.9	0.18	134	56	1.2	20
SIMS	IVZ-R36	g^c	Rt10	M	R				2157	1703	2.4	bd	112	102	1.4	18
SIMS	IVZ-R36	g^c	Rt10	M	C				1321	1721	2.1	bd	70	79	1.6	18
SIMS	IVZ-R36	g^c	Rt10	M	R				1080	1823	2.2	0.26	49	32	0.43	23
SIMS	IVZ-R36	g^c	Rt11	M	R				2642	1477	2.4	0.22	114	59	2.0	22
SIMS	IVZ-R36	g^c	Rt11	M	C				2536	1392	2.3	bd	110	60	2.1	19
SIMS	IVZ-R36	g^c	Rt11	M	R				2399	1247	2.1	bd	101	58	1.0	19
SIMS	IVZ-R36	g^c	Rt12	M	C				851	1431	1.5	0.21	49	61	1.9	18
SIMS	IVZ-R36	g^c	Rt12	M	R				805	1340	2.0	0.15	48	47	2.0	21
SIMS	IVZ-R36	g^c	Rt13	M	C				3093	1300	1.7	0.14	134	44	2.2	21
SIMS	IVZ-R36	g^c	Rt13	M	R				3312	1252	1.8	bd	141	41	1.7	19
SIMS	IVZ-R36	g^c	Rt14	I	C				2590	1149	1.8	bd	97	48	2.0	18
SIMS	IVZ-R36	g^c	Rt15	M	C				2019	1275	2.3	bd	100	57	2.9	27
SIMS	IVZ-R11		Rt1	M	C				970	1513	9.4	bd	47	92	4.0	12
SIMS	IVZ-R11		Rt2	M	C				2612	1754	9.4	0.23	97	87	12	10
SIMS	IVZ-R11		Rt3	M	C				2353	6573	11	bd	83	384	284	10
SIMS	IVZ-R11		Rt4	M	C				931	2343	11	0.13	45	88	43	11
SIMS	IVZ-R11		Rt5	M	C				3174	1639	12	0.19	116	57	24	14
EMP	IVZ-R11		Rt3	I	C	4532	635	4106	2806	6802					bd	
EMP	IVZ-R11		Rt4	M	C	3276	1121	537	900	2981					bd	
EMP	IVZ-R11		Rt4	M	R	3262	1211	1156	800	3737					bd	
EMP	IVZ-R11		Rt4	M	R	2930	1041	457	395	1604					bd	
EMP	IVZ-R11		Rt5	M	C	3690	1318	288	3307	1776					bd	
EMP	IVZ-R11		Rt6	M	C	3988	927	310	890	2611					bd	
EMP	IVZ-R11		Rt7	M	C	2959	858	618	1182	2202					bd	
EMP	IVZ-R11		Rt8	M	C	2387	808	496	1118	1425					bd	
EMP	IVZ-R11		Rt8	M	R	2392	788	524	1261	1579					bd	
EMP	IVZ-R11		Rt9	M	R	2190	912	489	727	896					bd	
EMP	IVZ-R11		Rt9	M	C	2398	877	1589	1070	1299					bd	
EMP	IVZ-R11		Rt9	M	R	2192	942	696	1287	1708					bd	
EMP	IVZ-R11		Rt10	M	R	3310	1180	802	2766	1997					bd	
EMP	IVZ-R11		Rt10	M	C	3365	1158	570	2472	1960					bd	
EMP	IVZ-R11		Rt11	M	C	3351	1288	362	1003	1821					bd	
EMP	IVZ-R11		Rt12	M	C	2719	1087	538	2106	1360					bd	
EMP	IVZ-R11		Rt13	M	C	3660	1170	358	2808	2051					bd	
EMP	IVZ-R11		Rt14	M	C	3894	1074	316	1132	1315					bd	
EMP	IVZ-R11		Rt15	M	C	3652	1200	392	1306	1519					bd	
EMP	IVZ-R11		Rt16	M	C	3425	1603	409	1551	2327					bd	
EMP	IVZ-R11		Rt17	M	C	4150	1345	1063	1341	2654					bd	
EMP	IVZ-R11		Rt18	M	C	3905	2861	1145	2131	4421					bd	
EMP	IVZ-R11		Rt19	M	C	3818	1622	414	2065	5113					bd	
EMP	IVZ-R11		Rt20	M	C	1311	411	902	173	201					bd	
EMP	IVZ-R11		Rt21	M	C	1622	472	1028	780	1145					bd	
EMP	IVZ-R11		Rt22	M	C	3502	1542	301	1022	1866					bd	
EMP	IVZ-R11		Rt23	I	C	4244	767	1412	2153	2061					bd	
EMP	IVZ-R11		Rt23	I	R	4096	801	1607	2338	2297					bd	
EMP	IVZ-R11		Rt24	M	C	3723	672	1655	1000	7330					bd	
EMP	IVZ-R11		Rt25	M	C	2131	984	1479	1220	2290					bd	
EMP	IVZ-R11		Rt26	M	C	3862	896	744	3280	2080					bd	
EMP	IVZ-R11		Rt27	M	C	3846	1254	344	2390	2440					bd	
EMP	IVZ-R11		Rt28	M	C	3798	1325	270	2050	2610					bd	
EMP	IVZ-R11		Rt29	M	C	3087	1682	791	1350	3530					bd	
EMP	IVZ-R11		Rt30	M	C	3055	1504	623	1400	3000					bd	

B Trace element concentrations of rutiles and ilmenites

Table B.1: Rutile (Rt) and ilmenite (Ilm) trace element concentrations (in ppm) obtained for the studied samples from the Erzgebirge. Textural relationship (Text.): M - matrix, I - included in garnet.

Tech.	Sample	Unit	Grain	Text.	Si	V	Cr	Fe	Zr	Nb	Sn	Sb	Hf	Ta	W	Th	U
SIMS	P2	GPU	Rt8	M	7947	bd			46	242	14	54	3	15	bd		7.6
SIMS	P2	GPU	Rt9	M	6708	bd			136	643	22	54	21	91	bd		13
EMP	P2	GPU	Rt1	M	1140	bd	bd	5760	bd	210					bd		
EMP	P2	GPU	Rt2	M	580	bd	bd	7240	bd	340					bd		
EMP	P2	GPU	Rt3	M	1310	bd	90	7120	bd	250					bd		
EMP	P2	GPU	Rt4	M	4060	bd	bd	6989	bd	1000					bd		
EMP	P2	GPU	Rt5	M	2370	bd	bd	8989	bd	480					bd		
EMP	P2	GPU	Rt6	M	3180	230	bd	3530	bd	760					bd		
EMP	P2	GPU	Rt7	M	630	bd	bd	6300	bd	1140					710		
EMP	P2	GPU	Rt9	M	99	bd	bd	1257	bd	880					bd		
SIMS	P2	GPU	Ilm1	M					bd	171	7.5	0.9		12	bd		0.18
EMP	P2	GPU	Ilm1	M	50	440	bd	303254	bd	100					bd		
EMP	P2	GPU	Ilm2	M	110	bd	75	306844	bd	150					bd		
EMP	P2	GPU	Ilm3	M	100	bd	bd	299524	bd	70					bd		
EMP	P2	GPU	Ilm4	M	60	bd	bd	304604	bd	370					bd		
EMP	P2	GPU	Ilm5	M	120	bd	59	292054	bd	410					bd		
EMP	P2	GPU	Ilm6	M	3890	bd	bd	280714	bd	420					610		
EMP	P2	GPU	Ilm7	M	70	bd	bd	295684	bd	540					bd		
EMP	P2	GPU	Ilm8	M	160	bd	bd	288664	bd	270					bd		
EMP	P2	GPU	Ilm9	M	20	bd	bd	310334	bd	540					bd		
EMP	P2	GPU	Ilm10	M	40	bd	bd	304944	bd	450					bd		
EMP	P38c	GPU	Rt1	M	190	bd	70	2010	bd	1330					bd		
EMP	P38c	GPU	Rt3	M	170	bd	bd	3560	bd	920					bd		
EMP	P38c	GPU	Rt6	M	1160	311	101	9660	bd	1180					bd		
EMP	P38c	GPU	Rt7	M	51	bd	bd	2989	bd	1269					bd		
EMP	P38c	GPU	Rt8	M	536	bd	bd	2970	bd	bd					bd		
EMP	P38c	GPU	Rt9	M	474	bd	bd	16283	46	424					bd		
EMP	P38c	GPU	Ilm1	M	90	bd	bd	321734	bd	320					bd		
EMP	P38c	GPU	Ilm1	M	110	bd	bd	320554	bd	220					bd		
EMP	P38c	GPU	Ilm2	M	110	bd	bd	318784	bd	360					bd		
EMP	P38c	GPU	Ilm3	M	360	bd	bd	314554	840	340					bd		
EMP	P38c	GPU	Ilm4	M	280	bd	bd	294724	bd	1110					bd		
EMP	P38c	GPU	Ilm5	M	120	bd	bd	320503	bd	700					bd		
EMP	P38c	GPU	Ilm6	M	3230	bd	bd	280545	bd	490					bd		
EMP	P38c	GPU	Ilm7	M	90	bd	bd	320963	bd	120					bd		
EMP	P38c	GPU	Ilm8	M	440	bd	60	319444	bd	560					bd		
EMP	P38c	GPU	Ilm9	M	1300	bd	bd	315543	bd	120					bd		
EMP	P38c	GPU	Ilm10	M	150	bd	bd	320723	bd	330					bd		
EMP	P38c	GPU	Ilm11	M	400	bd	bd	323794	bd	220					bd		
EMP	P38c	GPU	Ilm12	M	30	bd	bd	321054	bd	360					bd		
EMP	P38c	GPU	Ilm13	M	100	bd	bd	303424	bd	570					bd		
EMP	P38c	GPU	Ilm14	M	240	640	bd	310324	bd	850					bd		
SIMS	3/1	MEU	Rt3	I	34707				bd	2840	2156	796	1.80	110	503	0.23	2.8

B Trace element concentrations of rutiles and ilmenites

Table B.1 – continued from previous page

Tech.	Sample	Unit	Grain	Text.	Si	V	Cr	Fe	Zr	Nb	Sn	Sb	Hf	Ta	W	Th	U
SIMS	3/1	MEU	Rt4	I	948				bd	1012	2883	1062	1.08	101	bd	0.16	2.9
SIMS	3/1	MEU	Rt9	I	3556				bd	1844	67	4.9	1.83	144	bd	0.11	2.9
SIMS	3/1	MEU	Rt10	I	4576				87	1444			3.34	81	bd	0.08	5.2
EMP	3/1	MEU	Rt1	I	116	293	131	7997	42	2725					bd		
EMP	3/1	MEU	Rt2	I	120	bd	bd	8521	bd	3156					445		
EMP	3/1	MEU	Rt3	I	87	572	163	8896	bd	5013					1603		
EMP	3/1	MEU	Rt4	I	37	bd	85	5972	bd	1065					bd		
EMP	3/1	MEU	Rt5	I	97	386	228	9805	bd	2091					422		
EMP	3/1	MEU	Rt6	I	41	512	205	14411	bd	9526					bd		
EMP	3/1	MEU	Rt8	I	80	353	89	7356	46	1257					375		
SIMS	3/1	MEU	Ilm10	M	34				bd	341	21	4.6	0.14	18	bd	0.01	0.06
SIMS	3/1	MEU	Ilm12	M	1.4				bd	525	2270	729		35	bd		0.08
SIMS	3/1	MEU	Ilm14	I	978				bd	388	23		0.05	30	bd		0.06
EMP	3/1	MEU	Ilm1	I	50		bd	360823	bd	560					bd		
EMP	3/1	MEU	Ilm2	M	150	bd	bd	356523	bd	610					bd		
EMP	3/1	MEU	Ilm3	I	80	bd	bd	360333	bd	570					bd		
EMP	3/1	MEU	Ilm4	M	70	bd	bd	360783	bd	670					bd		
EMP	3/1	MEU	Ilm5	M	190	bd	bd	357523	bd	460					bd		
EMP	3/1	MEU	Ilm6	M	50	bd	bd	357613	bd	550					bd		
EMP	3/1	MEU	Ilm7	I	15449	bd	bd	359073	bd	850					380		
EMP	3/1	MEU	Ilm8	I	30	bd	bd	369102	bd	440					bd		
EMP	3/1	MEU	Ilm9	M	40	bd	bd	360783	bd	650					bd		
EMP	3/1	MEU	Ilm10	M	70	bd	bd	355973	bd	500					bd		
EMP	3/1	MEU	Ilm11	M	120	bd	bd	356523	bd	500					bd		
EMP	3/1	MEU	Ilm11	M	70	bd	bd	354513	bd	580					bd		
EMP	3/1	MEU	Ilm12	M	50	bd	bd	361073	bd	630					bd		
EMP	3/1	MEU	Ilm12	M	30	bd	bd	358273	bd	520					bd		
EMP	3/1	MEU	Ilm13	M	110	bd	bd	360423	bd	560					bd		
EMP	61c	MEU	Rt3	I	140	bd	bd	9830	bd	370					bd		
EMP	61c	MEU	Rt4	I	50	395	158	5230	bd	810					bd		
EMP	61c	MEU	Rt6	I	50	657	180	5090	50	2490					850		
EMP	61c	MEU	Rt7	I	60	539	174	5330	70	1190					590		
EMP	61c	MEU	Rt10	I	11	bd	bd	3281	203	770					bd		
EMP	61c	MEU	Rt10	I		297	bd	2656	62	499					bd		
EMP	61c	MEU	Rt11	I	64	486	76	7934	80	5640					2250		
EMP	61c	MEU	Rt12	I	16	244	53	3973	77	1125					bd		
EMP	61c	MEU	Ilm2	M	1400	bd	bd	270625	bd	430					bd		
EMP	61c	MEU	Ilm2	M	90	bd	bd	271484	bd	670					bd		
SIMS	EGB04-R10d	MEU	Rt1	M					bd	2634	769	84	2.1	198	1046		3.4
SIMS	EGB04-R10d	MEU	Rt2	M	1.0				bd	2351	639	72	2.2	206	961		4.6
EMP	EGB04-R10d	MEU	Rt3	I	40	841	510	4760	bd	4520					640		
EMP	EGB04-R10d	MEU	Rt4	I	90	831	280	5820	bd	4050					880		
EMP	EGB04-R10d	MEU	Rt5	I	70	801	240	6320	50	1970					1100		
EMP	EGB04-R10d	MEU	Rt6	I	150	bd	bd	3580	bd	830					bd		
EMP	EGB04-R10d	MEU	Rt7	M	470	bd	bd	4892	bd	1720					bd		
SIMS	EGB04-R10d	MEU	Ilm1	M					bd	671	10	0.7	0.10	72	bd		0.4
SIMS	EGB04-R10d	MEU	Ilm2	M					bd	751	12	0.4	0.09	96	bd		0.3
EMP	EGB04-R10d	MEU	Ilm3	M	90	bd	58	349506	bd	430					bd		
EMP	EGB04-R10d	MEU	Ilm4	M	60	bd	bd	347311	bd	570					bd		
EMP	EGB04-R10d	MEU	Ilm5	M	30	bd	bd	348101	bd	510					bd		
EMP	EGB04-R10d	MEU	Ilm6	M	40	bd	bd	345377	bd	300					bd		
EMP	EGB04-R10d	MEU	Ilm7	M	20	bd	bd	357262	bd	530					bd		
EMP	EGB04-R10d	MEU	Ilm8	M	110	bd	bd	348083	bd	880					bd		
EMP	EGB04-R10d	MEU	Ilm9	I	80	bd	bd	343777	bd	570					bd		
EMP	EGB04-R10d	MEU	Ilm10	M	30	bd	88	358461	bd	550					bd		
EMP	EGB04-R10d	MEU	Ilm11	M	50	bd	bd	338094	bd	1140					bd		
EMP	EGB04-R10d	MEU	Ilm12	M		bd	60	341814	bd	380					bd		
EMP	EGB04-R10d	MEU	Ilm13	I	40	bd	110	342103	bd	450					bd		
EMP	EGB04-S56	MEU	Rt1	M	240	bd	116	1153	50	380					bd		
EMP	EGB04-S56	MEU	Rt2	M	420	bd	88	2493	bd	860					bd		
EMP	EGB04-S56	MEU	Rt3	M	60	659	508	3590	60	3920					1000		

Tech.	Sample	Unit	Grain	Text.	Si	V	Cr	Fe	Zr	Nb	Sn	Sb	Hf	Ta	W	Th	U
EMP	EGB04-S56	MEU	Rt4	M	120	407	783	2948	50	2550					bd		
EMP	EGB04-S56	MEU	Rt5	M	90	501	96	3776	390	1950					850		
EMP	EGB04-S56	MEU	Rt6	M	120	309	518	2502	bd	1910					390		
EMP	EGB04-S56	MEU	Rt7	M	110	bd	bd	15233	bd	290					bd		
EMP	EGB04-S56	MEU	Rt8	M	90	475	454	2957	bd	2580					bd		
EMP	EGB04-S56	MEU	Rt9	M	100	564	679	3134	60	5680					400		
EMP	EGB04-S56	MEU	Ilm1	M	110	bd	bd	331241	bd	430					bd		
EMP	EGB04-S56	MEU	Ilm2	M	90	bd	bd	328414	bd	530					bd		
EMP	EGB04-S56	MEU	Ilm3	M	50	bd	bd	353021	bd	90					bd		
EMP	EGB04-S56	MEU	Ilm4	M	140	bd	bd	340764	bd	bd					bd		
EMP	EGB04-S56	MEU	Ilm5	M	40	bd	68	334635	bd	440					bd		
EMP	EGB04-S56	MEU	Ilm6	M		300	bd	346037	bd	350					bd		
EMP	EGB04-S56	MEU	Ilm7	M	240	bd	bd	331789	bd	300					bd		
EMP	EGB04-S56	MEU	Ilm7	M	40	bd	bd	344075	bd	90					bd		
SIMS	EGB04-R11e	GEU	Rt15	M	0.7				88	1803	112	37	4.6	117	bd		1.4
SIMS	EGB04-R11e	GEU	Rt16	M	511				53	1715	91	47	2.6	116	bd		1.6
SIMS	EGB04-R11e	GEU	Rt17	M	1675				71	1931	108	57	4.5	135	bd		1.7
SIMS	EGB04-R11e	GEU	Rt18	M	3.2				79	1949	92	48	4.1	140	bd		1.5
SIMS	EGB04-R11e	GEU	Rt19	I	225				388	2108	78	36	15	140	bd		2.5
SIMS	EGB04-R11e	GEU	Rt20	I	19				94	2275	83	22	3.2	124	bd		0.7
EMP	EGB04-R11e	GEU	Rt1	M	50	1045	775	3246	140	3050					440		
EMP	EGB04-R11e	GEU	Rt2	M	20	1306	579	2864	50	2060					510		
EMP	EGB04-R11e	GEU	Rt3	M	60	905	481	3199	bd	2480					420		
EMP	EGB04-R11e	GEU	Rt4	M	40	1287	461	2613	70	2190					370		
EMP	EGB04-R11e	GEU	Rt5	M	40	1012	449	2939	bd	1980					bd		
EMP	EGB04-R11e	GEU	Rt6	M	130	1260	600	3413	80	5150					bd		
EMP	EGB04-R11e	GEU	Rt7	M	180	1161	564	2781	bd	1930					bd		
EMP	EGB04-R11e	GEU	Rt8	M	100	527	293	2846	70	2020					bd		
EMP	EGB04-R11e	GEU	Rt9	M	140	1228	423	3013	60	1910					bd		
EMP	EGB04-R11e	GEU	Rt10	M	280	1464	317	2288	bd	1990					450		
EMP	EGB04-R11e	GEU	Rt11	M	410	960	650	2860	50	2090					bd		
EMP	EGB04-R11e	GEU	Rt12	M	510	1420	820	2310	bd	2180					bd		
EMP	EGB04-R11e	GEU	Rt13	M	130	1560	690	2270	80	2320					380		
EMP	EGB04-R11e	GEU	Rt14	M	180	1230	750	2440	bd	1930					bd		
SIMS	A15c	GEU	Rt1	M					103	2578	3207	219	5.8	224	1110		6.8
SIMS	A15c	GEU	Rt5	M					151	2308	2835	122	15	210	1085		143
EMP	A15c	GEU	Rt1	M	21	421	247	4138	117	2819					1228		
EMP	A15c	GEU	Rt1	M	36	376	267	4585	115	2800					1058		
EMP	A15c	GEU	Rt2	I		550	282	5212	58	2461					734		
EMP	A15c	GEU	Rt3	I	1.1	1347	459	4571	148	2504					676		
EMP	A15c	GEU	Rt4	I	144	780	276	9537	120	2307					436		
EMP	A15c	GEU	Rt5	M	31	821	384	5605	105	2508					1168		
EMP	A15c	GEU	Rt6	I	172	808	584	9338	201	2197					952		

C Co-authorship on scientific articles related to the topic of the thesis

C.1 Zack T & **Luvizotto GL (2006) Application of rutile thermometry to eclogites.** *Mineralogy and Petrology* **88, 69–85**

Application of rutile thermometry to eclogites

T. Zack and **G. L. Luvizotto**

Mineralogisches Institut, Universität Heidelberg, Heidelberg, Germany

Summary

Metamorphic temperatures can be derived from the Zr content in rutiles coexisting with quartz and zircon. To evaluate how well this recently calibrated rutile thermometer can be applied to eclogites, we analysed 8 samples that cover the whole temperature range of naturally-occurring eclogites (400–900 °C). Due to low concentrations expected at only 400 °C, very high precision (better than 5 percent on a 10 ppm level) secondary ion mass spectrometry (SIMS) is used in this study. In general, temperatures calculated from rutiles agree favourably with literature data as well as with our own estimates, based on several geothermobarometers and phase assemblages. However, the most important result of this study is the observation that temperatures calculated from 4–8 rutiles within a single sample always agree to within better than 25 °C, hence enforcing the claim that rutile thermometry is a powerful tool for relative temperature determinations.

Introduction

Temperature information of ordinary eclogites with high variance mineral assemblages can often only be obtained from Grt-Cpx (mineral abbreviation after *Kretz*, 1983, except Phe for phengite) Fe–Mg geothermometers. However, such calculations have large uncertainties (generally given as ± 50 °C. In unfavourable circumstances, however, uncertainties can reach up to ± 250 °C; e.g. *Proyer* et al., 2004) because Fe^{3+} in omphacites can not be reliably obtained by electron microprobe analysis unless Micro-XANES or Mössbauer analyses are available (*Schmid* et al., 2003; *Proyer* et al., 2004; *Li* et al., 2005). Rutile thermometry, which is based on the Zr content in rutile coexisting with quartz and zircon (*Zack* et al., 2004), is an attractive alternative for temperature estimates of such eclogites. Although absolute temperatures can be currently calculated to within ± 50 °C with rutile thermometry, relative temperature differences may be distinguished with much better precision.

163

The aim of this study is to evaluate how suitable rutile thermometry is for eclogite studies. The two major questions to be addressed are: (1) are the temperatures obtained from rutile thermometry consistent with results from P T estimates on well-studied eclogites, and even more important (2) how well-equilibrated are rutiles in low-T compared to high-T eclogites. To answer the first question, we chose a suite of eclogites with low-variance phase assemblages where temperatures can be constrained by several methods, e.g. stability fields of index minerals such as lawsonite, zoisite, glaucophane (*Schmidt* and *Poli*, 1998; *Poli* and *Schmidt*, 1998, 2002) and/or that allow thermobarometry by the critical assemblage Grt-Omp-Phe $\pm$ Qtz/Coe $\pm$ Ky (*Ravna* and *Terry*, 2004). The second question can be best answered if analytical uncertainties are minimised. We therefore utilized the secondary ion mass spectrometer (SIMS) where Zr in rutile can be measured with a precision of <5% even at the 10 ppm level. Please note that two samples, Syros sample SY-4 and Trescolmen sample Z6-52-1, were also used in the calibration of the rutile thermometer (*Zack* et al., 2004). Hence they are not used here to evaluate the rutile thermometer, but rather to study homogeneity in these two samples.

Analytical conditions

Zr contents were measured with a Cameca ims 3f SIMS at the Universität Heidelberg, Germany. Analyses were performed using a 14.5 keV/10 nA ^{16}O primary ion beam. An effective spot size on the sample surface of 40 μm results when no aperture is used. Positive secondary ions were nominally accelerated to 4.5 keV (energy window set to 40 eV) and an energy filtering technique with an offset of 90 eV at m/Δm (10%) of 370 was used. Count rates for ^{90}Zr were normalized to ^{47}Ti. TiO$_2$ is assumed to be always 100% in rutile, which introduces an error of <1%, as elements other than Ti and O occur only in minor amounts in eclogitic rutile (*Zack* et al., 2002b, 2004). Although matrix effects for Zr are minimal with the operating conditions employed in this study, we used two large, relatively homogeneous rutile crystals for calibration, one from Dissentis, Switzerland (Diss) and one from Gjerrestad, Norway (R10). High precision determination of Zr was conducted by isotope dilution MC-ICP-MS following the method of *Münker* et al. (2001). Values obtained are 98 $\pm$ 1 ppm for Diss and 769 $\pm$ 8 ppm for R10 (*Luvizotto* et al., in prep). Overall accuracy of the SIMS is estimated to be about 15% (*Ottolini* et al., 1993). ^{30}Si was measured together with ^{47}Ti and ^{90}Zr to detect and exclude possible contamination from zircon (*Zack* et al., 2004).

Electron microprobe analyses of selected minerals were performed with a Cameca SX51 at the Mineralogisches Institut, Heidelberg employing 5 WDS. The operating conditions were 15 kV acceleration voltage, 20 nA beam current on the Faraday cup and a 5 μm beam diameter. The matrix correction method for the raw counts was PAP. Counting times on the peak were 10 seconds for all elements, except 40 seconds for Ba.

Investigated samples

All samples for this study are from areas where extensive geothermobarometric studies have been performed. P T estimates for these areas as well as peak mineral

Application of rutile thermometry to eclogites 71

Table 1. *List of investigated samples with the assemblage grt omp rt zrc SiO₂*

Locality	Sample #	Additional phases	T in °C	P in GPa	References
Elekdag, Turkey	10d	Lws Gln Phe Pg Chl	420	1.9	this study, *Altherr* et al. (2004)
Syros, Greece	SY 4	Epi Gln Phe	480	1.8	*Trotet* et al. (2001)
Verpenesset, WGR, Norway	7a	Amp Ky Zo Phe	590	2.8	*Labrousse* et al. (2004)
Mt. Mucrone, Sesia, Italy	Mu 3 1	Gln Pg	600	1.8	*Tropper* and *Essene* (2002)
Trescolmen, Adula Nappe, Switzerland	Z6 52 1	Amp Ky Zo Phe	660	2.8	*Meyre* et al. (1999), *Ravna* and *Terry* (2004)
Liset, WGR, Norway	5b	Phl Amp	740	3.3	*Cuthbert* et al. (2000)
Lippersdorf, Erzgebirge, Germany	ERG04 R4g	Ky Zo Phe	850	3.5	this study, *Schmadicke* et al. (1992)
Saidenbach, Erzgebirge, Germany	ERG04 R2b		870	>2.9	*Schmadicke* et al. (1992)

assemblages in the samples studied are given in Table 1. The samples were chosen to cover the whole temperature range of naturally occurring eclogites, except for >1000 °C eclogite xenoliths from kimberlites where the assemblage rutile-zircon-quartz has not been reported so far.

The sample 10d from *Elekdag* can be classified as lawsonite eclogite, and represents therefore the lowest temperature group of eclogites. Inclusions of lawsonite and phengite in omphacite are common (Fig. 1a), indicating coexistence of these phases. Zoning in omphacite is comparable to zoning in other samples from this locality as described in *Altherr* et al. (2004). In BSE imaging, patchy relatively bright cores are surrounded by darker rims (due to higher X_{Jd} content) where they are in contact to late chlorite. In contact with the late chlorite, lawsonite pseudomorphed by paragonite and epidote are frequently found. Rutile is found as inclusions in omphacite (Fig. 1a), garnet and along grain boundaries. Retrogression of rutile to titanite is minor. Sample Sy4 from *Syros* is a glaucophane-bearing eclogite that contains epidote instead of lawsonite, indicating higher temperatures than the sample from Elekdag. Sample Mu3-1 from *Mt. Mucrone* is also glaucophane-bearing, but epidote/zoisite is not found in this sample; it is, however, common in other eclogites in the area. Rutile crystals large enough for SIMS analysis are found in the two Syros and Mt. Mucrone samples only in the matrix, except for one inclusion in garnet in Mu3-1. Sample Z6-52-1 from *Trescolmen* is characterized by a low variance assemblage (omp-grt-phe-ky-amp-zo-qtz-rt-zrn) and by trace element equilibrium among omphacite, amphibole and phengite (*Zack* et al., 2002a), making this sample an ideal candidate for thermobarometric studies. Although garnet in Trescolmen eclogites is often complexly zoned, Z6-52-1 garnets are less zoned due to destruction of garnet cores leading to atoll garnets, with newly crystallized phases of quartz, phengite, omphacite and a second generation of minute garnets (with compositions identical to garnet rims) within the "lagoon" (see Fig. 1b). Rutile occurs in strings of large rounded crystals following the main foliation with no sign of retrogression. From the Western Gneiss Region in Norway, a medium temperature (sample 7a from *Verpeneset*) and a high temperature eclo-

gite (sample 5b from *Liset*) have been chosen. The Verpeneset sample is characterized by the same low variance assemblage as the Trescolmen sample. Textural relationships indicate a well-equilibrated assemblage (phases occur in the matrix and as inclusions in garnet; see Fig. 1c). The Verpeneset sample is much coarser grained than the Trescolmen sample. Foliation is also less pronounced. The Liset sample is unusual as phlogopite is a stable peak pressure phase in the eclogite (*Nakamura*, 2003), which has only been reported for a few eclogites from the Western Gneiss Region and from North-East Greenland (see *Nakamura*, 2003). The highest temperature eclogites in this study are from the Erzgebirge. Sample ERG04-R4g from *Lippersdorf* is, besides samples from the Sulu-Dabie Shan area (see *Liou* et al., 1998) and from the Western Gneiss Region (*Wain* et al., 2000), the only reported sample where polycrystalline quartz (interpreted as coesite pseudomorph) is found as inclusions in zoisite (see Fig. 1e, f). All major phases (omp-grt-phe-zo) are unzoned and occur in an equal grain-sized assemblage (see Fig. 1d). Amphibole has not been observed as a primary phase and is present only as rare (<1 modal%) symplectitic albite-amphibole intergrowth. Absence of amphibole is manifestation of high peak temperatures as well as lack of retrogressive overprint, commonly observed in high-*T* eclogites. All these observations make this sample well-suited for thermobarometry (see below). Sample ERG04-R2b from *Saidenbach* is strongly retrogressed, more than 80% of omphacite are replaced by symplectitic diopside-albite ± amphibole intergrowth and phengite is completely replaced by biotite-quartz intergrowth. However, rare polycrystalline quartz (after coesite) inclusions in garnet (see also description of coesite from this locality by *Massonne*, 2001) as well as high-Zr rutile with only partial replacement by ilmenite are a manifestation of the UHP and high-*T* origin of this sample.

P–T conditions for Elekdag and Lippersdorf eclogites

In order to compare different thermobarometers with the rutile thermometer, we conducted a thorough thermobarometric analysis on one low and one high temperature eclogite from Elekdag and Lippersdorf, respectivly. Mineral analyses representing the compositions of the coexisting phases are given in Table 2.

Fig. 1. Back scattered images (**a e**) and crossed polarized photomicrograph (**f**) of characteristic textures from selected samples. **a** Inclusions of rutile, phengite and lawsonite in omphacite showing coexistence of these phases; sample 10d from Elekdag, Turkey. **b** Atoll garnet with growth of omphacite, phengite, zoisite, quartz and garnet (with composition of atoll garnet) in an area of former garnet core; sample Z6 52 1 from Trescolmen, Adula. **c** Inclusions of omphacite, amphibole, zoisite, kyanite and rutile in garnet; all inclusion phases are also found in the matrix; sample 7a from Verpeneset, Western Gneiss Region. **d** Equal grain size assemblage of garnet, omphacite, phengite, zoisite, kyanite, rutile and quartz; μm size zircon is also present; please note absence of amphibole; polycrystalline quartz inclusions after coesite are found in omphacite and zoisite (marked by black cross); sample ERG04 R4g from Lippersdorf, Erzgebirge. **e**) Detail of Fig. 1d showing two polycrystalline quartz inclusions in zoisite. Black cracks in inclusions mark boundaries between crystals. **f** Large polycrystalline quartz of Fig. 1e, but as crossed polarized photomicrograph
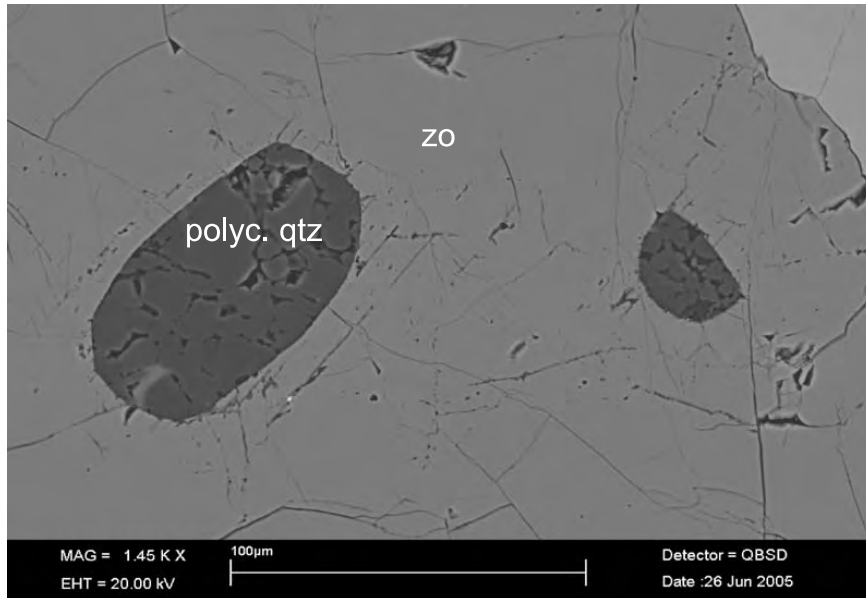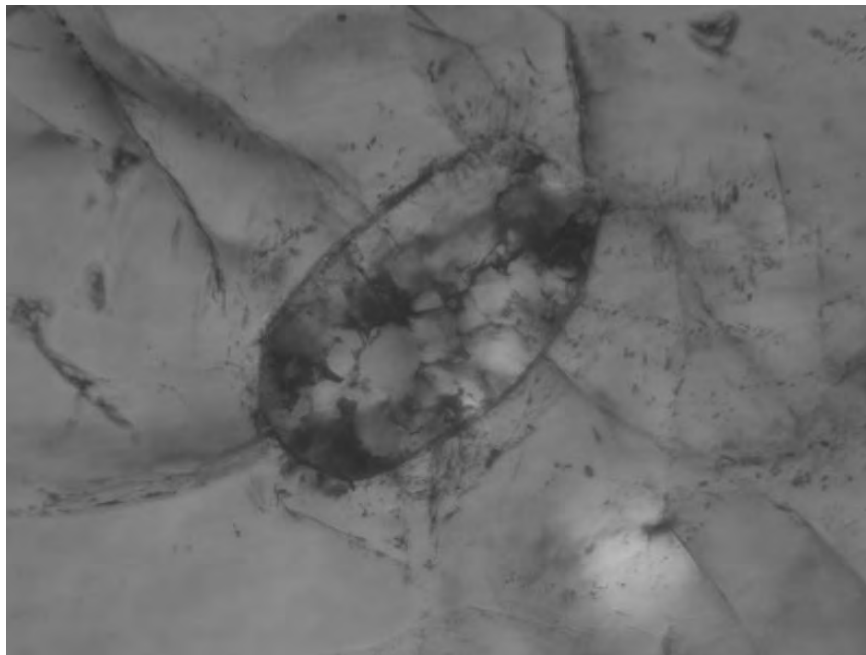
Application of rutile thermometry to eclogites 73

a

b

167

c

d

Fig. 1 (*continued*)

Application of rutile thermometry to eclogites   75
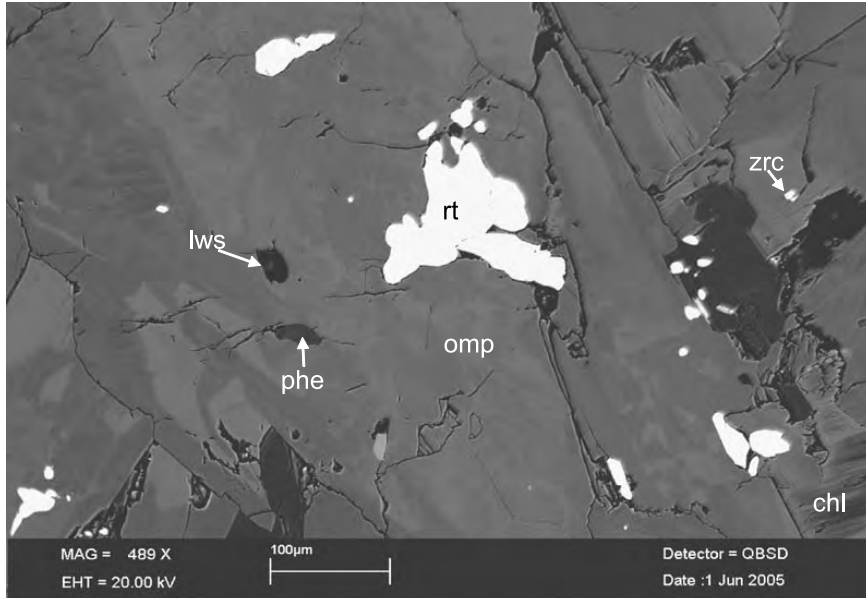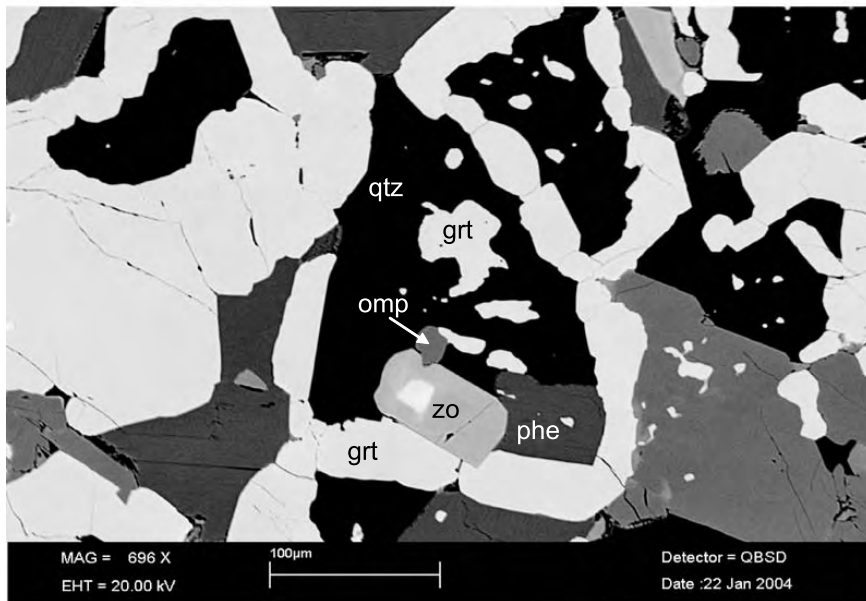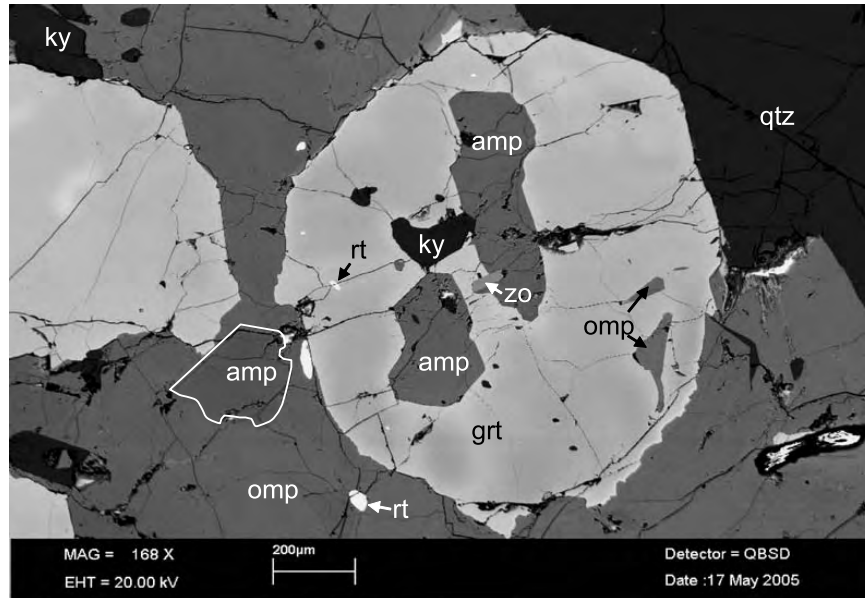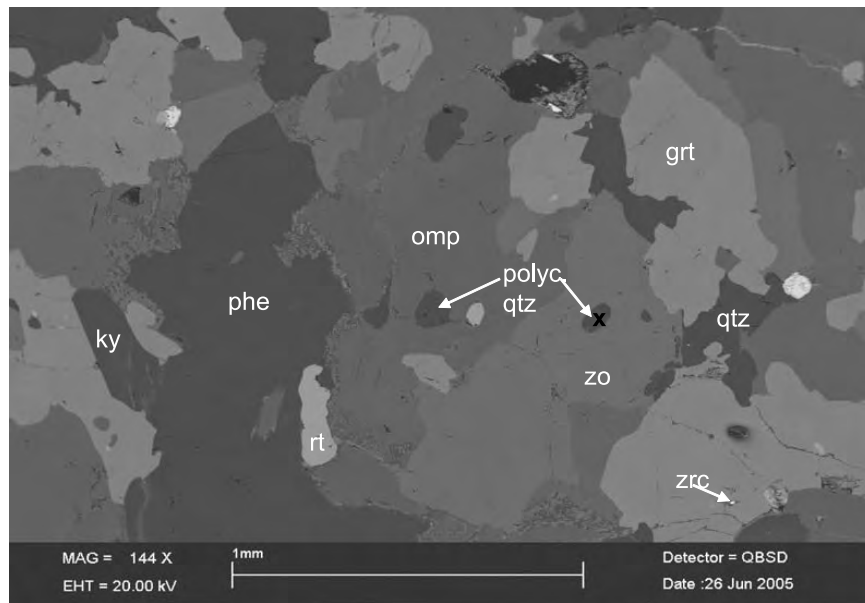
e

f

Fig. 1 (*continued*)

Table 2a. *Electron microprobe analysis of Elekdag sample 10d*

	Grt rim	Omp	Phe	Lws
SiO_2	38.13	56.44	50.90	36.65
TiO_2	0.05	0.06	0.20	0.11
Al_2O_3	21.46	9.39	27.44	28.55
Cr_2O_3	0.00	0.04	0.03	0.03
FeO	29.82	4.92	2.39	0.56
MnO	0.20	0.11	0.03	0.00
MgO	4.34	9.29	3.31	0.00
CaO	7.27	13.95	0.00	17.09
Na_2O	0.01	6.54	0.63	0.00
K_2O	0.00	0.00	10.25	0.00
BaO	n.a.	n.a.	0.16	n.a.
total	101.27	100.74	95.34	82.98
Si	2.967	1.994	3.404	2.055
Ti	0.003	0.001	0.010	0.005
Al	1.968	0.391	2.163	1.887
Cr	0.000	0.001	0.002	0.001
Fe	1.940	0.145	0.134	0.026
Mn	0.013	0.003	0.001	0.000
Mg	0.503	0.489	0.330	0.000
Ca	0.606	0.528	0.000	1.027
Na	0.001	0.448	0.081	0.000
K	0.000	0.000	0.874	0.000
Ba	0.000	0.000	0.008	0.000

Mineral formula normalized to 4 (omphacite), 5 (lawsonite), 7 (phengite) and 8 (garnet) cations

The most common thermometers for eclogite-facies rocks are calibrated for the Fe Mg exchange between omphacite and garnet according to

$$\text{diopside} + \text{almandine} = \text{hedenbergite} + \text{pyrope} \tag{1}$$

with exchange coefficient K_d defined as $(Fe^{2+}/Mg^{2+})_{grt}/(Fe^{2+}/Mg^{2+})_{cpx}$. The thermometer applied in this study is from *Krogh* (1988). Although different formulations give different results and especially the calculation of the hedenbergite component is prone to large errors due to Fe^{3+} uncertainties in electron microprobe analysis, it is clear from this reaction that sample 10d from Elekdag shows very low temperatures (K_d of 32) and sample ERG04-R4g from Lippersdorf very high temperatures (K_d of 6 at a very high grossular component in garnet of 39%). The recent paper by *Ravna* and *Terry* (2004) evaluates two more thermobarometers:

$$6 \text{ diopside} + 3 \text{ muscovite} = 2 \text{ grossular} + \text{pyrope} + 3 \text{ celadonite} \tag{2}$$

$$3 \text{ diopside} + 2 \text{ kyanite} = \text{grossular} + \text{pyrope} + 2 \text{ quartz/coesite} \tag{3}$$
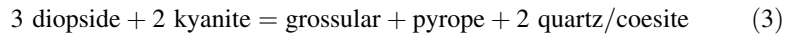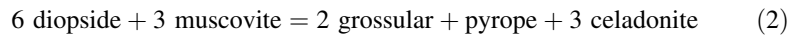
that can be applied to the samples using the activity models provided by *Ravna* and *Terry* (2004); reaction 3 is only applicable to the Lippersdorf sample. Both reactions will most likely find wide applications for the studies of eclogite-facies rocks

Application of rutile thermometry to eclogites   77

Table 2b. *Electron microprobe analysis of Lipersdorf sample ERG04 R4g*

	Grt	Omp	Phe	Zo
SiO_2	39.56	55.53	50.13	39.76
TiO_2	0.06	0.17	1.27	0.06
Al_2O_3	22.28	13.81	27.31	32.53
Cr_2O_3	0.03	0.07	0.03	0.05
FeO	17.00	2.93	0.91	0.63
MnO	0.39	0.04	0.03	0.03
MgO	6.77	8.22	3.93	0.05
CaO	14.36	14.02	0.00	24.21
Na_2O	0.05	6.03	0.47	0.02
K_2O	0.01	0.03	9.98	0.00
BaO	n.a.	n.a.	0.51	n.a.
total	100.52	100.85	94.58	97.33
Si	2.985	1.958	3.388	3.036
Ti	0.004	0.005	0.065	0.003
Al	1.981	0.574	2.175	2.927
Cr	0.002	0.002	0.001	0.003
Fe	1.073	0.087	0.052	0.040
Mn	0.025	0.001	0.002	0.002
Mg	0.762	0.432	0.396	0.006
Ca	1.161	0.529	0.000	1.980
Na	0.008	0.412	0.062	0.003
K	0.001	0.001	0.860	0.000
Ba	0.000	0.000	0.027	0.000

Mineral formula normalized to 4 (omphacite), 5 (lawsonite) and 8 (garnet and zoisite) cations

as they are almost independent of Fe^{3+} estimates, phases of interest are common and they are both fluid-absent reactions. It is noteworthy that reaction (2) could not be applied successfully to another sample from Elekdag due to high BaO contents in phengite (>2 wt%; *Altherr* et al., 2004), whereas phengite from sample 10d is low in BaO (0.16 wt%). Another geobarometer that can be applied is based on the grossular content in garnet coexisting with zoisite, kyanite and a SiO_2 phase:

6 zoisite = 5 kyanite + 4 grossular + quartz/coesite + 3 H$_2$O   (4)
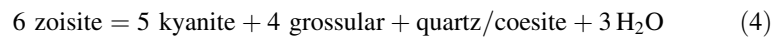
This reaction has been successfully applied by *Okay* (1995) to zoisite-bearing eclogites from the Alps and from Dabie Shan. Reaction (4) yields a pressure of 3.3 GPa (see Fig. 6 of *Okay*, 1995) for sample ERG04-R4g from Lippersdorf due to the high grossular content in garnet (a(grs) = 0.11 according to the activity model used by *Ravna* and *Terry*, 2004). It can therefore be concluded that evidence for coesite in zoisite can only be found in Ca-rich eclogites where the high grossular content in garnet stabilises zoisite up to UHP conditions. However, reaction (4) has its limitations as absolute pressure calculation requires an assumption on fluid composition (maximum pressure if a(H$_2$O) = 1).

Combining results from reactions (1) to (4) for the Elekdag and Lippersdorf samples, we calculate P T conditions of about 420 °C/1.9 GPa for Elekdag sample

10d and of about 850 °C/3.5 GPa for Lippersdorf sample ERG04-R4g (with uncertainties of ±50 °C and ±0.3 GPa; see Fig. 2a and b). These results are compatible with the coexistence of lawsonite + omphacite as well as lawsonite + rutile + omphacite in sample 10d according to the reactions

$$3 \text{ lawsonite} + 2 \text{ diopside} = \text{grossular} + 2 \text{ paragonite} + \text{quartz} + H_2O \quad (5)$$

$$\text{lawsonite} + \text{rutile} + \text{jadeite} = \text{titanite} + \text{paragonite} + H_2O \quad (6)$$
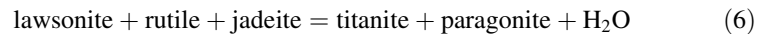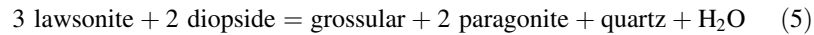
(see *Altherr* et al., 2004 for details on these reactions). Both paragonite and titanite have been found as secondary phases in Elekdag sample 10d. Results for sample ERG04-R4g are also compatible with the stability field of zoisite (lines 7 and 8), phengite (line 9) and coesite (see figure caption in Fig. 2). Compared to estimates from other studies, these results compare favourably with the 400 430 °C and

a
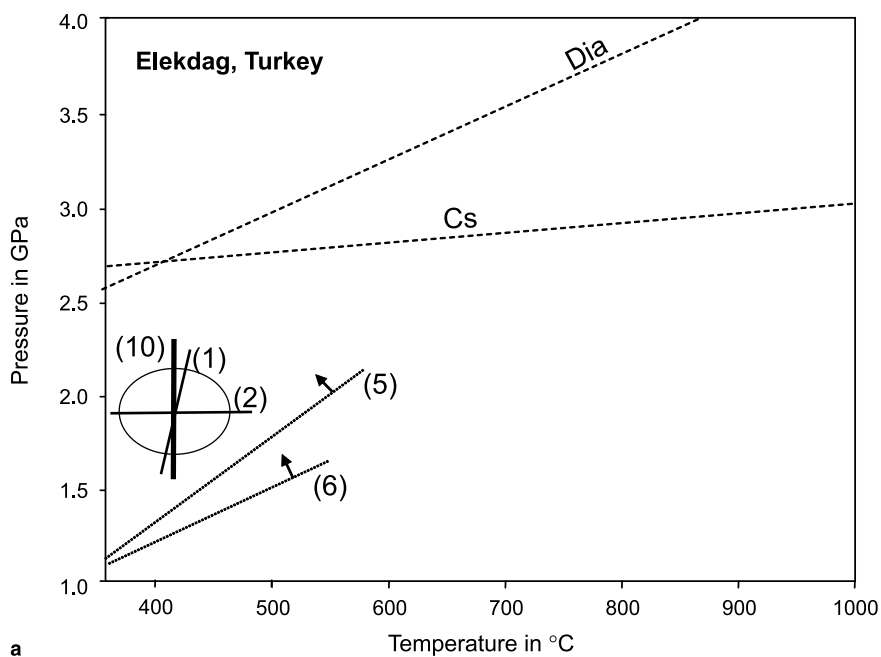
Fig. 2. Pressure temperature conditions of one low and one high temperature eclogite; gray ellipse shows approximate error of ±50 °C and ±0.3 GPa; coesite and diamond stability fields are shown for reference; equilibria for reaction curves (1) (6) are listed in the text. Activity models for reaction (2), (3) and (4) are calculated from mineral data given in Table 2 following the procedure of *Ravna* and *Terry* (2004). Arrows attached to dotted lines indicate side of stable assemblage for the given sample; curve (10) represents results from rutile thermometer as listed in Table 3. a) Low temperature eclogite represented by sample 10d from Elekdag, Turkey. b) High temperature eclogite represented by sample ERG04 R4g from Lippersdorf, Erzgebirge; reaction curve (7) indicates minimum temperature limit of zoisite (*Okay*, 1995), reaction curve (8) indicates fluid absent solidus of zoisite (*Okay*, 1995) and reaction curve (9) indicates fluid absent solidus of phengite (*Schmidt* et al., 2004)

Application of rutile thermometry to eclogites 79
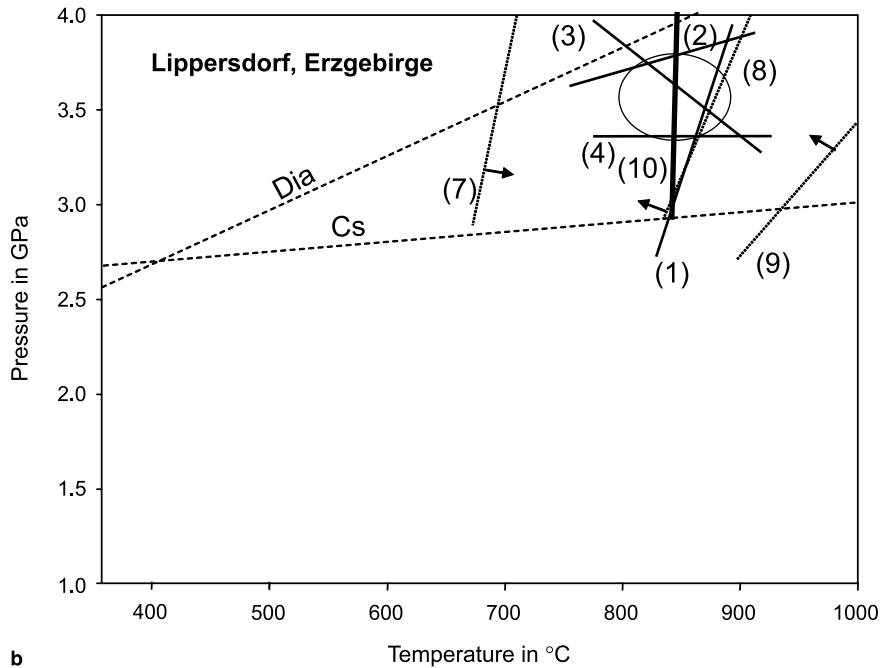
b

Fig. 2 (*continued*)

>1.35 GPa of *Altherr* et al. (2004) for other lawsonite eclogites from Elekdag and with the about 900 °C and 3.0 3.5 GPa of *Schmädicke* and *Evans* (1997) for other eclogites and garnet peridotites from the Central Erzgebirge (their Unit I). Considering our thermobarometric calculations for the Elekdag and the Lippersdorf eclogites, we conclude that these two samples represent well-equilibrated low-*T* (approx. 420 °C) and high-*T* (approx. 850 °C) eclogites, and are therefore suitable for testing other geothermobarometers.

Zr concentrations in rutile

A total of 49 spot analyses on 45 rutile grains could be obtained by SIMS (Table 3) that did show apparant Si concentrations of less than 20 ppm. Analyses with higher Si contents (together 4 analysis) were excluded from further investigation due to the possibility of minute zircon inclusions in rutile (*Zack* et al., 2004). For each sample, 4 8 rutile grains were analysed. Zr concentrations in rutile range from 15 to 1150 ppm. The calculated high precision of 3.2% (from counting statistics) on the 15 ppm analysis (see Table 3) demonstrates the advantage of SIMS analysis at these low Zr levels compared to EMP analysis (detection limit of about 20 ppm; *Zack* et al., 2004). Core-rim analyses on large rutiles demonstrates homogeneity of analysed rutiles on all concentration levels (43 vs. 43 ppm; 597 vs. 600 ppm; 953 vs. 971 ppm; 1120 vs. 1135 ppm). We would like to point out that large (≥50 μm) rutiles as inclusion phases are very rare. However, it was possible to

Table 3. *Summary of SIMS data for rutile. Zr concentration is given in ppm together with 2σ standard deviation (stdev) from counting statistics. Temperature is calculated from equation (3) of* Zack *et al. (2004); average temperature from all single spots (except analysis indicated by star) for each sample is given in bold*

	dia	tex	Zr in ppm	stdev	T in °C		dia	tex	Zr in ppm	stdev	T in °C
Elekdag (10d)						**Trescolmen (Z6-52-1)**					
r1	55	g	23	6.1%	395	r1	110	m	139	0.9%	640
r2	80	o	27	3.9%	420	r2	150	m	126	1.6%	627
r3	60	o	28	1.2%	425	r3	130	m	141	3.6%	642
r4	100	m	29	2.1%	427	r4	140	m	141	1.6%	641
r5	90	m	15	3.2%	342*						**637 ± 7**
r6	65	o	26	3.7%	414	**Liset (5b)**					
					416 ± 13	r1	200	p	303	1.7%	745
Syros (SY-4)						r2	240	a	208	1.5%	694
r1	270	m	52	2.5%	508	r3	180	m	285	1.7%	736
r2	110	m	51	2.1%	504	r4	360	m	244	2.1%	716
r3.1	210	m	43	1.5%	483	r5	100	o	257	1.4%	723
r3.2	210	m	43	4.7%	480						**723 ± 20**
r4	320	m	56	1.5%	518	**Lippersdorf (ERG04-R4g)**					
r5	250	m	43	4.2%	481	r1	95	m	583	0.7%	833
					493 ± 16	r2	90	o	608	0.9%	839
Mucrone (Mu3-1)						r3	90	g	601	0.5%	837
r1	170	m	104	1.3%	601	r4.1	85	o	597	0.4%	836
r2	170	m	100	1.3%	595	r4.2	85	o	600	0.7%	837
r3	60	g	108	1.5%	605	r5	85	o	613	0.6%	840
r4	130	m	93	1.9%	586						**837 ± 2**
r5	85	m	108	1.4%	606	**Saidenbach (ERG04-R2b)**					
r6	190	m	93	1.3%	585	r1.1	140	m	1135	0.9%	923
					596 ± 9	r1.2	140	m	1120	0.9%	921
Verpeneset (7a)						r2	70	m	1100	1.1%	918
r1	210	g	117	2.7%	617	r3	100	m	1149	1.5%	924
r2	85	o	103	1.3%	599	r4	100	m	1075	1.6%	915
r3	80	a	101	1.3%	597	r5	50	m	1040	1.0%	911
r4	55	a	114	2.2%	613	r6	50	g	1092	1.3%	917
r5	110	g	111	1.5%	609	r7	50	g	1065	1.6%	914
r6	190	g	89	0.6%	579	r8.1	150	m	953	0.3%	899
					602 ± 14	r8.2	150	m	971	1.2%	901
											914 ± 8

Labels refer to different rutiles in one thin section for each sample; repeated analysis is indicated by second digit. *dia* Diameter of rutiles in μm; *tex* textural relationship of rutiles: *m* matrix, *g* inclusion in garnet, *o* inclusion in omphacite, *a* inclusion in amphibile, *p* inclusion in phlogopite

analyse 8 rutile inclusions in garnet from 5 out of 8 samples (see Table 3 for textural information).

With the exception of one analysis (r5 from sample 10d), all rutiles from one sample give a tight clustering of Zr concentrations (see below) and we do not observe any systematic differences in composition for rutiles with different textural relationships (e.g. inclusion in garnet vs matrix). We therefore conclude that different rutile crystals in one sample (with the Elekdag sample as the only possible exception) represent one generation. As Zr concentration is strongly coupled with calculated peak temperatures in the sample set, we conclude that rutiles grew close to or at peak metamorphic conditions. Furthermore, composition was not influenced by later processes (diffusional resetting, fluid influx, etc.). This is in stark contrast to results in quartz-rich granulites where diffusional resetting is common (*Zack* et al., 2004). Diffusional resetting has the effect that rutile in the matrix has lower Zr contents than rutile included in garnet. Since inclusion rutiles and matrix rutiles in all eclogite samples have the same composition we conclude that diffusional resetting did not occur, probably due to relatively dry conditions during exhumation.

Temperatures can be derived from the Zr concentration in rutile coexisting with zircon and quartz. Following the conclusion that all rutiles from one eclogite sample can be grouped as one generation and that retrogression is negligible, we
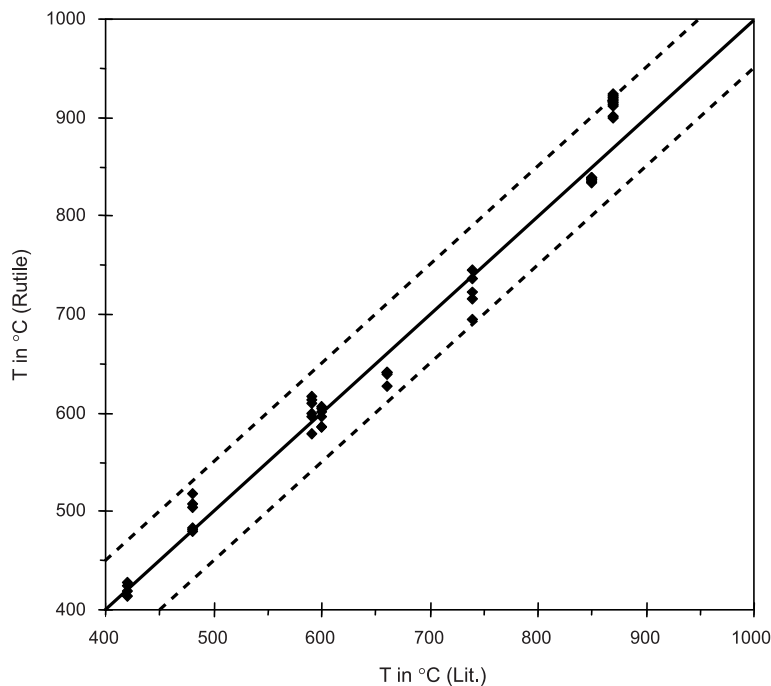
Fig. 3. Results of rutile thermometry for each single rutile analysis plotted against temperature estimates for a given eclogite locality as given in Table 1. Solid diagonal line marks an ideal 1:1 correlation, stippled lines indicate 50 °C difference between both estimates

can calculate temperatures for each rutile applying the empirical thermometer T (in °C) $= 134.7 \times \ln$ (Zr in ppm) -25 (equation 3 of *Zack* et al., 2004). This equation was derived by using average concentration instead of maximum concentration as used for equation 4 in *Zack* et al. (2004), however, results deviate from each other by only $+11$ °C at low-T eclogites to -27 °C at high-T eclogites. Applying equation 3 from *Zack* et al. (2004) has the advantage that each rutile analysis can be evaluated individually. Comparing the results obtained from the rutile thermometer of this study with literature data (Fig. 3), estimates agree to within 50 °C, the error inherited from the empirical calibration of the rutile thermometer. This confirms the reliability of rutile thermometry for a wide variety of eclogites.

The most significant result of this study is the finding that, at least for the samples investigated here, rutiles in eclogites are extremely well-equilibrated on a thin section scale, independent of textural relationships to coexisting minerals. This is illustrated in Fig. 4, where the average temperature calculated from all rutiles from one sample is plotted against the difference of calculated temperature of each single rutile from the average. With two exceptions, single rutile analyses plot within 25 °C of the average for each sample. Such a tight clustering of calculated temperatures within a sample is surprising, as equilibration is more difficult to approach with decreasing temperature.

Discussion

We would like to point out that significant improvement has been made in the calculation of pressure-temperature conditions of eclogite-facies assemblages compared to 15 years ago (see e.g. *Carswell*, 1990) when temperature estimates were
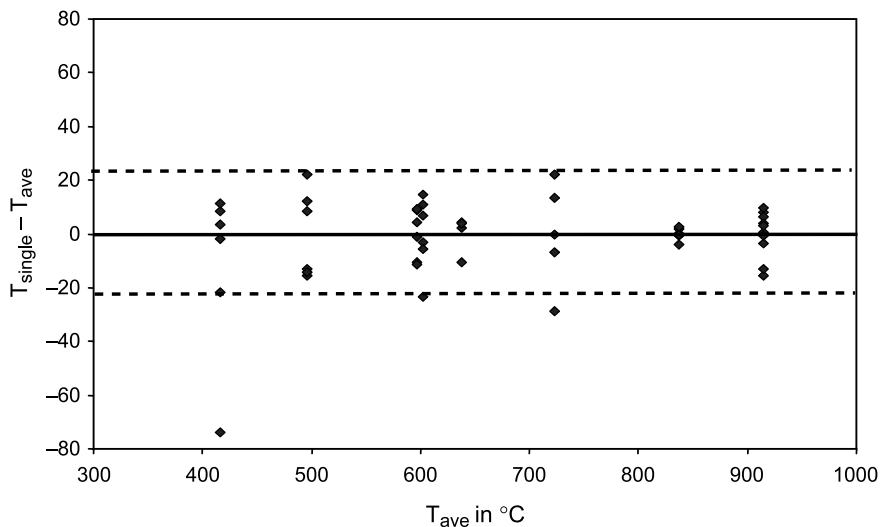
Fig. 4. Average temperature for each sample calculated with the rutile thermometer (T_{ave}) plotted against the difference of calculated temperature of each single rutile from the aver age ($T_{single} \quad T_{ave}$). Please notice that with only two exceptions, all single rutile analyses plot to within 25 °C of the average for each sample (indicated by stippled lines) indepen dent of temperature estimates for each sample

mostly based on Fe Mg cpx-grt exchange and minimum pressure was only presumed from the absence of plagioclase. As exemplified by the Lippersdorf eclogite, for the rare but world-wide occurring assemblage omp-grt-phe-ky-zo-qtz/coe-rt-zrn, 5 independent methods exist now to derive robust P T estimates from such samples if equilibrium is texturally indicated. Especially for pressure estimates, coexistence of hydrous phases (here phengite and zoisite) are crucial. All 5 methods, including rutile thermometry, give consistent results only when all phases coexisted at a given P T condition. This can be best envisioned for a rock that was fluid saturated during progressive metamorphism, so that the full assemblage was frozen in at its least hydrated stage. Hence it can be concluded that convergent P T calculations including zoisite and/or phengite require a wet protolith, e.g. hydrothermally altered basalts. On the contrary, divergent P T estimates for a given sample could imply that hydrous phases were introduced during retrograde metamorphism by fluids (for paragonite see *Zack* et al., 2001). A careful petrographic search for fluid introduction is therefore required when P T and/or a(H_2O) estimates (e.g. *Tropper* and *Manning*, 2004) involve hydrous phases.

Unfortunately, petrographic evidence for fluid infiltration under HP conditions is not always unequivocal, and hence the general question has to be asked what is the significance of a given P T estimate, including information from rutile thermometry, from a sample that has seen a more or less complex P T path. Important insight has been gathered from eclogites of the Western Gneiss Region. Here, several eclogite bodies with evidence for normal HP eclogites (zoned garnets, amphibole and monocrystalline quartz inclusions in garnet) in parts of the body contain UHP eclogites (presence of polycrystalline quartz $\pm$ coesite) in other parts of the same body. These UHP domains have been linked with recrystallization during fluid influx (*Carswell* and *Cuthbert*, 2003a). The eclogite locality Verpeneset also shows HP adjacent to UHP domains on a 10 metre scale (*Cuthbert* and *Carswell*, 2003b). Additionally, temperature calculations (non-dependent on Fe^{3+} estimates) for different samples from this locality range from 590 °C (*Labrousse* et al., 2004) to 745 °C (*Cuthbert* and *Carswell*, 2003b; *Labrousse* et al., 2004), demonstrating that different samples in one body record different stages of the P T history of the whole body. Sample 7a from this study has all petrogrographic evidence for an assemblage equilibrated at the low-T end rather than at the high-T end (presence of amphibole and zoisite in the matrix and as garnet inclusions, see Fig. 1c). Rutile thermometry is consistent with this mineral assemblage, returning temperatures of only 602 °C. Furthermore, all rutile analyses cluster tightly together (6 grains from inclusions in amphibole, omphacite as well as from garnet give a temperature range between 579 617 °C). This implies that rutiles record temperature conditions during the last stage of equilibration of the whole mineral assemblage and not neccessarily the peak temperature condition experienced during its entire P T path.

Although it has to be tested on a sample by sample basis, this study shows that it is possible now by rutile thermometry to distinguish relative temperature differences between two samples with very high precision. For example, samples 7a and Z6-52-1 (both having the same mineral assemblage) can be clearly distinguished from one another by their Zr content in rutile (temperature range is 579 617 °C and 627 642 °C, respectively), although the calculated average temperatures are only 35 °C apart. It will therefore be advantageous in future studies if metamorphic field gradients proposed for several eclogite terrains (including the Western Gneiss region,

84   T. Zack and G. L. Luvizotto

e.g. *Griffin* et al., 1985) and/or selective *P T* recordings within single eclogite bodies (e.g. *Carswell* and *Cuthbert*, 2003a) can be distinguished by rutile thermometry.

References

Altherr R, Topuz G, Marschall H, Zack T, Ludwig T (2004) Evolution of a tourmaline bearing lawsonite eclogite from the Elekdag area (Central Pontides, N Turkey): evidence for infil tration of slab derived B rich fluids during exhumation. Contrib Mineral Petrol 148: 409 425

Carswell DA (1990) Eclogite facies rocks. Chapman & Hall, New York, pp 396

Carswell DA, Cuthbert SJ (2003a) Review of the mineralogicl and microstructural evolution of ultra high pressure eclogites in the Western Gneiss region. In: *Carswell DA* (ed) Guidebook to the field excursrions in the Nordfjord Stadtlandet Almklovdalen area. Norges Geologiske Undersokelse Report no 2003.056: 3 47

Cuthbert SJ, Carswell DA (2003b) Excursion to the eclogites and gneisses of outer Nordfjord. In: *Carswell DA* (ed) Guidebook to the field excursions in the Nordfjord Stadtlandet Almklovdalen area. Norges Geologiske Undersokelse Report no 2003.056: 91 104

Cuthbert SJ, Carswell DA, Krogh Ravna EJ, Wain A (2000) Eclogites and eclogites in the Western Gneiss Region, Norwegian Caledonides. Lithos 52: 165 195

Griffin WL, Austrheim H, Brastad K, Bryhni I, Krill AG, Krogh EJ, Mørk MBE, Qvale H, Tørudbakken B (1985) High pressure metamorphism in the Scandinavian Caledo nides. In: *Gee DG, Sturt BA* (eds) The Caledonide Orogen. J. Wiley, New York, pp 783 801

Kretz R (1983) Symbols of rock forming minerals. Am Mineral 68: 277 279

Krogh EJ (1988) The garnet clinopyroxene Fe Mg geothermometer: a reinterpretation of existing experimental data. Contrib Mineral Petrol 99: 44 48

Labrousse L, Jolivet J, Andersen TB, Agard P, Hubert H, Maluski H, Shurer U (2004) Pressure temperature time deformation history of the exhumation of ultra high pressure rocks in the Western Gneiss Region, Norway. In: *Whitney DL, Teyssier C, Siddoway GS* (eds), Gneiss domes in orogeny. Geol Soc Am Spec Pap 380: 155 183

Li YL, Zheng YF, Fu B (2005) Mossbauer spectroscopy of omphacite and garnet pairs from eclogites: Application to geothermobarometry. Am Mineral 90: 90 100

Liou JG, Zhang RY, Ernst WG, Rumble D, Maruyama S (1998) High pressure minerals from deeply subducted metamorphic rocks. In: *Hemley RJ* (ed), Reviews in Mineralogy 37. Mineralogical Society of America, Washington, DC, 33 96

Massonne HJ (2001) First find of coesite in the ultrahigh pressure area of the central Erzgebirge, Germany. Eur J Mineral 13: 565 570

Meyre C, De Capitani C, Zack T, Frey M (1999) Petrology of high pressure metapelites from the Adula nappe (Central Alps, Switzerland). J Petrol 40: 199 213

Münker C, Weyer S, Scherer EE, Mezger K (2001) Separation of high field strength elements (Nb, Ta, Zr, Hf) and Lu from rock samples for MC ICPMS measurements. Geochem Geophys Geosyst 2: 2001GC000183

Nakamura D (2003) Stability of phengite and biotite in eclogites and characteristics of biotite and orthopyroxene bearing eclogites. Contrib Mineral Petrol 145: 550 567

Application of rutile thermometry to eclogites   85

Okay AI (1995) Paragonite eclogites from Dabie Shan, China   reequilibration during exhumation. J Metam Geol 13: 449 460

Ottolini L, Bottazzi P, Vannucci R (1993) Quantification of lithium, beryllium, and boron in silicates by secondary ion mass spectrometry using conventional energy filtering. Anal Chem 65: 1961 1968

Poli S, Schmidt MW (1998) The high pressure stability of zoisite and phase relationships of zoisite bearing assemblages. Contrib Mineral Petrol 130: 162 175

Poli S, Schmidt MW (2002) The petrology of subducting slabs. Annu Rev Earth Planet Sci 30: 207 235

Proyer A, Dachs E, McCammon C (2004) Pitfalls in geothermobarometry of eclogites: Fe^{3+} and changes in the mineral chemistry of omphacite at ultrahigh pressures. Contrib Mineral Petrol 147: 305 318

Ravna EJK, Terry MP (2004) Geothermobarometry of UHP and HP eclogites and schists   an evaluation of equilibria among garnet clinopyroxene kyanite phengite coesi te/quartz. J Metam Geol 22: 579 592

Schmadicke E, Evans BW (1997) Garnet bearing ultramafic rocks from the Erzgebirge, and their relation to other settings in the Bohemian Massif. Contrib Mineral Petrol 127: 57 74

Schmadicke E, Okrusch M, Schmidt W (1992) Eclogite facies rocks in the Saxonian Erzge birge, Germany high pressure metamorphism under contrasting P T conditions. Contrib Mineral Petrol 110: 226 241

Schmidt MW, Poli S (1998) Experimentally based water budgets for dehydrating slabs and consequences for arc magma generation. Earth Planet Sci Let 163: 361 379

Schmidt MW, Vielzeuf D, Auzanneau E (2004) Melting and dissolution of subducting oceanic crust at high pressures: the key role of white mica. Earth Planet Sci Let 228: 65 84

Schmid R, Wilke M, Oberhansli R, Janssens K, Falkenberg G, Franz L, Gaab A (2003) Micro XANES determination of ferric iron and its application in thermobarometry. Lithos 70: 381 392

Tropper P, Essene EJ (2002) Thermobarometry in eclogites with multiple stages of mineral growth: an example from the Sesia Lanzo Zone (Western Alps, Italy). Schw Mineral Petrog Mitt 82: 487 514

Tropper P, Manning CE (2004) Paragonite stability at 700 °C in the presence of H_2O NaCl fluids: constraints on H_2O activity and implications for high pressure metamorphism. Contrib Mineral Petrol 147: 740 749

Trotet F, Vidal O, Jolivet L (2001) Exhumation of Syros and Sifnos metamorphic rocks (Cyclades, Greece). New constraints on the P T paths. Eur J Mineral 13: 901 920

Wain A, Waters D, Jephcoat A, Olijynk (2000) The high pressure to ultrahigh pressure eclogite transition in the Western Gneiss Region, Norway. Eur J Mineral 12: 667 687

Zack T, Rivers T, Foley SF (2001) Cs Rb Ba systematics in phengite and amphibole: an assessment of fluid mobility at 2.0 GPa in eclogites from Trescolmen, Central Alps. Contrib Mineral Petrol 140: 651 669

Zack T, Foley SF, Rivers T (2002a) Equilibrium and disequilibrium trace element partitioning in hydrous eclogites (Trescolmen, Central Alps). J Petrol 43: 1947 1974

Zack T, Kronz A, Foley SF, Rivers T (2002b) Trace element abundances in rutiles from eclogites and associated garnet mica schists. Chem Geol 184: 97 122

Zack T, Moraes R, Kronz A (2004) Temperature dependence of Zr in rutile: empirical calibration of a rutile thermometer. Contrib Mineral Petrol 148: 471 488

Author's address: *T. Zack* (e mail: tzack@min.uni heidelberg.de), *G. L. Luvizotto*, Minera logisches Institut, Universität Heidelberg, INF 236, 69120 Heidelberg, Germany

**C.2 Triebold S, von Eynatten H, Luvizotto GL, Zack T (2007)
Deducing source rock lithology from detrital rutile
geochemistry: An example from the Erzgebirge, Germany.
Chemical Geology 244, 421-436.**

Deducing source rock lithology from detrital rutile geochemistry: An example from the Erzgebirge, Germany

Silke Triebold [a,*], Hilmar von Eynatten [a], George Luiz Luvizotto [b], Thomas Zack [b]

[a] *Abt. Sedimentologie und Umweltgeologie, GZG, Universität Göttingen, Goldschmidtstr. 3, 37077 Göttingen, Germany*
[b] *Mineralogisches Institut, Universität Heidelberg, Im Neuenheimer Feld 236, 69120 Heidelberg, Germany*

Editor: R.L. Rudnick

Abstract

This study evaluates the applicability of rutile trace element geochemistry to provenance studies. The study area is the Erzgebirge in eastern Germany, where metamorphic rocks ranging from lower greenschist facies conditions up to granulite facies conditions are exposed. We collected sand and rock samples from small catchment areas for a comparative analysis of rutile geochemistry using wavelength-dispersive electron microprobe. Our results show that rutile geochemistry is a powerful tool in provenance studies, allowing for the identification of source lithologies and an evaluation of the host orogen's metamorphic history.

The log (Cr/Nb) ratio has proven to be decisive in discriminating between mafic and metapelitic lithologies. It is also useful for identifying different source rocks when plotted versus a third element or proxy. Furthermore, our results suggest that rutile thermometry can be applied to a much wider range of lithologies than previously assumed.

A quantification of temperature populations within single sand samples shows that at high-grade metamorphic conditions, such as those found in the Erzgebirge, more than 65% of rutiles do not re-equilibrate during retrograde metamorphism and thus retain their peak temperature chemistry. Such samples, which have equilibrated at recent metamorphic conditions, can be identified by their 2-σ standard deviations of less than 120 °C. Below 550 600 °C, no complete equilibration is reached. Rutiles from greenschist facies and lower metamorphic conditions in the Erzgebirge still inherit relict temperatures from a former metamorphic cycle. They partly record very high temperatures >950 °C and supposedly derive from erosion of the west African craton in Ordovician time.

© 2007 Elsevier B.V. All rights reserved.

Keywords: Rutile; Trace elements; Geothermometer; Provenance; Erzgebirge; West African craton

1. Introduction

Using the chemical and radiometric analysis of detrital minerals as tracers in ancient and modern sediments to decipher source rock lithology, metamorphic grade, and geochronology has found widespread application in recent decades. These studies focus primarily on the

* Corresponding author. Tel.: +49 551 39 3455; fax: +49 551 39 7996.
E-mail addresses: striebo@gwdg.de (S. Triebold),
hilmar.von.eynatten@geo.uni-goettingen.de (H. von Eynatten),
gluvizot@min.uni-heidelberg.de (G.L. Luvizotto),
tzack@min.uni-heidelberg.de (T. Zack).

characteristics of zircon (e.g., McLennan et al., 2001; Rahl et al., 2003; Carter and Bristow, 2003; Jacobsen et al., 2003; Griffin et al., 2007), and some other, most commonly heavy, mineral species (e.g., Morton, 1987; Pober and Faupl, 1988; Morton, 1991; von Eynatten et al., 1996; von Eynatten and Gaupp, 1999; von Eynatten, 2003; von Eynatten and Wijbrans, 2003; Griffin et al., 2007). Recently, rutile's trace element geochemistry has received greater attention (Götze, 1996; Preston et al., 2002; Zack et al., 2004b; Stendal et al., 2006). Rutile constitutes an important tool for source rock characterisation and holds supplementary information, which cannot be derived from other mineral species.

Due to its high physical and chemical stability during erosion, weathering, transport, and diagenesis, rutile is one of the most stable heavy minerals (e.g., Morton and Hallsworth, 1999). The dominant host rock types for rutile are medium to high grade metamorphic rocks and sediments (Force, 1980, 1991). Other common rock types, such as low grade metamorphic rocks or most igneous rocks, are thought to lack rutile. This rutile absent definition excludes occurrences of needles and small crystals (<63 μm in diameter; sagenite and authigenic rutile), as these are commonly not processed during detrital

mineral separation. According to Force (1980, 1991), rutile forms under amphibolite facies and higher metamorphic conditions. During new metamorphic cycles, it reacts to form other Ti rich phases under greenschist facies conditions. Thus unlike zircon, rutile commonly witnesses only one metamorphic cycle, and the recorded information is not obscured by previous metamorphic events. These characteristics make rutile a complimentary, if not a preferable candidate in provenance studies.

Zack et al. (2002) have shown that there exists a strong correlation between whole rock Nb/Ti ratios and Nb contents in associated rutiles. The same is true regarding Cr characteristics. Zack et al. (2004b) constrain concentration ranges for Nb and Cr in rutile deriving from pelitic and mafic source rocks: Nb contents between 900 and 2700 ppm together with Cr<1000 ppm point to metapelitic sources, whereas Nb<900 ppm and/or high Cr contents >1000 ppm point to mafic source lithologies. Rutile derived from kimberlitic source rocks has very high concentrations (often $>10,000$ ppm) of Cr and/or Nb (Haggerty, 1991). Lastly, high U contents provide the opportunity to apply U/Pb or (U Th)/He dating techniques (e.g., Mezger et al., 1989; Vry et al., 2003; Vry and Baker, 2006).
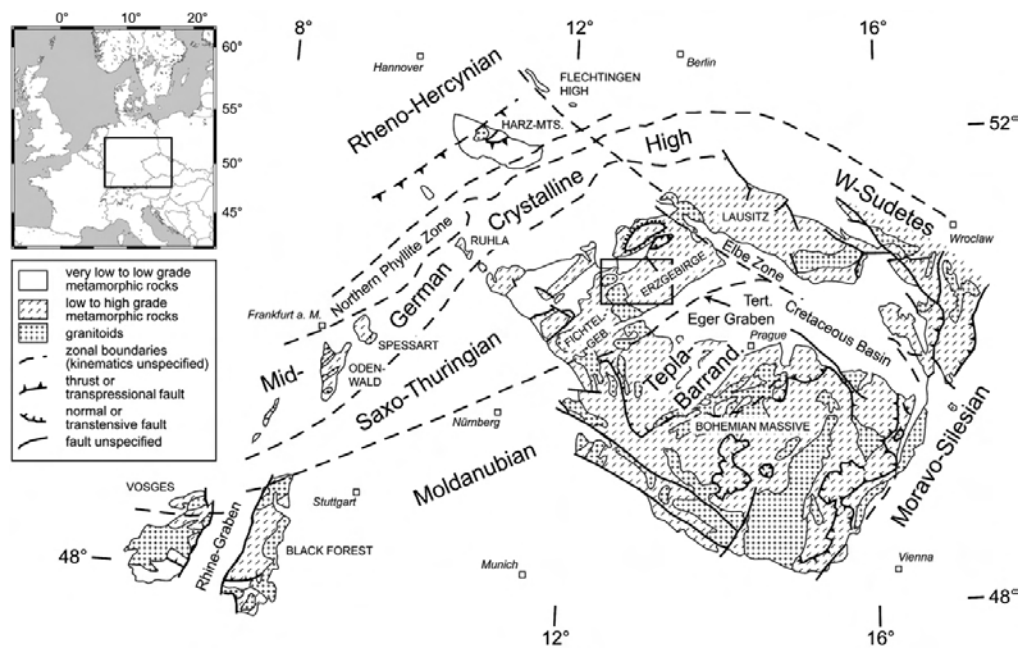
Fig. 1. Geological sketch of the Central European Variscides, modified after Dallmeyer et al. (1995). The rectangle shows the position of the map in Fig. 2. The small inset figure shows a political map of Europe with the location of the geological sketch marked by a rectangle.

Zack et al. (2004a) and Watson et al. (2006) established rutile thermometry based on Zr contents. The description of this thermometer and its application in the Erzgebirge will be discussed separately in Section 4.

In order to further explore the applicability of rutile geochemistry for provenance studies, and to investigate and directly compare trace element characteristics between sediments and their source rocks, modern sands and rocks from the same drainage areas were sampled. The Erzgebirge (Germany) was chosen as a sampling area, because it has a great number of various rock types displaying a large range in metamorphic conditions from lower greenschist to granulite facies. Here we concentrate on Nb and Cr systematics as a proxy for source rock lithology as well as on Zr systematics as a tool for source rock temperatures, but note that further geochemical signals in rutiles should store important additional information (e.g., Mezger et al., 1989; Zack et al., 2002; Vry and Baker, 2006).

2. Geological setting

The Erzgebirge metamorphic crystalline complex is situated at the northwestern border of the Bohemian Massive (Fig. 1). It belongs to the Saxo Thuringian zone of the central European Variscides and is bordered by the Elbe Zone in the east, the Tertiary Eger Graben in the south, and by very low grade Paleozoic sediments of the Saxothuringian basin in the northwest. The Erzgebirge is characterised by a large scale antiformal structure consisting of several tectonometamorphic units, intruded by post tectonic (Hercynian) granitoids of late Variscan age. Today it is widely accepted that the Erzgebirge represents a stack of tectonic units resulting from continent continent collision processes (deformation, metamorphism and exhumation) during the Variscan orogeny (e.g., Willner et al., 1997, 2000; Rötzler et al., 1998; Mingram, 1998).

According to Rötzler et al. (1998), the western Erzgebirge consists of a sequence of five tectonometamorphic units with low to high grade *PT* histories (up to at least 950 °C and 4.5 GPa; Massonne, 1998). The division is based on petrological studies, tectonic investigations and geochemical correlations, being the units defined on the basis of dominant rock associations and their general trends in metamorphic evolution (Schmädicke et al., 1992; Mingram, 1998; Rötzler et al.,
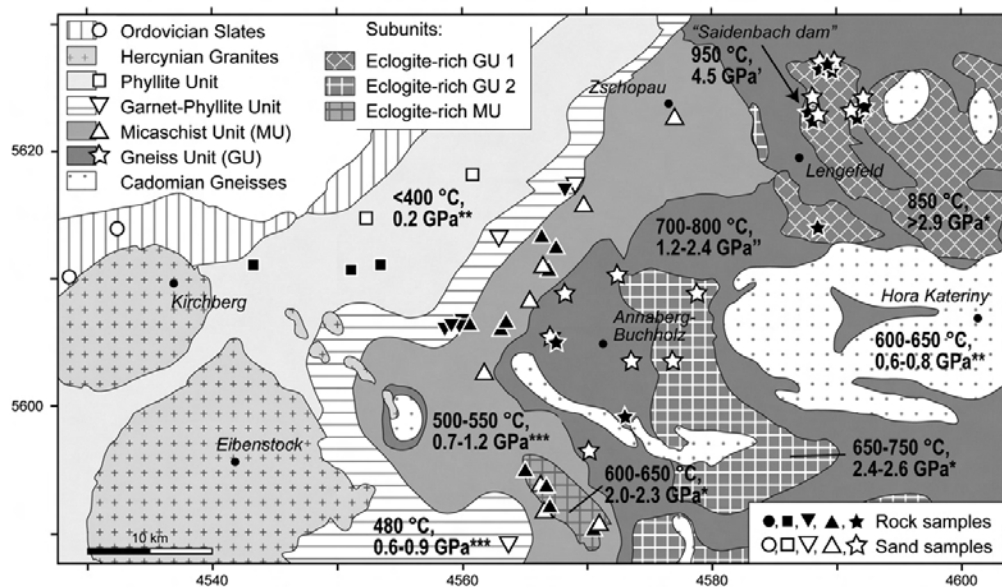
Fig. 2. Geological sketch of the western part of the Erzgebirge showing the locations of rock- and sand samples containing rutile. Samples from the same units are shown in similar symbols. The temperature and pressure estimates from preserved metamorphic assemblages are from: *Schmädicke and Müller (2000), **Mingram and Rötzler (1999), ***Rötzler et al. (1998), 'Massonne (1998), and ''Willner et al. (1997). The coordinate grid is Gauss-Krüger (Potsdam). Compiled and redrawn from Willner et al. (1997), Mingram and Rötzler (1999), Schmädicke and Müller (2000), and geological maps of the Erzgebirge (1:25000 and 1:200000).

1998; Willner et al., 1997). However, as highlighted by Willner et al. (1997), even these units cannot be regarded as homogeneous and coherent bodies. In the present study, we label these units, from tectonically lowermost to uppermost, the Cadomian Gneisses, Gneiss Unit (GU), Micaschist Unit (MU), Garnet Phyllite Unit (GPU), Phyllite Unit (PU), and Ordovician Slates (OS). This labelling system is mainly adapted from Mingram (1998). After Schmädicke et al. (1992) the GU and MU both have experienced a *PT* path, which went through eclogite facies peak metamorphic conditions. Because lithology is a crucial issue in this study, we further define subunits: eclogite rich Gneiss Units 1 (EGU1) and 2 (EGU2), both sections having earlier, higher *PT* conditions preserved, and likewise an eclogite rich Micaschist Unit (EMU). In this work the term "eclogite" is only used for rocks with mafic bulk compositions, predominantly composed of garnet and clinopyroxene. The eclogite rich Gneiss Unit 1, eclogite rich Gneiss Unit 2, and the eclogite rich Micaschist Unit, respectively, correspond to the High Pressure Units 1, 2 and 3 defined by Schmädicke et al. (1992) and Schmädicke and Evans (1997). A summary of the published *P* and *T* conditions of the best preserved metamorphic stage in each unit and subunit is shown in Fig. 2.

Mingram (1998) has shown that the protoliths of all Variscan metamorphic units are similar and correspond to the very low grade Ordovician Slates unit (OS). They largely consist of mature sediments, which were exposed to prolonged tropical weathering and extensive reworking. As these characteristics reappear in several depositional sequences, Mingram (1998) concludes that it was on a passive margin setting with similar erosion , transport and sedimentation conditions over a long time period from upper Proterozoic to Ordovician. Linne mann and Romer (2002) relate this passive margin to the west African craton.

3. Sampling and methods

Samples cover all metamorphic units with tempera tures ranging from <400 °C to 950 °C. One sand sample was collected in the Hercynian Granites (near Kirchberg) to test for rutile occurrence. Since no rutile was found, we regard these granites generally as rutile free. They cannot deliver significant amounts of rutile to the sediments exported from such areas. Fig. 2 shows the locations of all samples containing rutile. The Cadomian (Ortho) Gneisses were excluded from the sampling campaign.

In order to ensure the comparability between sands and associated rock samples, and to keep the sands'

compositions simple in terms of distinguishable rutile types, small catchment areas were investigated ranging from 100 m^2 (in quarries) up to 10 km^2. Rock samples from 28 locations and 28 sand samples were collected, with the rocks' sampling locations generally relating to the sampled sands' drainage areas. Sand samples were collected in the kg range, depending on how much material was available. Attention was paid to gain a large proportion of fine sand in a sample. Rock samples were hand sample sized, except for the quartzites, in which case extra material was collected. The main rock types studied include eclogite, garnet gneiss, felsic granulite, garnet micaschist and quartzite in the Gneiss Unit; garnet (+/ chloritoid) micaschist, quartzite, and eclogite in the Micaschist Unit, and phyllites in the Grt Phyllite and Phyllite units. A list of all samples together with the sample locations can be reviewed in Table S1 (electronic supplement).

Rock samples were prepared as polished thin sections. These were coated with carbon to ensure conductivity in electron microprobe (EMP) analysis. From the sand samples and one crushed quartzite sample from the eclogite rich Micaschist Unit, rutile was extracted via sieving, heavy liquid separation, magnetic separation, and handpicking. von Eynatten et al. (2005) stated that trace elements in rutiles are not systematically related to grain size fractions (63 125 and 125 250 μm). Therefore, investigated crystals derive from one fraction containing the largest fraction of rutile (80 200 μm). Yet, as it was observed that magnetic separation fractionates rutiles, especially according to contents of Fe and V, special care was taken to extract rutile from all magnetic fractions. Extracted separates were embedded in epoxy resin discs, polished, and coated with carbon to ensure conductivity for EMP analysis.

The investigated crystals were identified as rutiles with micro Raman spectroscopy (Horiba Jobin Yvon Labram HR UV 800, 633 nm laser excitation, 17 mW laser power, 1200 l/mm grating, Peltier cooled CCD detector).

Electron microprobe analyses on rutile separates from sands were performed in Göttingen using a JEOL JXA 8900 and 25 kV accelerating voltage. The beam current was set to 80 nA. Matrix correction was performed using CITZAF after Armstrong (1995). No analysis obtained Mg above detection limit. Rock samples were analysed in Heidelberg on a CAMECA SX51. The accelerating voltage was set to 20 kV and the beam current to 100 nA. All EMP measurement conditions can be reviewed in Table 1. EMP analyses on rutile standards (Luvizotto et al., in preparation)

Table 1
EMP analysis conditions for the setups used in Göttingen and Heidelberg

Element	Ti	W	Nb	Sb	Ta	Si	Zr	Sn	Hf	Al	V	Cr	Mg	Fe
EMP-Göttingen														
X-ray line	Kβ	Lα	Lα	Lα	Lα	Kα	Lα	Lα	Lα	Kα	Kα	Kα	Kα	Kα
Counting time (s)	30	200	300	300	300	150	300	200	300	150	200	200	150	150
Background time (s)	15	100	150	150	150	50	150	100	150	50	100	100	50	50
2-σ DL (ppm)	920	80	70	40	50	70	40	60	50	60	220	50	20	40
2-σ error (ppm)	4050	140	100	100	100	40	30	40	50	20	70	20		20
EMP-Heidelberg														
X-ray line	Kβ	Lα	Lα			Kα	Lα					Kα		Kα
Counting time (s)	100	100	300			50	200					200		100
Background time (s)	50	50	150			25	100					100		50
2-σ DL (ppm)	130	350	60			20	40					50		40
2-σ error (ppm)	990	90	60			20	40					20		20

"Counting time" refers to the counting times on peak positions, "Background time" to the counting times on upper-and lower background positions. Errors and detection limits (DL) are median values calculated according to counting statistics.

performed in both laboratories were compared in order to ascertain the comparability between results from the Heidelberg and Göttingen electron microprobes.

4. Rutile thermometry

Rutile thermometry, as discussed by Zack et al. (2004a) and Watson et al. (2006), is based on the increasing incorporation of Zr into rutile with increasing temperature. In many natural systems, as in the rocks and experimental assemblages investigated by both authors, the activity of ZrO_2 in rutile is buffered by quartz and zircon to a constant value, and the reaction can be written as

$$ZrSiO_4(\text{zircon}) \leftrightarrow ZrO_{2(\text{rutile})} + SiO_2(\text{quartz}). \quad (1)$$
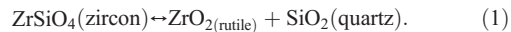
In sediments or sedimentary rocks, the buffer assemblage zircon rutile quartz cannot be directly observed. However, Zack et al. (2002, 2004a,b) proved that Nb and Cr systematics provide a tool to identify pelitic (implying felsic) source rock lithologies. Assuming that felsic and
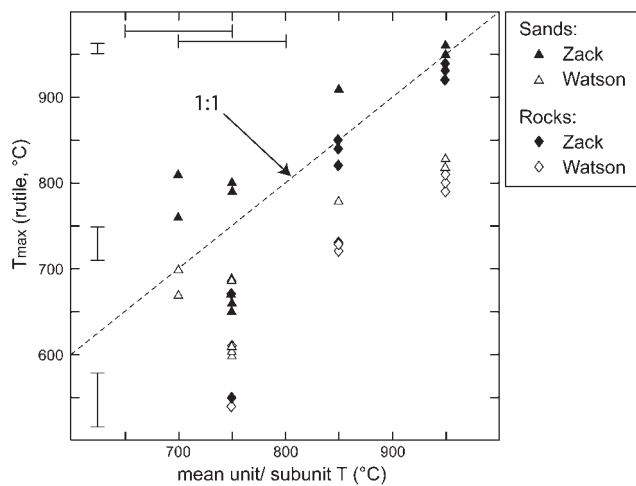
Fig. 3. Plot of maximum temperatures calculated from Zr contents analysed by EMP in rutile after Zack et al. (2004a) ("Zack") and Watson et al. (2006) ("Watson") versus mean unit-or subunit temperatures (ranges are shown as horizontal bars) for sand samples (triangles) and rock samples (diamonds). The 2-σ counting statistical errors are shown as vertical bars.

pelitic rocks contain quartz and zircon, the rutile thermometer can reliably be applied to crystals with high Nb and low Cr contents, as explained in the introduction section.

The Zack et al. (2004a) empirical thermometer equation is calibrated on natural samples from a wide range of temperatures and pressures. It therefore inherits uncertainties from the temperature/pressure estimates of these samples calculated from other geothermobarom eters. On the other hand, Watson et al. (2006) calibrated their thermodynamically robust thermometer equation based on experiments at 1 GPa backed up by a few natural samples also mostly from the same pressure range.

In the Erzgebirge, metamorphic temperatures higher than 600 °C, and thus sensitive to the choice of the thermometer equation (compare Watson et al., 2006), are displayed in the whole GU and the EMU. Fig. 3 shows that maximum temperatures calculated for GU samples from rutile geochemistry after Zack et al. (2004a) generally agree very well with those found in conventional thermometry by Schmädicke and Müller (2000), Massonne (1998), and Willner et al. (1997). For the same samples the thermometry after Watson et al. (2006) yields maximum temperatures that are too low, especially for the higher grade (>800 °C) subunits with more uniform metamorphic temperatures.

Thermometry differences at very low temperatures <450 °C will not be addressed in this study, as we refer to EMP analyses and hence Zr contents larger than 40 ppm.

The influence of high pressures as found in the Erzgebirge (e.g., diamond bearing gneisses at Saiden bach dam) on temperatures at 1 GPa calculated after Watson et al. (2006) has not been quantified yet, but experimental results by Degeling (2003) show that these most likely account for the differences observed here. Hence failing a better approximation, we conclude that for metamorphic conditions like those in the Erzgebirge the Zack et al. (2004b) thermometer equation is more suitable, and will be used for all further temperature calculations in this study. However, it should be stressed that for normal sedimentary provenance studies, the choice of the thermometer is not crucial, as pressure conditions for the source rocks are unknown and thus no reliable temperature estimation can be made. With the purpose of merely discriminating temperature popula tions, both Zack et al. (2004a,b) and Watson et al. (2006) thermometer equations are equally suitable.

5. Results

5.1. Geochemical tools: Cr, Nb and the Zr thermometer

As expected (Mingram, 1998), different metamorphic units in the Erzgebirge cannot be distinguished comparing Cr and Nb characteristics of rutiles in sand samples from all locations (Fig. 4). EMP analyses of sand samples can be reviewed in Table S2 (electronic supplement). Nb contents range up to 10,000 ppm, with the majority
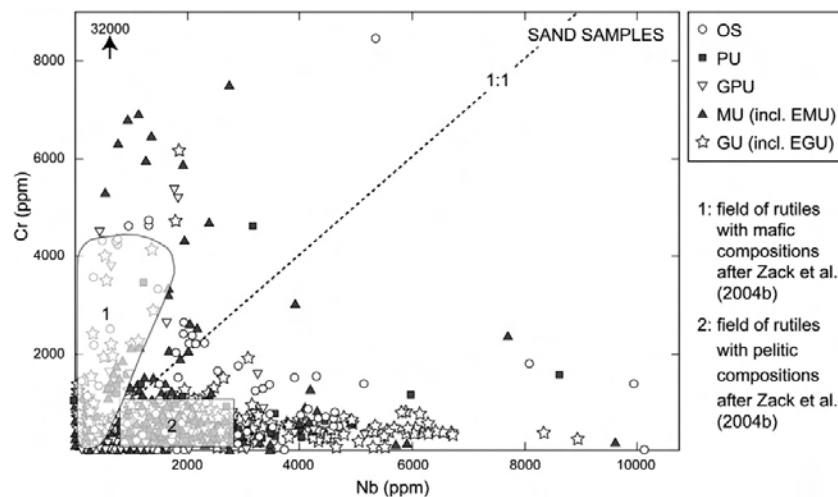
Fig. 4. Plot of Nb vs. Cr (ppm) for Erzgebirge sand samples. The symbols represent the samples' geological units, analogous to those used in Fig. 2. Analyses are performed by EMP. The 2-σ errors are as large as the symbols' size. OS: 2 samples; PU: 2 samples; GPU: 3 samples; MU (incl. EMU): 8 samples; GU (incl. EGU): 13 samples.
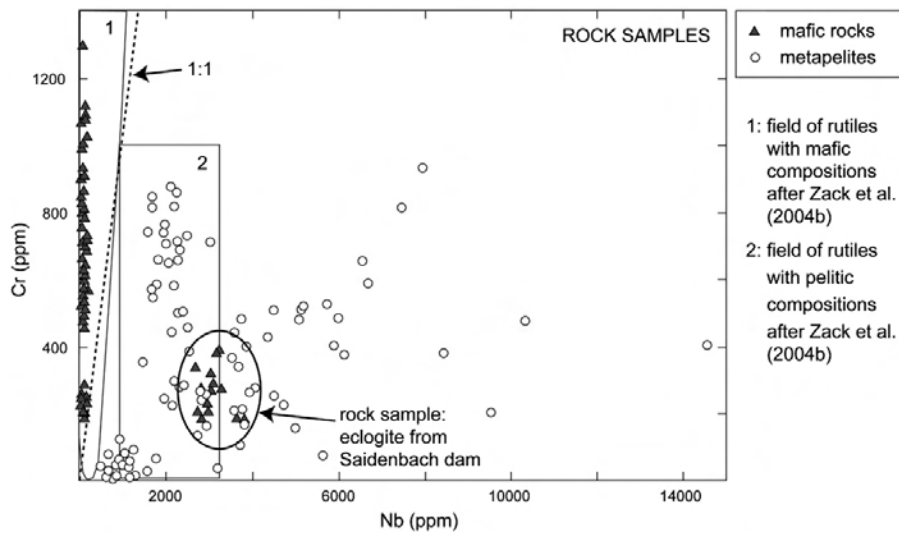
Fig. 5. Plot of Nb vs. Cr (ppm) for rock samples from the Erzgebirge. Analyses were performed by EMP. The 2-σ errors are approximately as large as the symbols' sizes. Metapelites: 11 samples; mafic rocks: 9 samples.

plotting below 7000 ppm. The highest obtained Cr values are around 32,000 ppm, but the frequency thins out after >2000 ppm. Especially regarding Nb, rutiles from the Erzgebirge exhibit higher contents than suggested for classification by Zack et al. (2004b) into mafic and pelitic provenances (Fields 1 and 2 in Fig. 4). Thus it needs to be
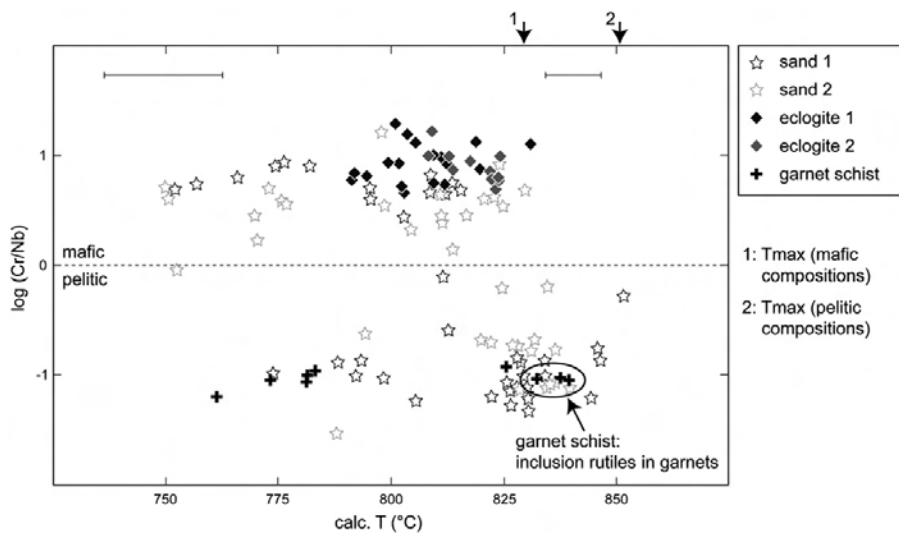
Fig. 6. Plot of temperatures calculated from Zr contents after Zack et al. (2004a) vs. log(Cr/Nb) for the northernmost sampling area, ca. 4 km north of Saidenbach dam (Fig. 2). Mafic and pelitic compositions are plotted according to their log(Cr/Nb). The error bars correspond to 2-σ analytical errors in Zr contents by EMP. For the garnet schist, rutile inclusion analyses are indicated, all other analyses from this rock are matrix rutiles. Inclusion and matrix rutile analyses for the eclogite samples do not show contrasting temperature distributions and therefore are combined. The plotted samples accord to samples EGB-04-S44, EGB-04-S45, EGB-04-R3a2, EGB-04-R4f1, and EGB-04-R4g in Tables S1 and S2 (electronic supplement).

determined whether all analyses can be used for the purpose of source lithology discrimination.

When consequently evaluating analyses of rutiles in rock samples (Fig. 5), it is evident that those grains originating from metapelites (11 samples are represented in Fig. 5) plot at high Nb contents compared to the majority of rutiles from mafic rocks (9 samples are represented in Fig. 5), while mafic rutiles in all but one sample exhibit low Nb contents. EMP analyses of rock samples can be reviewed in Table S2 (electronic supplement).

One mafic sample (an eclogite from the ultra high pressure Saidenbach dam region in the EGU1) contains rutile plotting within the field for pelitic compositions.

Massonne and Czambor (2007) relate eclogites from the region around Saidenbach to a within plate basaltic protolith, formed from a relatively low degree of melting. High Nb/Ti ratios of the protolith then result in rutiles with high Nb contents. This example shows that the classification of rutiles by Nb and Cr contents into mafic and pelitic host rocks needs to be treated with care in these, although rather rare, examples.

The fields for mafic and pelitic compositions, as confirmed by rutile analyses from confined source lithologies (Figs. 4 and 5), are well separated by a 1:1 line between Cr and Nb contents. Log (Cr/Nb) values are calculated in order to obtain a simple provenance indicator and to compare one parameter (mafic vs. pelitic source lithologies) with other factors (e.g., Zr or calculated temperature).

To test the significance of this logratio and the validity of high Cr and Nb values for provenance study purposes, one small catchment area <1 km^2 is chosen as an example: Fig. 6 shows rutile compositions of two sand samples, two eclogites and one garnet schist deriving from the northernmost sampling region in the Gneiss Unit, ca. 4 km north of Saidenbach dam. Cr contents of these samples range up to 1440 ppm, Nb contents up to 8950 ppm (Table 2). These samples in

their mean trace element contents are representative of the majority of analyses from the Erzgebirge.

Comparing the minimum and maximum Cr and Nb contents, we can demonstrate that the rocks' compositions are mirrored in the sands. The slightly lower temperature mafic composition group found in sand compositions (Fig. 6) was not found in the sampled source rock equivalents.

Further, the garnet schist and the two eclogites are perfectly separated by the 0 line in log (Cr/Nb) values. Also, maximum temperatures calculated from these samples using rutile thermometry by Zack et al. (2004a) are in good agreement with the 850 °C for EGU1 rocks (Fig. 2) obtained with conventional thermometry by Schmädicke and Müller (2000).

It can be observed in this example (Fig. 6) that rutile analyses form high and low temperature populations, which are separated by gaps of ca. 20 °C in width at 800 to 820 and 780 to 800 °C for pelitic and mafic compositions, respectively. It is remarkable, that this separation of analyses into two temperature populations occurs not only in the sand samples, which constitute a mixture of different source rocks, but also within distinct source rocks (here: the garnet schist). In these and other investigated rock samples, it was found that rutile as inclusions in other mineral phases always has high Zr contents, while matrix rutiles in many samples tend on average to lower Zr contents (Figs. 6 and 7).

Although rutiles with mafic compositions give an observably lower maximum temperature than rutiles deriving from metapelites (Fig. 6), the difference between both is smaller than 25 °C. This fact and the observation that the investigated mafic rocks from the Erzgebirge (all sampled mafic rocks were eclogites) contain small amounts of quartz and zircon, indicate that mafic rutile compositions may also be suitable for thermometry. Peak temperature characteristics of mafic and pelitic rutiles in all samples from the Erzgebirge

Table 2

EMP analyses of five rock-and sand samples from the northernmost sampling area, ca. 4 km north of Saidenbach dam (Figs. 2 and 6)

Sample	Number of analyses	Cr (ppm)			Nb (ppm)			Zr (ppm)		
		Minimum	Maximum	Mean	Minimum	Maximum	Mean	Minimum	Maximum	Mean
Sand 1	40	313	1004	548	bdl	6728	3193	390	847	626
Sand 2	36	125	1440	539	171	8954	1349	383	769	614
Eclogite 1	21	528	1125	781	bdl	142	92	529	720	604
Eclogite 2	11	579	1110	809	bdl	127	100	604	683	653
Garnet schist	9	381	936	602	5093	7921	6212	418	768	588

Minimum, maximum, and arithmetic mean values for Cr (ppm), Nb (ppm), and Zr (ppm) are displayed, together with the number of analyses performed on each sample. bdl – below detection limit. The samples accord to samples EGB-04-S44, EGB-04-S45, EGB-04-R3a2, EGB-04-R4f1, and EGB-04-R4 g in Tables S1 and S2 (electronic supplement).
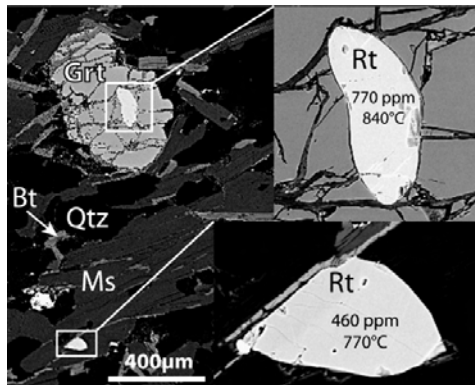
Fig. 7. Backscattered electron images of the garnet-biotite micaschist (EGB-04-R4f1; see Table S1, electronic supplement) from the northernmost sampling area, ca. 4 km north of Saidenbach, which is also displayed in Fig. 6. The temperatures calculated from Zr contents are rounded to 10 °C. Mineral abbreviations refer to Kretz (1983).

(Fig. 8) follow the trend observed in Fig. 6: Analyses of pelitic rutiles (best shown in the "GU" group) exceed the maximum temperature obtained from mafic rutiles by about 40 °C, a number which is larger than the difference observed for the example in Fig. 6, but which is still lower than the calibration error (50 °C) found by Zack et al. (2004a). Hence the observation that

the application of Zack et al. (2004a) 's thermometry gives similar results for mafic and pelitic rutiles is valid for the entire Erzgebirge   an outcome, which is supported by Zack and Luvizotto (2006), who report good fits with conventional thermometry for eclogites from other regions.

5.2. Rutile derived temperature characteristics in the Erzgebirge

In order to test homogeneity of single rutile grains, a third of all investigated crystals in each sample were analyzed three times. Less than one percent of our analysed crytals were found to, due to inhomogeneity with respect to Zr, produce calculated temperature differences larger than 50 °C.

The gap in analysed temperatures, which was shown for the local example (Fig. 6), can also be observed in temperature frequency distributions (Fig. 9): Most sand and rock samples exhibit two, very rarely three, temperature populations.

As has already been stated in Section 4, rutiles from metamorphic grades higher than MU conditions, exhibit peak metamorphic temperatures, which correspond well with conventionally obtained unit temperatures (unit temperatures = temperatures of the latest metamorphic event). The large scatter of maximum temperatures in
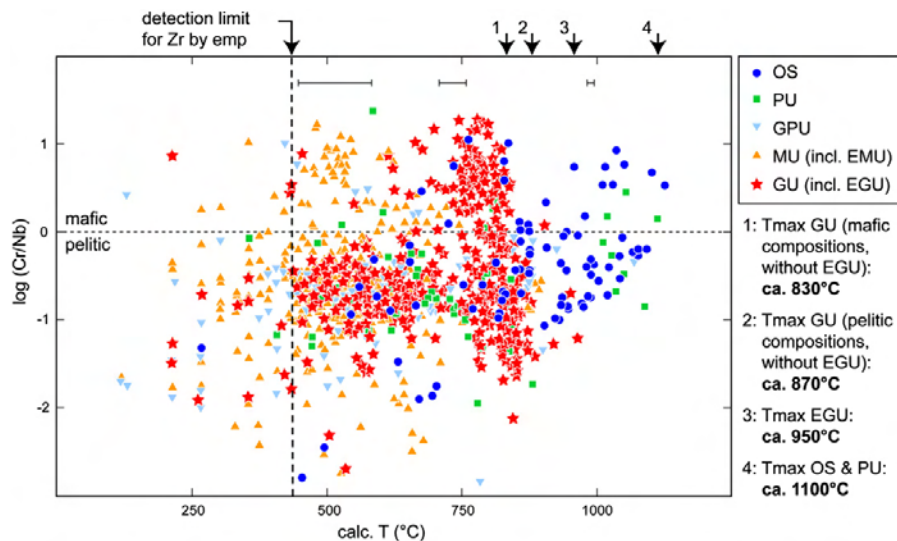
Fig. 8. Plot of temperatures calculated from rutile Zr contents from sand samples after Zack et al. (2004a) vs. log(Cr/Nb), analysed by EMP. Mafic and pelitic compositions according to log(Cr/Nb) are indicated. The same symbology as in Fig. 2 is used. Error bars correspond to 2-σ analytical errors of Zr contents measured by EMP. Although undefined, analyses below the 2-σ detection limit are shown because an omission would be misleading. OS: 2 samples; PU: 2 samples; GPU: 3 samples; MU (incl. EMU): 8 samples; GU (incl. EGU): 13 samples.
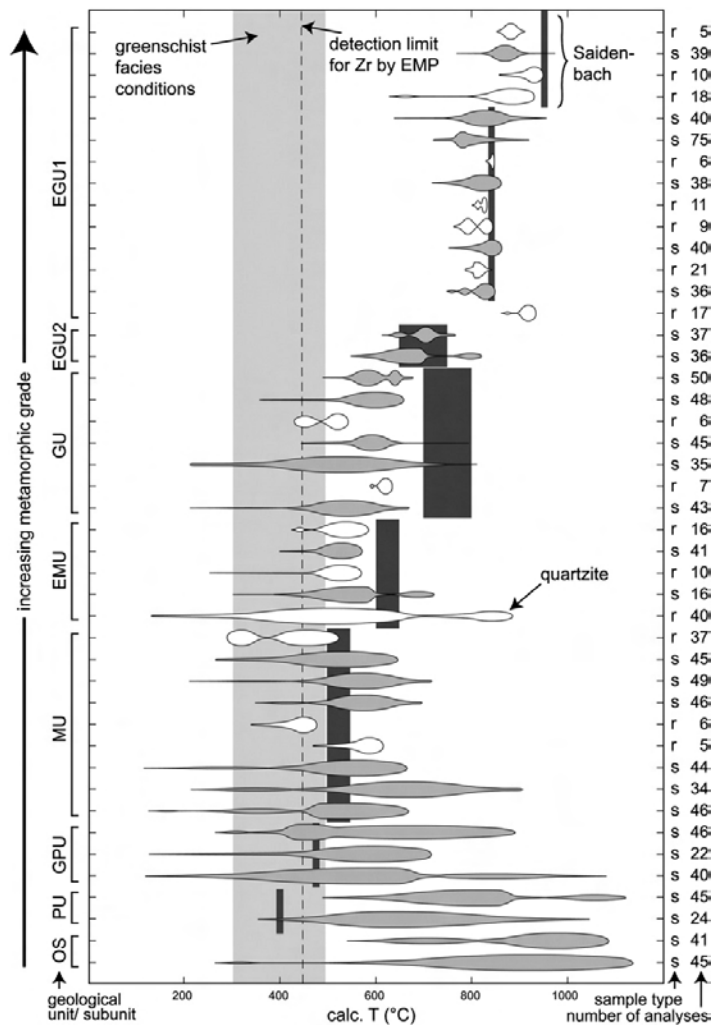
Fig. 9. Temperature distributions based on single-grain rutile thermometry after Zack et al. (2004a) for all investigated sand (s, grey fill) and rock (r, white fill) samples, sorted roughly with increasing metamorphic grade. Zr analyses for this plot were performed by EMP. Distribution shapes are drawn from Gaussian distributions fitted via least-squares fits to temperature histograms. Histograms in turn are calculated with class numbers according to the square root of the number of analyses used, which are displayed on the right of the plot. Temperature ranges from conventional thermometry are drawn as grey rectangles in the background. Although undefined, analyses below the 2-σ detection limit are shown because an omission would be misleading.

the GU (without EGU) rock samples group shows that *PT* conditions within this unit vary strongly with locality, and that sand samples derived from different rocks within this unit exhibit rutile populations more representative of the whole unit. The only investigated quartzite sample (EMU) displays the worst fit with unit temperatures. In the MU (without EMU), only two of nine samples give appropriate temperatures. Some samples display maximum temperatures exceeding unit temperatures. Samples from the lower metamorphic GPU, PU and OS report high values, which in most cases even exceed the highest temperature recorded for the Variscan orogeny in this part of the Erzgebirge (950 °C) and show more than 1100 °C.
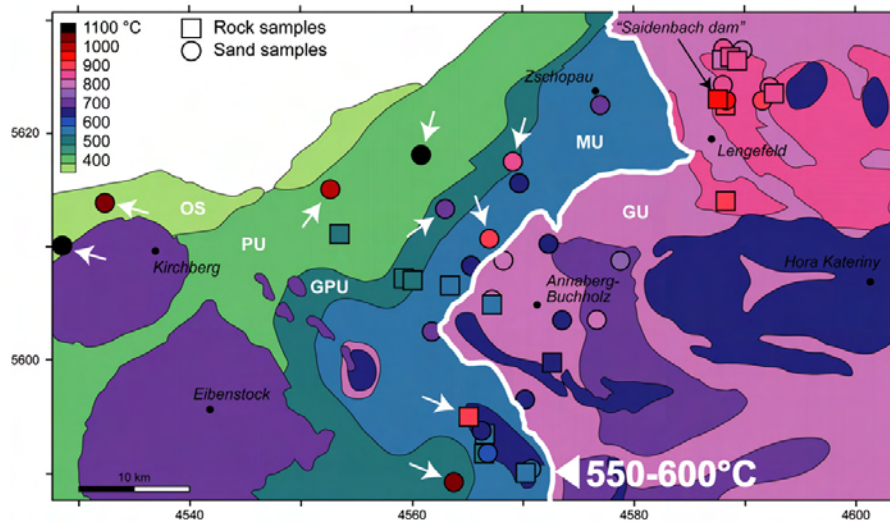
Fig. 10. Temperature map of the western Erzgebirge (Fig. 2). The unit-/subunit temperatures are the same as those in Fig. 2. Displayed abbreviations indicate unit-/subunit names. Using EMP data, sample maximum temperatures are calculated from Zr contents in rutile after Zack et al. (2004a). All temperatures are rounded to 50 °C. The arrows highlight sample temperatures strongly exceeding unit temperatures. The bold white line indicates the location of the 550–600 °C boundary (see text for explanation).

Rock samples exhibit slightly smaller temperature variances than sand samples, a fact which was anticipated due to sampling statistics. Superimposed on this effect, samples from high metamorphic grades have smaller standard deviations compared to low grade samples.

In order to further examine the occurrence of sample peak temperatures exceeding unit temperatures, we have constructed a temperature map (Fig. 10). Samples reporting significantly (>100 °C) higher temperatures than unit metamorphic conditions are indicated by arrows. In the GU (incl. EGU), only equilibrated samples can be observed. Thus the border between the MU and the GU (550 600 °C) constitutes a *T* boundary for Zr in rutile equilibration processes.

6. Discussion

6.1. Lithology and log (Cr/Nb)

Mafic and pelitic source rock lithologies can be well separated by means of log (Cr/Nb) ratios (Figs. 4 and 5). Rutiles from felsic source lithology that have Nb contents outside the field for a metapelitic provenance after Zack et al. (2004b) can be classified using logratios of Cr and Nb. Log (Cr/Nb) is a valuable provenance indicator and moreover ideally suited for comparison with a third element or proxy, such as temperature, in cross plots.

In the application to samples from the Erzgebirge, plotting log (Cr/Nb) vs. calculated temperatures (Fig. 6) for rocks and sands from a common, small catchment area shows a low temperature mafic group of rutile compositions, which lacks a rock sample equivalent. Thus source lithology components superimposed on a simple separation into mafic and felsic compositions can be characterised, which is often not possible from a comparison of Cr vs. Nb or *T* characteristics alone.

6.2. Eclogites in rutile thermometry

It was shown (Figs. 6 and 8) that rutiles with mafic composition record maximum temperatures, which are similar within the thermometric calibration error to rutiles deriving from felsic host rocks. These data support the validity of applying rutile thermometry to mafic host rocks, at least in the Erzgebirge.

Zack et al. (2004a) and Watson et al. (2006) both have stated that in the absence of quartz and/or zircon the equilibrium exchange reaction (Eq. (1)) is not buffered. While zircon is mostly the only phase where Zr constitutes a major element, silica activity can be buffered by a larger variety of Si bearing mineral phases to values lower, but close to unity. Hence rutile thermometry is generally much more sensitive to the existence or absence of zircon than quartz. These considerations in turn

loosen the constraints put on lithologies, where rutile thermometry is applicable and, moreover, they indicate that thermometry will produce acceptable results in a large number of, in particular silica saturated, rock types.

A lack of coexisting zircon (or a decrease in Zr activity) will always lead to diminished incorporation of Zr into rutile, while a lack of coexisting quartz (or a decrease in silica activity) will lead to an increase in Zr incorporation. As silica activity, following our argumen tation above, is usually better buffered than Zr activity, underestimation of a sample's maximum metamorphic temperature is much more likely than overestimation.

However the application of rutile thermometry to lithologies with questionable quartz and particularly zircon contents must still be treated with care, when the obtained maximum temperatures cannot be validated by the means of other methods: we can observe that our investigated mafic rock samples contain small amounts of quartz and zircon. Anyway, a mineral paragenesis cannot be derived from rutile geochemistry alone, as would be needed in sedimentary studies.

6.3. Zr in rutile equilibration conditions and processes

From our results we conclude that there exists a tem perature, above which most rutiles equilibrate at the current metamorphic conditions (Figs. 9 and 10). In the Erzgebirge, the critical temperature range lies at 550 600 °C. The decreasing degree of equilibration within the rutile population towards lower metamorphic grades is expressed by a) an increasing variance in the samples' temperature distribution, and b) the increasing occurrence of maximum temperatures exceeding Variscan temperatures:

a) In terms of an application of the rutile thermometer, it can be seen from the *T* variances displayed in Fig. 9 that samples exhibiting larger standard deviations than ca. 120 °C (2 σ) in the Erzgebirge are not equilibrated and must be treated with care. This is supported by Spear et al. (2006), who find equili brated rutile compositions at within sample temper ature ranges of less than 55 °C.

b) During metamorphism, a newly grown rutile is very unlikely to incorporate more Zr than the equilibrium reaction allows. Furthermore, large part of the high *T* rutiles in question can be characterised as metapelitic (Fig. 8) and hence are ensured to have equilibrated at adequate phase compositions. Thus, rutiles with significantly higher Zr contents than maximum Variscan temperatures must be relicts from an earlier metamorphic event. The decreasing average maxi mum temperature from the OS to MU obtained from

rutiles results either from the increasing tendency of crystals to approximate equilibration at metamorphic temperature, or the increasing abundance of newly grown, equilibrated rutiles (Fig. 9).

6.3.1. The influence of lithology

Samples from similar metamorphic units within the transition zone between non equilibrated and equilibrat ed rocks do not show corresponding maximum cal culated temperatures (Fig. 9). Assuming that samples from the same rock units underwent similar metamor phic histories, this variability is most likely the result of differences in lithology between single samples. One outstanding example is the quartzite sample from the EMU: Rutiles from this sample have resisted equilibra tion even at more than 600 °C as seen in the extremely large temperature variance compared to all other samples from the same subunit. Interestingly, many of the rutiles record temperatures much higher than 600 °C. A possible explanation is that quartzites are relatively unreactive compared to other lithologies as their lack of Fe and Ca bearing phases leads to a diminished ability to form titanite or ilmenite during, e.g., greenschist facies conditions, where rutile is not stable.

6.3.2. The influence of general metamorphic conditions

Rutile closure temperatures are ~560 , 635 , and 730 °C for cooling rates of 1 , 10 , and 100 °C/Ma, respectively, for grains of ca. 100 μm in diameter (cited in Watson et al., 2006), which approximates the sizes of rutile grains in sands analysed in this study. The values for the slow to medium cooling rates <10 °C/Ma cited above correspond to the equilibration boundary at 550 600 °C found in this study. However, in addition to lithology, metamorphic grade, and rate of change in metamorphic conditions (as explained above), the possible influence of fluids can change the timescales and velocities, in which rutile dissolves, re grows, and/ or equilibrates (Luvizotto and Zack, 2006).

Hence in order to explain the existence of relict, high temperature rutiles and lowered frequencies of equili brated rutiles in sediments from low metamorphic units, two scenarios can be envisaged. 1.) Detrital rutiles in meta sediments are stable during the whole metamor phic cycle, and diffusive equilibration becomes signif icant only above 550 600 °C. 2.) Detrital rutiles are unstable at greenschist facies metamorphic conditions. As explained above, due to their low reactivity only rutiles in quartzites resist re equilibration. Above 550 600 °C, significant amounts of newly grown rutile suppress the relict signal, and smaller temperature variances evolve. To assess the influence of these two

mechanisms, the samples' rutile/zircon ratios should be studied, as zircon is stable during the entire metamorphic cycle. Hence low rutile/zircon ratios would be expected if rutile occurs only rarely (e.g., only in quartzites). On the contrary, metamorphic rutile growth in common lithologies (e.g., metapelites) would be visible in form of increasing rutile/zircon ratios.

6.4. Temperature populations and retrograde processes

A prominent feature, which is common to all individual sands and most rocks, can be observed in Fig. 9: Although the total range in calculated temperatures changes with metamorphic grade, the recorded temperatures in most samples are separated into two (very rarely three) populations. Different interpretations must be applied for high and low temperature samples to explain these groupings.

As explained in the last chapter, for high temperature rutiles from the Gneiss units we can presume equilibration with peak temperatures of the last (Variscan) metamorphic cycle. Thus, lower Zr contents must originate from more or less pronounced re equilibration processes during retrograde conditions. A clustering of analyses into sub populations, as has been observed for the garnet schist in Fig. 6, in retrograde processes can only evolve, if rutile populations are exposed to resetting with differing intensities. This can only be achieved if some of the crystals are isolated as inclusions within other mineral species with lower Zr diffusion coefficients (e.g., garnet and pyroxene) in comparison to the rest of the mineral assemblage. Inclusion rutiles must have higher or similar Zr contents than matrix rutiles, a feature, which is commonly observed in Erzgebirge rocks (e.g., Fig. 7) and elsewhere (Zack et al., 2004a).

A calculation of multiple normal (Gaussian) distributions fitted to temperature distributions of single sand samples, achieved by weighted mass balance calculations (see example in Fig. 11), provides estimates on the relative proportions of inclusion rutile (groups A and C) and matrix rutile (groups B and D) compositions. This approach reveals that 65 70% (according to the total number of peak temperature rutile analyses) of rutiles have not been reset during retrograde conditions and are available in sands for proper temperature calculations.

A resetting to new metamorphic conditions is mainly achieved by diffusion and dynamic recrystallisation processes, both of which occur most often at high temperature conditions. Prograde metamorphism is more efficient in equilibrating mineral assemblages and crystal chemical conditions due to the common presence of fluids, compared to retrograde conditions.
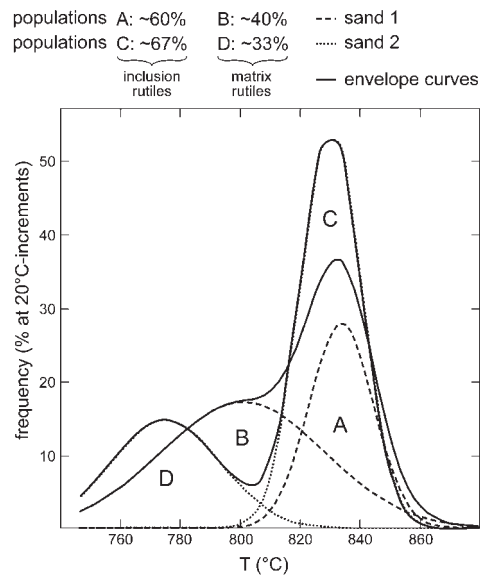
Fig. 11. Normal (Gaussian) distributions fitted to temperature frequency distributions (EMP) of two sand samples from the northernmost sampling area, ca. 4 km north of Saidenbach dam (Figs. 2 and 6). Sand 1 is subdivided into populations A (inclusion rutiles) and B (matrix rutiles), sand 2 is subdivided accordingly into populations C and D. The respective approximate proportions of each population as calculated from the temperature distributions are shown.

In contrast to high temperature rocks, low grade samples exhibit complex histories. Slower diffusion processes at low temperature and the existence of rutile from earlier metamorphic cycles are superimposed on re equilibration processes. Spear et al. (2006) for low temperature (<500 °C) samples from Sifnos (Greece), applying unpublished Zr diffusivity data cited in Watson et al. (2006), argue that at such low temperature, diffusion will not exceed distances >10 μm and therefore will not modify Zr compositions of rutiles subsequent to their growth. Spear et al. (2006) found that matrix rutiles sometimes display higher temperatures matching the concurrent metamorphic conditions, while inclusion rutiles only provide minimum growth temperatures of their host minerals. However, this is not generally observed in low grade samples (see Zack and Luvizotto, 2006). The discrepancy between the results of this study and those found by Spear et al. (2006) concerning Zr characteristics of matrix and inclusion rutiles shows that on the one hand at high grade metamorphic conditions, host minerals with low Zr diffusivities keep inclusion rutiles from re equilibrating during retrograde conditions. On the other hand, at low grade metamorphic conditions,

where rutile is unlikely to be reset during retrograde metamorphism, it is more likely that matrix rutiles display peak temperature conditions.

6.5. Relict rutiles

Some rutiles in the very low grade samples, particularly from the OS, PU and GPU, inherit relict temperatures from an earlier metamorphic event. These relicts are characterised by extremely high Zr contents, corresponding to temperatures of >950 °C or >1100 °C, using the calibrations of Watson et al. (2006) and Zack et al. (2004a), respectively. As we are not able to put constraints on metamorphic pressures, additional thermometry methods (e.g., zircon thermometry, as described by Watson and Harrison, 2005, and Watson et al., 2006) need to be applied in order to assess the true metamorphic temperature of these relicts.

Linnemann and Romer (2002) in their studies on Early Paleozoic Saxo Thuringian sedimentary rocks of central Europe infer a provenance from the west African craton. Guerrot et al. (1989) find the same source rocks for metamorphically overprinted sediments in the west European Hercynian belt, which shows that this provenance apparently applies to a broad region. Studies on metamorphic conditions in the west African craton reveal ultra high temperature granulites, which were generated at 800 °C up to ca. 1100 °C and about 1 GPa (e.g., Bernard Griffiths et al., 1996; Caby, 1996; Peucat et al., 1996; Ouzegane et al., 2003), and which hence come into question as potential rutile source rocks. Also there are kimberlite provinces in the west African craton, which might have made a small contribution to a high Zr rutile population (e.g., Williams and Williams, 1977; Taylor et al., 1994). Thus, our temperature estimates from relict rutiles fit into the common picture of a derivation of Early Paleozoic sediment of central Europe from source rocks from the west African craton.

7. Summary and conclusions

We have shown that rutile composition in modern sand sized sediments from the western Erzgebirge correspond very well with the presently outcropping rocks. Thus rutile is considered an accurate tracer of source rock characteristics in sedimentary systems. Furthermore the investigation of sand samples has the advantage of interpreting larger sampling bandwidths, which results in a better representation of source lithology compared to single rock samples. We conclude that the study of any region in terms of, e.g., rutile peak metamorphic temperatures, can be greatly improved if modern sand samples are investigated

as well as rocks. These findings underline the importance of further investigations on the application of rutile geochemistry to provenance studies.

From our studies in the Erzgebirge, we infer that rutiles can be classified in terms of source lithology using Nb Cr analyses by a 1:1 line or, accordingly, by the 0 line in log (Cr/Nb) ratios. A predominance of Cr content points to mafic host rocks, and a predominance of Nb content to metapelites. The use of log (Cr/Nb) values in combination with other trace elements allows for a better assessment of provenance characteristics than using element contents alone.

Our results support that a larger variety of rock types can be used for rutile thermometry than was initially assumed by Zack et al. (2004a). In the Erzgebirge, eclogites provide rutile grains appropriate for thermometry after Zack et al. (2004a). This increases the variety of suitable source lithologies, because detrital rutile grains need not be characterised as metapelitic in origin before applying the thermometer.

From single sample temperature distributions, we can show that the consistency between rutile thermometry with the actual metamorphic conditions depends on a complex mixture of influencing factors, such as lithology, metamorphic grade, and effects of migrating fluids. Additionally, retrograde re equilibration can lead to the development of large temperature variances or, due to shielding effects for rutile as inclusions in other mineral phases, to the formation of higher and lower temperature populations within one rock or sand sample. Nb and Cr characteristics are not affected. In high grade samples >550 600 °C from the Erzgebirge, peak temperature rutiles are most likely to be found as inclusions in, e.g., garnet. The evolving temperature populations can be quantified applying simple statistical models: more than 65% of rutiles under high grade metamorphic and similar lithological conditions such as in the Erzgebirge, retain peak metamorphic conditions.

Rutile sand and rock samples equilibrated at peak metamorphic conditions exhibit 2 σ standard deviations in calculated temperatures smaller than 120 °C. Below 550 600 °C, equilibration at current metamorphic conditions was not reached, giving us the opportunity to observe relict rutile grains originating from the erosion of pre Variscan terranes. This in turn puts constraints on the high grade metamorphic (>950 °C) nature of these source rocks, which most likely derive from the west African craton in Ordovician time.

Our results show that investigating rutile trace element characteristics in order to infer host rock lithology and metamorphic conditions as established by Zack et al. (2002, 2004a,b) and Watson et al. (2006),

constitutes an extremely useful tool for provenance studies. In the case of temperature distributions of single sand samples, we have shown that a quantification of subpopulations is possible via fitting of multiple normal distributions. In future studies, this technique may help in quantifying different source lithology components. In order to test the application of rutile trace element studies on ancient sands and sandstones, where neither source lithology nor geomorphology are known, the next step to make must be an upscaling of the approved methods.

Acknowledgements

Appendix A. Supplementary data

Supplementary data associated with this article can be found, in the online version, at doi:10.1016/j.chemgeo.2007.06.033.

References

Armstrong, J.T., 1995. A package of correction programs for the quantitative electron microbeam X-ray analysis of thick polished materials, thin films and particles. Microbeam Anal. 4, 177–200.

Bernard-Griffiths, J., Fourcade, S., Kienast, J.-R., Peucat, J.-J., Martineau, F., Rahmani, A., 1996. Geochemistry and isotope (Sr, Nd, O) study of Al–Mg granulites from the In Ouzzal Archaean block (Hoggar, Algeria). J. Metamorph. Geol. 14 (6), 709–724.

Caby, R., 1996. A review of the In Ouzzal granulitic terrane (Tuareg shield, Algeria): its significance within the Pan-African Trans-Saharan belt. J. Metamorph. Geol. 14, 659–666.

Carter, A., Bristow, C.S., 2003. Linking hinterland evolution and continental basin sedimentation by using detrital zircon thermochronology: a study of the Khorat Plateau Basin, eastern Thailand. Basin Res. 15, 271–285.

Dallmeyer, R.D., Franke, W., Weber, K. (Eds.), 1995. Pre-Permian Geology of Central and Eastern Europe. Springer, Berlin.

Degeling, H.S., 2003. Zr equilibria in metamorphic rocks. Unpublished PhD thesis, Australian National University.

Force, E.R., 1980. The provenance of rutile. J. Sediment. Petrol. 50 (2), 485–488.

Force, E.R., 1991. Geology of titanium-mineral deposits. Special Paper, vol. 259. Geological Society of America, Boulder. 112 pp.

Götze, J., 1996. Genetic information of accessory minerals in clastic sediments. Zentralbl. Geol. PalaÉontol., I 1995, 101–118.

Griffin, W.L., Belousova, E.A., O'Reilly, S.Y., 2007. TerraneChron™ analysis of zircons from Western Australian samples. Western Australia Geological Survey, Record 2007/4.

Guerrot, C., Peucat, J.J., Capdevila, R., Dosso, L., 1989. Archean protoliths within Early Proterozoic granulitic crust of the west European Hercynian belt: possible relics of the west African craton. Geology 17, 241–244.

Haggerty, S.E., 1991. Oxide mineralogy of the upper mantle. In: Lindsley, D.H. (Ed.), Oxide Minerals: Petrologic and Magnetic Significance. Reviews in Mineralogy, vol. 25, pp. 355–416.

Jacobsen, Y.J., Münker, C., Mezger, K., 2003. Hf isotope compositions in detrital zircons as a new tool for provenance studies. Geophys. Res. Abstr. 5, 10282.

Kretz, R., 1983. Symbols for rock-forming minerals. Am. Mineral. 68 (1–2), 277–279.

Linnemann, U., Romer, R.L., 2002. The Cadomian Orogeny in Saxo-Thuringia, Germany: geochemical and Nd–Sr–Pb isotopic characterization of marginal basins with constraints to geotectonic setting and provenance. Tectonophysics 352, 33–64.

Luvizotto, G.L., Zack, T., 2006. Tracing dehydration melting and late fluid influx of metapelitic rocks using the texture and geochemistry of rutile. Granulites and Granulites Conference, Brasilia, 2006. Program and Abstracts, vol. 45. Available online at http://www.geol.umd.edu/pages/meetings/Gran&GranTables.htm.

Luvizotto, G.L., Zack, T., Münker, C., Prowatke, S., Klemme, S., Stöckli, D., Triebold, S., Meyer, H.P., Ludwig, T., in preparation. Rutile mineral standards for microanalysis: Homogeneity tests and ID-MC-ICP-MS results.

Massonne, H.-J., 1998. A new occurrence of microdiamonds in quartzofeldspathic rocks of the Saxonian Erzgebirge, Germany, and their metamorphic evolution. 7th International Kimberlite Conference, pp. 533–539.

Massonne, H.-J., Czambor, A., 2007. Geochemical signatures of Variscan eclogites from the Saxonian Erzgebirge, central Europe. Chem. Erde 67, 69–83.

McLennan, S., Bock, B., Compston, W., Hemming, S., McDaniel, D., 2001. Detrital zircon geochronology of Taconian and Acadian foreland sedimentary rocks in New England. J. Sediment. Res. 71, 305–317.

Mezger, K., Hanson, G.N., Bohlen, S.R., 1989. High-precision U–Pb ages of metamorphic rutile: application to the cooling history of high-grade terranes. Earth Planet. Sci. Lett. 96, 106–118.

Mingram, B., 1998. The Erzgebirge, Germany, a subducted part of northern Gondwana: geochemical evidence for repetition of early Paleozoic metasedimentary sequences in metamorphic thrust units. Geol. Mag. 135 (6), 785–801.

Mingram, B., Rötzler, K., 1999. Geochemische, petrologische und geochronologische Untersuchungen im Erzgebirgskristallin-Rekonstruktion eines Krustenstapels. Schriftenreihe für Geowissenschaften, vol. 9. 80 pp.

Morton, A.C., 1987. Influences of provenance and diagenesis on detrital garnet suites in the Forties sandstone, Paleocene, central North Sea. J. Sediment. Petrol. 57, 1027–1032.

Morton, A.C., 1991. Geochemical studies of detrital heavy minerals and their application to provenance research. In: Morton, A.C., Todd, S.P., Haughton, P.D.W. (Eds.), Developments in Sedimentary Provenance Studies. Geological Society Special Publication, vol. 57, pp. 31–45.

Morton, A.C., Hallsworth, C.R., 1999. Processes controlling the composition of heavy mineral assemblages in sandstones. Sediment. Geol. 124, 3–29.

Ouzegane, K., Guiraud, M., Kienast, J.R., 2003. Prograde and retrograde evolution in high-temperature corundum granulites (FMAS and KFMASH systems) from In Ouzzal Terrane (NW Hoggar, Algeria). J. Petrol. 44 (3), 517–545.

Peucat, J.J., Capdevila, R., Drareni, A., Choukroune, P., Fanning, M., Bernard-Griffiths, J., Fourcade, S., 1996. Major and trace element geochemistry and isotope (Sr, Nd, Pb, O) systematics of an Archaean basement involved in a $2 \cdot 0$ Ga VHT (1000 °C) metamorphic event: In Ouzzal massif, Hoggar, Algeria. J. Metamorph. Geol. 14, 667–692.

Pober, E., Faupl, P., 1988. The chemistry of detrital chromian spinels and its implications for the geodynamic evolution of the Eastern Alps. Geol. Rundsch. 77, 641–670.

Preston, J., Hartley, A., Mange-Rajetzky, M., Hole, M., May, G., Buck, S., Vaughan, L., 2002. The provenance of Triassic continental sandstones from the Beryl field, northern North Sea: mineralogical, geochemical and sedimentological constraints. J. Sediment. Res. 72, 18–29.

Rahl, J.M., Reiners, P.W., Campbell, I.H., Nicolescu, S., Allen, C.M., 2003. Combined single-grain (U–Th)/He and U/Pb dating of detrital zircons from the Navajo Sandstone, Utah. Geology 31, 761–764.

Rötzler, K., Schumacher, R., Maresch, W.V., Willner, P., 1998. Characterization and geodynamic implications of contrasting metamorphic evolution in juxtaposed high-pressure units of the Western Erzgebirge (Saxony, Germany). Eur. J. Mineral. 10, 261–280.

Schmädicke, E., Evans, B.W., 1997. Garnet-bearing ultramafic rocks from the Erzgebirge and their relation to other settings in the Bohemian Massif. Contrib. Mineral. Petrol. 127, 57–74.

Schmädicke, E., Müller, W.F., 2000. Unusual exsolution phenomena in omphacite and partial replacement of phengite by phlogopite +kyanite in an eclogite from the Erzgebirge. Contrib. Mineral. Petrol. 139, 629–642.

Schmädicke, E., Okrusch, M., Schmidt, W., 1992. Eclogite-facies rocks in the Saxonian Erzgebirge, Germany: high pressure metamorphism under contrasting $P–T$ conditions. Contrib. Mineral. Petrol. 110, 226–241.

Spear, F.S., Wark, D.A., Cheney, J.T., Schumacher, J.C., Watson, E.B., 2006. Zr-in-rutile thermometry in blueshists from Sifnos, Greece. Contrib. Mineral. Petrol. 152 (3), 375–385.

Stendal, H., Toteu, S.F., Frei, R., Penaye, J., Njel, U.O., Bassahak, J., Nni, J., Kankeu, B., Ngako, V., Hell, J.V., 2006. Derivation of detrital rutile in the Yaounde region from the Neoproterozoic Pan-African belt in southern Cameroon (Central Africa). J. Afr. Earth Sci. 44 (4-5), 443–458.

Taylor, W.R., Tompkins, L.A., Haggerty, S.E., 1994. Comparative geochemistry of West African kimberlites: evidence for a micaceous kimberlite endmember of sublithospheric origin. Geochim. Cosmochim. Acta 58 (19), 4017–4037.

von Eynatten, H., 2003. Petrography and chemistry of sandstones from the Swiss molasse basin: an archive of the Oligocene to Miocene evolution of the Central Alps. Sedimentology 50, 703–724.

von Eynatten, H., Gaupp, R., 1999. Provenance of Cretaceous synorogenic sandstones in the Eastern Alps: constraints from framework petrography, heavy mineral analysis, and mineral chemistry. Sediment. Geol. 124, 81–111.

von Eynatten, H., Wijbrans, J.R., 2003. Precise tracing of exhumation and provenance using Ar/Ar-geochronology of detrital white mica: the example of the Central Alps. Spec. Publ. - Geol. Soc. Lond. 208, 289–305.

von Eynatten, H., Gaupp, R., Wijbrans, J.R., 1996. 40Ar/39Ar laser-probe dating of detrital white micas from Cretaceous sedimentary rocks from the Eastern Alps: evidence for Variscan high-pressure metamorphism and implications for Alpine orogeny. Geology 24, 691–694.

von Eynatten, H., Tolosana-Delgado, R., Triebold, S., Zack, T., 2005. Interactions between grain size and composition of sediments: two examples. In: Mateu-Figueras, G., Barceló-Vidal, C. (Eds.), Proceedings CoDaWork'05 – 2nd Compositional Data Analysis Workshop. Universitat de Girona, Girona. 12 pp.

Vry, J.K., Baker, J.A., 2006. LA-MC-ICPMS Pb–Pb dating of rutile from slowly cooled granulites: confirmation of the high closure temperature for Pb diffusion in rutile. Geochim. Cosmochim. Acta 70 (7), 1807.

Vry, J., Baker, J., Waight, T., 2003. In situ Pb–Pb dating of rutile from slowly cooled granulites by La-Mc-ICP-MS: confirmation of the high closure temperature (>600 °C) for Pb diffusion in rutile. Geophys. Res. Abstr. 5, 10199.

Watson, E.B., Harrison, T.M., 2005. Zircon thermometer reveals minimum melting conditions on earliest earth. Science 308 (5723), 841.

Watson, E., Wark, D., Thomas, J., 2006. Crystallization thermometers for zircon and rutile. Contrib. Mineral. Petrol. 151 (4), 413.

Williams, H.R., Williams, R.A., 1977. Kimberlites and plate-tectonics in West Africa. Nature 270, 507–508.

Willner, A.P., Rötzler, K., Maresch, W.V., 1997. Pressure-temperature and fluid evolution of quartzo-feldspathic metamorphic rocks with a relict high-pressure, granulite-facies history from the Central Erzgebirge (Saxony, Germany). J. Petrol. 38 (3), 307–336.

Willner, A.P., Krohe, A., Maresch, W.V., 2000. Interrelated $P–T–t–d$ paths in the Variscan Erzgebirge dome (Saxony, Germany): constraints on the rapid exhumation of high pressure rocks from the root zone of a collisional orogen. Int. Geol. Rev. 42, 64–85.

Zack, T., Luvizotto, G.L., 2006. Application of rutile thermometry to eclogites. Mineral. Petrol. 88, 69–85.

Zack, T., Kronz, A., Foley, S.F., Rivers, T., 2002. Trace element abundances in rutiles from eclogites and associated mica schists. Chem. Geol. 184, 97–122.

Zack, T., Moraes, R., Kronz, A., 2004a. Temperature dependence of Zr in rutile: empirical calibration of a rutile thermometer. Contrib. Mineral. Petrol. 148 (4), 471–488.

Zack, T., Eynatten, H., von Kronz, A., 2004b. Rutile geochemistry and its potential use in quantitative provenance studies. Sediment. Geol. 171, 37–58.

C.3 Marschall HR, Korsakov AV, Luvizotto GL, Nasdala L, Ludwig, T (Submitted) On the occurrence and boron isotopic composition of tourmaline in (ultra)high-pressure metamorphic rocks. *Journal of the Geological Society*

On the occurrence and boron isotopic composition of tourmaline in (ultra)high-pressure metamorphic rocks

Horst R. Marschall [a,*] Andrey V. Korsakov [b] George L. Luvizotto [c] Lutz Nasdala [d]
Thomas Ludwig [c]

[a] *Department of Earth Sciences, Wills Memorial Building, Queen's Road, University of Bristol, Bristol BS8 1RJ, UK*
[b] *Institute of Geology and Mineralogy, Siberian Branch of the Russian Academy of Science, Koptyug Pr. 3, Novosibirsk 630090, Russia*
[c] *Mineralogisches Institut, Universität Heidelberg, Im Neuenheimer Feld 236, D-69120 Heidelberg, Germany*
[d] *Institut für Mineralogie und Kristallographie, Universität Wien, Althanstr. 14, A-1090 Wien, Austria*

Abstract

The extensive $P - T$ stability and the high chemical variability of tourmaline (Tur) together with its common occurrence in meta-sediments suggests a high potential of this mineral group for petrologic and (isotope) geochemical studies on fluid-rock interaction in subduction and collision-related rocks. This paper presents a short review on the occurrence, major element chemistry and boron isotopic composition of Tur in high and ultra-high pressure (UHP) metamorphic rocks, and presents a new discovery of coesite-bearing Tur (schorl) from the Erzgebirge (Germany), as well as Tur (dravite) related to the retrograde history of coesite and diamond-bearing rocks from the Erzgebirge and the Kokchetav Massif (Kazakhstan).

The scarce data on world-wide occurrences of (U)HP Tur available to date, do not reveal any distinctiveness in its major element composition when compared to Tur from low-P rocks, except for the high occupation of the crystallographic X-site (dominated by Na) and the presence of excess B. Tourmaline with exceptionally high K_2O contents from Kokchetav is crowded with quartz inclusions and thus must have formed during or after decompression of the rock unit. The B isotopic composition of (U)HP Tur analysed so far ranges in $\delta^{11}B$ from -16 to $+1\,‰$ with many samples in or below the range of continental crust. In contrast, Tur formed during retrograde fluid influx in most cases shows high $\delta^{11}B$ values, bearing evidence for heavy-B fluids infiltrating the exhuming (U)HP units.

Key words: tourmaline, ultra-high pressure, boron isotopes, coesite, Raman spectroscopy

1. Introduction

The tourmaline (Tur) group $(XY_3Z_6[Si_6O_{18}$-$(BO_3)_3]V_3W)$ displays a large variation in chemical composition in a wide range of different host rocks. The Tur group has been employed extensively in the study of hydrothermal ore deposits as a monitor of fluid-rock interaction (see Slack, 2002). Stable isotope studies of Tur major elements O, B, Si and H (e.g. Jiang, 1998; Dyar *et al.*, 1999) and trace elements, such as Sr, Li and Pb (King & Kerrich, 1989; Frei & Pettke, 1996; Jiang, 1998; Maloney, 2007) have been successfully applied to decipher the fluid history of fluid-melt-rock systems. The preservation of growth zones in hydrothermal and metamorphic Tur related to its slow intracrystalline diffusivity predestines Tur to be used as a key to the fluid-chemical history of metamorphic rocks. For

---

unambiguous conclusions, however, it is essential to investigate the various stages and mechanisms of Tur growth.

Tourmaline is the most wide-spread boro-silicate mineral and a major carrier of B in a variety of rocks. Its occurrence in natural rocks of various metamorphic grade, as well as experimental data, demonstrate that Tur is stable in an exceptionally large $P - T$ range, including conditions in subducting slabs to a depth of at least $\sim 150\,\mathrm{km}$, possibly even $250\,\mathrm{km}$. Tourmaline growth and stability in subducting metasediments could be responsible for recycling of B with an isotopic composition influenced by surface processes into the deep mantle. Previous B isotope studies on high-pressure metamorphic Tur have revealed important insights into B isotope fractionation within dehydrating subducting crust (Nakano & Nakamura, 2001; Bebout & Nakamura, 2003; Marschall et al., 2008).

In this paper we briefly review the reports on Tur in (U)HPM rocks with its major element chemistry and B isotopic composition form the literature, and we present Tur samples from coesite and diamond-bearing rocks from the two renown UHP localities of Kokchetav (Kazakhstan) and Erzgebirge (Germany). Chemical analyses from electron probe and secondary-ion mass spectrometry (SIMS) and rim-core-rim profiles of boron isotopes (SIMS) are presented together with Raman-spectroscopic analyses of coesite inclusions in Tur and garnet that prove the UHPM nature of these rocks and of some of the Tur.

2. Occurrence of tourmaline in (ultra-)high-pressure metamorphic rocks

(U)HP metamorphic rocks sampled on the surface are the products of more or less complex $P-T-t-D$ histories, and the occurrence of Tur in a given sample may be related to one or several of a number of different processes. The first aim in a petrologic or geochemical study involving Tur, therefore, has to be the identification of the Tur-forming process and ideally its quantification in terms of P, T, t and of chemical budgets. Various genetic types of Tur are recognised in (U)HP metamorphic rocks:

2.0.0.1. *Type A* Tourmaline may form by net-transfer reactions from other Na and Mg/Fe-bearing alumo-silicates, such as phyllosilicates or amphiboles. The critical component, however, distin-

guishing Tur from other rock-forming minerals is, of course, boron. The abundance of this element in most HP minerals is generally very low ($< 10\,\mathrm{\mu g/g}$) with the exception of white mica (Domanik et al., 1993; Marschall et al., 2006a; Bebout et al., 2007). Hence, a source of B during prograde metamorphic growth of Tur is white mica. Nakano & Nakamura (2001) have demonstrated that Tur in HP metasediments from the Sambagawa belt (Japan) grew from B that was progressively released from phengite at increasing P and T. This process does not change the B content of the bulk rock, and it is probably restricted to the prograde section of the $P-T$ path, when B is released from the mica. The crystals typically show a strong chemical (Mg-Fe; Na-Ca) and isotopic core-to-rim zonation, due to continuous or episodic growth over an extended part of the $P-T$ path.

2.0.0.2. *Type B* A second source of B may be available in boro-silicates or phases that contain B as a minor constituent in substitution for Al. Breakdown of minerals, such as dumortierite, osumilite or boro-muscovite may lead to the formation of Tur induced by a change in $P-T$. This mechanism of Tur formation is probably more common during high-T metamorphism, but may operate in (U)HP rocks during their exhumation. Small Tur grains occurring in pseudomorphs (see sample K86 below) are probably of this type.

2.0.0.3. *Type C* Metasomatic formation of Tur may be the most common mechanism and has been documented for HP rocks from several localities (Altherr et al., 2004; Marschall et al., 2006b). This type of Tur is formed by reactions of silicates with incoming B-bearing fluids, a mechanism that has been demonstrated experimentally for amphibole and chlorite-bearing assemblages (Morgan & London, 1989; Fuchs & Lagache, 1994; Dingwell et al., 2002). Fluid influx in (U)HP rocks is common during exhumation, and, hence, many occurrences of Type-C Tur may be related to the decompression history of the rocks. However, influx of fluids, melt or supercritical fluids in eclogites and (U)HP gneisses at prograde or peak-pressure conditions has also been documented (John & Schenk, 2003; Korsakov & Hermann, 2006). Maximum B abundances of $200 - 300\,\mathrm{\mu g/g}$ in pelitic rocks and altered oceanic crust (Leeman & Sisson, 2002) restricts the amount of Types-A and B Tur to $< 1\,\%$ and make

2

any higher modal abundance of this mineral highly suspect of metasomatic B enrichment. Apart from its high modal abundance, Type-C Tur may be also recognised by a larger grain size and core-rim zonation with only two or three wide zones with relatively small differences in chemical composition. Metasomatic Tur often displays exotic B isotopic compositions, depending on the source and history of the metasomatising agent.

2.0.0.4. *Type D* Tourmalin in metamorphic rock may be a relic from the precursor rock, and may have survived the entire metamorphic cycle without re-crystalisation or changing its chemistry or isotopic composition. In meta-sediments, detrital Tur grains (**Type D1**) have been identified, usually occurring as cores overgrown by metamorphic Tur (Henry & Dutrow, 2002; Marschall *et al.*, 2008).

In poly-cyclic (U)HP metamorphic rocks, Tur may form relics from an earlier orogenic cycle (**Type D2**). It may have formed during Barrow-type metamorphism or in or near a granitic intrusion in a metamorphic or magmatic rock, which was subsequently subjected to (U)HP metamorphism. In the Armorican massif of western France, Godard (2007) has documented rocks that had equilibrated at 0.5 GPa and $\sim 770\,^{\circ}$C during pre-Variscan metamorphism and were later subjected to HP metamorphism (1.6 GPa at $\sim 650\,^{\circ}$C) during eo-Variscan subduction (Godard, 1988, 2007). Tourmaline is found in leucosomes formed during crustal melting in the course of the earlier HT metamorphism. The rocks are now Grt+Ky+Phe+Rt-bearing HP metamorphic rocks with Tur still preserved in the former leucosomes.

3. (Ultra-)High-pressure stability of tourmaline

Temperature stability of Tur extends from surface conditions below $150\,^{\circ}$C to high-grade metamorphic and magmatic conditions of $> 850\,^{\circ}$C at pressures between 0.1 and 0.5 GPa (Robbins & Yoder, 1962; Manning & Pichavant, 1983) and increases with increasing pressure. Werding & Schreyer (2002) report stability of dravite ($NaMg_3Al_6[Si_6O_{18}(BO_3)_3](OH)_4$) in experiments to temperatures of $> 950\,^{\circ}$C at pressures between 3 and 5 GPa (Fig.1). These experimental studies demonstrated the breakdown of dravite to a number of Mg-Al phases between 6 and 8 GPa

(Krosse, 1995; Werding & Schreyer, 2002, Fig.1). In SiO_2 saturated rocks, i.e. in the presence of coesite, Tur has been demonstrated to break down to Grt+Phe+fluid/melt at 4.0 GPa in the temperatures range $800 - 850\,^{\circ}$C and between 4.5 and 5.0 GPa at $T = 700\,^{\circ}$C (Ota *et al.*, 2008) (Fig.1).

Tourmaline has also been observed in natural (U)HP metamorphic rocks (Reinecke, 1998; Johnson & Oliver, 2002; Hacker *et al.*, 2003; Bebout & Nakamura, 2003). Reinecke (1998) and Bebout & Nakamura (2003) report Mg-rich Tur with coesite inclusions from Lago di Cignana (Western Alps) formed at UHP conditions of ~ 2.8 GPa and $\sim 620\,^{\circ}$C (Fig.1). Coesite inclusions are strong evidence for the growth of this Tur under UHP metamorphic conditions. The authors argue that B for the coesite-bearing cores of the Tur crystals was derived from phengite in the rock, as described above for type A. Quartz-bearing rims of different chemical and isotopic composition of the same grains are ascribed to influx of B-bearing fluids during decompression (Type C).

The pyrope quartzites from Parigi, Dora Maira (Western Alps) contain dravite inclusions in coesite-bearing pyrope and in kyanite, as well as in Phl+Ky+Qtz pseudomorphs after pyrope (Schreyer, 1985; Schertl *et al.*, 1991). Chemically, both petrographic varieties are close to endmember dravite with X_{Mg} [Mg/(Mg + Fe)] of $0.96 - 0.99$ (Table1; Fig.2a; Schertl *et al.*, 1991). Several identically oriented inclusions of dravite in pyrope were taken as evidence for the growth of pyrope and kyanite at the expense of Tur (Schreyer, 1985; Schertl *et al.*, 1991). Experimental work by Hermann (2003) revealed that peak conditions of the pyrope quartzites were at 4.5 GPa and $750\,^{\circ}$C. Interestingly, these conditions are very similar to where the reaction Tur + Cs = Grt + Cpx + Ky + fluid was experimentally found to occur (Ota *et al.*, 2008) (Fig.1). This indicates that Tur in the Dora Maira pyrope quartzites survived diamond facies conditions as monomineralic inclusion in garnet and kyanite, but was decomposed to garnet + kyanite + (supercritical) fluid, where it was in contact to coesite. The initial formation of Tur and its isotopic composition have not been investigated, yet.

Chromian dravite and uvite ($CaMg_3MgAl_5[Si_6O_{18}$-$(BO_3)_3](OH)_4$) in Opx eclogites from coesite-bearing units of the Western Gneiss Region (WGR, Norway) where reported (Smith, 1971, 1988; Lappin & Smith, 1978), for which peak $P - T$ estimates are ~ 3.2 GPa and $\sim 800\,^{\circ}$C (Smith, 1988). Tour-
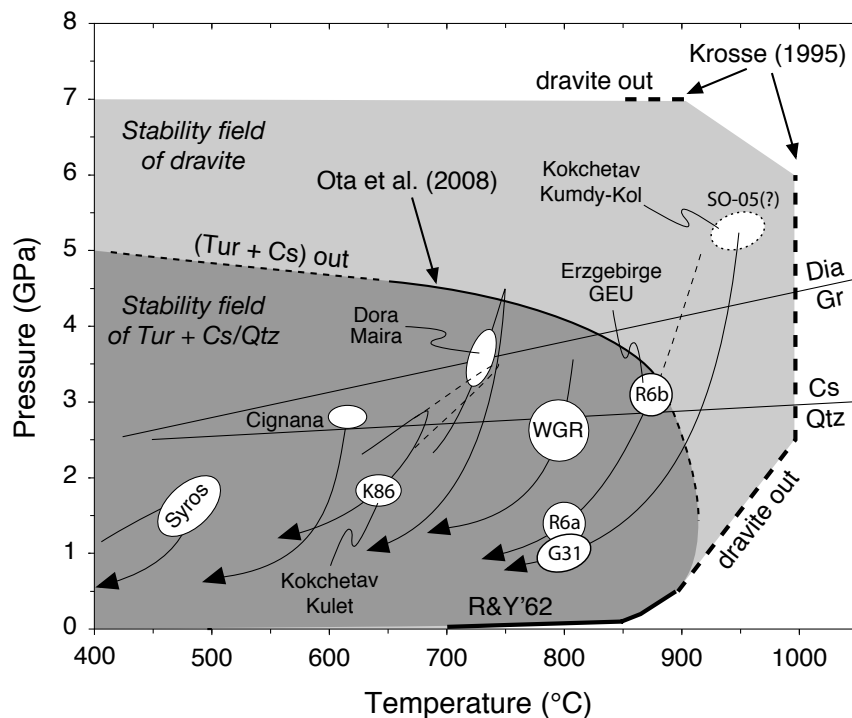
3

Fig. 1. $P-T$ diagram displaying (i) experimentally determined stability of dravitic Tur (light grey field) (Robbins & Yoder, 1962; Krosse, 1995; Werding & Schreyer, 2002) and Tur + coesite/quartz (dark grey field) (Ota *et al.*, 2008), and (ii) peak-metamorphic conditions of different Tur-bearing natural (U)HP rocks with most likely conditions of Tur formation marked by white ellipses: Syros (Marschall *et al.*, 2008); Coesite-bearing pelagic metasediments from Lago di Cignana, Western Alps, Italy (Reinecke, 1998; Bebout & Nakamura, 2003); Coesite-kyanite-pyrope quartzite from the Dora Maira massif, Western Alps, Italy (Schreyer, 1985; Schertl *et al.*, 1991); Eclogite from Sunnmøre, in the coesite-bearing unit of the Western Gneiss Region (WGR), Norway (Smith, 1988); Coesite-bearing schists from Unit II of the Kokchetav massif with $P-T$ estimates for Phe-Qtz-Grt-Ky rocks (solid line; Korsakov, unpubl.) and for whiteschist (dotted line; Parkinson, 2000); Diamond-coesite-bearing metapelites from Unit I of the Kokchetav massif, Kazakhstan (Hermann *et al.*, 2001; Shimizu & Ogasawara, 2005); Diamond-coesite-bearing gneisses from the Gneiss-Eclogite Unit (GEU) of the Erzgebirge, Germany (Massonne, 2003; Schmädicke & Müller, 2000; Massonne *et al.*, 2007). Equilibria of graphite-diamond after Bundy (1980) and quartz-coesite after Bohlen & Boettcher (1982).

maline forms part of a lower-pressure assemblage of hydrous minerals that formed after initial decompression of the eclogites to ~ 2.3 GPa and $\sim 750\,°$C (Fig.1; Lappin & Smith, 1978). Hence, the WGR Tur appears to be of Type C.

K_2O-rich Tur (Table1; Fig.2) with diamond inclusions occurring in metapelites has been described by Shimizu & Ogasawara (2005) from Kumdy-Kol in the Kokchetav massif, Kazakhstan, for which metamorphic peak conditions of $900 - 1000\,°$C and ~ 5 GPa have been estimated (Dobretsov *et al.*, 1995; Theunissen *et al.*, 2000a,b; Ota *et al.*, 2000; Okamoto *et al.*, 2000; Hacker *et al.*, 2003). However, some of the Kumdy-Kol rocks also contain dia-

mond in the Qtz-Fsp aggregates (Korsakov *et al.*, 2004). Thus, it is apparently possible that diamond survives decompression and recrystallisation of the surrounding minerals without being transformed to graphite. Therefore, the occurrence of diamond inclusions in Tur may not be sufficient to prove the growth of the Tur under UHP conditions. To date, no coesite inclusions have been reported from Kokchetav Tur, and high-K_2O Tur investigated in this study contains numerous inclusions of quartz, suggesting low-pressure formation (Fig.1).
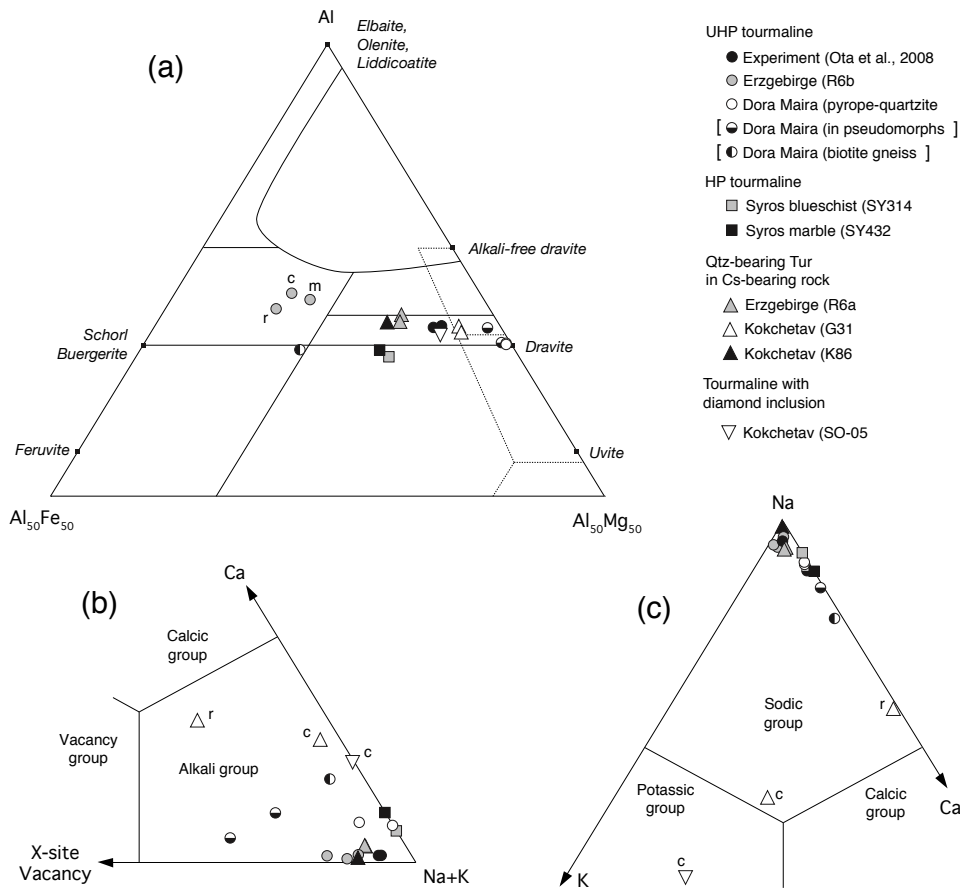
4

Fig. 2. Major element composition of Tur occurring in (U)HP metamorphic rocks. (a) Al-Mg-Fe classification plot after Hawthorne & Henry (1999). (b) (Na+K) apex of the (Na+K)-Ca-vacancy ternary diagram showing occupation of the crystallographic X-site. (c) Na apex of the Na-K-Ca ternary diagram displaying the occupancy of the crystallographic X-site. c = core; m = mantle; r = rim of Tur grain.

4. Boron isotope signatures in (U)HP tourmaline

Tourmaline shows a range of $\delta^{11}B$ values of more than 50 ‰ in natural rocks, from −27 ‰ (Broken Hill; Slack *et al.*, 1993) to +28 ‰ (Syros; Marschall *et al.*, 2006b). Volume diffusion for major and trace elements and B isotopes within Tur up to temperatures of 600 °C is uneffective (Henry & Dutrow, 1994, 2002; Dutrow *et al.*, 1999; Bebout & Nakamura, 2003). Therefore, chemical and isotopic heterogeneities of different growth zones are readily preserved even in high-grade rocks with complex metamorphic and metasomatic histories. The internal B

isotopic zonation of Tur can be used to monitor the B isotopic evolution of a rock throughout its metamorphic history, unless it was reset by diffusion or recrystallisation. The development of the SIMS technique for in-situ analyses of B isotope ratios allows for detailed investigations of multiple zoned Tur in metamorphic rocks (e.g. Smith & Yardley, 1994; Chaussidon & Appel, 1997; Nakano & Nakamura, 2001; Bebout & Nakamura, 2003; Altherr *et al.*, 2004; Marschall *et al.*, 2006b, 2008; van Hinsberg & Marschall, 2007).

Tourmaline in metasediments from the Sambagawa belt is strongly zoned with $\delta^{11}B$ values decreasing from −3 ‰ in the core to −10 ‰ at the rim of

5

a single grain (Nakano & Nakamura, 2001) (Fig.3). The growing Tur is thought to have incorporated B with decreasing $^{11}B/^{10}B$ ratios in the course of progressive metamorphism, due to a preferentially release of ^{11}B from the mica. The B isotopic composition of the metasediments during any stage of metamorphism is recorded in the respective growth zone of this Type-A Tur.

Type-A Tur in HP metamorphic rocks from the Catalina Schist, California (USA) displays decreasing $\delta^{11}B$ values from -7 (core) to $-15\,\permil$ (rim; Fig.3), (Bebout & Nakamura, 2003). At the outermost rims ($\sim 30\,\mu m$), $\delta^{11}B$ values increase again to approx. $-7\,\permil$. Bebout & Nakamura (2003) accredit the core-to-rim decrease in $\delta^{11}B$ values to prograde redistribution of B from mica into Tur, following the interpretation of Nakano & Nakamura (2001), and the increase of $\delta^{11}B$ at the outer rims to growth of Tur during influx of B-rich fluids (Type C) at retrograde metamorphic conditions (Fig.3).

UHP Tur from Lago di Cignana displays homogeneous B isotopic compositions of approx. $-10\,\permil$ in cores, but a strong increase of $\delta^{11}B$ values at the outermost $100\,\mu m$ (Bebout & Nakamura, 2003). The increase of $\delta^{11}B$ values to $+4\,\permil$ again is interpreted as the result of retrograde enrichment of B by fluids (Type C; Fig.3). The cores show inclusions of coesite, garnet and rutile, while the high-$\delta^{11}B$ rims contain quartz and epidote. The authors explain the homogeneous core plateau by diffusive re-equilibration of B isotopes at the peak of metamorphism ($T \sim 620\,°C$). An alternative interpretation would be a formation of these relatively large cores ($\sim 500\,\mu m$) during an influx of B-bearing fluids (at UHP conditions), which tends to form large, homogeneous crystals. Recently, Meyer et al. (2008) have suggested that large, homogeneous Tur crystals in metamorphic rocks may result from solution and re-precipitation, as opposed to simple diffusive re-equilibration.

Type-C Tur from Elekdağ (Turkey) formed during re-hydration of exhuming lawsonite eclogite. Its boron isotopic composition ranges from $-2.2\,\permil$ in the core to $+1.7\,\permil$ in the rim (Altherr et al., 2004) (Fig.3). The source of the B-bearing fluid is thought to be dehydrating altered oceanic crust and sediments in an underlying subducting slab at the time of exhumation of the eclogites.

Very similar Type-C Tur is found on Syros (Greece), where it formed during rehydration of HP rocks during decompression of the HP unit (Marschall et al., 2006b). Boron in all investigated samples is very heavy ($\delta^{11}B > +18\,\permil$) with values up to $+28\,\permil$ (Fig.3). The fluid is thought to have been chromatographically enriched in the heavy isotope during its migration from a dehydrating slab into the exhuming eclogite blocks (Marschall et al., 2006b).

The B isotopic compositions of detrital Tur (Type D1) from HP meta-sediments from Syros (Greece) show a grain-to-grain variation in a single sample ranging from -10.7 to $+3.6\,\permil$ (Marschall et al., 2008). Despite of the small size of these detrital cores ($\sim 20\,\mu m$), the chemical and isotopic zonation was preserved through the metamorphic cycle with a peak temperature of $500\,°C$. Metamorphic growth zones (Type A) in the same sample show homogeneous $\delta^{11}B$ values of $+0.9\,\permil$ (Marschall et al., 2008) (Fig.3).

5. Tourmaline in UHP gneisses from Kokchetav and Erzgebirge

5.1. Kokchetav samples

The Kokchetav Massif forms part of the Caledonian Central-Asiatic fold belt and is situated between the Siberian platform and the East European platform in Kazakhstan (Dobretsov et al., 1995). Diamonds have been found in all rock types of Unit I of the Zerenda Series (except eclogites and migmatites) providing evidence for UHP metamorphism ($> 4.0\,GPa$) (Sobolev & Shatsky, 1990; Shatsky et al., 1995). The Zerenda Series consists mainly of garnet-biotite-kyanite gneisses and schists with intercalated dolomitic marbles, calc-silicates and eclogites (Dobretsov et al., 1995). Unit I diamondiferous rocks are interpreted as part of a mega-melange (Dobretsov et al., 1995) consisting of rocks types exhibiting contrasting metamorphic conditions. Unit II also contains HP to UHP relics, but metamorphic peak conditions ($T = 720 - 760\,°C$, $P = 3.4 - 3.6\,GPa$) seem to be significantly lower than for rocks of Unit I (Parkinson, 2000).

In the Kulet region, coesite-bearing garnet in micaschists and in whiteschist of Unit II (e.g. Parkinson, 2000) are evidence for the UHP formation of the unit. At Kumdy-Kol, UHPM rocks of Unit I are best exposed in a former mining gallery, which comprises a concordant succession of four different rock types: diamond-bearing metacarbonate rocks, metasomatic gneisses, diamond-bearing garnet-biotite-
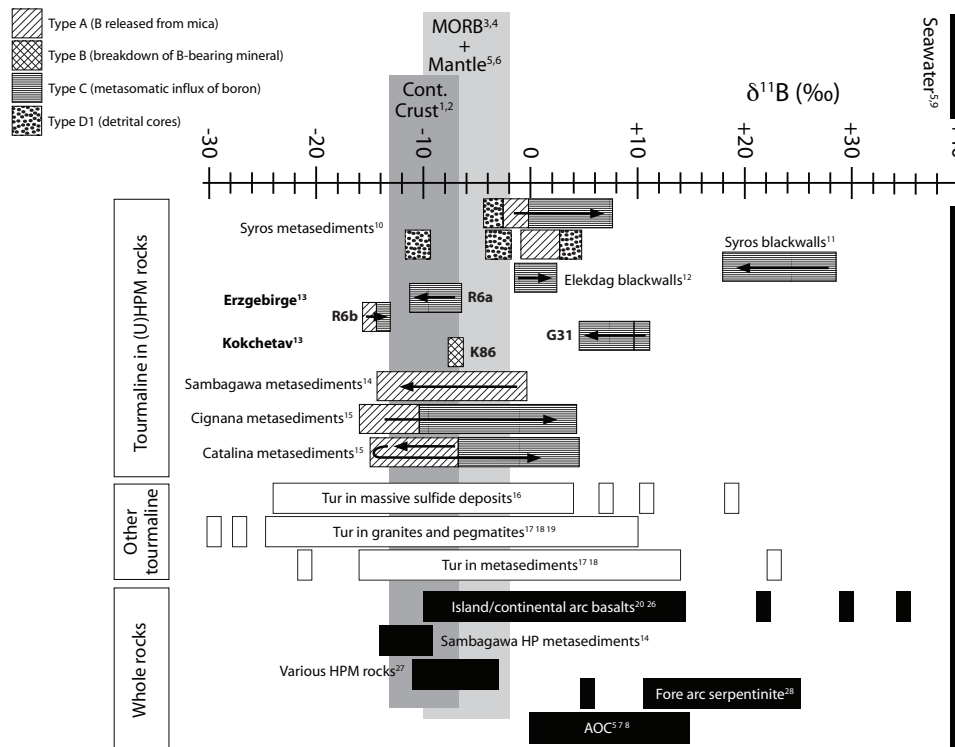
6

Fig. 3. Compilation of boron isotopic compositions of Tur from (U)HP metamorphic rocks in comparison to other Tur and some important geochemical reservoirs. Arrows mark zoned grains pointing from core to rim compositions. Values were taken from: [1]Chaussidon & Albarède (1992), [2]Kasemann *et al.* (2000), [3]Chaussidon & Jambon (1994), [4]le Roux *et al.* (2004), [5]Spivack & Edmont (1987), [6]Chaussidon & Marty (1995), [7]Ishikawa & Nakamura (1992), [8]Smith *et al.* (1995), [9]Barth (1993), [10]Marschall *et al.* (2008), [11]Marschall *et al.* (2006b), [12]Altherr *et al.* (2004), [13]this study, [14]Nakano & Nakamura (2001), [15]Bebout & Nakamura (2003), [16]Palmer & Slack (1989), [17]Swihart & Moore (1989), [18]Palmer & Swihart (1996), [19]Marschall & Ludwig (2006), [20]Ishikawa & Nakamura (1994), [21]Ishikawa & Tera (1997), [22]Smith *et al.* (1997), [23]Tonarini *et al.* (2001), [24]Clift *et al.* (2001), [25]Ishikawa *et al.* (2001), [26]Straub & Layne (2002), [27]Peacock & Hervig (1999), [28]Benton *et al.* (2001).

pyroxene gneisses and migmatites. Peak metamorphic conditions of $T = 900 - 1000\,^{\circ}\mathrm{C}$ and $P = 4 - 6\,\mathrm{GPa}$ were estimated for the diamond-bearing rocks (Sobolev & Shatsky, 1990; Okamoto *et al.*, 2000; Katayama *et al.*, 2000; Hermann *et al.*, 2001). Retrograde equilibration of the Kumdy-Kol gneisses at $T \approx 800\,^{\circ}\mathrm{C}$ and $P \approx 1.0\,\mathrm{GPa}$ marks the end of rapid near-isothermal decompression (Katayama *et al.*, 2001; Hermann *et al.*, 2001). Beside differences in peak-metamorphic conditions, melting under UHPM conditions becomes increasingly evident for the diamond-grade rocks in western Kokchetav (Massonne, 2003; Korsakov *et al.*, 2004, 2006; Korsakov & Hermann, 2006), but was so far not observed in rocks of the coesite-bearing Kulet area in eastern Kokchetav.

Sample K86 from Kulet (eastern Kokchetav) is a garnet-kyanite-phengite-quartz gneiss (Fig.4a) with prismatic to rhombohedral pseudomorphs consisting of a symplectitic intergrowth of Ms+Ab+Qtz (Fig.4b). These symplectites consistently contain several short-prismatic Tur grains adding up to $\sim 1\,\%$ of the pseudomorphs (Fig.4b,c). The grains are euhedral, $50 - 150\,\mu\mathrm{m}$ long, show a pale brown colour in thin section, and a weak zonation visible in back-scattered electron (BSE) images (Fig.4c). Rare inclusions of albite and quartz were found. The composition of the grains is very homogeneous and close to the ideal schorl-dravite series ($X_{\mathrm{Mg}} \sim 0.67$; Fig.2), but contains some tetrahedral B (Table1). Boron isotope analyses of several grains in different pseudomorphs show a constant δ^{11}B value of
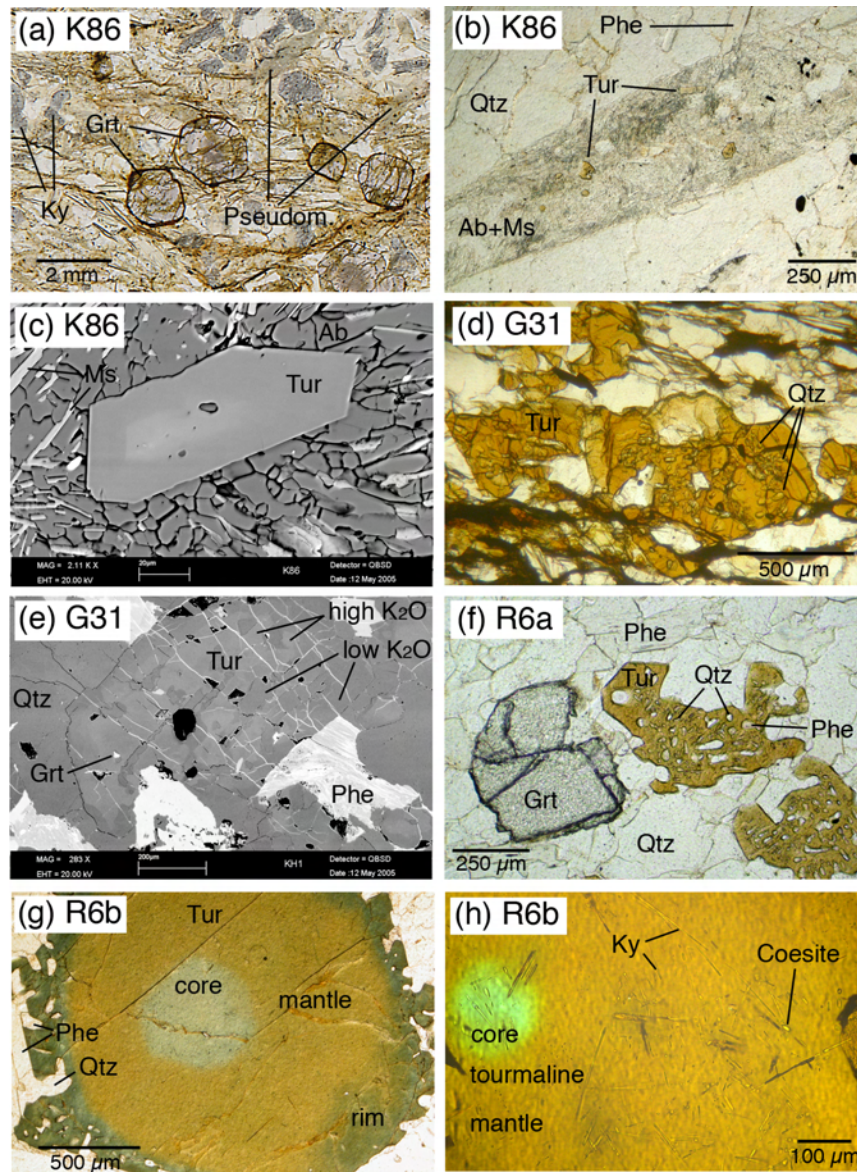
7

Fig. 4. Microphotographs and back-scattered electron (BSE) images of Tur in UHP metamorphic rocks from Kokchetav and Erzgebirge. (a) Kyanite and coesite-bearing garnet porphyroblasts and Tur-bearing Ab+Ms pseudomorphs in Phe-Qtz-Grt-Ky rock K86 from Kokchetav. (b) Brownish Tur crystals in Ab+Ms pseudomorph. (c) BSE image of Tur in Ab+Ms pseudomorph. (d) Brownish high-K_2O Tur porphyroblast with abundant Qtz inclusion in diamond-bearing rock G31 from Kokchetav. (e) BSE image displaying Tur porphyroblast with high-K_2O core (brighter) and low-K_2O rim (darker grey). (f) Garnet ($\pm$coesite bearing) and brownish, Qtz-bearing Tur porphyroblast in Grt-Phe-Bt gneiss R6a from the Erzgebirge. (g) Zoned Tur prophyroblast in Phe-Qtz gneiss R6b from the Erzgebirge. (h) Thick section ($\sim 100\,\mu m$) microphotograph, showing inclusions of coesite and kyanite in Tur in Phe-Qtz gneiss R6b from the Erzgebirge.

8

$-7.4 \pm 0.7\,‰$ (Table2; Fig.6a). Garnet shows optical zonation, marked by a dusty core zone with fine-grained silica inclusions, surrounded by a clean mantle zone (Fig.4a). Coesite as inclusion in the clean mantle zone was identified by Raman spectroscopy (Fig.5).

The restriction of Tur to the Ab+Ms pseudomorphs and the inclusions of Ab in this Tur shows that Tur in this sample formed during or after decompression, either from B introduced into the pseudomorphs by fluids (Type C), or from B derived from the (unidentified) precursor mineral of the pseudomorphs (Type B). The constant proportion of Tur observed in all pseudomorphs may suggest that a constant amount of B was available during formation of the psudomorphs. The interpretation of a B-bearing precursor mineral is thus preferred. A boron concentration of $\sim 300\,\mu g/g$ would be required to form the observed amount of Tur. The B isotopic composition of K86 Tur is within the range of typical Continental Crust (Fig.3).

Sample G31 was taken from the metasomatic gneisses in the mining gallery at Kumdy-Kol. The sample contains abundant octahedral diamond inclusions in zircon. The metasomatic rocks lack garnet, but contain abundant Tur ($\sim 8\,\%$ of the rock), which forms $1 - 4\,mm$ large, brown porphyroblasts (Fig.4d) in a coarse-grained Qtz-Fsp-Bt matrix. It probably replaced garnet during metasomatism. Inclusions in Tur are quartz, graphite, garnet, apatite and zircon. An extensive search using the Raman facility revealed hundreds of quartz inclusions ranging from $< 5\,\mu m$ to $> 100\,\mu m$, but no coesite or diamond. Tourmaline displays large, homogeneous cores, truncated by tiny cracks that are filled with Fe-oxide (Fig.4e). Along a $\sim 50\,\mu m$ wide zone at the rims and along larger internal cracks and inclusions it shows a lower BSE signal (Fig.4d). The core domain is Mg-Na-F rich (Table1; Fig.2), but is distinct from dravite by significant amounts of Ca (~ 0.3pfu), excess B (~ 3.3pfu) and – most remarkable – K (0.32pfu; Table1; Fig.2c). The darker rim region is also Mg-B-F-Ca rich, but shows significant X-site vacancies ($0.2 - 0.3$pfu) and a very low K_2O content (< 0.05 wt%, i.e. close to the detection limit) (Table1; Fig.2). The B isotopic composition of the Tur decreases from core to rim and along the larger cracks. It is very high with $\delta^{11}B$ values of $+9.4 \pm 0.4\,‰$ in the core and $+6.5 \pm 1.0\,‰$ in the low-K zones (Table2; Fig.6b).

The lack of UHP mineral inclusions (i.e. coesite) and the ubiquitous appearance of quartz inclusions in all investigated Tur porphyroblasts proves that Tur in G31 formed in the Qtz stability field. The concordant succession of metasomatic Tur-bearing gneisses and garnet-bearing gneisses together with garnet relics as inclusions in Tur suggests that Tur formed from garnet during metasomatism (Type C). The high modal abundance of Tur ($\sim 8\,\%$) translating to whole-rock B concentrations of $\sim 2500\,\mu g/g$ requires a significant metasomatic enrichment of B in the rocks during this event. The B isotopic composition of G31 Tur cores at close to $+10\,‰$ is exceptionally heavy compared to crust, mantle and other HPM Tur (Fig.3). A strong metasomatic enrichment of heavy B in (U)HPM rocks during exhumation has previously only been documented for eclogites from Syros (Greece), where it has been taken as evidence for heavy-B fluids in subduction zones at a depth of $\sim 25\,km$ (Marschall $et\ al.$, 2006b). Sample G31 shows that such heavy-B fluids also exist in continental collision zones, possibly at $\sim 30\,km$ depth, when the rocks equilibrated after decompression.

One is inclined to speculate that the unusually high K_2O contents of Tur cores in G31 may be related to UHP conditions. However, the metasomatic formation of Tur from garnet during or after decompression in the Qtz stability field demonstrates that the K-rich Tur formed at relatively low P.

5.2. *Erzgebirge samples*

The Erzgebirge, situated at the northwestern border of the Bohemian Massif, is part of the Devonian-Carboniferous metamorphic basement of the Mid-European Variscides exposed in Saxony and the northern Czech Republic. It is characterized by a stack of five tectonometamorphic units with contrasting $P - T$ histories (Willner $et\ al.$, 1997; Rötzler $et\ al.$, 1998). The invetigated samples R6a and R6b are from the diamond and coesite-bearing Gneiss-Eclogite Unit (GEU). $P - T$ estimates on eclogite pods revealed conditions of $> 2.9\,GPa$ at $870\,°C$ (Schmädicke & Müller, 2000), and the occurrence of diamond in the felsic gneisses requires pressures in excess of $4.0\,GPa$ (Massonne, 2003; Massonne $et\ al.$, 2007). $P - T$ estimates as high as $8.0\,GPa$ at $> 1050\,°C$ have been published for the GEU (Massonne, 2003). Our samples were collected as lose decimeter-sized blocks from a small creek $5\,km$ ENE of the village of Saidenbach.

Sample R6a is a banded fine-grained granulite with bands rich in quartz + feldspar+ phengite

9

Table 1. Chemical composition of tourmaline from (U)HP metamorphic rocks and from experiments (this study and literature data)

Locality	Syros (Greece)		Kokchetav (Kazakhstan)				Erzgebirge (Germany)					Dora Maira (Alps)		Experiment				
Sample	SY314[a]	SY432[a]	K86	SO-05[b]	G31		R6a		R6b			Dora Maira[c]					Piston cylinder[d]	
Domain	core	rim	core	core	core	rim	core	rim	core	mantle	rim	in Prp	in Pseudo	in Prp	in Pseudo	in Bt gneiss	4.0 GPa 800 °C	4.5 GPa 700 °C
Type	A (HP)	A (HP)	B (LP)	C? (UHP?)	C (Qtz)	C (LP)	C (Qtz)	C (LP)	A (UHP)	A (UHP)	C (LP)	C? (UHP)	C? (UHP?)	C? (UHP)	C? (UHP?)	C? (UHP?)		
SiO_2	35.85	35.45	36.07	36.45	35.90	36.00	35.84	35.85	34.95	34.79	34.77	37.85	37.57	37.51	38.12	35.25	35.9	35.6
TiO_2	0.19	0.27	0.64	1.12	0.66	0.72	1.00	0.88	0.22	0.82	0.54	0.13	0.25	0.10	0.12	0.24	0.5	0.5
B_2O_3	10.39*	10.38*	11.18	10.57*	11.95	11.87	11.42	11.42	11.04	11.09	11.18	10.89*	10.76*	10.71*	10.87*	10.29*	10.5*	10.4*
Al_2O_3	29.31	29.83	32.57	31.07	32.11	32.76	32.47	33.16	35.33	34.28	33.66	31.82	31.42	32.55	31.30	29.80	32.0	31.8
Cr_2O_3	0.07	0.06	0.06	n.a.	0.04	0.10	0.05	0.05	0.02	0.00	0.00	0.00	0.00	0.00	0.00	n.a.	n.a.	n.a.
FeO^t	7.86	7.92	6.00	3.35	2.47	2.36	5.35	4.95	9.44	8.71	11.02	0.23	0.48	0.73	0.28	12.42	3.1	3.6
MnO	0.00	0.05	0.01	0.01	0.02	0.01	0.06	0.06	0.07	0.02	0.02	0.00	0.00	0.00	0.00	0.09	0.0	0.0
MgO	8.58	7.90	6.97	8.65	9.88	9.56	7.39	7.19	3.28	3.91	3.21	12.02	11.66	10.33	11.94	5.16	8.6	8.4
ZnO	0.07	0.15	0.04	n.a.	0.02	0.05	0.10	0.07	0.09	0.12	0.20	n.a.	n.a.	n.a.	n.a.	n.a.	n.a.	n.a.
CaO	0.04	0.69	0.03	1.24	1.56	1.42	0.19	0.18	0.08	0.05	0.09	0.53	0.65	0.33	0.51	1.03	0.1	0.1
Na_2O	2.87	2.94	2.78	0.73	1.18	1.42	2.74	2.73	2.54	2.58	2.63	2.72	2.19	2.01	3.00	2.25	2.8	2.8
K_2O	0.01	0.01	0.04	2.62	1.57	0.04	0.12	0.14	0.06	0.18	0.16	0.05	0.02	0.02	0.04	0.06	0.1	0.1
Li (µg/g)	n.a.	n.a.	4.9	n.a.	19.3	16.1	22.7	20.8	52.2	30.9	24.0	n.a.	n.a.	n.a.	n.a.	n.a.	n.a.	n.a.
Be (µg/g)	n.a.	n.a.	0.54	n.a.	0.94	2.4	0.31	0.26	0.01	0.01	0.02	n.a.	n.a.	n.a.	n.a.	n.a.	n.a.	n.a.
H_2O	3.46*	3.23*	3.18	3.64*	3.10	3.20	3.14	3.14	2.81	2.79	2.86	3.76*	3.71*	3.70*	3.75*	3.55*	3.6*	3.6*
F	0.16	0.73	0.27	n.a.	0.57	0.53	0.26	0.23	0.14	0.10	0.17	n.a.	n.a.	n.a.	n.a.	n.a.	n.a.	n.a.
Cl	0.00	0.00	0.00	n.a.	0.03	0.01	0.01	0.01	0.00	0.01	0.00	n.a.	n.a.	n.a.	n.a.	n.a.	n.a.	n.a.
$-(F+Cl)=O$	0.07	0.31	0.11		0.25	0.23	0.11	0.10	0.06	0.04	0.07							
Total	99.15	99.30	99.73	99.44	100.81	100.21	99.97	99.97	100.03	99.40	100.43	100.00	98.71	97.99	99.93	100.14	97.20	96.90

Formulas calculated to 31 oxygens, $Fe^{2+} = Fe^t$

Si	5.99	5.94	5.92	6.00	5.78	5.78	5.86	5.85	5.81	5.82	5.81	6.04	6.07	6.09	6.09	5.96	5.97	5.95
Ti	0.02	0.03	0.08	0.14	0.08	0.09	0.12	0.11	0.03	0.10	0.07	0.02	0.03	0.01	0.01	0.03	0.06	0.06
B	3.00*	3.00*	3.17	3.00*	3.32	3.29	3.22	3.22	3.17	3.20	3.23	3.00*	3.00*	3.00*	3.00*	3.00*	3.00*	3.00*
Al	5.78	5.89	6.30	6.03	6.10	6.20	6.26	6.38	6.92	6.75	6.63	5.99	5.98	6.22	5.90	5.94	6.27	6.26
Cr	0.01	0.01	0.01		0.00	0.01	0.01	0.01	0.00	0.00	0.00	0.00	0.00	0.00	0.00			
Fe^{2+}	1.10	1.11	0.82	0.46	0.33	0.32	0.73	0.68	1.31	1.22	1.54	0.03	0.07	0.10	0.04	1.76	0.43	0.50
Mn	0.00	0.01	0.00		0.00	0.00	0.00	0.01	0.01	0.00	0.00	0.00	0.00	0.00	0.00	0.01	0.00	0.00
Mg	2.14	1.97	1.71	2.12	2.37	2.29	1.80	1.75	0.81	0.98	0.80	2.86	2.81	2.50	2.85	1.30	2.13	2.09
Zn	0.01	0.02	0.00		0.00	0.01	0.01	0.01	0.01	0.02	0.03	0.03		0.00	0.00			
Ca	0.07	0.12	0.01	0.22	0.27	0.31	0.03	0.03	0.02	0.01	0.02	0.09	0.11	0.06	0.09	0.19	0.02	0.02
Na	0.93	0.96	0.88	0.23	0.37	0.44	0.87	0.87	0.82	0.83	0.85	0.84	0.69	0.63	0.93	0.74	0.90	0.91
K	0.00	0.00	0.01	0.55	0.32	0.01	0.02	0.03	0.01	0.04	0.04	0.01	0.00	0.00	0.01	0.01	0.02	0.02
Total	19.05	19.06	18.90	18.75	18.96	18.75	18.94	18.92	18.94	18.96	19.00	18.88	18.76	18.61	18.91	18.94	18.80	18.82
X_{Mg}	0.660	0.640	0.674	0.822	0.877	0.878	0.711	0.721	0.383	0.445	0.342	0.989	0.977	0.962	0.987	0.426	0.832	0.806
OH	3.86*	3.61*	3.48	4.00*	3.33	3.43	3.42	3.42	3.12	3.11	3.19	4.00*	4.00*	4.00*	4.00*	4.00*	4.00*	4.00*
F	0.14	0.39	0.14		0.29	0.27	0.14	0.12	0.08	0.05	0.09							
Cl	0.00	0.00	0.00		0.01	0.00	0.00	0.00	0.00	0.00	0.00							

[a]Marschall et al. (2008); [b]Shimizu & Ogasawara (2005); [c]Schertl et al. (1991); [d]Ota et al. (2008); * H_2O and B_2O_3 calculated stoichiometrically. H, Li, Be and B analysed by SIMS; all other elements analysed by EPMA. n.a. = not analysed.

10

Table 2
Boron isotope values of tourmaline from UHP metamorphic rocks determined by SIMS

Locality	Kokchetav (Kazakhstan)			Erzgebirge (Germany)				
Sample	K86	G31		R6a		R6b		
Domain	core	core	rim	core	rim	core	mantle (UHP)	rim (ret)
Type	B	C	C	C	C	A	A	C
δ^{11}B	-7.4	$+9.4$	$+6.5$	-7.2	-10.5	-15.0	-14.7	-13.2
$2RSD_{mean}$	0.7	0.4	1.0	0.3	0.8	0.2	0.3	0.5
n	9	11	6	12	7	12	15	7

$2RSD_{mean} = 2\times$ relative standard deviation of the mean; n = number of isotope analyses.

alternating with bands rich in garnet + biotite. Tourmaline forms $0.5 - 1\,\mathrm{mm}$ large porphyroblasts, which are brown in thin section (Fig.4f), and show inclusions of quartz and phengite. Composite coesite + α-quartz inclusions in garnet were identified by Raman spectroscopy (Fig.5). The chemical composition of R6a Tur is very similar to K86 in all major elements. It is close to the schorl-dravite series ($X_{Mg} \sim 0.72$) with high occupation of the X-site by Na (Fig.2) and some excess B (Table1). B isotopes show a core-to-rim decrease from $-7.2 \pm 0.3\,\%_0$ to $-10.5 \pm 0.8\,\%_0$ (Table2; Fig.6c).

The high abundance and large grain size Tur with ubiquitous Qtz inclusions in R6a suggests that Tur formed during influx of B-rich fluids during decompression. Its B isotopic composition is within the typical range of continental crust (Fig.3), although a decrease of δ^{11}B to $-10\,\%_0$ towards the rim of the grains is unusual for retrograde Tur.

Sample R6b is a felsic medium-grained mylonitic granulite displaying strongly elongated (ribbon) quartz and feldspar with black turmaline porphyroclasts. Tourmaline is short-prismatic and $1 - 3\,\mathrm{mm}$ in cross section. In thin section cut perpendicular to the c-axis, it shows three distinct colour zones that display diffuse boundaries: a blue core, a honey-brown mantle, and a greenish-grey anhedral rim zone, which is intimately intergrown with Qtz, Fsp and Phe from the matrix (Fig.4g). A $\sim 15\,\mu\mathrm{m}$ large inclusion of coesite in the mantle zone of Tur (Fig.4h) was identified by Raman spectroscopy (Fig.5). Tourmaline in this sample shows detectable tetrahedral B and a low proportion of X-site vacancies, similar to all investigated samples. X_{Mg} in this sample is distinctly lower, though, increasing from 0.38 in the core to 0.45 in the mantle, and dropping to 0.34 in the rim (Table1; Fig.2). In fact, this sample displays the only *schorl* observed so far in any HPM or UHPM rock. K_2O contents show a steady increase from $\sim 0.05\,\mathrm{wt}\%$ in the core to $\sim 0.18\,\mathrm{wt}\%$

in the mantle and the rim. The B isotopic composition is light and very homogeneous throughout the core (δ^{11}B $= -15.0 \pm 0.2\,\%_0$) and mantle (δ^{11}B $= -14.7 \pm 0.3\,\%_0$) and slightly heavier in the rim (δ^{11}B $= -13.2 \pm 0.5\,\%_0$) (Table2; Fig.6d).

The Fe-rich composition of coesite-bearing Tur demonstrates that not only dravitic Tur is stable under UHP conditions, and thus that high X_{Mg} is neither a sufficient nor a necessary feature of Tur to be stable at UHP. The occurrence of kyanite and coesite inclusions in core and mantle of the large porphyroclasts shows that the entire grain must have grown or at least re-crystallised under HP to UHP conditions. The unzoned B isotopes throughout core and mantle of the Tur may also be explained by re-crystallisation of the grains, or by diffusional equilibration after growth. The preservation of the major element core-mantle zoning, however, shows that the homogenisation of other major and minor elements, such as Ti, Fe and Mg was incomplete (Table2; Fig.4g,h). The light B-isotopic composition of approx. $-15\,\%_0$ is below the range of continental crust, but similar to coesite-bearing Tur from Lago di Cignana (Alps) and to other HP metasediments (Fig.3).

5.3. *Results from Raman spectroscopy*

Using Raman micro-spectroscopy as a simple fingerprinting technique, several SiO_2 inclusions were identified as either coesite or a mixture of coesite and α-quartz (Fig.5). These inclusions were found in host garnet and Tur crystals.

The SiO_2 inclusions were found to be affected by compressive strain, indicated by notable upshifts of Raman bands. This phenomenon, which is frequently described as "fossilized pressure" (e.g. Sobolev *et al.*, 2000), is due to (i) heterogeneous expansion of the host-inclusion couple upon pressure release and (ii) volume expansion of the in-
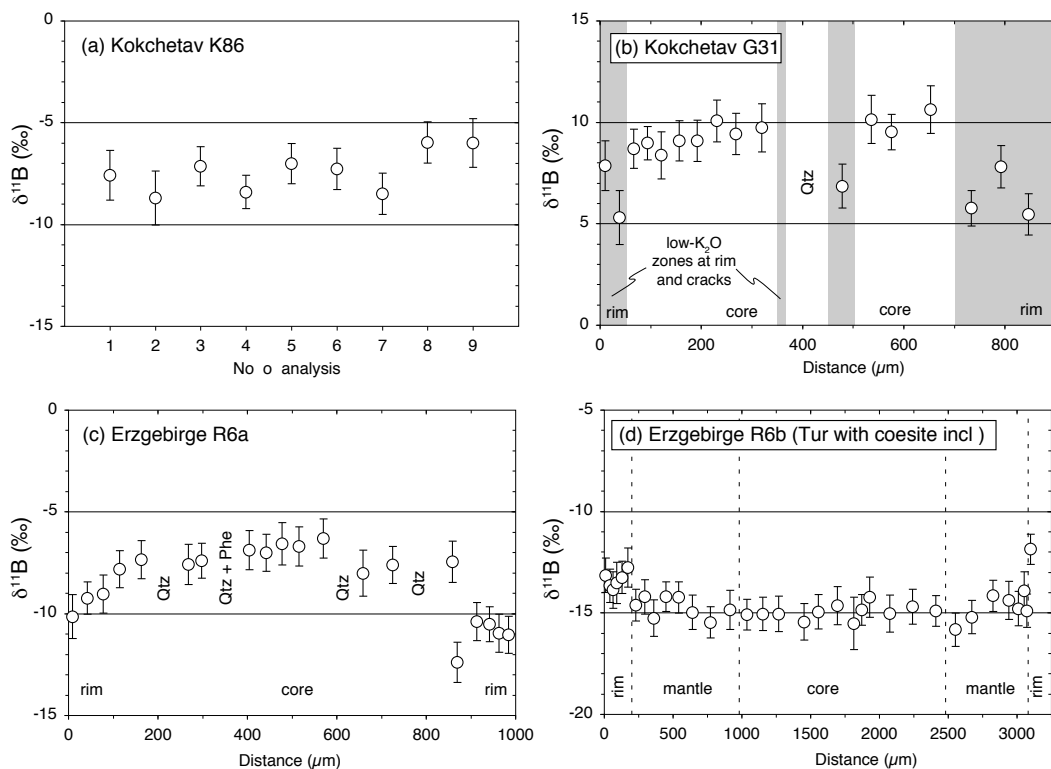
11

Fig. 6. Boron isotopic composition of Tur analysed by SIMS during this study. (a) Erzgebirge sample R6b: UHP schorl with coesite and kyanite inclusions in the mantle and quartz inclusions in the rim. (b) Erzgebirge sample R6a with numerous inclusions of quartz and phengite. (c) K_2O-rich Tur G31 from Kokchetav. Grey fields mark domains that show low K_2O concentrations and are close to cracks or at the rim. (d) Analyses of various Tur grains (core and rim) from sample K86.

clusion as caused by the beginning transformation of coesite to α-quartz during uplift. In general, the extent of compressive strain acting on SiO_2 inclusions tend to be higher in the case of inclusions in garnet, whereas inclusions in Tur seem to be somewhat less affected by strain. For instance, the following strain values were determined from the spectrum of a two-phase SiO_2 inclusion (sample R6a; Fig.5): The main coesite band (Raman shift $520.6\,cm^{-1}$ under ambient conditions) was recorded at $525.3 \pm 0.5\,cm^{-1}$, which corresponds to compressive strain of $\sim 1.6 \pm 0.2\,GPa$ (cf. Hemley, 1987). The three main Raman bands of α-quartz ($128\,cm^{-1}$, E mode; $206\,cm^{-1}$, A_1 mode; $464\,cm^{-1}$, A_1 mode) were observed at $134.3 \pm 0.5\,cm^{-1}$, $232.2 \pm 0.5\,cm^{-1}$, and $474.3 \pm 0.5\,cm^{-1}$. Based on the calibration of Liu & Mernagh (1992) and Schmidt & Ziemann (2000), these band up-shifts

correspond to compressive strain on the order of $1.0 - 1.5\,GPa$ and $0.8 - 1.3\,GPa$, respectively. Rather moderate strain of only $0.5 \pm 0.2\,GPa$ was determined for a coesite included in Tur (sample R6b; Figs. 4h and 5).

6. Conclusions

The review on the (scarce) data on (U)HP Tur major element chemistry available so far, reveals that most samples are dravitic, but exceptions include uvite from the WGR (Norway) and schorl from the Erzgebirge (Germany). High occupation of the crystallographic X-site ($> 0.8\,cpfu$) is apparently a consistent feature of all Tur in (U)HP rocks. High-K Tur has been observed only in metasomatic gneisses from Kokchetav, which formed in the stability field of Qtz, i.e. not at UHP conditions. Ex-

12

212
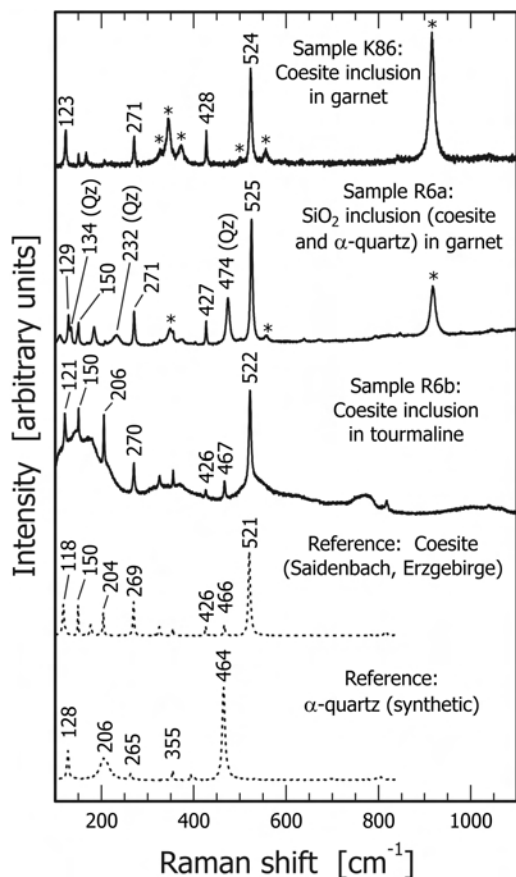
Fig. 5. Raman spectra obtained from two SiO_2 inclusions in garnet crystals and one coesite inclusion in Tur (solid graphs), along with reference spectra (dotted graphs) of synthetic α-quartz (Nasdala *et al.*, 2004a) and natural coesite (Nasdala *et al.*, 2004b). In the upper two spectra, bands of the host garnets are marked with asterisks. In the spectrum of sample R6a, α-quartz bands are marked "(Qz)".

cess B $(3.2 - 3.3\,\text{cpfu})$ is apparent from all analysed samples. Other consistencies among the samples include low abundances of Ti, Mn, Li and Cl. In conclusion, the major element chemistry of (U)HP Tur seems to be similar to that of metamorphic Tur from "normal" high-grade metapelites (Henry & Dutrow, 2002), and thus does not provide a diagnostic tool.

Inclusions of Tur in (U)HP phases, or of (U)HP phases in Tur are probably the best indicators for (U)HP stability and/or formation of Tur. Coesite found as inclusions in Tur can be recognised by Raman spectroscopy, which allows for rapid analyses of a large number of inclusions down to micrometer size. The low "fossilised pressure" observed in coesite inclusions in the Erzgebirge Tur may be due to formation of the host Tur close to the quartz-coesite phase boundary, or due to similar elasticity of Tur ($K_S = 127.2\,\text{GPa}$) and coesite ($K_S = 113.7\,\text{GPa}$), compared to garnet ($K_S = 177.0\,\text{GPa}$) and coesite (Bass, 1995). Diamond inclusions have also been described from Kokchetav Tur before (Shimizu & Ogasawara, 2005), but are controversial as evidence for the formation of the host Tur in the stability field of diamond.

Clearly, more investigation on Tur in (U)HPM rocks is needed, to fully exploit the potential of this mineral as a geochemical archive for several isotope systems (e.g. H, Li, B, O, Sr, Pb) in subduction and collision-related rocks. Rare-earth element (REE) patterns may be used to demonstrate (U)HP formation of Tur. Depletion in heavy REE is expected in Tur that grew in the presence of garnet, and small or absent Eu anomalies should result from growth in rocks devoid of plagioclase.

7. Acknowledgements

References

Altherr R, Topuz G, Marschall H, Zack T, Ludwig T (2004) Evolution of a tourmaline-bearing lawsonite eclogite from Elekdag area (Central Pontides, N Turkey): evidence for infiltration of slab-derived B-rich fluids during exhumation. *Contrib Mineral Petrol* 148: 409–425

Barth S (1993) Boron isotope variations in nature: a synthesis. *Geol Rund* 82: 640–651

Bass JD (1995) Elasticity of minerals, glasses, and melts. In: Ahrens TJ (ed.) *Mineral Physics and Crystallography: A Handbook of Physical Constants*, 45–63, Am. Geophys. Union, Washington, D.C.

Bebout GE, Nakamura E (2003) Record in metamorphic tourmaline of subduction-zone de-

13

volatilization and boron cycling. *Geology* 31: 407–410

Bebout GE, Bebout AE, Graham CM (2007) Cycling of B, Li, and LILE (K, Cs, Rb, Ba, Sr) into subduction zones: SIMS evidence from micas in high-P/T metasedimentary rocks. *Chem Geol* 239: 284–304

Benton LD, Ryan JG, Tera F (2001) Boron isotope systematics of slab fluids as inferred from a serpentine seamount, Mariana forearc. *Earth Planet Sci Lett* 187: 273–282

Bohlen SR, Boettcher AL (1982) The quartz-coesite transformation: A pressure determination and the effects of other components. *J Geophys Res* 87: 7073–7078

Boyer H, Smith DC, Chopin C, Lasnier B (1985) Raman microprobe (RMP) determinations of natural and synthetic coesite. *Phys Chem Minerals* 12: 45–48

Bundy FP (1980) The P,T phase and reaction diagram for elemental carbon. *J Geophys Res* 88: 6930–6936

Catanzaro FJ, Champion CE, Garner EL, Marinenko G, Sappenfield KM, Shields WR (1970) Boric acid: isotopic and assay standard reference materials. *NBS (US) Spec Publ* 260: 1–70

Chaussidon M, Albarède F (1992) Secular boron isotope variations in the continental crust: an ion microprobe study. *Earth Planet Sci Lett* 108: 229–241

Chaussidon M, Appel PWU (1997) Boron isotopic composition of tourmalines from the 3.8-Ga-old Isua supracrustals, West Greenland: implications on the Delta^{11}B value of early Archean seawater. *Chem Geol* 136: 171–180

Chaussidon M, Jambon A (1994) Boron content and isotopic composition of oceanic basalts: Geochemical and cosmochemical implications. *Earth Planet Sci Lett* 121: 277–291

Chaussidon M, Marty B (1995) Primitive boron isotope composition of the mantle. *Science* 269: 383–386

Clift PD, Rose EF, Shimizu N, Layne GD, Draut AE, Regelous M (2001) Tracing the evolving flux from the subducting plate in the Tonga-Kermadec arc system using boron in volcanic glass. *Geochim Cosmochim Acta* 65: 3347–3364

Dingwell DB, Pichavant M, Holtz F (2002) Experimental studies of boron in granitic melts. In: Grew ES, Anovitz LM (eds.) *Boron: mineralogy, petrology and geochemistry*, vol. 33 of *Rev. Mineral.*, chap. 8, 331–385, Mineral. Soc. Am., Washington, DC, 2nd edn.

Dobretsov NL, Sobolev NV, Shatsky VS, Coleman RG, Ernst WG (1995) Geotectonic evolution of diamondiferous paragneisses of the Kokchetav complex, Northern Kazakhstan - the geologic enigma of ultrahigh-pressure crustal rocks within Phanerozoic foldbelt. *The Island Arc* 4: 267–279

Domanik KJ, Hervig RL, Peacock SM (1993) Beryllium and boron in subduction zone minerals: an ion microprobe study. *Geochim Cosmochim Acta* 57: 4997–5010

Dutrow BL, Foster CT Jr, Henry DJ (1999) Tourmaline-rich pseudomorphs in sillimanite zone metapelites: Demarcation of an infiltration front. *Am Mineral* 84: 794–805

Dyar MD, Taylor ME, Lutz TM, Francis CA, Guidotti CV, Wise M (1998) Inclusive chemical characterization of tourmaline: Mössbauer study of Fe valence and site occupancy. *Am Mineral* 83: 848–864

Dyar MD, Guidotti CV, Core DP, Wearn KM, Wise MA, Francis CA, Johnson K, Brady JB, Robertson JD, Cross LR (1999) Stable isotope and crystal chemistry of tourmaline across pegmatite-country rocks boundaries at Black Mountain and Mount Mica, southwestern Maine, USA. *Eur J Mineral* 11: 281–294

Dyar MD, Wiedenbeck M, Robertson D, Cross LR, Delaney JS, Ferguson K, Francis CA, Grew ES, Guidotti CV, Hervig RL, Hughes JM, Husler J, Leeman W, McGuire AV, Rhede D, Rothe H, Paul RL, Richards I, Yates M (2001) Reference minerals for the microanalysis of light elements. *Geostand Newsl* 25: 441–463

Etchepare J, Merian M, Smetankine L (1974) Vibrational normal modes of SiO$_2$. I. α and β quartz. *J Chem Phys* 60: 1873–1876

Frei R, Pettke T (1996) Mono-sample Pb-Pb dating of pyrrhotite and tourmaline: Proterozoic vs. Archean intracratonic gold mineralization in Zimbabwe. *Geology* 24: 823–826

Fuchs Y, Lagache M (1994) La transformation chlorite-tourmaline en milieu hydrothermal, exemples naturels et approche expérimentale. *C R Acad Sci, Paris, Série II* 2: 907–913

Godard G (1988) Petrology of some eclogites in the Hercynides: the eclogites from the southern Armorican Massif, France. In: Smith DC (ed.) *Eclogites and eclogite-facies rocks*, vol. 12 of *Developments in Petrology*, 451–519, Elsevier

Godard G (2007) A Variscan equivalent of the Alpine Monte Mucrone: two orogenic cycles

14

recorded in eclogite-facies gneiss from the southern Armorican Massif (Vendée, France). *Int Ecl Field Symp, Lochalsh, Scotland, Abstr* 33–34

Hacker BR, Calvert A, Zhang RY, Ernst G, Liou JG (2003) Ultrarapid exhumation of ultrahigh-pressure diamond-bearing metasedimentary rocks of the Kokchetav Massif, Kazakhstan? *Lithos* 70: 61–75

Hawthorne FC, Henry DJ (1999) Classification of the minerals of the tourmaline group. *Eur J Mineral* 11: 201–215

Hemley RJ (1987) Pressure dependence of Raman spectra of SiO_2 polymorphs: α-quartz, coesite and stishovite. In: Manghnani MH, Syono Y (eds.) *High-pressure research in mineral physics*, 347–359, American Geophysical Union, Washington, DC

Henry DJ, Dutrow BL (1994) Tourmaline in metamorphic rocks: A monitor of boron flux. *Geol Soc Am, Abstr Progr* 26: A449

Henry DJ, Dutrow BL (2002) Metamorphic tourmaline and its petrologic applications. In: Grew ES, Anovitz LM (eds.) *Boron: mineralogy, petrology and geochemistry*, vol. 33 of *Rev. Mineral.*, chap. 10, 503–557, Mineral. Soc. Am., Washington, DC, 2nd edn.

Hermann J (2003) Experimental evidence for diamond-facies metamorphism in the Dora-Maira massif. *Lithos* 70: 163–182

Hermann J, Rubatto D, Korsakov A, Shatsky VS (2001) Multiple zircon growth during fast exhumation of diamondiferous, deeply subducted continental crust (Kokchetav massif, Kazakhstan). *Contrib Mineral Petrol* 141: 66–82

van Hinsberg VJ, Marschall HR (2007) Boron isotope and light element sector zoning in tourmaline; Implications for the formation of B-isotopic signatures. *Chem Geol* 238: 141–148

Ishikawa T, Nakamura E (1992) Boron isotope geochemistry of the oceanic crust from DSDP/ODP Hole 504B. *Geochim Cosmochim Acta* 56: 1633–1639

Ishikawa T, Nakamura E (1994) Origin of the slab component in arc lavas from across-arc variation of B and Pb isotopes. *Nature* 370: 205–208

Ishikawa T, Tera F (1997) Source, composition and distribution of the fluid in the Kurile mantle wedge: constraints from across-arc variations of B/Nb and B isotopes. *Earth Planet Sci Lett* 152: 123–138

Ishikawa T, Tera F, Nakazawa T (2001) Boron isotope and trace element systematics of the three

volcanic zones in the Kamchatka arc. *Geochim Cosmochim Acta* 65: 4523–4537

Jiang S-Y (1998) Stable and radiogenic isotope studies of tourmaline: an overview. *J Czech Geol Soc* 43: 75–90

John T, Schenk V (2003) Partial eclogitisation of gabbroic rocks in a late Precambrian subduction zone (Zambia): prograde metamorphism triggered by fluid infiltration. *Contrib Mineral Petrol* 146: 174–191

Johnson SP, Oliver GJH (2002) High fO_2 metasomatism during whiteschist metamorphism, Zambezi Belt, Northern Zimbabwe. *J Petrol* 43: 271–290

Kalt A, Schreyer W, Ludwig T, Prowatke S, Bernhardt HJ, Ertl A (2001) Complete solid solution between magnesian schorl and lithian excess-boron olenite in a pegmatite from the Koralpe (eastern Alps, Austria). *Eur J Mineral* 13: 1191–1205

Kasemann S, Erzinger J, Franz G (2000) Boron recycling in the continental crust of the central Andes from the Paleozoic to Mesozoic, NW Argentina. *Contrib Mineral Petrol* 140: 328–343

Katayama I, Zayachkovsky AA, Maruyama S (2000) Prograde P-T records from inclusions in zircons from ultrahigh-pressure rocks of the Kokchetav massif, northern Kazakhstan. *The Island Arc* 9: 417–427

Katayama I, Maruyama S, Parkinson CD, Terada K, Sano Y (2001) Ion micro-probe U-Pb zircon geochronology of peak and retrograde stages of ultrahigh-pressure metamorphic rocks from the Kokchetav massif, northern Kazakhstan. *Earth Planet Sci Lett* 188: 185–198

King RW, Kerrich R (1989) Strontium isotope composition of tourmaline from gold lode deposits of th Archean Abitibi Greenstone Belt (Ontario-Quebec, Canada): implications for source reservoirs. *Chem Geol* 79: 225–240

Korsakov AV, Hermann J (2006) Silicate and carbonate melt inclusions associated with diamonds in deeply subducted carbonate rocks. *Earth Planet Sci Lett* 241: 104–118

Korsakov AV, Theunissen K, Smirnova LV (2004) Intergranular diamonds derived from partial melting of crustal rocks at ultrahigh-pressure metamorphic conditions. *Terra Nova* 16: 146–151

Korsakov AV, Theunissen K, Kozmenko OA, Ovchinnikov YI (2006) Reaction textures in clinozoisite gneisses. *Russ Geol Geophys* 47: 497–510

Krosse S (1995) *Hochdrucksynthese, Stabilität*

15

und Eigenschaften der Borsilikate Dravit und Kornerupin sowie Darstellung und Stabilitätsverhalten eines neuen Mg-Al-borates. Dr. rer. nat. thesis, Ruhr-Univ. Bochum, Germany

Lappin MA, Smith DC (1978) Mantle-equilibrated orthopyroxene eclogite pods from the basal gneisses in the Selje district, western Norway. *J Petrol* 19: 530–584

Leeman WP, Sisson VB (2002) Geochemistry of boron and its implications for crustal and mantle processes. In: Grew ES, Anovitz LM (eds.) *Boron: mineralogy, petrology and geochemistry*, vol. 33, 645–708, Mineral. Soc. Am., Washington, DC, 2nd edn.

Leeman WP, Tonarini S (2001) Boron isotopic analysis of proposed borosilicate mineral reference samples. *Geostand Newsl* 25: 399–403

Liu L, Mernagh TP (1992) High-pressure Raman study of the α-quartz forms of SiO_2 and GeO_2 at room temperature. *High Temp-High Press* 24: 13–21

Ludwig T, Stalder R (2007) A new method to eliminate the influence of in situ contamination in SIMS analysis of hydrogen. *J Analyt Atom Spectrom* 22: 1415–1419

Maloney J (2007) *Lithium and lithium isotopes in tourmaline as indicators of crystallization processes: A study of San Diego County pegmatites, California*. Master's thesis, University of Missouri-Columbia, USA

Manning DAC, Pichavant M (1983) The role of fluorine and boron in the generation of granitic melts. In: Atherton MP, Gribble CD (eds.) *Migmatites, Melting and Metamorphism*, chap. 7, 94–109, Shiva Publ., Cheshire

Marschall HR, Ludwig T (2006) Re-examination of the boron isotopic composition of tourmaline from the Lavicky granite, Czech Republic, by secondary ion mass spectrometry: back to normal. Critical comment on "Chemical and boron isotopic composition of tourmaline from the Lavicky leucogranite, Czech Republic" by S.-Y. Jiang et al., Geochemical Journal, 37, 545-556, 2003. *Geochem J* 40: 631–638

Marschall HR, Altherr R, Ludwig T, Kalt A, Gméling K, Kasztovszky Zs (2006a) Partitioning and budget of Li, Be and B in high-pressure metamorphic rocks. *Geochim Cosmochim Acta* 70: 4750–4769

Marschall HR, Ludwig T, Altherr R, Kalt A, Tonarini S (2006b) Syros metasomatic tourmaline: evidence for very high-δ^{11}B fluids in subduction

zones. *J Petrol* 47: 1915–1942

Marschall HR, Altherr R, Kalt A, Ludwig T (2008) Detrital, metamorphic and metasomatic tourmaline in high-pressure metasediments from Syros (Greece): intra-grain boron isotope patterns determined by secondary-ion mass spectrometry. *Contrib Mineral Petrol* in press

Massonne HJ (2003) A comparison of the evolution of diamondiferous quartz-rich rocks from the Saxonian Erzgebirge and the Kokchetav massif: are so-called diamondiferous gneisses magmatic rocks? *Earth Planet Sci Lett* 216: 347–364

Massonne HJ, Kennedy A, Nasdala L, Theye T (2007) Dating of zircon and monazite from diamondiferous quartzofeldspathic rocks of the Saxonian Erzgebirge – hints at burial and exhumation velocities. *Mineral Mag* 71

Meyer C, Wunder B, Meixner A, Romer RL, Heinrich W (2008) Boron-isotope fractionation between tourmaline and fluid: an experimental re-investigation. *Contrib Mineral Petrol* doi:10.1007/s00410-008-0285-1

Morgan GB IV, London D (1989) Experimental reactions of amphibolite with boron-bearing aqueous fluids at 200 MPa: implications for tourmaline stability and partial melting in mafic rocks. *Contrib Mineral Petrol* 102: 281–297

Nakano T, Nakamura E (2001) Boron isotope geochemistry of metasedimentary rocks and tourmalines in a subduction zone metamorphic suite. *Phys Earth Planet Inter* 127: 233–252

Nasdala L, Smith DC, Kaindl R, Ziermann M (2004a) Raman spectroscopy: Analytical perspectives in mineralogical research. In: Beran A, Libowitzky E (eds.) *Spectroscopic methods in mineralogy*, vol. 6 of *EMU Notes in Mineralogy*, chap. 7, 281–343, European Mineral. Union, Budapest

Nasdala L, Wopenka B, Lengauer CL (2004b) Transformation of SiO_2 to the amorphous state by shearing at high pressure - Comment. *Am Mineral* 89: 912–913

Nasdala L, Widner M, Wirth R, Groschopf N, Pal DC, Möller A (2006) Alpha particle haloes in chlorite and cordierite. *Mineral Petrol* 86: 1–27

Okamoto K, Liou JG, Ogasawara Y (2000) Petrology of the diamond-bearing eclogite in the Kokchetav Massif, northern Kazakhstan. *The Island Arc* 9: 379–399

Ota T, Terabayashi M, Parkinson CD, Masago H (2000) Thermobaric structure of the Kokchetav ultrahigh-pressure–high-pressure massif deduced from north-south transect in the Kulet and

16

Saldat-Kol regions, Northern Kazakhstan. *The Island Arc* 9: 328–357

Ota T, Kobayashi K, Katsura T, Nakamura E (2008) Tourmaline breakdown in a pelitic system: impplications for boron cycling through subduction zones. *Contributions to Mineralogy and Petrology* in press

Palmer MR, Slack JF (1989) Boron isotopic composition of tourmaline from massive sulfide deposits and tourmalinites. *Contrib Mineral Petrol* 103: 434–451

Palmer MR, Swihart GH (1996) Boron isotope geochemistry: an overview. In: Grew ES, Anovitz LM (eds.) *Boron: mineralogy, petrology and geochemistry*, vol. 33 of *Rev. Mineral.*, chap. 13, 709–740, Mineral. Soc. Am., Washington, DC, 1st edn.

Parkinson CD (2000) Coesite inclusions and prograde compositional zonation of garnet in whiteschist of the HP-UHPM Kokchetav massif, Kazakhstan: a record of progressive UHP metamorphism. *Lithos* 52: 215–233

Peacock SM, Hervig RL (1999) Boron isotopic composition of subduction-zone metamorphic rocks. *Chem Geol* 160: 281–290

Pearce NJG, Perkins WT, Westgate JA, Gorton MP, Jackson SE, Neal CR, Chenery SP (1997) A compilation of new and published major and trace element data for NIST SRM 610 and NIST SRM 612 glass reference materials. *Geostand Newsl* 21: 115–144

Reinecke T (1998) Prograde high- to ultrahigh-pressure metamorphism and exhumation of oceanic sediments at Lago di Cignana, Zermatt-Saas Zone, western Alps. *Lithos* 42: 147–189

Robbins CR, Yoder HS Jr (1962) Stability relations of dravite, a tourmaline. *Carnegie Inst Washington Ybk* 61: 106–108

Rötzler K, Schumacher R, Maresch WV, Willner AP (1998) Characterization and geodynamic implications of contrasting metamorphic evolution in juxtaposed high-pressure units of the western Erzgebirge (Saxony, Germany). *European Journal of Mineralogy* 10: 261–280

le Roux PJ, Shirey SB, Benton L, Hauri EH, Mock TD (2004) In situ, multiple-multiplier, laser ablation ICP-MS measurement of boron isotopic composition (δ^{11}B) at the nanogram level. *Chem Geol* 203: 123–138

Schertl HP, Schreyer W, Chopin C (1991) The pyrope-coesite rocks and their country rocks at Parigi, Dora Maira Massif, Western Alps: detailed petrography, mineral chemistry and $P - T$ path.

Contrib Mineral Petrol 108: 1–21

Schmädicke E, Müller WF (2000) Unusual exsolution phenomena in omphacite and partial replacement of phengite by phlogopite plus kyanite in an eclogite from the Erzgebirge. *Contrib Mineral Petrol* 139: 629–642

Schmidt C, Ziemann MA (2000) In-situ Raman spectroscopy of quartz: A pressure sensor for the hydrothermal diamond-anvil cell experiments at elevated temperatures. *Am Mineral* 85: 1725–1734

Schreyer W (1985) Metamorphism of crustal rocks at mantle depth: high pressure minerals and mineral assemblages in metapelites. *Fortschr Mineral* 63: 227–261

Sharma SK, Mammone JF, Nicol MF (1981) Raman investigation of ring configurations in vitrous silica. *Nature* 292: 140–141

Shatsky VS, Sobolev NV, Vavilov MA (1995) Diamond-bearing metamorphic rocks of the Kokchetav massif (Northern Kazakhstan). In: Coleman RG, Wang X (eds.) *Ultrahigh pressure metamorphism*, 427–455, Cambridge University press, Cambridge

Shimizu R, Ogasawara Y (2005) Discovery of K-tourmaline in diamond-bearing quartz-rich rock from the Kokchetav Massif, Kazakhstan. *Mitt Österr Mineral Ges* 150: 141

Slack JF (2002) Tourmaline associations with hydrothermal ore deposits. In: Grew ES, Anovitz LM (eds.) *Boron: mineralogy, petrology and geochemistry*, vol. 33 of *Rev. Mineral.*, chap. 11, 559–644, Mineral. Soc. Am., Washington, DC, 2nd edn.

Slack JF, Palmer MR, Stevens BP, Barnes RG (1993) Origin and significance of tourmaline-rich rocks in the Broken Hill district, Australia. *Econom Geol* 88: 505–541

Smith DC (1971) A tourmaline-bearing eclogite from Sunnmöre, Norway. *Norsk Geol Tidsskrift* 51: 141–147

Smith DC (1988) A review of the peculiar mineralogy of the "Norwegian coesite-eclogite province" with crystal-chemical, petrological, geochemical and geodynamical notes and an extensive bibliography. In: Smith DC (ed.) *Eclogites and eclogite-facies rocks*, vol. 12 of *Developments in Petrology*, chap. 1, 1–206, Elsevier, Amsterdam

Smith HJ, Spivack AJ, Staudigel H, Hart SR (1995) The boron isotopic composition of altered oceanic crust. *Chem Geol* 126: 119–135

Smith HJ, Leeman WP, Davidson J, Spivack AJ (1997) The B isotopic composition of arc lavas

17

from Martinique, Lesser Antilles. *Earth Planet Sci Lett* 146: 303–314

Smith M, Yardley BWD (1994) The boron isotopic composition of tourmaline as a guide to fluid processes and boron source in the South-west England orefield: an ion microprobe study. *Mineral Mag* 58A: 856–857

Sobolev NV, Shatsky VS (1990) Diamond inclusions in garnets from metamorphic rocks: a new environment for diamond formation. *Nature* 343: 742–746

Sobolev NV, Fursenko BA, Goryainov SV, Shu JF, Hemley RJ, Mao HK, Boyd FR (2000) Fossilized high pressure from the Earth's deep interior: The coesite-in-diamond barometer. *Proc Nat Acad Sci, USA* 97: 11 875–11 879

Spivack AJ, Edmont JM (1987) Boron isotope exchange between seawater and the oceanic crust. *Geochim Cosmochim Acta* 51: 1033–1043

Straub SM, Layne GD (2002) The systematics of boron isotopes in Izu arc front volcanic rocks. *Earth Planet Sci Lett* 198: 26–39

Swihart GH, Moore PB (1989) A reconnaissance of the boron isotopic composition of tourmaline. *Geochim Cosmochim Acta* 53: 911–916

Theunissen K, Dobretsov NL, Korsakov A, Travin A, Shatsky VS, Smirnova L, Boven A (2000a) Two contrasting petrotectonic domains in the Kokchetav megamelange (north Kazakhstan): difference in exhumation mechanisms of ultrahigh-pressure crustal rocks, or a result of subsequent deformation? *The Island Arc* 9: 428–438

Theunissen K, Dobretsov NL, Shatsky VS, Smirnova L, Korsakov A (2000b) The diamond-bearing Kokchetav UHP massif in Northern Kazakhstan: exhumation structure. *Terra Nova* 12: 181–187

Tonarini S, Leeman WP, Ferrara G (2001) Boron isotopic variations in lavas of the Aeolian volcanic arc, South Italy. *J Volcanol Geotherm Res* 110: 155–170

Werding G, Schreyer W (2002) Experimental studies on borosilicates and selected borates. In: Grew ES, Anovitz LM (eds.) *Boron: mineralogy, petrology and geochemistry*, vol. 33 of *Rev. Mineral.*, 117–163, Mineral. Soc. Am., 2nd edn.

Willner AP, Rötzler K, Maresch WV (1997) Pressure-temperature and fluid evolution of quartzo-feldspathic metamorphic rocks with a relic high-pressure, granulite-facies history from the Central Erzgebirge (Saxony, Germany). *J Petrol* 38: 307–336

Appendix A. Analytical Methods

Compositions of Tur were determined using a Cameca SX 51 electron microprobe equipped with five wavelength-dispersive spectrometers (Mineralogisches Institut, Heidelberg). Operating conditions were 20 nA beam current and 15 kV acceleration voltage. The electron beam was defocused to 5 μm. A modified matrix correction was applied assuming stoichiometric oxygen and all non-measured components to be B_2O_3. The accuracy of the electron microprobe analyses of Tur and the correction procedure was checked by measuring three samples of reference tourmaline (98144: elbaite, 108796: dravite, 112566: schorl, Dyar *et al.*, 1998, 2001). Under the described conditions, analytical errors on all analyses are ±1 % relative for major elements and ±5 % relative for minor elements. A detailed description of the applied electron microprobe techniques for Tur analysis is given in Kalt *et al.* (2001).

Concentrations of H, Li, Be and B in Tur were measured by secondary ion mass spectrometry (SIMS) with a modified Cameca IMS 3f ion microprobe at the Mineralogisches Institut, Heidelberg, equipped with a primary beam mass filter. Secondary ions ^{7}Li, ^{9}Be and ^{11}B were collected under an ion-imaged field of 150 μm diameter (Kalt *et al.*, 2001).

Hydrogen was analysed with a nominal imaged field of 25 μm, reduced to ∼ 12 μm by using field aperture #2 (d = 750 μm). Magnetic field coils were used to compensate for (stray) magnetic fields and water contamination was further reduced using a cold-trap cooled with liquid nitrogen attached to the sample chamber of the IMS 3f . Due to the high H concentration in tourmalines the H analyses were performed at a constant beam current of 20 nA. Except for the constant beam current the method is described in Ludwig & Stalder (2007).

The relative ion yields (RIY) for H and B were determined using three different tourmalines as reference material: elbaite (98144), dravite (108796) and schorl (112566). The relative reproducibility (1σ) of the analyses of B was < 1 %. For Li the reference material was NIST SRM 610 (Pearce *et al.*, 1997) with a relative reproducibility of < 1 %. The accuracy is limited by matrix effects and the uncertainty of the element concentrations in the reference material; the relative uncertainty is estimated to be < 25 % for H, < 20 % for Li and < 10 % for B (Kalt *et al.*, 2001).

18

Between 6 and 17 Li, Be and B analyses and 3 to 6 H analyses were performed on Tur in each sample. However, note that the determination of the accurate amount of B cations per formula unit requires a full chemical analysis including H_2O and Li_2O contents and Fe^{2+}/Fe^{3+} ratios. The amount of B calculated with all Fe as Fe^{2+} decreases by 0.01 cpfu per 1 wt% FeO converted to Fe_2O_3.

B isotope ratios of Tur were also measured with the Heidelberg Cameca IMS 3f. Primary ion beam was $^{16}O^-$ accelerated to 10 keV with a beam current of 1 nA, resulting in count rates for ^{11}B of $\sim 2 \times 10^5\,s^{-1}$ and $\sim 5 \times 10^4\,s^{-1}$ for ^{10}B on Tur, collected by a single electron multiplier. Diameter of the 1 nA spot was $5 - 10\,\mu m$. The energy window was set to 50 eV and no offset was applied. 50 cycles were measured on each analysis spot with counting times of 3.307 s and 1.660 s on ^{10}B and ^{11}B, respectively. Presputtering lasted for 5 min and settling time between two different masses was 200 ms, resulting in total analysis time for one spot of approximately 10 min. Internal precision of a single analysis was 1 ‰ (2σ). Boron isotopic compositions of samples are reported in delta notation ($\delta^{11}B$ in ‰) relative to the SRM 951 accepted value (Catanzaro *et al.*, 1970). Instrumental mass fractionation was corrected by using three samples of proposed reference tourmaline (98114: elbaite, 108796: dravite, 112566: schorl; Leeman & Tonarini, 2001). Reproducibility of measured isotope ratios during the analytical session (eight days) was ± 1.0 ‰ (2σ).

Raman spectra were obtained by means of a Horiba Jobin Yvon LabRam-HR800 spectrometer equipped with Olympus BX41 optical microscope, a grating with 1800 grooves per mm, and Peltier-cooled charge-coupled device (CCD) detector. Spectra were excited with the He-Ne 632.8 nm emission. The laser power was ~ 8 mW, which is well below the threshold for any heating effects that hypothetically could be caused by intense local absorption of the laser light. With confocal arrangement of the optical beam path, and using the Olympus $100\times$ objective (numerical aperture 0.9), the lateral resolution was on the order of $1.5\,\mu m$. Wavenumber calibration was done using the Rayleigh line and neon lamp emissions. The wavenumber accuracy was better than $0.5\,cm^{-1}$ and the spectral resolution was $\sim 0.8\,cm^{-1}$. For reference spectra and band assignment of coesite see Sharma *et al.* (1981) and Boyer *et al.* (1985), and for a description of the α-quartz spectrum see Etchepare *et al.* (1974). More experimental details are given in Nasdala *et al.* (2006).

19

D Author's publications related to this thesis

D.1 Papers in peer-reviewed journals

Luvizotto G, Zack T, Meyer H, Ludwig T, Triebold S, Kronz A, Münker C, Stockli D, Prowatke S, Klemme S, Jacob DE, von Eynatten H (in press) Rutile crystals as potential secondary standards for microanalysis. *Chemical Geology* doi: 10.1016/j.chemgeo.2008.04.012

Luvizotto GL and Zack T (in press) Nb and Zr behavior in rutile during high–grade metamorphism and retrogression: An example from the Ivrea–Verbano Zone. *Chemical Geology* doi: /10.1016/ j.chemgeo. 2008.07.023

Triebold S, von Eynatten H, Luvizotto GL, Zack, T (2007) Deducing source rock lithology from detrital rutile geochemistry: An example from the Erzgebirge, Germany. *Chemical Geology* 244, 421436.

Zack T, Luvizotto GL (2006) Application of rutile thermometry to eclogites. *Mineralogy and Petrology* 88, 1438–1168.

D.2 Papers submitted to peer-reviewed journals

Marschall HR, Korsakov AV, Luvizotto GL, Nasdala L, Ludwig, T (Subm.) On the occurrence and boron isotopic composition of tourmaline in (ultra)high-pressure metamorphic rocks. *Submitted to the Journal of the Geological Society*

Zack T, Luvizotto GL, Triebold S, von Eynatten H (Subm.) Rutile occurrence and trace element behavior in low- to medium-grade metasedimentary rocks. *Submitted to Mineralogy and Petrology.*

D.3 Abstracts

Luvizotto GL, Zack T (2006) Tracing dehydration melting and late fluid influx of metapelitic rocks using the texture and geochemistry of rutile. In: *Granulites and Granulites 2006* (available on: http://www.geol.umd.edu/pages/meetings/Gran&Gran Tables.htm) p. 45

Luvizotto GL, Zack T (2007) Geochemical trends in rutile forming reactions. *Geochimica et Cosmochimica Acta* 71, A604–A604

Stockli D, Wolfe M, Blackburn T, Blackburn T, Zack T, Walker J, Luvizotto GL (2007) He diffusion and (U-Th)/He thermochronometry of rutile. In: *American Geophysical Union, Fall Meeting 2007*, abstract V23C-1548

Triebold S, von Eynatten H, Zack T, Luvizotto GL, (2006) A temperature history of the Erzgebirge (Germany): rutile records in modern sands. In: von Eynatten, H., Dunkl, I., Fischer, C., Karius, V., Ruppert, H. (Eds.), Sediment 2006, Abstracts and Field Trips. Schriftenreihe der Deutschen Gesellschaft für Geowissenschaften 45, p. 171

Triebold S, von Eynatten H, Zack T, Luvizotto GL (2006) Application and evaluation of the new Zr-in-rutile thermometer: An example from the Erzgebirge, Germany. In: *Berichte der Deutschen Mineralogischen Gesellschaft* 1/2006

Triebold S, von Eynatten H, Zack T, Luvizotto GL (2006) The Geochemistry of rutile in modern sediments from the Erzgebirge, Germany. *Geophysical Research Abstracts* 8, 09733, 2006

Zack T, Luvizotto GL, (2005)   Application of rutile thermometry to eclogites. In: *AGU Fall Meeting Abstracts* pp. A1565+

Zack T, Moraes R, Luvizotto GL (2005)   Rutile thermometry: State of the art and outlook. *Mitt. Österr. Miner. Ges.* 150, 170

Zack T, Luvizotto GL, Moraes R, Moeller A, Kronz A (2006)   Rutile and Zircon Thermometry of Granulites: Premetamorphic Relicts, Prograde Growth, Disequilibrium and Diffusional Resetting. In: *Granulites and Granulites 2006* (available on: www.geol.umd.edu/pages/meetings/ Gran&GranTables.htm). p. 98

Zack T, Luvizotto GL, Barth M, Stockli D (2007)   U/Pb Rutile Dating in Granulite-Facies Rocks by LA-ICP-MS. *Eos Trans. AGU, Eos Trans. AGU*, 88, Fall Meet. Suppl., Abstract V34C-05

Zack T, Luvizotto GL, Stockli DF, Barth M (2008)   Texturally controlled U/Pb dating of rutile from the Ivrea Zone. *Geochimica et Cosmochimica Acta* 72, A1069

Acknowledgements

your patience during my *"why age"* in Germany. I'll never forget those *after six beers* in our office ...

I would like to thank, from the bottom of my heart, my friends Peter and Suzana. You've always been our family here in Germany.

I wish to thank, and I'll always do, Jimi Hendrix, Stevie Ray Vaughan, John, George, Paul and Ringo for giving me endless inspiration.

I sincerely thank my parents, Angela and Ismael, for many years of constructive support and for making all my dreams come true. I also thank my brothers and *bandmates* Andre Luiz Luvizotto and Mauly Bottene for all the good moments we've spent together (essentials, I would say!). Remember guys: *It is a long way to the top if you want to rock 'n' roll*.

I would especially like to thank my wife, Paula, for her love, understanding and patience and for making our *German adventure* a very pleasant one.

Eidesstattliche Erklärung

Hiermit erkläre ich, George Luiz Luvizotto, geboren am 04.04.1978 in Cerquilho - SP, Brasilien, an Eides statt, dass ich die vorliegende Dissertation selbst verfasst und mich dabei keiner anderen als der von mir ausdrücklich bezeichneten Quellen und Hilfen bedient habe.

Ich, George Luiz Luvizotto, geboren am 04.04.1978 in Cerquilho - SP, Brasilien, erkläre zudem an Eides statt, dass ich an keiner anderen Stelle ein Prüfungsverfahren beantragt habe, dass ich die Dissertation nicht in dieser oder anderer Form bereits anderweitig als Prüfungsarbeit verwendet habe und dass ich sie an keiner anderen Fakultät als Dissertation vorgelegt habe.

Heidelberg, October 26, 2008

George Luiz Luvizotto

Declaration of independent research achievements

Hereby I, George Luiz Luvizotto, declare that I have made the following contributions to the scientific articles presented in this thesis.

Title: Rutile crystals as potential trace element and isotope mineral standards for microanalysis

Authors: G. L. Luvizotto, T. Zack, H.P. Meyer, T. Ludwig, S. Triebold, A. Kronz, C. Münker, D. Stockli, S. Prowatke, S. Klemme, D. E. Jacob, H. von Eynatten.

Status: Article in press in Chemical Geology (doi: 10.1016/j.chemgeo.2008.04.12)

George L. Luvizotto carried out the selection, documentation and characterization of potential rutile mineral standards by reflected light microscopy, BSE imaging and WDS, EMP and SIMS analyses. The most homogeneous rutiles were sent to other laboratories by him in order to get high precision trace element and isotope data (ID-MC-ICP-MS, LA-ICP-MS, TIMS - techniques not available at the Mineralogisches Institut, Universität Heidelberg). Further EMP data was also obtained an the Geowissenschaftliches Zentrum, Universität Göttingen. Analyses carried out outside the Universität Heidelberg were performed by the co-authors. G. L. Luvizotto interpreted the results obtained by all techniques (homogeneity of the grains, comparison of techniques, etc.) and prepared the manuscript (text, images and tables). Co-authors participated in the discussion, especially regarding topics related to the analytical techniques.

PD Dr. Thomas Zack
(supervisor)

Dr. Hans-Peter Meyer
(co-author)

Title: Nb and Zr behavior in rutile during high–grade metamorphism
and retrogression: An example from the Ivrea–Verbano Zone

Authors: G. L. Luvizotto and T. Zack

George L. Luvizotto carried out field work (sample collection), sample description, petrography, BSE imaging and trace element analyses (EMP and SIMS) of rutile and biotite. George L. Luvizotto also interpreted the data (textural relationships between rutile and biotite, trace element behavior and temperature records) and prepared the manuscript (text, figures and tables). Dr. Thomas Zack took part in the field work, carried out LA-ICP-MS analyses of rutiles and biotite (in order to check results obtained by EMP and SIMS) and actively participated in the interpretation and discussion of the results.

PD Dr. Thomas Zack
(supervisor / co-author)

Title: Rutile occurrence and trace element behavior in low- to medium-grade metasedimentary rocks

Authors: G. L. Luvizotto, T. Zack., S. Triebold, H. von Eynatten

Status: Article submitted to Mineralogy and Petrology

George L. Luvizotto carried out field work (sample collection), sample description, petrography, BSE imaging and trace element analyses (EMP and SIMS) of rutile and ilmenite. George L. Luvizotto also interpreted the data (textural relationships between rutile and ilmenite, trace element behavior during prograde rutile formation and temperature records) and prepared the manuscript (text, figures and tables). Dr. Thomas Zack, Prof. Dr. Hilmar von Eynatten and Silke Triebold took part in the field work and helped in the interpretation and discussion of the results. Prof. Dr. Hilmar von Eynatten and Silke Triebold were particularly involved in the discussions about rutile in recent sediments.

PD Dr. Thomas Zack   Prof. Dr. Hilmar von Eynatten
(supervisor)   (co-author)

Title: Application of rutile thermometry to eclogites

Authors: T. Zack. and G. L. Luvizotto

Status: Article published in Mineralogy and Petrology 88, 69–85

George L. Luvizotto carried out the characterization (petrography, BSE imaging) and EMP and SIMS analyses (rock forming minerals and rutiles) of the eclogites form Erzgebirge. G. L. Luvizotto also helped in the interpretation and discussion of the data.

PD Dr. Thomas Zack
(supervisor / author)

Title: Deducing source rock lithology from detrital rutile geochemistry: An example from the Erzgebirge, Germany

Authors: S. Triebold, H. von Eynatten, G. L. Luvizotto, T. Zack

Status: Article published in Chemical Geology 244, 421-436

George L. Luvizotto provided all data regarding rutiles from rock samples (sample description, petrography, BSE imaging and trace element analyses). G. L. Luvizotto also took part in the discussion about the geological divisions of the area (including the preparation of the geological map), the metamorphic conditions of the rocks and the correlation between the data obtained for detrital rutiles and rutiles from rock samples.

PD Dr. Thomas Zack   Prof. Dr. Hilmar von Eynatten
(supervisor)   (co-author)

Title: On the occurrence and boron isotopic composition of tourmaline in (ultra)high-pressure metamorphic rocks

Authors: H. R. Marschall, A. V. Korsakov, G. L. Luvizotto, L. Nasdala, T. Ludwig

Status: Article submitted to the Journal of the Geological Society

George L. Luvizotto provided the tourmaline bearing samples from the Erzgebirge and carried out preliminary investigations (petrography and SEM imaging) on these samples. G. L. Luvizotto provided the geological description of the area and participated in the discussions regarding the metamorphic conditions of the samples.

PD Dr. Thomas Zack   Dipl.-Phys. Thomas Ludwig
(supervisor)   (co-author)

George Luiz Luvizotto
Heidelberg, October 26, 2008